

**STATOR CORE INTERLAMINATION FAULTS AND
THEIR DETECTION BY ELECTROMAGNETIC MEANS**

A thesis submitted to The University of Manchester for the degree of
Doctor of Philosophy
in the Faculty of Engineering and Physical Sciences

2014

David Ronald Bertenshaw

School of Electrical and Electronic Engineering

CONTENTS

FIGURES	7
TABLES	11
GLOSSARY	13
NOTATIONS	14
ABSTRACT	18
DECLARATION	19
COPYRIGHT STATEMENT	19
ACKNOWLEDGEMENTS	20
Chapter 1. Introduction	21
1.1. Condition monitoring of electrical machines	21
1.2. Stator core interlamination insulation and its testing	22
1.3. Thesis aims and objectives	24
1.4. Contribution of work	24
1.5. Thesis outline	25
Chapter 2. Literature and Industrial Practice Review	28
2.1. The developing need for stator core testing	28
2.2. The high flux stator core test	29
2.3. EL CID — the first and dominant electromagnetic stator core test	32
2.4. Alternate offline electromagnetic test systems	34
2.4.1. ABB DIRIS	34
2.4.2. ICEMENERG PROFIM system	36
2.4.3. GE Racer	36
2.4.4. Siemens SMCAS	37
2.4.5. Russian EMK	37
2.4.6. INDUCOR and KES equivalent EL CID systems	39
2.4.7. Other test approaches not commercialised	39
2.5. Higher frequency testing	40
2.5.1. High flux high frequency testing	40
2.5.2. Electromagnetic high frequency testing	40
2.6. Online approaches to stator core testing	41
2.6.1. Generator Condition Monitors	41
2.6.2. Shaft voltage detection	43

2.6.3.	Research into improved online stator core fault detection	43
2.7.	Economic considerations of stator core testing.....	44
2.8.	Research into stator core fault development	46
2.9.	Research into stator core fault electromagnetic detection.....	47
2.10.	Discussion and summary.....	50
Chapter 3.	Analysis of the EL CID Electromagnetic Test	52
3.1.	Stator core excitation.....	52
3.2.	Chattock potentiometer sensor	53
3.3.	Electromagnetic detection of fault current.....	54
3.4.	EL CID phasor analysis	56
3.5.	Analysis of current and power in stator core faults.....	60
3.6.	Synchronous detection of fault signals	63
3.6.1.	Square wave synchronous demodulation	63
3.6.2.	Sine wave synchronous demodulation	65
3.7.	Fault interpretation	66
3.8.	Discussion and summary.....	67
Chapter 4.	Correlation of High Flux and Electromagnetic Tests in the Field	69
4.1.	The problem of core heating	69
4.2.	Assumed correlation of the tests	70
4.3.	Field evidence for the correlation	70
4.4.	EPRI Core Model studies.....	71
4.4.1.	Correction of standing test errors	72
4.4.2.	Correction of Quad recovery errors.....	72
4.4.3.	High flux test anomalies	72
4.5.	Normalisation of field data.....	73
4.5.1.	Selection of results	73
4.5.2.	Core size correction.....	73
4.5.3.	Short fault length correction.....	74
4.5.4.	High flux test level correction	75
4.5.5.	Buried faults correction	75
4.6.	Final high flux and EL CID correlation analysis	75
4.7.	Results statistical study	77
4.7.1.	Test for normal distribution.....	77
4.7.2.	Data analysis.....	78

4.7.3.	Correlation improvement in EPRI study	79
4.7.4.	Influence of artificial faults	80
4.8.	Discussion and summary of correlation results	80
Chapter 5.	Electromagnetic FE Models.....	83
Chapter 6.	Interaction of Multiple Faults	85
6.1.	The phenomenon of Quad recovery	85
6.2.	Practical effect of Quad recovery.....	86
6.3.	Transverse FE models	87
6.4.	Transverse lamination magnetostatic 2D FE model	87
6.5.	Transverse lamination time-harmonic 2D FE model	91
6.6.	Modelled eddy currents	95
6.7.	Discussion of transverse 2D FE model results.....	97
6.8.	Summary	99
Chapter 7.	Impact of Varying Stator Core Loss and Permeability on Electromagnetic Tests	101
7.1.	Potential scale of core loss variation	101
7.2.	Analytic study of core loss and permeability variation on EL CID	102
7.3.	Numeric example of core loss and permeability variation on Quad signals ..	103
7.4.	Field confirmation of core loss and permeability variation	106
7.5.	Discussion and summary on the problem of testability	108
Chapter 8.	Impact of Non-linear Permeability on Electromagnetic Tests	109
8.1.	Source and scale of non-linearity	109
8.2.	Relative proportions of loss components at EMT flux density levels.....	110
8.3.	Rayleigh hysteresis and magnetic field.....	112
8.4.	Determination of Rayleigh parameters	114
8.5.	Harmonic analysis and impact on measurements	118
8.6.	Discussion on impact of varying and non-linear permeability	122
8.7.	Summary	124
Chapter 9.	Construction and Validation of an Experimental Stator Core	125
9.1.	Design and construction	125
9.1.1.	Lamination keybar contact	126
9.1.2.	Lamination clamping pressure	127
9.1.3.	Model excitation level	129
9.2.	DAX8 experimental stator verification tests.....	129
9.3.	Sinusoidal flux excitation drive	131

9.4.	Core magnetic tests	131
9.4.1.	Core loss phase angle	131
9.4.2.	Epstein material tests	132
9.4.3.	DAX8 experimental core B/H curves.....	133
9.5.	Artificial fault application	134
9.6.	DAX8 scaling factor to TCS core results.....	135
9.7.	Discussion and summary.....	136
Chapter 10. Lamination Joint Reluctance in Stator Cores.....		138
10.1.	The problem of lamination joint reluctance	138
10.1.1.	Literature research	139
10.1.2.	Design advice	139
10.1.3.	Test advice.....	140
10.2.	Electrical steel anisotropy and the Toroidal model.....	141
10.3.	Development of a saturated steel B/H model.....	143
10.4.	Lamination joint magnetostatic FE analysis	145
10.5.	Lamination joint time-harmonic FE model and experimental study	148
10.6.	Discussion and review of test and manufacturing impacts	149
10.7.	Summary	150
Chapter 11. Experimental Verification of Buried Fault FE Models.....		151
11.1.	The problem of buried faults.....	151
11.2.	Fault position and application	152
11.3.	Design and FE modelling of buried fault test sites	153
11.4.	Scaling between 3D FE model and DAX8 core.....	155
11.5.	Measurement results of buried faults at equal flux	157
11.6.	Fault current measurements	158
11.7.	Measurement results of buried faults at equal fault current	160
11.8.	Modelling the impact of packet air gaps on buried faults.....	161
11.8.1.	Magnetic potential developed by axial fault current	164
11.8.2.	Core body transverse 2D FE model of axial flux divergence	166
11.8.3.	Fault region transverse 2D FE model of fault mpd	169
11.8.4.	Transverse tooth 2D model of axial flux divergence	171
11.8.5.	Application of transverse 2D models to 3D FE models.....	173
11.9.	Analysis of errors	174
11.10.	Detection sensitivity of fault currents.	175

11.11. Discussion	177
11.12. Summary	180
Chapter 12. Conclusions	181
12.1. Review of presented work.....	181
12.1.1. Literature review and comparison of stator core tests.....	181
12.1.2. Analysis of EL CID electromagnetic test	182
12.1.3. Correlation of EMT and HFT in the field	182
12.1.4. Interaction of multiple faults	183
12.1.5. Impact of varying core loss and permeability on electromagnetic tests.....	183
12.1.6. Impact of varying and non-linear permeability on electromagnetic tests ..	183
12.1.7. Impact of lamination joint reluctance on stator core tests	184
12.1.8. Experimental verification of buried fault FE models	184
12.2. Significant contributions of thesis.....	185
12.3. Limitations of the research.....	186
12.4. Published work from this research	186
12.5. Relevance to Industry.....	187
12.6. Future work	187
REFERENCES.....	190
APPENDICES	
Appendix A. Analysis of Alternate Electromagnetic Test Systems	205
Appendix B. Stator Reliability Studies	223
Appendix C. Field Experience with Quad Recovery	227
Appendix D. Power in Stator Magnetic Fields.....	232
Appendix E. Test Equipment.....	235
Appendix F. DAX8 Excitation Drive and Linearisation	236
Appendix G. Lamination Toroidal Permeability	240

Word count including footnotes and endnotes: 76,523

FIGURES

Figure 1.1	Stator core fault circuit	22
Figure 1.2	(a) Core teeth damage (© Iris Power 2005), (b) Stator core fault with melt holes burnt through (© IEEE [19]).....	23
Figure 2.1	Turbo-generator maximum ratings from 1940–2010 (US and EU)	29
Figure 2.2	(a) HFT windings of turbo-generators (© C. Maughan [40]), (b) hydro-generator (© Electrical Times [41]).....	30
Figure 2.3	HFT IR images, (a) single core fault, (b) distributed damage.....	31
Figure 2.4	(a) Original CEGB EL CID equipment (© CEGB Research [65]), (b) EL CID Evolution (© Qualitrol Iris Power 2008).....	33
Figure 2.5	(a) EL CID test in a turbo-generator, (b) a hydro-generator	34
Figure 2.6	DIRIS measurement coil on stator core (© IEEE 2001 [71]).....	35
Figure 2.7	Total fault powers and temperature rise for DIRIS and EL CID detected faults	36
Figure 2.8	GE iron core probe in slot (© IEEE 2003 [77])	37
Figure 2.9	Specific fault power with tooth width for varying test voltage field.....	38
Figure 2.10	Hydro Quebec injection probe [104].....	39
Figure 2.11	Qualitrol Iris Power RIV-702 robotic vehicle entering air gap of turbo-generator	46
Figure 3.1	Stator core excitation winding and induced flux	52
Figure 3.2	(a) 250 mm Chattock potentiometer, (b) Chattock positioned across stator fault.....	53
Figure 3.3	Chattock potentiometer fault current detection	54
Figure 3.4	Chattock field integration paths in practice.....	55
Figure 3.5	Original EL CID phasor diagram with assumed Phase and Quad axes	57
Figure 3.6	Excitation and Chattock relationship.....	57
Figure 3.7	Core loss angle variation with excitation for M310-50A electrical steels ...	59
Figure 3.8	Combined phasor diagram and EL CID axes.....	59
Figure 3.9	Stator core excitation and fault circuit with phase relationships.....	60
Figure 3.10	(a) Normalised Quad signal and service fault power, (b) Quad error compared to no core loss, with ratio of $R_f/\omega L_f$ and core loss angle.	62
Figure 3.11	EL CID functional block diagram	63

Figure 3.12	Slot trace with fault. Left scale Quad (red trace) -200 to +80 mA, right scale Phase (blue trace) 0 to 2000 mA, horizontal scale Distance 0 to 2 m).....	66
Figure 4.1	Chattock relative sensitivity curve fitted to 3D FE and experimental results.....	74
Figure 4.2	Uncorrected field data correlation with mean	76
Figure 4.3	Corrected field data correlation with mean and lower/upper quartiles	76
Figure 4.4	(a) Turbo-generator corrected correlation, (b) hydro-generator corrected correlation.....	77
Figure 4.5	Test and Normal correlation distributions.....	77
Figure 4.6	Probability plot test.....	78
Figure 4.7	(a) Original EPRI study correlation, (b) corrected EPRI study correlation.....	79
Figure 6.1	Plot of Quad mpd obtained from 2D FE (© C. W. Ho [72]).....	86
Figure 6.2	Detection of buried tooth fault on multiple slots.....	86
Figure 6.3	Model orientation and axes (© C. W. Ho [72]).....	88
Figure 6.4	Segmentation layout with fault axis (red line)	89
Figure 6.5	Magnetostatic FE model fault regions and axes for all models. View on edge of laminations inside bore (lamination joint air gaps inset).....	89
Figure 6.6	Magnetostatic FE model — whole 180° model (axes as Figure 6.5).....	90
Figure 6.7	20 mm fault magnetostatic FE flux distribution model (axes as Figure 6.5).....	90
Figure 6.8	10, 40 and 136 mm fault length Quad recovery potentials around half-circumference	91
Figure 6.9	30 mm fault length half-packet ac model (axes as Figure 6.5)	92
Figure 6.10	10 mm model flux distribution for first 200 mm x-axis (axes as Figure 6.5).....	93
Figure 6.11	20 mm model flux distribution (flux density as Figure 6.10).....	93
Figure 6.12	30 mm model flux distribution (flux density as Figure 6.10).....	93
Figure 6.13	40 mm model flux distribution (flux density as Figure 6.10).....	93
Figure 6.14	Plot of detected 100 mm Chattock mpd along x-axis for modelled faults ...	94
Figure 6.15	Plot of total fault flux along x-axis for modelled faults.	95
Figure 6.16	Fault and eddy current density distribution in 30 mm fault model near fault.....	96

Figure 6.17	Eddy current density distribution in 30 mm fault model around half-core	96
Figure 6.18	Mean eddy current density around packet for positive half modelled 30 mm fault.....	97
Figure 6.19	Half-overlap eddy currents from axial flux (© IEEE [209]).....	99
Figure 7.1	Varying core loss phasor diagram around core	103
Figure 7.2	Stator core normal and variance regions	104
Figure 7.3	DAX8 Quad signal from local variation in core loss and permeability, for 10 & 50% proportion of affected core at constant 4% flux density	105
Figure 7.4	False colour map of Quad signals for 30 inches of stator length	106
Figure 7.5	Robotic stator core stacking (© Siemens 2010).....	107
Figure 7.6	Spread of core loss and relative permeability at 0.05 T	107
Figure 8.1	50 Hz relative permeability variation with magnetic field strength of DAX8 stator.....	109
Figure 8.2	Computed magnetic field strength and flux density waveforms for DAX8 Rayleigh hysteresis	110
Figure 8.3	Hysteresis and eddy current magnetic field strength phasors	111
Figure 8.4	Magnetic field strength reduction to eliminate eddy current loss with varying core loss.....	112
Figure 8.5	DAX8 low flux density measured and Rayleigh predicted B/H curves.....	115
Figure 8.6	Measured and predicted DAX8 Rayleigh hysteresis loops	115
Figure 8.7	50 Hz magnetic field strength estimation of μ_{ri} from Cogent steel data	116
Figure 8.8	Flux density estimation of μ_{ri} and γ from Cogent steel data	117
Figure 8.9	Core loss extrapolation to 0.05 T from Cogent steel data	118
Figure 8.10	EL CID phasor diagram of detected harmonic signals.....	120
Figure 9.1	DAX8 lamination drawing	126
Figure 9.2	(a) Stator 3D design models, (b) assembled experimental stator core	126
Figure 9.3	Conductive packing between laminations and part inserted keybar	127
Figure 9.4	Core stacking factor with compression pressure	128
Figure 9.5	Electromagnetic verification test results maximum -ve Quad signal	130
Figure 9.6	(a) Slot 9 HFT test results after 120 mins, (b) HFT temperature rises with time.....	130
Figure 9.7	Normalised DAX8 flux and current waveforms at 0.056 T flux density ...	132
Figure 9.8	CDW M310-50A B/H datasheet curve and comparators	132

Figure 9.9	DAX8 B/H stator core test with CDW Toroidal model and Cogent M310-50A toroidally corrected steel.....	134
Figure 9.10	(a) Surface fault locations, (b) microscope image of etched fault surface .	134
Figure 9.11	(a) Fault clamp for Fault_1, (b) fault wire application.....	135
Figure 9.12	Scans of Quad values for Fault_1 faults (top to base).....	136
Figure 10.1	Typical and actual B/H curves for high flux tests	140
Figure 10.2	Variation of flux density and permeability anisotropy K_A with magnetic field.....	141
Figure 10.3	Rolling (RD) and transverse (TD) lamination directions	142
Figure 10.4	Flux density and excitation current waveforms at 1.2 T for DAX8 core ...	143
Figure 10.5	(a) Extrapolated differential susceptibility to 2.8 T, (b) resultant B/H curve	145
Figure 10.6	Lamination joints with flux streamlines (red) and model region (not to scale).....	146
Figure 10.7	Lamination joint flux density FE model at 1.2 T stator flux density	146
Figure 10.8	FE magnetostatic model B/H curve and test results.....	147
Figure 10.9	DAX8 core excitation increase due to lamination joints.....	147
Figure 10.10	Proportion of total lamination flux transferred to flanking lamination with increasing flux density.....	147
Figure 10.11	Slot mpd of test and FE models.....	148
Figure 11.1	FE model of surface and buried faults (from [72] Fig. 6.2)	152
Figure 11.2	FE Model of three buried faults, with Fault_4 active.....	154
Figure 11.3	Buried fault actual DAX8 locations	154
Figure 11.4	Buried fault test jig	155
Figure 11.5	(a) Flux density distribution in DAX8 yoke, (b) flux density variation with radius	155
Figure 11.6	Detected signal dependence on slot root pitch	156
Figure 11.7	Measured and 3D FE buried fault Quad signals scaled to 3D FE flux.....	157
Figure 11.8	(a) 3D FE flux scaled, mean fault currents from test, (b) scaled test current as proportion of 3D FE model.....	158
Figure 11.9	3D FE model fault current distributions (a) Fault_4, (b) Fault_5 and (c) Fault_6.....	159
Figure 11.10	Test fault current distributions, 3D FE flux scaled (a) Fault_4, (b) Fault_5 and (c) Fault_6	159

Figure 11.11	Measured and 3D FE buried fault Quad signals at equal fault current	160
Figure 11.12	DAX8 axial 2D FE model with Fault_6 active (detail in Figure 11.13)	163
Figure 11.13	DAX8 axial 2D FE Fault_6 model detail	164
Figure 11.14	Biot-Savart model of short fault	165
Figure 11.15	Core body transverse model section, locus visualisation	167
Figure 11.16	Core body transverse 2D FE model for 20 mm Fault_6 without packet air gap	167
Figure 11.17	Fault mpd variation with core body reluctance.	169
Figure 11.18	Detected fault mpd increase with fault length and packet air gap.....	169
Figure 11.19	Fault and tooth region transverse model loci visualisations.....	170
Figure 11.20	20 mm Fault_6 fault transverse 2D FE section model	170
Figure 11.21	MPD developed across section DE along z-axis with and without packet air gaps for 1 A fault current	171
Figure 11.22	(a) 20 mm Fault_6 tooth transverse 2D FE model without packet air gaps, (b) with packet air gaps	172
Figure 11.23	Air gap corrected 3D FE model results compared to tests at equal current.....	174
Figure 11.24	(a) 3D FE model error distributions, (b) model average error by fault length	175
Figure 11.25	3D FE modelled and experimental Quad fault current detection sensitivities	176

TABLES

Table 2.1	Correlation between K_a , EL CID Quad and EMK Fault power	38
Table 3.1	Typical STV excitation field levels for 4% flux	53
Table 4.1	Short fault corrections	74
Table 4.2	Statistical analysis of original and corrected correlations	79
Table 4.3	Effect of correlation corrections.....	79
Table 4.4	Statistical analysis of original and corrected EPRI study correlations.....	80
Table 6.1	Stator core model data	88
Table 7.1	Typical stator tooth pitches	105
Table 8.1	DAX8 magnetic loss coefficients between 0.03–0.1 T and 25–100 Hz.....	111

Table 8.2	Detection sensitivity and phase lead of harmonics relative to fundamental	119
Table 8.3	Rayleigh parameters and harmonics as % fundamental at 0.056 T.....	121
Table 9.1	Lamination resistance measurements	127
Table 9.2	Turbo-generator flux density field survey.....	129
Table 9.3	DAX8 experimental stator core parameters	129
Table 9.4	DAX8 to TCS scaling.....	135
Table 9.5	Test result of DAX8 – TCS comparison	136
Table 11.1	Buried fault positions in Ho’s FE model and DAX8	153
Table 11.2	FE records for buried faults.....	153
Table 11.3	DAX8 to 3D FE compensations for equal core flux density.....	156
Table 11.4	Biot-Savart prediction of detected Fault_6 mpd	166
Table 11.5	Packet air gap correction factors from 2D FE transverse models	174
Table 11.6	Analysis of error of 3D FE prediction of buried fault test results.....	175
Table 11.7	Quad fault current detection sensitivities, 3D FE modelled and measured.....	176

GLOSSARY

A-V	Vector magnetic potential electromagnetic FE formulation
BHEL	Bharat Heavy Electricals Limited (Indian electrical manufacturer)
CCGT	Combined Cycle Gas Turbine generating plant
CDW	C.D. Wälzholz Gmbh (German electrical steel manufacturer)
CEGB	Central Electricity Generating Board (1957-1990, UK)
Cogent	Cogent Power Ltd (UK electrical steel manufacturer, part of Tata Steel)
Core yoke	The stator core back region from slot base to rear, around the core.
DIRIS	Diagnostic Investigation with Rotor In Situ system (from Alstom)
DSP	Digital Signal Processing
EL CID	ELectromagnetic Core Imperfection Detector
ELIN	Austrian electrical manufacturer, now VA Tech ELIN since 1997
EPRI	Electrical Power Research Institute (USA)
EMK	Electromagnetic Control (ЭлектроМагнитный Контроль, Russian)
emf	ElectroMotive Force
EMT	ElectroMagnetic stator core Test
Eskom	Electricity Utility of South Africa
FE	Finite Element
FEMM	Finite Element Method Magnetics (FE software program)
FFT	Fast Fourier Transform
GCM	Generator Condition Monitor
HFT	High Flux stator core Test
HF	High Frequency (higher than 50/60 Hz)
IEC	International Electrotechnical Commission
IEEE	Institute of Electrical and Electronics Engineers (USA)
IET	Institution for Engineering and Technology (UK)
IR	InfraRed (infrared thermography)
MLS	Mean Least Squares (for trend lines)
mmf	MagnetoMotive Force (from winding or magnetizing source)
mpd	Magnetic Potential Difference (line integral of \mathbf{H} field)
MTBF	Mean Time Between Failure
NiCr	Nickel Chrome alloy
OEM	Original Equipment Manufacturer
RD	Rolling Direction (of electrical steel)

SD	Standard Deviation
TCS	Experimental stator core (made by Ho)
TD	Transverse to rolling Direction (of electrical steel)
TK	ThyssenKrupp AG (German steel manufacturer)
SiFe	Ferrosilicon steel (electrical steel)
T- Ω	Scalar magnetic potential electromagnetic FE formulation
VNIIE	Electric Power Research Institute (Russia)

NOTATIONS

Symbol	Description	SI unit
\hat{X}	^ Peak value of variables or unit vectors	
a	Proportion of core loss variance region	
A	Area	m ²
\mathbf{A}	Magnetic vector potential	T.m
b	Instantaneous magnetic flux density	T
\mathbf{B}	Magnetic flux density vector	T
B	Magnetic flux density (peak value unless stated)	T
B_D	Design magnetic flux density (peak value unless stated)	T
C_n	Constants	
D	Core yoke depth	m
$dia.$	Diameter	m
F	Fault length	m
FoS	Factor of Safety	
G_{Pn}	Phase signal detection sensitivity for harmonic n relative to fundamental	
G_{Qn}	Quad signal detection sensitivity for harmonic n relative to fundamental	
\mathbf{H}	Magnetic field strength vector	A.m ⁻¹
H	Magnetic field strength (peak value unless stated)	A.m ⁻¹
H_a	Magnetic field strength in variance area a	A.m ⁻¹
H_E	Magnetic field strength component solely generating eddy current loss	A.m ⁻¹
H_{-E}	Magnetic field strength excluding H_E	A.m ⁻¹
H_H	Magnetic field strength solely generating hysteresis loss	A.m ⁻¹
$H_{inductive}$	Magnetic field strength in phase with flux density	A.m ⁻¹

H_{real}	Magnetic field strength in phase quadrature to flux density	$A.m^{-1}$
H_n	Magnetic field strength for harmonic n	$A.m^{-1}$
H_x	Magnetic field strength on x-axis	$A.m^{-1}$
H_y	Magnetic field strength on y-axis	$A.m^{-1}$
$H_{\#}$	Magnetic field strength in material #	$A.m^{-1}$
i_e	Instantaneous excitation current	A
I	Current	A
I_e	Excitation current (total mmf from multiple turns)	A
I_f	Fault current	A
$\mathcal{I}m$	Imaginary component of complex variable	
J	Current density vector	$A.m^{-2}$
J	Current density	$A.m^{-2}$
J_S	Saturation polarization of material	T
k	Thermal conductivity	$W.K^{-1}.m^{-1}$
k_A	Anomalous core loss coefficient	$W.s.T^{-1}.rad^{-1}$
k_E	Eddy current core loss coefficient	$W.s.T^{-1}.rad^{-1}$
k_H	Hysteresis core loss coefficient	$W.s.T^{-1}.rad^{-1}$
k_S	Steinmetz hysteresis loss coefficient	
K_{1-3}	Constants	
K_A	Anisotropy of permeability	
K_E	Excitation drive error proportion due to resistance	
K_H	Hysteresis loss proportion of total loss	
l	Length	m
L_f	Fault inductance	H
M_{DE}	MPD across locus DE	A
M	Magnetisation of material	$A.m^{-1}$
M_S	Saturation Magnetisation of material	$A.m^{-1}$
n	Index number	
N	Total number of indexed items	
o/d	Outside diameter	m
p	Probability	
P (Phase)	Phase current signal	A
P_f	Fault power	W
P_L	Spatial core loss density	$W.m^{-3}$
q	Heat flow density vector	$W.m^{-2}$

Q (<i>Quad</i>)	Quadrature current signal	mA
Q_n	Quadrature current signal for slot n	mA
Q_{in}	Indicated Quadrature current signal for slot n	mA
r	Radius	m
R^2	Pearson product-moment correlation coefficient.	
R	Reluctance	H ⁻¹
R_0	Normal core body reluctance	H ⁻¹
\mathcal{R}_e	Real component of complex variable	
R_f	Fault resistance	Ω
SF	Stacking factor	
S_n	Constants	
S_C	Chattock signal detection sensitivity	V/A/Hz
S_R	Relative Chattock detection sensitivity (relative to infinite fault length)	
STV	Single Turn Voltage (total longitudinal core voltage during EL CID test)	V
t	Time	s
T	Temperature	°K or °C
THD	Total Harmonic Distortion	
v_p	EL CID instantaneous Phase signal as voltage	V
v_q	EL CID instantaneous Quad signal as voltage	V
V_C	Chattock sensor voltage	V
V_f	Fault axial voltage	V
V_P	EL CID Phase signal demodulated as a voltage	V
V_Q	EL CID Quad signal demodulated as a voltage	V
V_R	Reference voltage	V
W	Specific mass core loss	W.kg ⁻¹
W_a	Specific mass core loss in variance area a	W.kg ⁻¹
W_A	Anomalous core loss	W.kg ⁻¹
W_E	Eddy current core loss	W.kg ⁻¹
W_H	Hysteresis core loss	W.kg ⁻¹
W_L	Core loss energy density	J.m ⁻³
W_M	Magnetic energy density	J.m ⁻³
W_T	Total core loss	W
x	X axis and variable	
$\hat{x} \hat{y}$	Unit vectors	

X_W	Variance factor for regional core loss	
X_μ	Variance factor for regional permeability	
y	Y axis and variable	
z	Z axis and variable	
Z	Bipolar constant	
	Angle subtended from core axis or constant	rad
β	Constant	
γ	Rayleigh hysteresis constant	Wb.A ⁻²
ε	Quad signal error constant	mA
θ	Core loss angle (lead of H field to flux density)	rad or °
θ_a	Core loss angle in variance area a	rad or °
$\theta_{aggregate}$	Core loss angle in aggregate area	rad or °
θ_n	Harmonic loss angle (lead of H_n field to flux density)	rad or °
θ_{ref}	Angle lead of Reference axis to flux density	rad or °
λ	Angle	rad
μ	Magnetic permeability of material	H.m ⁻¹
μ_a	Magnetic permeability of material in variance area a	H.m ⁻¹
μ_0	Magnetic permeability of free space	H.m ⁻¹
μ_i	Magnetic material initial permeability at zero flux	H.m ⁻¹
μ_r	Magnetic material relative permeability	
μ_{ri}	Magnetic material initial relative permeability at zero flux	
μ_{net}	Net relative permeability along flux density mean line	
μ_{RD}	Relative permeability on RD axis	
μ_{TD}	Relative permeability on TD axis	
ρ	Density	kg.m ⁻³
ρ	Resistivity	Ω.m
σ	Standard deviation (SD)	
ϕ	Phase angle of Chattock signal to Reference	rad or °
ϕ_n	Phase angle of Chattock signal harmonic n to Reference	rad or °
Φ	Total magnetic flux	Wb
χ	Magnetic susceptibility	m.H ⁻¹
χ'	Differential magnetic susceptibility	m.H ⁻¹
ψ_n	Phase lead of filtered signal for harmonic n	rad or °
ω	Angular frequency	rad.s ⁻¹

ABSTRACT

Name of University: The University of Manchester, UK
Candidate's Name: David Ronald Bertenshaw
Degree Title: Doctor of Philosophy
Thesis Title: Stator Core Interlamination Faults and their Detection by Electromagnetic Means
Date: October 2014

Condition monitoring of large electrical machines, especially power station generators, is now an integral part of their operation to maintain reliability. This thesis studies the use of electromagnetic test (EMT) methods for the stator cores of large generators to detect interlamination insulation faults before they propagate to a level that can lead to machine failure. While the EMT has been long established, its competence compared to reference thermal tests remains anecdotal. The work seeks to establish confidence in this correlation, research certain phenomena causing potential false test results, and prove the test sensitivity of short buried faults. This is important since it is also shown that the offline EMT is the only cost-effective condition monitoring method for large stator cores.

The various EMT systems in use and the dominant EL CID system are reviewed. It is shown that despite their apparently uncorrelated metrics, there is a close equivalence between the differing fault power and current thresholds. The reference thermal high flux stator core test is assumed to be correlated to the EL CID test, but without evidence. Field research showed that there is quite a strong statistical correlation between the two tests, in accordance with the expectations. The studies also revealed the unrecognised impact of lamination segment joints on the high flux test excitation requirements.

The basic theory of EL CID is analysed to determine the test's dependence on core loss and fault inductance, showing that core loss can substantially attenuate severe fault signal detection. The demodulation of the fault signal is also analysed to determine its susceptibility to harmonics generated by variable permeability and hysteresis. A method is developed to estimate low flux density Rayleigh hysteresis from commercial steel specification data, which showed that harmonic errors will remain minor for normal steels. The impact of local variations in core loss and permeability are also analysed, and shown capable of generating substantial false error signals, verified by field experience. Their profile is identified and mitigation test strategies proposed. It is also shown that multiple substantial faults when axially aligned can interact and attenuate each other, with the influence extending around the whole circumference due to lamination eddy currents. A compensating interpretation algorithm is proposed.

Previous research had developed 3D FE models of faults buried in the core teeth and yoke to determine their detection sensitivity, but without experimental verification. A new experimental technique is developed to introduce such faults, with correction for the effects of intrusion. It is shown that the original models suffered from inaccurate fault current computation, and did not include the effect of core packet air gaps. A method of compensating for measured fault current is developed, together with new FE models to estimate the impact of packet air gaps. After correction for the problems, it was shown that the combined FE model's electromagnetic detection correlated closely with experiment, enabling a reliable determination of the EL CID sensitivity to short buried faults.

DECLARATION

No portion of the work referred to in the thesis has been submitted in support of an application for another degree or qualification of this or any other university or other institute of learning.

COPYRIGHT STATEMENT

- i. The author of this thesis (including any appendices and/or schedules to this thesis) owns certain copyright or related rights in it (the “Copyright”) and s/he has given The University of Manchester certain rights to use such Copyright, including for administrative purposes.
- ii. Copies of this thesis, either in full or in extracts and whether in hard or electronic copy, may be made **only** in accordance with the Copyright, Designs and Patents Act 1988 (as amended) and regulations issued under it or, where appropriate, in accordance with licensing agreements which the University has from time to time. This page must form part of any such copies made.
- iii. The ownership of certain Copyright, patents, designs, trademarks and other intellectual property (the “Intellectual Property”) and any reproductions of copyright works in the thesis, for example graphs and tables (“Reproductions”), which may be described in this thesis, may not be owned by the author and may be owned by third parties. Such Intellectual Property and Reproductions cannot and must not be made available for use without the prior written permission of the owner(s) of the relevant Intellectual Property and/or Reproductions.
- iv. Further information on the conditions under which disclosure, publication and commercialisation of this thesis, the Copyright and any Intellectual Property and/or Reproductions described in it may take place is available in the University IP Policy (see <http://documents.manchester.ac.uk/DocuInfo.aspx?DocID=487>), in any relevant Thesis restriction declarations deposited in the University Library, The University Library’s regulations (see <http://www.manchester.ac.uk/library/aboutus/regulations>) and in The University’s Policy on Presentation of Theses.

ACKNOWLEDGEMENTS

The first appreciation must go to my supervisor Professor Sandy Smith for initially believing that I could achieve the goal after many years from academia, and then for his support, advice and helpful encouragement in all aspects of the research.

The support of ENELEC Ltd is also acknowledged for the research, and for materials, use of test equipment and field experience.

The support of Brush Electrical Machines Ltd is acknowledged for materials supplied for the project.

But most importantly my heartfelt thanks must go to my family for their encouragement in this endeavour, especially my wife Jennifer who has endured much but given only support and unconditional love. This thesis is dedicated to her.

Chapter 1. Introduction

1.1. Condition monitoring of electrical machines

The 20th century has witnessed a remarkable series of technological developments, with the rapid rise and ubiquitous use of electro-technology being probably the most astounding. Dubbed the ‘Electric Century’ by the historian Nebeker [1], this sobriquet is supported by the almost simultaneous centennial celebrations of related institutions, IEC, IET and IEEE, while CIGRE recently celebrated its 90th anniversary [2]. The ubiquitous availability has resulted in a dependence on a continuous supply of electricity for the daily life of much of the world, and in Western society even has the attributes of an addiction [3]. This has resulted in very high requirements for the reliability and availability of public electrical supply.

The parallel drive for efficiency has however led to the dominance of large central generation facilities, with single generators sometimes exceeding 1,000 MW. This has increased dependence on their individual reliability due to the impact of singular failures. Recent trends to include substantial renewable generation have not assisted this. Horner [4] warns that their must-run status, despite irregularity of supply, is putting ‘enormous strain’ on the system with brownouts increasing, despite politicians promising policies to ensure ‘the lights can stay on’ [5]. To manage this, condition monitoring to maintain reliability of generating plant is now a critical aspect of electrical plant maintenance, as described by Tavner et al. [6] (§1) and [7], and Klempner & Kerszenbaum [8] (§12.1.2). Organisations such as CIGRE [9] and EPRI [10] issue periodic reports on the subject.

The condition monitoring area of concern in this thesis is the stator core interlamination insulation. The most common stator failure in both ac generators and related large electrical ancillary motors is the winding insulation [11-13], with stator core failures fortunately rare. GE [11] reports that the stator core represented only about 4% of all stator failures. However the financial consequences of a serious stator core failure can be catastrophic; the Hunter generator failure [14] in 2000 resulted in the total destruction of the stator, and a final cost of \$287M to return to service. While Hunter was an extreme example, the potential costs of unscheduled repairs and lost generation ensures operators maintain regular programmes of inspection and test [9], to try to detect stator core degradation at an early and more readily repairable stage.

The reliability of stator core interlamination insulation condition monitoring test methods and interpretation is consequently of great importance. The lack of any effective

online monitoring methods results in a sole reliance on the effectiveness of scheduled offline tests for detecting developing faults. These need to avoid both false positive results, incurring unnecessary cost and delay, and false negatives where dangerous developing faults may go undetected.

1.2. Stator core interlamination insulation and its testing

The stator cores of large ac electrical machines, especially power station generators, are constructed from stacks of electrical steel laminations, each coated with a thin layer of electrical insulation to limit the influence of induced eddy currents in the core. Large generators (e.g. 500 MW) can weigh over 200 tonnes and contain some 200,000 laminations. The cores are constructed using ‘keybars’ or building bars to link all the laminations together. The laminations are normally in metallic contact with (and often welded to) the keybars, which transmit the machine torque to the supporting frame. Consequently if damage occurs which connects the laminations together, an electrical circuit is formed around the toroidal core flux, and a fault current can flow, as shown in Figure 1.1.

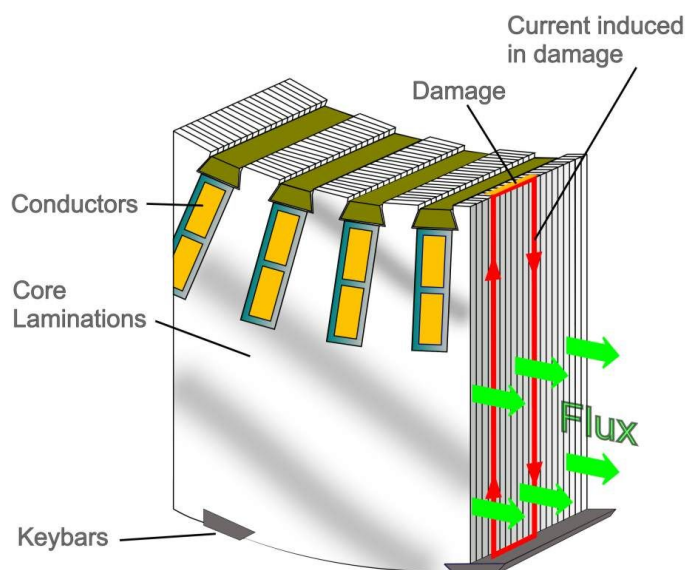


Figure 1.1 Stator core fault circuit

Such a stator core fault can occur from a number of sources such as incorrect manufacture, overheating, vibration, core looseness, foreign body impact and many other mechanisms [15, 16] that can damage the interlamination insulation. The very low electrical resistance of the laminations and keybars causes the majority of the heating from the fault current to occur within the fault, resulting in local ‘hot-spots’. Even if modest, these can reduce the life expectancy of nearby winding insulation [17] (§8.1), and as they worsen potentially develop enough energy to melt the stator iron [18, 19]. The surface and

fatigue damage example in Figure 1.2(a) will reduce machine life, while an unknown fault led to the previously mentioned Hunter failure illustrated in Figure 1.2(b). Here the core developed a melt-hole from one end to the other (5.7 m), in around 44 minutes [19].



Figure 1.2 (a) Core teeth damage (© Iris Power 2005), (b) Stator core fault with melt holes burnt through (© IEEE [19])

Monitoring and maintaining the integrity of interlamination insulation is thus an important and routine function of service testing, with the traditional high flux test (HFT) method (aka ‘Loop Test’ and ‘Ring Flux Test’) in use since c1952 [20]. While this test directly detects problematic heating, the required power levels can be very high (>1 MVA) and hazardous, and the test takes several days and staff to conduct.

Alternate low flux electromagnetic stator core test (EMT) methods have been in use since 1980 [21], with the EL CID system dominant. There are several other low flux methods of determining interlamination insulation damage, as surveyed by Tallam *et al.* [22] and Bertenshaw [23], however all require internal machine access to test. There is also no successful online means of early stator core fault detection.

The EL CID method involves inducing a toroidal ac flux in the core at typically 4% of operating level, using a temporary excitation winding inserted through the generator bore. Any fault currents induced in damaged areas are measured by sensing the mpd developed by them across slot teeth edges using a simple air-cored Chattock potentiometer [24]. Since the voltage induced in any fault circuit is in proportion to the rate-of-change of coupled flux, the resultant fault current can be detected as that mpd component in quadrature to the flux. This is recorded as the ‘*Quad*’ current with the normal recommendation that a *Quad* signal above 100 mA ‘should be regarded as significant and investigated further’ [25, 26]. The complete core bore is scanned axially along all the slots, and the detected currents recorded to develop a map of the magnetic potentials in the core, so as to identify areas of potential interlaminar insulation breakdown.

Electromagnetic stator core testing, and in particular EL CID, is in use worldwide [25] on the assumption that the test results can be relied upon to predict the thermal risk of core faults. But despite its >30 year maturity the test remains relatively little studied in terms of its efficacy and immunity to error. Industry confidence in the technique stems much more from experience than analysis. This thesis seeks to research and quantify a number of sources of error in certain circumstances, and to improve the reliability of result interpretation. The research is inevitably specific to the EL CID test due to its dominance in the industry, however many results can be read across to alternate EMT techniques with little difficulty.

1.3. Thesis aims and objectives

- i Investigate the methodologies and correlate the metrics between the differing EMT systems.
- ii Investigate and test the assumed correlation between HFT and EL CID testing.
- iii Determine the interaction of axially aligned multiple faults on test results.
- iv Determine the impact of lamination material variation on test results.
- v Investigate the source and determine the impact of varying permeability with flux density at low flux density levels on test results.
- vi Research and identify the reasons for major magnetic performance differences between electrical steel as lamination sheet and when assembled in a stator core.
- vii Develop an experimental means of testing ‘buried’ core faults situated in the core back (yoke) and use it to validate electromagnetic Finite Element (FE) models.

1.4. Contribution of work

This research contributes to the reliability of stator core interlamination insulation condition monitoring test methods and interpretation. It does this by analysing the correlation between the differing tests and existing models, and investigating previously unexpected or unexplained sources of stator core fault signal artefacts. The assumed commonplace correlation of the HFT and EL CID is investigated by analysis of field data, with results corrected by work in this thesis. This provides new statistical support for the correlation.

The interaction of axially aligned multiple faults is shown to significantly depress fault signals, while circumferential core material loss and permeability variances are proven to cause false fault signals. The means to identify and accommodate these artefacts is determined. The variation of stator steel permeability with flux density at EMT flux

levels is also shown to generate potentially interfering harmonics, however the resulting artefacts are proven to be insignificant in normal circumstances.

The poor prediction of an assembled stator core's magnetic performance from its published electrical steel data is investigated. While this is revealed to be a long known problem due to segmentation joints, the impact on stator design appears to be a forgotten issue, and the unexpected impact on high flux stator tests is analysed.

An experimental stator core was constructed and tested and used to validate previous 3D FE models of faults buried in the core yoke. A method was developed to apply the modelled buried faults, and to scale their intensity to match the model. Deficiencies in the 3D FE models are identified, requiring corrections determined from extra FE models to finally show a close correlation between model and experiment.

Six papers have been published from this work (four peer reviewed), detailed in section 12.3. In addition results from this work have been used to resolve industrial problems in several cases.

1.5. Thesis outline

The thesis is divided into sections reflecting the research aspects. The principal contents are summarised in the sections below.

Chapter 2. Literature and Industrial Practice Review

A review is completed of the origin and different approaches to testing interlamination insulation in stator cores. The HFT and many differing EMT systems are considered, with their various merits, drawbacks and differing metrics analysed and their correlation demonstrated. The approaches attempted for online testing are also studied and weaknesses examined. The prior research into electromagnetic stator core fault modelling and detection is reviewed, identifying the achievements to date and current knowledge base on which to build.

Chapter 3. Analysis of the EL CID Electromagnetic Test

The detailed operation of the EL CID test and its detection of core faults is studied with the phasor resolution of faults. An analytic model is developed of the power in core faults and the impact of core loss on their detection by Quadrature phase resolution. The demodulation process of the instrument is analysed to determine how it will respond to harmonic signals from the core.

Chapter 4. Correlation of Electromagnetic and High Flux Tests in the Field

The origins of the EL CID test 100 mA *Quad* industry threshold are studied and how, without proof, it has come to reflect an expected correlation with HFT core heating. Previous research into this issue is re-analysed using new techniques developed in this thesis, and problems corrected to show the underlying correlation. From this a full study of all accessible field data is completed, and a strong statistical correlation shown.

Chapter 5. Electromagnetic FE Models

A short review is given of the theory and methodology of the electromagnetic finite element models developed in this thesis.

Chapter 6. The Interaction of Multiple faults

The presence of multiple axially aligned faults causes a phenomenon of ‘Quad recovery’ which can act to suppress their detection. A study is completed to improve the understanding of how the flux from a core fault, and hence its magnetic field strength, is distributed in a core. This required developing transverse FE models of the core to lamination level complete with segmentation structures. The time-harmonic results show that the eddy currents develop a solenoidal field constraining the flux, in addition to the radial vents. An analytic technique is proposed to compensate test results.

Chapter 7. Impact of Varying Stator Core Loss and Permeability on Electromagnetic Tests

The standard model for the EMT assumes that the core is composed of steel with uniform magnetic properties. However variances in core loss and permeability caused by non-uniform steel have been shown to develop substantial fault signal artefacts, not due to actual interlamination insulation defects. The impact of varying electrical steel loss and permeability on the test is researched and a new model derived to quantify the effects. An interpretation technique to compensate for these artefacts is also given.

Chapter 8. The Impact of Non-linear Permeability on Electromagnetic Tests.

These tests are conducted at low flux density levels where the steel permeability is varying substantially due to Rayleigh hysteresis, shown to cause the development of harmonics in the magnetic field. A method to determine the Rayleigh hysteresis from specification data is developed, however the use of sinusoidal test flux is shown to require a numeric integration to compute the resultant harmonics. The impact of these on the EL CID test is analysed and shown to be minor and not a threat to test interpretation.

Chapter 9. Construction and Validation of an Experimental Stator Core

A short experimental stator core was needed to validate models, and is constructed with laminations designed for a 125 MVA turbo-generator. The core is validated as fault-free and correlation factors proven between it and existing 3D FE models.

Chapter 10. Lamination Joint Reluctance in Stator Cores

The stator cores of large electrical machines most commonly use half-overlap lamination joints, which cause magnetic saturation in the region of the joints at service flux levels. This effect is suspected as being the cause for a poor performance match between the laminations and assembled experimental stator core at high flux densities. While long predicted, the joint's impact on magnetic circuit design and especially high flux stator core testing is shown to remain apparently unrecognized in design and test guides. A new simulation of deeply saturated electrical steel is developed to allow the toroidal B/H response at high flux densities of an assembled stator core to be predicted with FE models. The joints are validated by experiment as the cause for the poor match. The impact on the HFT is studied.

Chapter 11. Experimental Verification of Buried Fault FE Models

A previous researcher developed 3D FE models of a range of core faults, however he only progressed to verification of surface faults. A method to artificially apply buried faults on the experimental stator core is developed, with a study to determine the compensation required due to the intrusion of the fault.

While geometric differences between the cores are accommodated, it is also shown that the original 3D FE model's omission of packet air gaps, inaccurate modelling of fault currents, and circumferential interfering images due to use of symmetry, affects the detected fault magnetic potentials. To compensate for these effects, further FE models are constructed to enable validation of the combined FE models from the test results.

Chapter 12. Conclusions

The results of the various sections of the work are brought together, indicating the significant contributions made and benefits to industry, including industrial projects that have already benefited. Papers published from this research are summarised and potential further research identified.

Chapter 2. Literature and Industrial Practice Review

The development of the electromagnetic stator core test is a significant part of the story of large electrical machines and the power supply industry. The growth of this industry and its requirements led to the development of a number of differing stator core test methods. This chapter considers the HFT and many differing EMT systems and how they correlate, the particular circumstances that favoured the EL CID system, together with various approaches attempted for online testing. The prior research into electromagnetic stator core fault modelling and detection is reviewed, identifying the achievements to date.

2.1. The developing need for stator core testing

The historical development of ac electrical generators is well known [27-32], with rapid development from the initial small dc machines of the 1870s. The invention of the Parsons steam turbine in 1884 [31], the 1891 Lauffen-Frankfurt 175 km, 3 phase demonstration transmission of Tesla's polyphase ac [30, 32]¹, the high speed cylindrical alternator rotor in 1901 [27] and silicon steel in 1902 [33] (§3) combined to deliver 25 MW machines by 1912 [28] (§X). These inventions essentially gave the turbo-generators that are still in use over 100 years later.

Initial further growth in ratings was modest. However hydrogen cooling introduced in 1936 with water cooled stator windings [32, 34, 35] by 1959, enabled the higher electrical loadings needed to deliver 500 MW in the 1960s. Growth then slowed again, with a 2 GW design threshold only just achieved at Olkiluoto² [36] in 2010. Figure 2.1 shows how the main rating enhancements occurred between 1950 and 1975 [23], when a compound power growth rate of ~32% p.a. was achieved, using BBC, Westinghouse, Siemens and Alstom data [36-38]. It can also be seen how, once the requirements for major nuclear generators (>1 GW) had been met, attention focussed on more economic air-cooled machines.

¹ Neidhöfer [32] considers that in fact Dolivo-Dobrowolsky invented the 'rotary current' concept of 3 phase ac, while Haselwander invented the first 3 phase synchronous generator in 1887.

² It will however only operate at 1792 MW.

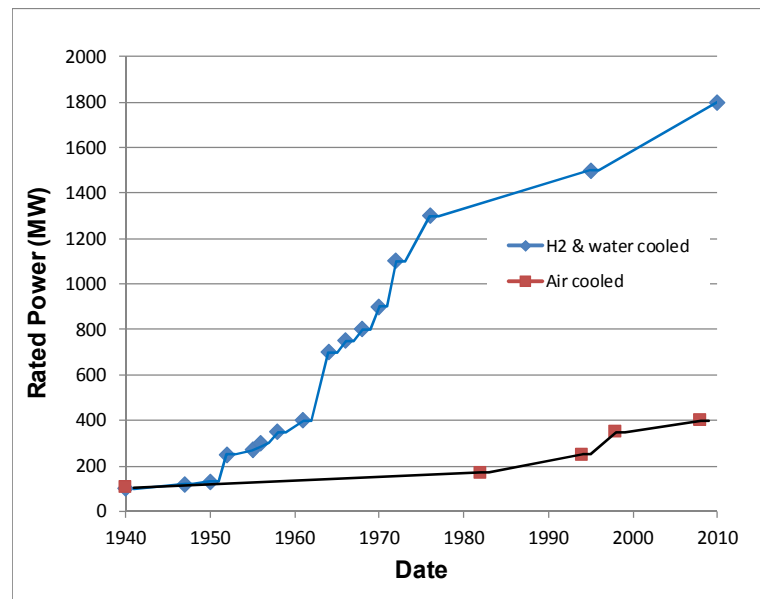


Figure 2.1 Turbo-generator maximum ratings from 1940–2010 (US and EU)

2.2. The high flux stator core test

While the modern laminated stator core structure was already dominant by 1910, initial testing was of only total core loss at full flux. The first evidence of testing for localised core faults on turbo-generators was from Tomlinson [20] in the USA in 1952 and Harbord in the UK in 1953 [39], though Maughan [40] reported it was in common use by GE in the USA in 1950. It was not yet included by Ross in his comprehensive report on tests of UK ‘waterwheel’ generators in 1955 [41], though Ridley [42] thought it was being unofficially conducted in the UK on such machines by 1953. It can be seen that these coincided with the start of the rapid rise in maximum ratings in Figure 2.1.

The technique initially was to induce a toroidal flux as near as possible to the service flux level, then to find hot-spots by touch, or cobalt chloride impregnated paper³ [43] (§14.5), paraffin wax slivers [44] and for known trouble spots, thermocouples. The metric was just to look for an ‘excessive rise’ or ‘hot spot’. By 1971 Lodge reports [45] the development of infrared (IR) thermal imaging cameras allowed establishment of a 10 °C acceptance threshold in the CEGB, being a hot-spot temperature that was realistic to repair. Lodge also demonstrated the severe thermal attenuation of core yoke faults, where a fault on a slot base under a winding was shown to have a 20:1 temperature attenuation after 1 hour between fault and tooth surface. This further supported setting a modest surface temperature threshold to avoid deep-seated faults developing severe unnoticed temperatures.

³ Turns from red to blue when crystallised water dries off. It is now considered carcinogenic.

The first HFT public standardisation in 1977 was IEEE Std 56-1977 [46], which still just looked for ‘hot spots’ after 10–20 minutes excitation at 100% flux, raised to 105% for hydro-generators in 1992 by IEEE Std 432-1992 [47] (now withdrawn). It was not until 2004 that IEEE Std 62.2-2004 [48] prescribed the HFT in detail, with a 10 °C hot-spot limit if ‘at or close to’ the rated flux density for 2 hours. It permits testing at less than 100% flux density when a ‘meaningful test can be made’, but fails to advise how to interpret this. There is no formal evidence of how 10 °C was chosen, the precedence was just hot-spots that were hot to the touch. However a committee member [49] advised that it principally derived from a US manufacturer’s in-house standards being adopted, now being reflected in procurement specifications. It has however passed the test of time, in that users find that >10 °C hot-spots can generally be repaired or at least ameliorated, thus meeting the life enhancement objective.

The only other public standards that can be identified are in Russia where RD 34.45-51.300-97 [50] requires testing at 1.0 or 1.5 T flux for 90 or 45 minutes respectively, with a <15 °C temperature rise criteria. The Romanian standard PE 116-94 [51] has the same requirements. Many OEMs have their own test standards, but are confidential.

Despite the undoubted popularity of the EMT (esp. EL CID), the tangible thermal measure ensures the HFT remains the touchstone test for many. Both CIGRE [25] and Klemptner & Kerszenbaum [8] (§11.2.1) consider that ‘both the EL CID and Flux Testing together are still required to give the best information’, while Maughan [16] advises that major repairs such as restacking should never be initiated on EL CID evidence alone. Only in Russia is an EMT officially preferred, where the Life-expired Guidelines [52] recommend it over the HFT for conducting periodic tests of turbo-generators.

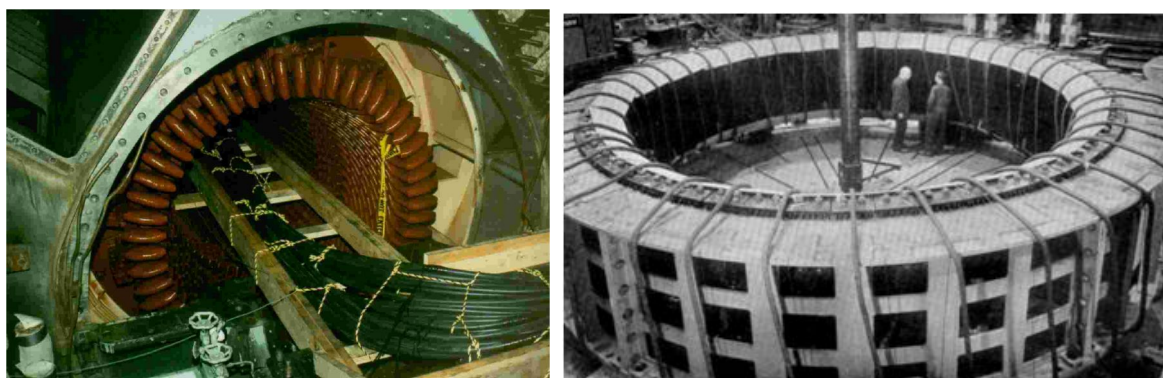


Figure 2.2 (a) HFT windings of turbo-generators (© C. Maughan [40]), (b) hydro-generator (© Electrical Times [41])

The HFT requires winding several turns of high current and voltage cable around the core, sufficient to induce 80–100% of rated flux. A separate winding turn around the core

monitors the test flux. The power needed to high flux test a large generator core can be several MVA, an example 500 MW generator [45] required 16 turns at 11 kV and 300 A for just 80% flux. Figure 2.2(a & b) gives some indication of the complexity of the setup. The high currents and voltages pose substantial safety risks to the personnel, and also the machine in case of winding fault.

IEEE Std 62.2 requires an operating flux density (1.0–1.5 T) for 2 hours, with no part of the core exceeding 10 °C differential rise over the surrounding temperatures for flux density levels ‘close to’ 100%. Testing is ceased at any time if temperatures exceed 100 °C to avoid damage. Hot spot temperatures may exceed 10 °C temporarily, as long as they blend in eventually as the core heats up. Cickaric et al. [53] report that some manufacturers advise just a 5 °C rise on new machines, as do Stone et al. [17] (§17.2.3) for large generators. Temperatures are nowadays always assessed with IR cameras with typical results illustrated in Figure 2.3(a) for a single fault and (b) for distributed major core damage.

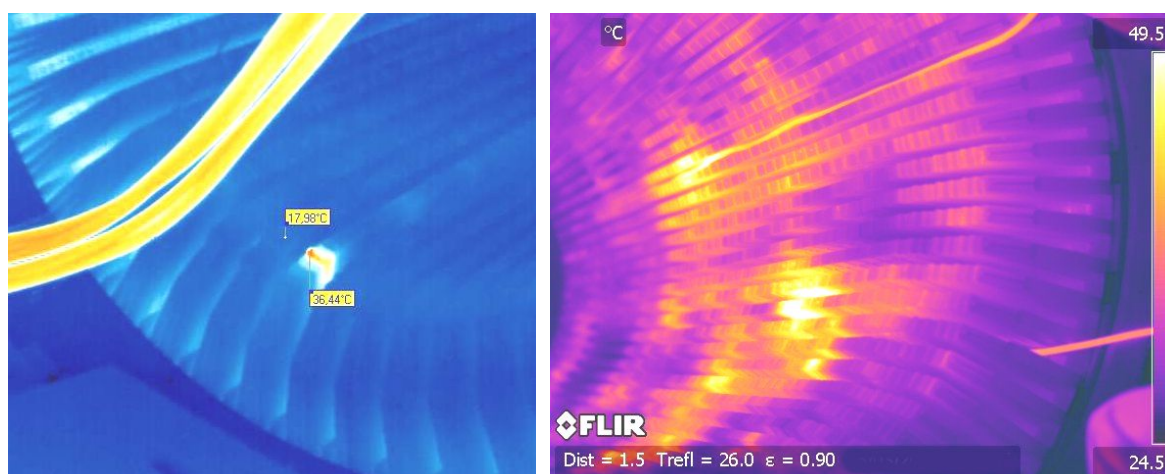


Figure 2.3 HFT IR images, (a) single core fault, (b) distributed damage

IEEE Std 62.2 supports testing at lower flux densities down to 0.9 T (i.e. typically 60% of full flux density) but is silent on interpretation. The other literature which considers this (other than the Russian method discussed in appendix A.3.1) is EPRI [15] who encourage lower flux testing if there are power limitations (rather than not test), plus an unexplained option of a 5 °C threshold. Klempner & Kerszenbaum [8] (§11.2.2) also advise that ‘some...test as low as 60%’ though does consider 80% the norm. The early CEGB tests [45] from 1975 required from 80–100% flux with constant 10 °C limit. An ad hoc 2008 EPRI user survey [54] indicated the mean test level was 81%, but showed wide variations from 60–100%. From this, the HFT is shown to be considered as an 80–100% service flux test.

Reducing the flux will have a substantial thermal effect. It is assumed that the great majority of the cooling of a fault region is conductive to the cooler body of the core (which it can only be for any fault not on the surface), and that a steady state has been reached where no more energy is being absorbed by the steel's specific heat. Then from *Fourier's law* the heat flow rate density vector \mathbf{q} will be related to the material's thermal conductivity k (a 3D field) and temperature vector gradient ∇T by the equation

$$\bar{q} = -k\nabla T. \quad (2.1)$$

The material properties are assumed unaffected by the temperature, and the heat flow rate is the electrical power input into a resistive core fault with longitudinal fault voltage V_f . The power will thus be proportional to V_f^2 , and thus flux density B^2 . From this it can be shown that the hot spot temperature rise over the surroundings ΔT is given by

$$\Delta T \propto B^2. \quad (2.2)$$

Hence a test at say 80% of full flux should have an acceptance threshold of just 6.4 °C for a hot spot fault, yet the only evidence of the 10 °C threshold reducing for reduced flux is from Siemens [55] when testing at low flux levels at a higher frequency.

This analysis assumes the heating of a core fault reaches a steady state within the normal 2 hour test time. The experimental evidence is definitely supportive of this for the temperature measured at the fault source, where a test on a slot base for a 20–90 MW class generator [56] core had stabilised in ~10 minutes. On the 400 MW class core used in the EPRI study [57], the surface fault temperatures had similarly stabilised within 30 minutes, and thereafter just rose in line with the stator core temperature rise.

2.3. EL CID — the first and dominant electromagnetic stator core test

The HFT might have been sufficient for many years, but by the 1960s in the UK the CEGB commissioned a rapid build of radical new designs using hydrogen and water-cooled windings to rebuild the UK infrastructure [34]. In 1960, 47 new design 500 MW generators were ordered [29] from four different suppliers, despite only completing trials up to 200 MW in 1959.

Installations started in 1966 and the inevitable serious problems appeared. Between 1969 and 1975, 18 core faults occurred [58], of which eight were catastrophic (a core melt), with all 4 machines at one site failing within 4 months one winter. This unheard of rate of core failure (38% of the fleet) triggered a major investigation into the root causes and even parliamentary concern due to power shortages [59]. The machines had design errors with core end heating due to excess axial flux density at high load and leading PF,

were susceptible to core faults triggered by pole slipping and also suffered a number of manufacturing faults. Core failures continued to occur on the first units of the larger 660MW machines whose installation started in 1976 [60].

This increase in stator core failure rate with the rapidly rising machine loading in the 1970s seems to have been most critical in the UK, and it was here that the EMT originated. The average outage time for these UK faults was 200 days, thus there was a strong incentive to invent a faster test than the HFT which took 3–4 days [44] and needed to be conducted several times during repairs. Between 1977–1980 the CEGB scientific research facilities⁴ developed a system to measure the magnetic field from any core fault current at just 4% of service flux levels. The resultant ELeCtromagnetic Core Imperfection Detector (EL CID) low power test [21, 61] enabled a complete core test to be done in one day, with local retesting of repairs in minutes. Five systems were eventually in use in-house [21].

The first commercialisation in 1982 by Adwel Industries⁵ [62] was based on the CEGB design shown in use⁶ in Figure 2.4(a). It consisted of an analogue Signal Processing Unit (SPU) and separate X-Axis Transducer, with results recorded on a pen plotter. This could only record the *Phase* and *Quad* values in separate tests (see section 3.4 for explanation). The benefits of digital electronics and the microprocessor led to the introduction of the Digital EL CID Model 601 in 1995 [63], recording all data with position to a PC. This was superseded in 2007 by the latest model, EL CID Evolution [64], in Figure 2.4(b).



Figure 2.4 (a) Original CEGB EL CID equipment (© CEGB Research [65]), (b) EL CID Evolution (© Qualitrol Iris Power 2008)

⁴ Developed by the Northeast region and the HQ office under John Sutton.

⁵ Qualitrol Iris Power LP in Canada now manufactures EL CID.

⁶ The person in the white coat is the main inventor John Sutton.

A typical modern test is shown in progress in Figure 2.5(a) in a 106 MW turbo-generator and (b) in a 100 MW hydro-generator. EL CID's basic means of operation is well documented [66, 67], and is analysed in Chapter 3. The EL CID metric of fault is the *Quad* fault current (analysed in section 3.4) which is proportional to the current flowing in the fault circuit. Given the stator's constant axial voltage field, the axial fault power density is thus proportional to the current. The original 1981 EL CID procedures [68] suggested 100 mA was a 'safe' level above which to start repairs because normal responses were 'flat within 50 mA'. The EL CID OEM now advises that *Quad* signals >100mA (at the standard excitation level of 4%) 'should be regarded as significant and should be investigated further' [26].

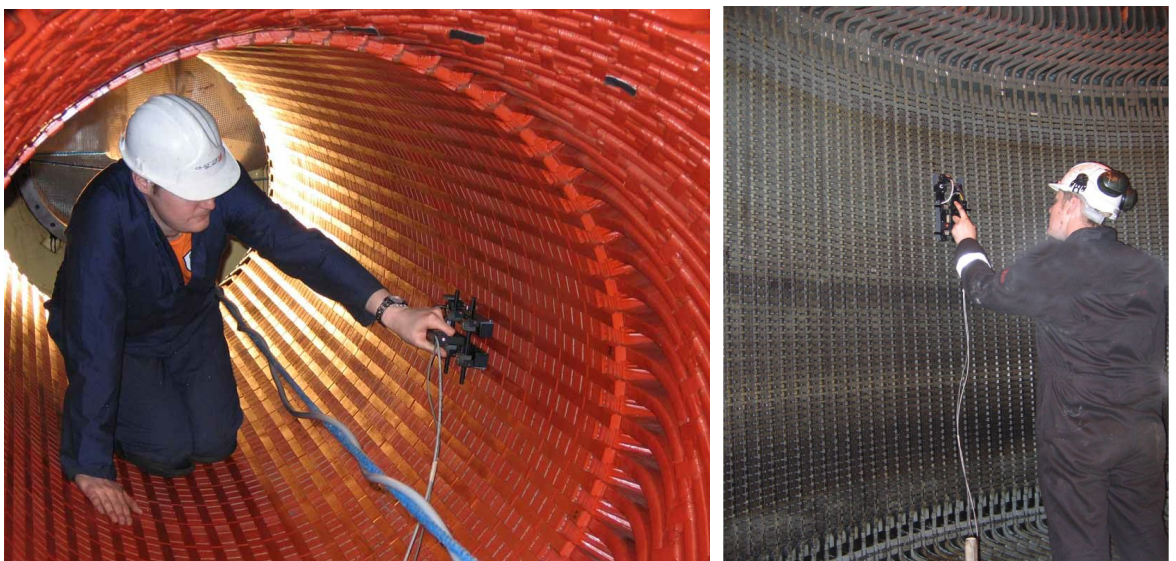


Figure 2.5 (a) EL CID test in a turbo-generator, (b) a hydro-generator

2.4. Alternate offline electromagnetic test systems

The ease and simplicity of the test compared to the HFT spurred several generator OEMs to develop similar products for their in-house use, with other companies introducing emulations or more novel variations of their own design.

2.4.1. ABB DIRIS

The Alstom DIRIS system (Diagnostic Investigation with Rotor in Situ) is analysed in full in Appendix A.1. It is the most significant alternate EMT system used internationally. It is not sold commercially but used in-house by some Alstom and ABB offices for service work. It was patented in 1991 and 2004 [69, 70] and described by Posedel in 2001 [70, 71].

Faults are detected by a flat air-cored coil spanning a core slot as shown in Figure 2.6 with the core torroidally excited at a low flux level. The coil's voltage and its phase shift

with respect to excitation is analysed to determine any increase in local mpd over normal, which is ascribed to fault current.

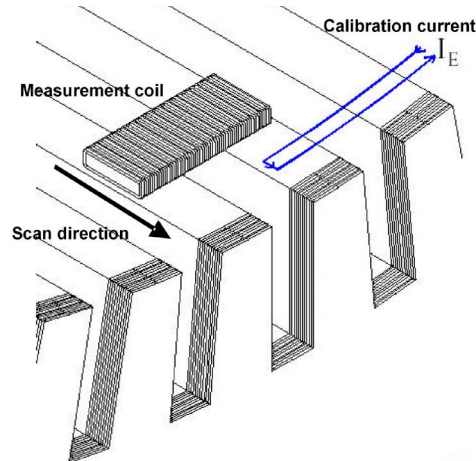


Figure 2.6 DIRIS measurement coil on stator core (© IEEE 2001 [71])

Since fault lengths are generally shorter than the coil's axial dimension, the detected currents are much less than the actual current. The system is thus calibrated against a test loop simulating a known fault current and length, with the result then scaled and ascribed a full service flux total fault power (not fault current).

The recommended DIRIS threshold power for all faults in all classes of machine is 15 W to avoid the risk of an 'iron fire' [71]. This power is the total fault power, with the fault lengths considered critical being 4–10 mm for turbo-generators and 10–20 mm for hydro-generators⁷. This power appears to be both a very different measure and a substantially higher threshold than EL CID's 100 mA *Quad* current. In a typical turbo-generator 4% rated flux generates a ~5 V/m axial voltage field, at which a 100 mA nominal *Quad* fault current apparently equates to ~3 W power in a 10 mm fault at rated flux. However when an allowance is made for the rapidly reducing Chattock sensitivity to short faults as analysed by Ho [72], then in reality the total fault power has a 12 W asymptote in a typical large turbo-generator (tested at 4% = 5 V/m) for an EL CID *Quad* reading of 100 mA.

This is estimated in Appendix A.1 for a nominal 10 mm dia. fault region where the axial thermal conductivity is assumed to be 10% of the radial [73], and shown in Figure 2.7. It leads to the surprising conclusion that the DIRIS and EL CID thresholds for fault warning are very comparable for fault lengths up to 40 mm, despite seemingly being very different. The DIRIS reported power is that in the total fault, while the heat dissipation in the core will differ greatly with length. For the same nominal 10 mm dia. fault region

⁷ The rather wide DIRIS sensor in practice prevents reliable estimation of fault lengths < 20 mm.

Figure 2.7 shows temperatures $>50\text{ }^{\circ}\text{C}$ may occur similarly for both tests at 100 mA and 15 W. This also demonstrates the common user complaint that EL CID appears to miss very small faults that still appear as a bright pinprick of heat in an IR scan.

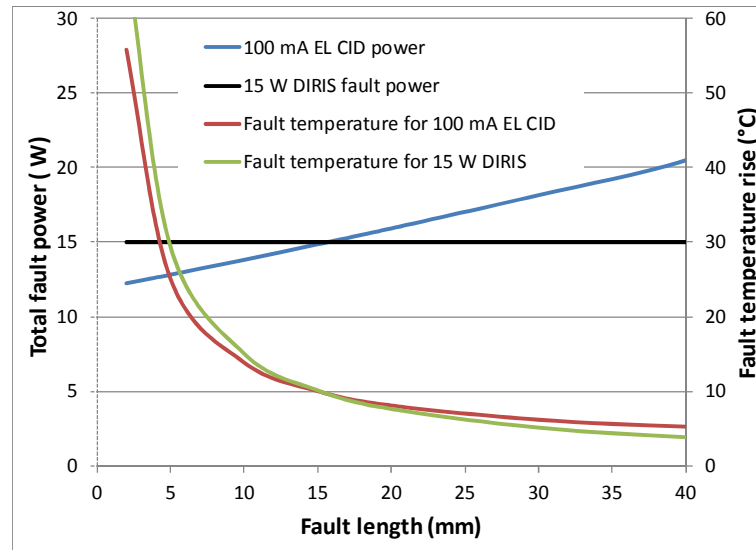


Figure 2.7 Total fault powers and temperature rise for DIRIS and EL CID detected faults

2.4.2. ICEMENERG PROFIM system

A Chattock based stator core test system called PROFIM emulating the EL CID was developed by Prof. Zlatanovici and is used by the Romanian ICEMENERG Institute [74-76]. It operates at a low $\sim 4\%$ flux and any core fault current is detected by the voltage from a Chattock sensor across adjacent teeth, while a core flux reference is measured with an iron-cored sensor across two teeth. To separate the detected fault and excitation mpd, the quadrature fault current signal is detected as the instantaneous Chattock signal at the zero-crossing of the flux, using LabVIEW virtual instrumentation. There is no equivalent *Phase* signal. Any detected fault mpd indicated as $>250\text{ mV}$ (interpreted as $>100\text{ mA}$) is recorded as problematic damage, regardless of polarity. Zlatanovici considers that the correlation to the HFT at 80% service flux is $15\text{ }^{\circ}\text{C}/100\text{mA}$ [74]. It is not reported in use outside ICEMENERG.

2.4.3. GE Racer

In the decade from 1998, GE in the USA was active in attempting to develop a number of improvements to electromagnetic stator test systems. GE described the ‘RACER’ (Rapid Analysis Core Evaluation Report) test system between 2003–8 in a series of papers [77-80] and patents [81-84]. This uses an in-slot, iron-cored probe shown in Figure 2.8, to notionally reduce noise and improve reliability in fault detection. This also avoids the problem that iron-cored probes have of greatly varying sensitivity with surface spacing.

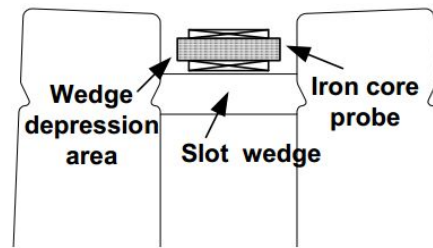


Figure 2.8 GE iron core probe in slot (© IEEE 2003 [77])

Whilst this elegantly solves the problem of obtaining constant net magnetic air gap, the sensitivity to slot width means the system still needs calibration to the machine. Other problems emerge, particularly of very poor sensitivity to tooth tip faults and the problem of flush-wedged machines. Later papers [78, 79] show some test results, where it seems >10 laminations welded together are needed to obtain reliable detection on tooth tip or slot base. This is discussed and analysed in more detail in Appendix A.2. The product was advertised in 2011 [85] but by 2012–14 only the EL CID was being offered for turbo and hydro-generator stator core testing [86–88].

2.4.4. Siemens SMCAS

Siemens in the USA has also developed an EMT, claimed to ‘duplicate...the standard EL CID equipment’ [89] with additional features. Patented in 2004 [90] ‘SMCAS’ (Siemens Multi-frequency Core Analysis System) was launched in 2007 [91]. The updated system announced in 2010 uses an eddy current tester and can energise the core simultaneously at 50/60Hz and higher frequencies (HF) at a low toroidal flux density from a large power amplifier (3–5 KVA). The system detects core faults with a normal Chattock and outputs equivalent *Phase* and *Quad* values.

Siemens claimed in 2010 [92] that the SMCAS is ‘qualified’ for use at 50/60Hz, but they are still working on the HF aspect (discussed in section 2.5.2), though the sales publicity [89] is silent on this. It is only planned as an in-house service offering [93].

2.4.5. Russian EMK

In Russia a significant amount of alternate low flux electromagnetic core fault detection development has also occurred, though almost none is recorded in use outside the former Iron-curtain. A fuller study is given in Appendix A.3.

The EMK method was devised in 1995 by Berezhanski et al. [94] and used an iron-cored probe, but by 2000 [95] the Russian Electric Power Research Institute (VNIIE) had changed to a 10 mm dia. air-cored Rogowski coil. The detected signal phase change at a fault is used to compute an apparent full flux power, assessed in Table 2.1.

Gorodov	EL CID <i>Quad</i>	EMK Life-expired Guidelines
$K_a < 1.3$ ($< 3-4^\circ$) normal background Power < 15 W	< 100 mA Normal background HFT $< 5-10$ °C	Power < 20 W No fault
$K_a = 1.3-1.8$ ($4-10^\circ$) warning region Power 20–40 W	100–260 mA Warning region, HFT $\sim 10-25$ °C	20–40 W May exceed the HFT acceptance level (> 15 °C)
$K_a > 1.8$ ($> 10^\circ$) core heating inadmissible Power > 40 W	> 260 mA Danger region HFT > 25 °C	Power 40–70 W May exceed the generator capability
		Power 70–120 W May damage winding insulation
		> 120 W Risk of stator ‘iron fire’

Table 2.1 Correlation between K_a , EL CID *Quad* and EMK Fault power

From 2002–6 Gorodov et al. [96] [97] researched iron-cored sensors further, and proposed a flat sensor where the increase in signal phase angle from the fault-free value is used as the measure of damage. From this a relative loss metric K_a from the fault phase angle is established. By 2003 the product was commercialised as the Introskan-IS200 core tester [98]. Gorodov et al.’s recommendations [99, 100] are found to be comparable to typical EL CID practice and the Life-expired Guidelines [52] for a one packet fault (50mm long) as discussed in their paper [97]. This is laid out in Table 2.1.

However when a metric is studied that assesses a fault’s heating in proportion to the core’s ability to accommodate it, then in fact EL CID is substantially better. This is shown in Figure 2.9, where the power per unit tooth width of a 50 mm fault is plotted for a family of typical machines for comparable fault signals. These range from smaller hydro-generators to major turbo-generators which have increasing test excitation axial voltage field as their size increase. It can be seen that EL CID specific fault power (W/m of tooth width) is the most constant amongst the measures.

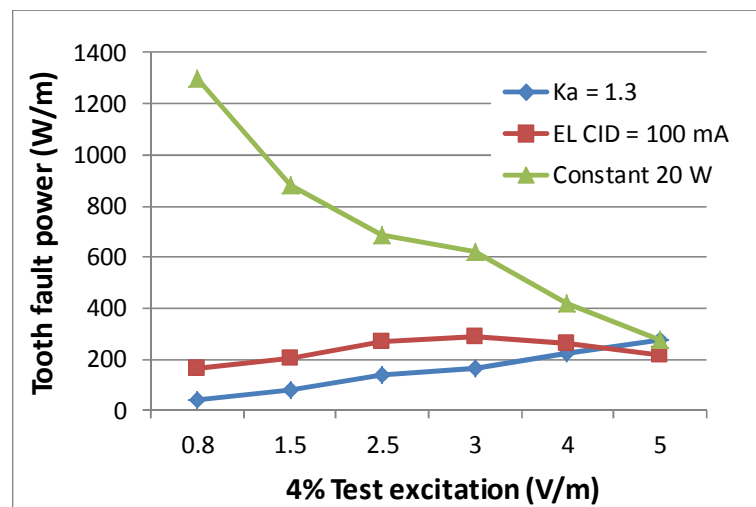


Figure 2.9 Specific fault power with tooth width for varying test voltage field

2.4.6. INDUCOR and KES equivalent EL CID systems

INDUCOR in Argentina disclosed in 2013 an EMT system called EL CID [101]. It also uses Chattock air-cored sensors and appears to be based on a commercial lock-in amplifier. Measurements comparable to the original EL CID system (section 2.3) are made, with a Quad signal >100 mA stated as showing a core fault warranting attention. It appears to be only used for INDUCOR's Argentinian service business [102].

KES International Ltd in Canada supplies a similar system to the EL CID termed CDA, described by Gavric et al. [103]. It uses a higher induction of 5-15% of full flux, with a phase shifting detector to resolve the fault currents from a Chattock sensor. The fault currents are then scaled to equivalent full flux current for recording, but no fault threshold is disclosed. It is unique in being the only direct EL CID competitor openly sold.

2.4.7. Other test approaches not commercialised

Several researchers have investigated stator core testing using local injection of excitation flux rather than toroidal induction. The benefits seen are reduced test power, absence of excitation windings, and the ability to test cores which might not be complete. A 1999 patent by Bourgeois and Lalonde [104] from Hydro Quebec induced a local flux from a C-shaped probe across 2 teeth. The drive field and flux density are measured to determine the core loss locally, with variations ascribed to core faults.

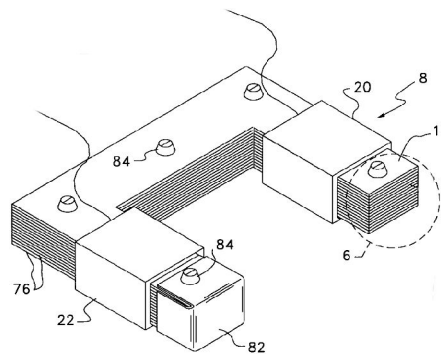


Figure 2.10 Hydro Quebec injection probe [104]

Later work by Kliman et al. for GE [105-107] similarly used local flux injection and later an improved differential probe [107] to attempt to overcome poor fault sensitivity. This system still had the expected major drawback in use of varying tooth/yoke contact, and appears to have been dropped in favour of the iron-core probe described in section 2.4.3.

Other researchers have investigated resonant systems, where a pulse of flux is locally induced in the core through a wound magnetic probe across 2 teeth, and the severity of any local fault determined by the damping of the response. ELIN first proposed this in 1984

[108], after which Ramirez-Nino and Pascacio in 2003 [109] described their similar MLM system. The benefit is the elimination of any excitation winding, however the system is very sensitive to probe-core spacing, and requires custom probes for each machine geometry. It has not been adopted.

2.5. Higher frequency testing

It has long been speculated that testing at higher than operational frequencies could provide some detection or analysis benefits, but remains unproven. Testing at higher frequencies has thus remained in limited use for high flux testing using the normal thermal measure.

2.5.1. High flux high frequency testing

The massive power required to test larger stators has encouraged the use of higher frequencies to reduce the excitation flux density and power, while still achieving the full axial voltage field to enable the normal thermal fault assessment. Alstom in Bilboa [110] have used 200 Hz excitation in their hydro-generator factory for >15 years now to reduce the current needs. More recently in 2007, Siemens in Mülheim [111] patented 500 Hz high flux testing of turbo-generator cores. The claimed benefit is much less power required, thus the test gear becomes more portable in the limited field use shown [55], though the high power inverter is expensive.

2.5.2. Electromagnetic high frequency testing

It is expected that the excitation current would reduce substantially as the frequency is raised, allowing easier excitation and faster scanning of the stator core. This was first patented by Sutton [112] and researched extensively by Sasic and Bertenshaw [113], where the main advantage perceived was in hydro-generators with core joints. Here the excitation mpd across the joint can be very large and due to joint gap dimensional variation, causes intrusion of the excitation mpd variation into the *Quad* signal. This can mask small faults, thus a reduced joint excitation mpd should assist.

The reduction in excitation with frequency proved to be considerably less than expected, down only to 20% vs. the expected 10% at 500 Hz. Further the rising core loss angle meant that tests had to reference to flux rather than excitation current. This resulted in a standing no-fault *Quad* level requiring subtraction from any measurement, similarly discovered by Gandshu et al. [97]. Most critically fault inductance was shown to be problematic with rising frequency, limited to 500 Hz to allow a reasonable discrimination

between faults up to 1 A. The complex interpretation needed on turbo-generators, with only modest gains on hydro-generators with jointed cores, discouraged commercialisation.

The Siemens SMCAS system discussed in section 2.4.4 claims higher frequencies (e.g. 1 kHz) provide better symptomatic diagnosis of the fault depth by scanning cores both at 50/60Hz and HF to compare the results. Initial claims [90] that the greater the fault depth, the less the fault signal is attenuated with rising frequency are later changed to the opposite but still seen as a virtue [92] even though unquantified.

Others have speculated and attempted to patent alternate approaches to HF testing. Hobelsberger [114] claims that a stator core is linear and faults are resistive up to 2 kHz (disproved in [113]). This proposes a square wave excitation to give a predictable family of harmonics, whose amplitude and phase can be analysed to determine the fault intensity.

The idea of using higher frequencies has also been discussed in patents for flux injection test schemes, with Kliman et al. [106] suggesting higher frequencies or even pulsed waveforms to better discriminate core faults (by undisclosed means).

2.6. Online approaches to stator core testing

The drive for effective condition monitoring discussed in section 1.1 would ideally be met by monitoring the stator core in service (on-line). There are however no known techniques able to detect nascent core faults. EPRI issued a call for ideas [115] in a proposed 2004 communally funded research project, however nothing transpired. The nearest approaches are the Generator Condition Monitor (GCM) and shaft voltage detection methods discussed below. Of these only the GCM is shown to be of possible value in preventing a serious core fault spreading further.

2.6.1. Generator Condition Monitors

Often also called Core Monitors, these operate by sensing aerosols or particulates in the H₂ stator cooling gas. They were developed in the 1960s and patented in 1966 [116] to detect the onset of burning in the new larger stator cores. Lodge [117] reports them in UK use since 1977. The GCM is supported in IEEE Std 1129 [118] and CIGRE [119] as an online monitoring tool for hydrogen and air-cooled machines. They operate by passing the coolant gas through a radioactive ionisation chamber where a current through the normally pure ionised H₂ stream is monitored. When (especially organic) aerosols or particulates are present they attach to the ions increasing their mass and reducing their ion mobility, hence reducing the current. A reduction in current of 50% is generally considered an alarm.

Overheating of interlamination insulation in the core produces particulates in the cooling gas stream which are thus detected.

Many sources of burning other than from interlamination insulation, from for example overheated winding insulation or mechanical rubbing, will of course be similarly detected. Interpretation of the alarm is thus a challenge, especially since after an area of insulation has burnt away, the particulates dissipate and the alarm condition clears, but the fault has not. In addition, quite substantial areas need to burn to be detected. Wallis [60] demonstrated how in the laboratory, interlamination insulation varnish needed to exceed 344 °C to start detection, and over 150 cm² of lamination varnish at 600 °C was needed to reach the 50% alarm threshold. Westinghouse in 1989 [120] also considered that the conventional use of non-organic lamination insulation resulted in few particulates and thus poor sensitivity.

A partial solution to the problem of discriminating the source of the overheating has been the use of a series of encapsulated volatile tagging compounds, whose chemical composition is sufficiently unique that if painted on different parts of the machine, can allow identification of the overheated area by chemical analysis. Six different compounds were devised by Barton et al. in 1981 [121], still supplied today as ‘Gen-Tag’ from Environment One [122]. The drawback is that a 24 hr chemical analysis cycle is required for identification, and since the tagging paint can only be applied to the core surface, any buried burning remains a generic alarm. Gonzalez et al. [123] note that inorganic lamination insulation burning may be poorly detected and thus definitely requires tagging compounds with thus little chance of detecting buried overheating.

Tavner et al. [6] (§7.4) illustrates that one may have <10 minutes from a GCM alarm starting to detect a core failure to a machine trip. CIGRE reports in 1999 [119] and 2010 [124] found them very common on machines >250 MW and yielding ‘useful information’, but only moderately reliable and that they only respond after the core has burnt. Maughan [125] reports that in a survey of 17 reported alarms, there were two from stator core overheating events. One was where a full core fault/melt occurred after 30 minutes of alarm (cost \$15M to repair) and may have been saved if attended to at once? The second was from a 25 cm² patch of overheated core surface, so the core was saved, though it is uncertain if it would have degenerated to a full core fault.

There remain concerns regarding false alarms [125], especially due to oil mist contamination, while Tavner [7] on balance considers that heated chambers insensitive to oil are best, even though less sensitive to particulates. Consequently the GCM is not

considered a very reliable online monitor of incipient stator core faults, but remains popular for its multi-faceted monitoring capability.

2.6.2. Shaft voltage detection

The shafts of generators are usually earthed with brushes at the turbine end, and insulated bearing(s) at the opposing end. Voltages can be developed along the rotor shaft from many sources, capacitive coupling from static exciters, asymmetric core steel, rotor asymmetry etc. [126]. A significant interlamination core defect will also cause a magnetic asymmetry in the core, which combined with the rotating field acts to produce an alternating voltage along the generator rotor. Thus detecting core faults by monitoring the rotor axial voltage has been a long-known possibility.

The first record is from Exxon [127] in 1970 who claims to have detected a major fault's instant of failure by the shaft voltage produced by the unbalanced core flux, which resulted from current flow in the fault. Jackson et al. [128] in 1980 then demonstrated how when even 25 laminations are shorted together, the induced shaft voltage would only be 25 mV, readily masked by the shaft voltage due to just 50 μm of rotor eccentricity. They conclude that practical shaft voltage measurement would only indicate the gross melting of the stator core by which time a lengthy repair is inevitable. This position was supported in 1996 by EPRI [10], who concluded that high shaft voltages require severe and long core faults to occur, sufficient to overcome the very variable shaft voltages that can reach 68 Vpk-pk [129]. Tavner et al. [6, 7] (§9.5.5) also considers that shaft voltages are too insensitive to detect early stage core or winding faults, in addition to the difficulties in making reliable shaft contact. Regardless Nippes from Magnetics Products and Services Inc. continues to promote shaft voltage monitoring as a means of detecting stator core faults [130], whose system was also supported by EPRI in 2010 [131].

In terms of other public recommendations, in 2010 CIGRE [124] reported that shaft voltage measurement was only being used for shaft ground monitoring. However in 2014 IEEE Std 1129 [118] advised that shaft voltage waveform monitors 'may be able to detect anomalies in the core, such as shorted laminations', but without evidence.

2.6.3. Research into improved online stator core fault detection

A 2010 paper by Lee et al. [132] proposes detection of induction motor core faults using a modified inverter to rotate a single phase flux field 360° around the core axis from a set of 3-phase machine windings. The total power input less winding losses is measured to detect if there are any flux angles where the losses increase, indicating a fault. However

in experimentation a very severe artificial fault caused only 3% loss change, while the test is also sensitive to other motor faults, such as broken bars and winding shorts.

Wang and Liu [133] in 2012 proposed monitoring motor negative sequence currents to determine core loss change and its likely physical orientation to the phase windings. However this technique is similarly sensitive to other motor failure mechanisms.

While the use of axial and radial leakage flux has been promoted for some time as a means of detecting general induction motor defects [134], Romary et al.[135, 136] studied the radial magnetic flux on the core outside diameter that is caused by a core fault. FE and experimental modelling showed that the effect was very small; a 2013 study [137] on a 125 MW stator core driven by a synthetic ‘exciter’ (simulating a rotor) detected flux changes behind the keybar of just $\sim 150 \mu\text{T}$ for major fault. From this the core back flux signal would be just $3 \mu\text{T}$ for a normal EL CID detected fault of 100 mA, which is $<10\%$ of the natural variance. Thus it can be seen that flux signatures on the core rear are very insensitive to embryonic core faults.

Bytnar [138] has demonstrated, in a thermal model, that an ‘iron fire’ core fault in the stator teeth of just two packets will give a very distinct conductor coolant temperature rise of up to 8°C in water-cooled windings. Since local coolant water temperature is routinely monitored for blockage analysis, and development of a molten core fault will be more rapid than oxide/sediment accumulation, this interpretation is quite practical. However it still requires a major fault to achieve detection, is insensitive to core yoke faults and limited to water-cooled windings.

2.7. Economic considerations of stator core testing

Apart from the CEGB crises in the 1970s, serious⁸ stator core faults remain fortunately a rare event, however specific reliability statistics are scant. Those available are studied in Appendix B in detail, where the limited data from 1920–2004 shows a core interlamination insulation damage or failure rate of around 4% of total turbo-generator failures. The base reliability data for utility scale turbo-generators is very varied, (Bollen [139] showed variability in reported MTBF data from 1.7 to 140 years), however over all sources it indicates a median MTBF of $\sim 50,000$ hrs, with 10x this for large motors and hydro-generators. Consequently serious stator core faults are rare, however when they occur, they require a disproportionately long time to repair. Their impact may also be

⁸ Normally a core fault is only discovered in service once it has caused a winding failure.

broader than recorded, since local hotspots are known to reduce winding insulation life [17] (§8.1).

Considering the reliability impact, an example 300 MW mid-range generator, running at 50% duty, with typical 5 year major services [9] would have a 1.8% chance of serious core failure over that period. Such a failure could readily incur a repair cost of £500K (costs have exceeded £10M [125]), and with lost generation margin could in total cost £1M over 60–90 days. Thus if it can be assumed that testing and correcting any incipient core faults will prevent failure until the next major service, the aggregate value saved is potentially $1.8\% \times £1M = £18K$. Compared to the cost of an EL CID test of between £5–10K the testing regime thus has to be at least 30% effective in ensuring the machine is fault-free until the next service to make the economic case, a number that is by no means certain.

It further demonstrates that routine HFT testing, despite the continued confidence in it, is unattractive. The cost of an HFT is estimated at 15–30x the manpower cost of an EMT [44, 64], thus remains uneconomic except for particularly high risk machines.

Drommi [140] reports a new core failed after one year, while the catastrophic Hunter failure [14] occurred 17 months after an overhaul where ‘all tests showed this machine to be in good operating condition’. Regardless, few utilities (and especially their insurers⁹) now accept the risk of £M+ failures which they could at least partially mitigate with a quick, relatively cheap test. The 1987 CIGRE survey of utilities [141] before EL CID became internationally common showed the high flux test used in only 29% of major services, whereas by 2010 [9] the major service usage of the EL CID test had risen to 64%, with high flux test falling to 20%. The rate of stator core testing due to the EMT has thus risen 290%.

Ideally the machine rotor should be removed for an EMT, both to ease access and to remove any source of extraneous magnetic fields. However in hydro-generators individual salient poles are often removed instead to give limited stator surface access, with the rotor turned to progress testing. For turbo-generators with predominantly cylindrical rotors, there is growing interest in testing with the rotor in place, to allow more frequent condition monitoring, and potentially allow extension of major overhaul periods.

Robotic vehicles as illustrated in Figure 2.11 have been developed by Siemens, GE, Alstom and Qualitrol Iris Power [86, 142-144] which can carry sensors into the air gap for remote inspection and testing, and their benefits reviewed by CIGRE [145], where 75% of

⁹ Hartford Steam Boiler, a major equipment insurer, ‘recommends’ stator core testing every 60 months [87]

respondents used them for EL CID testing. An EPRI turbo-generator study in 2000 [146] compared conventional and robotic (rotor-in-place) EL CID tests on the same machine, and found a mean *Quad* signal difference of just 3.4 mA.



Figure 2.11 *Qualitrol Iris Power RIV-702 robotic vehicle entering air gap of turbo-generator*

A major issue in performing the test with the rotor in place is the unexpected cost and time for the task of rotor removal in case any repair appears needed. Consequently the owner/engineer will need to make a more difficult than usual judgement of the economic risk of leaving any discovered defect uncorrected vs. the delay and high cost of repair. While this issue has encouraged industry discussion [147] little guidance has emerged on the economic imperative for differing test levels, save that a 300 mA *Quad* level could be considered the ‘must repair’ level[148]. This also requires extra confidence that fault signals are not a measurement artefact.

2.8. Research into stator core fault development

Despite the serious consequences of a substantial core fault, their root cause is little researched. An extensive summary of the studies up to 2005 is given by Tavner and Anderson [18]. These principally describe work studying core losses, especially at the core end regions where under-excited operation can cause damaging axial flux density level, being the root cause of many core faults. Tavner and Anderson then study the development of existing core faults via two processes, local eddy current within the fault and linkage of yoke flux into the fault-keybar circuit, demonstrating the high powers possible particularly in the latter. This also showed that fault cross-sections are limited by fault cooling, while Bertenshaw et al. [149] and Edmonds et al. [19] also showed that fault self-inductance is the limiting factor. All agree that axial fault progression is unconstrained.

Exon in 1970 (1974) [127] also considered the development of damaging fault power in embryonic faults. He showed that at least 4 laminations need to connect to generate

damaging power, and that fault self-inductance limited molten fault diameters to ~10 cm. The study however had to assume a number of unquantified ‘spread factors’. Jackson in 1976 [150] investigated how excess axial fluxes can cause high interlaminar voltages of ~600 mV, potentially escalating embryonic faults, then in 1978 [151] showed that poor keybar contact can similarly cause 600 mV interlaminar voltages. Finally in 1980 [152] he reported measurements on a 500 MW machine on a ‘partially earthed’ core giving from 500 mV to 4 V interlaminar voltages. Compared to the normal 60 mV in service, these values are potentially very threatening to otherwise innocuous slight damage.

Anderson and Guile [153, 154] investigated the evidence from certain types of ‘meandering’ breakdowns seen on some damaged cores. These were shown as possible from arcs developing at a pre-existing contact if the interlamination voltage reached 17–18 V. However related experiments by Platt et al.[155] gave interlamination voltage measurements of only 2.5 V peak, though still surprisingly high. The similarity of the lamination damage to filiform steel corrosion was also investigated, but the lack of corrosive elements in many stator cooling gasses made the argument weak.

By 2007 Anderson [156] had developed a theory of inductive-capacitive resonant induced breakdown stimulated by intermittent core-bar contacts under vibration. However there is no evidence of its existence in large stators. Anderson also suggested the idea that H₂ will dissociate in a breakdown spark to liberate hydrogen atoms. These can then recombine very exothermically at nearby bare iron sites causing concentrated local heating and spreading the fault, possibly explaining the ‘meandering’ breakdown phenomena. However no further evidence exists and comparable faults also occur on air-cooled machines.

2.9. Research into stator core fault electromagnetic detection

While the EL CID system has been extensively described in the literature, detailed in Chapter 3, there is little study of its effectiveness beyond field anecdote. Given that the precedence was the high flux test and the perceived threat is thermal, comparability with this was significant and is analysed in Chapter 4.

After the 1979 patent [157], it was not until 1995 [158] that Sutton developed a detailed 3D analytic model of the core fault detection, analysing the magnetic scalar potentials developed by a 10 mm surface fault. This showed the particular benefit of the laminated structure in minimising attenuation due to the spread of the Chattock, however it did not consider sensitivity variation with length or depth in core. The theory was also

extended in 2D only to model the detection of faults buried in the core yoke, which showed a relatively rapid attenuation to 50% at 15% of depth.

Fault interpretation in the EL CID test did not develop significantly for over 20 years since its inception, despite several new product developments. Eventually in 2004 Bertenshaw and Sutton [159] and Otaka et al. [160] showed how circulating current in stator windings can affect results. Following this, in 2006 Bertenshaw [66] extended the understanding of the EL CID operation with a corrected phasor diagram describing how EL CID detects faults considering core loss, the relevance of the *Phase* signal, circulating currents and core joints. This was also adopted by Ridley in [161].

The first published electromagnetic FE studies of the detection of core faults was by Rettler and Brauer [162] who completed two 2D studies in 1999. One computed the expected eddy current power in 1–4 lamination connections, which showed a rapid escalation, while another modelled the detection of faults down slots showing their comparable sensitivity. Bertenshaw et al.[56] also published 2D FE models in 2004, similarly showing the unchanging sensitivity of detection for fault positions down a slot, with their comparison to measurements. In 2006, Makuc et al.[163] developed a 2D FE model and demonstrated similar fault detection results, while Gandshu et al.[97] completed some 2D FE models of iron-cored sensors on stator cores (as section 2.4.5) also in 2006, which modelled the fault power metric.

Ho completed a PhD thesis in 2006 [72] which developed both 2D and 3D FE models [164] of stator core faults, and showed the strong dependence of detection sensitivity on fault length. In this a 3D analytic study was also made of the fault current distribution [149] and the Chattock sensitivity to varying fault length, validated on a test stator core. Ho's 3D FE model of a laminated core structure investigated the detectability of both surface and buried faults [165], and gave a close match to experimental surface fault results. However the buried faults remained unverified, a challenge now addressed in Chapter 11. The work also demonstrated and resolved the problem of axial images in partial FE models which rely on symmetry for economy.

The only other research has come from a team in Lille. Rather than use commercial FE modelling software with reduced axial permeability and conductivity to 'homogenise' the lamination structure, Müller et al.[166] in 2009 studied a more general A-V vector magnetic potential formulation to include the effect of eddy current losses in faults, obtaining realistic results. In the same year Roger et al. [167] used instead the T- Ω scalar magnetic formulation to study fault powers in a limited number of faulted laminations,

modelling at the lamination level. However the conductive fault diameters considered were massive at >10 mm, thus not representative of embryonic faults. In 2011 Henneron [168] investigated a dual mesh FE arrangement to better compute eddy/fault currents comparing the A-V and T- Ω formulations, but on just two laminations. A comparable study was then completed by Müller et al. [169] in 2011 on four laminations, which demonstrated that homogenised A-V and T- Ω models can both be successfully used to simplify the modelling of stator lamination stacks. Curiously they modelled very anisotropic grain-oriented electrical steel, despite nearly all machines using non-oriented steel for reasons explained by Neidhoefer and Schwengler [170].

Using these results, Müller et al. [171] in 2012 compared a 3D FE model with a physical test system consisting of a pair of axially anti-symmetric 3-slot segments of grain-oriented stator core, described in greater detail by Romary et al. [172]. The current in a severe experimental welded fault was constrained to just the outer-most laminations of the 20 lamination fault, by using selective connections on the core rear. The modelled fault signal however differed substantially from experiment at 193% of that measured, despite being measured directly across the fault on the tooth face rather than conventionally across a slot. The authors suggested that experimental fault resistance errors were contributory, and obtained closer results with $<20\%$ error using injected fault currents. Regardless the use of severe and un-calibrated welded faults, just a small section of experimental stator core rather than a whole annulus, and no interconnectivity of the laminations at a rear keybar is likely to limit the validity of this model.

There has been no reported research, though some speculation, into the impact of stator core materials or construction on core faults and test results. Klempner [173] suggests core pressure relaxation is contributory to fault, whereas Danilevich et al. [174] consider higher modern construction pressures of ~ 2 MPa potentially damaging to insulation. Klempner and Kerszenbaum [8] (§11.2.1) also consider that lamination steel grade (especially grain-oriented vs non-oriented) will affect results, but in an unspecified way.

The detection of buried faults (in the yoke) is recognised as challenging, with Maughan [16] warning that damage in the yoke may not be detected. Sutton [158] used a 2D FE model to show a 50% signal attenuation for a fault at just 15% of yoke depth, while a 2D analysis by Gandshu et al. [97] considered that a fault $>25\%$ deep in the yoke is undetectable. The research by Ho [72] into 3D FE models of buried faults is studied in Chapter 11.

On the practical side, Ridley extensively studied the subject of EL CID testing of hydro-generators from 1993–2010, with the many papers collected into a book [148]. The majority of the work concerns application and interpretation of the test in the field. He also extensively studied the problem of interpreting test results at hydro-generator core joints, developing the ‘zero-delta’ approach to deduce the fault current mpd in the presence of the intense excitation field developed at the joint air gap [175-177]. Klemptner and Kerszenbaum [8] (§11.2.1) describe how stator cores using insulated keybars will generally not develop a detectable fault circuit (except in the region of the single earthed keybar), but that multiple co-axial faults may then become dangerous.

2.10. Discussion and summary

The maintenance of stator core interlamination insulation condition is shown to be a particular challenge in large electrical machines. While their stator cores are shown to be very reliable, the scale of damage that a fault can cause ensures that it remains an important facet of condition monitoring. There are no effective online monitoring systems for incipient core faults, nor is any likely to be developed in the foreseeable future. This requires that the sole methodology of routine offline testing requires a level of competence that will ensure that all incipient core faults are detected, ideally at a level that ensures that none will develop into a damaging fault during service periods. The EMT offline test has not yet completely achieved this.

The first stator core fault tests introduced by the 1950s were thermal tests at rated flux to detect core faults by their self-heating, with a 10 °C warning threshold. An alternate low flux (4% service) EMT system was developed in 1979, known as EL CID. This senses instead the magnetic field generated from fault currents using a Chattock potentiometer, scaled to a notional fault current with a 100 mA warning threshold. Commercialised in 1982, it is now the dominant EMT in use around the world with several emulators. The EMT results are assumed to reflect the expected service overheating. However there is no known proof of this, hence the HFT has remained a reference.

Other comparable EMT systems have been developed, the most common being DIRIS which uses a metric of equivalent fault power at full flux, with a 15 W warning threshold. Analysis of the relative detection sensitivities shows that for short faults the two test thresholds are in fact closely aligned. Siemens also developed SMCAS with Chattock detection comparable to EL CID, plus multi-frequency operation claimed to improve diagnosis, but still unproven.

The probability of a major generator stator core fault occurring in normal service over 5 years was estimated at just 1.8%, but the cost of failure makes online stator core condition monitoring desirable. The only technique that has shown some limited success is the Generator Condition Monitor which detects combustion products in the cooling gases, however it is not a reliable online monitor of incipient stator core faults. Attempts to detect developing core faults by shaft voltage monitoring, external electromagnetic fields or electrical parameter change have also failed.

Research into the development of stator core faults is sparse. No proven process of fault initiation is known, though studies have shown how high interlaminar voltages (>1 V) can occur and act as possible fault initiators. Three studies have shown fault cooling and fault self-inductance as radial limiting factors in the development of runaway faults.

Research into electromagnetic stator core fault detection is also limited. There has been no study of the effect of stator core material parameters on the development or detection of fault signals. The impact of a laminated structure on EL CID detection sensitivity was first analytically studied in 3D in 1995 for one case. Some 2D FE studies were also completed in 1999, with other researchers publishing similar studies in 2004–2006, including the first full phasor analysis of the EL CID fault detection process.

A 3D FE analysis of the Chattock sensitivity to short surface faults was completed for the first time in 2006. It was validated by experiment, which also investigated the expected fault current distribution. However no work has been validated on short buried faults. By 2012 some general 3D FE models developed using both A-V and T- Ω vector formulations were poorly matched when trying to model an experimental welded fault. This demonstrated the difficulty of experimentally generating calibrated core faults, and the need to develop reliable experimental methods.

Chapter 3. Analysis of the EL CID Electromagnetic Test

The dominant EMT is the EL CID system considered here. This method induces a low level toroidal alternating magnetic flux in the stator core, as shown in Figure 3.1, then measures any interlamination insulation defect which results in a fault circuit by detecting the magnetic field generated from current in that fault circuit. This chapter investigates the detection methodology, and analyses how fault detection is affected by core loss in the stator and harmonics.

3.1. Stator core excitation

The induced flux is generated by excitation current in a low power axial winding shown in Figure 3.1, which is usually a series-connected multi-conductor cable with adjustable number of turns to obtain sufficient mmf¹⁰. In addition a second winding around the core is used to measure the test flux by the single turn voltage (*STV*) induced.

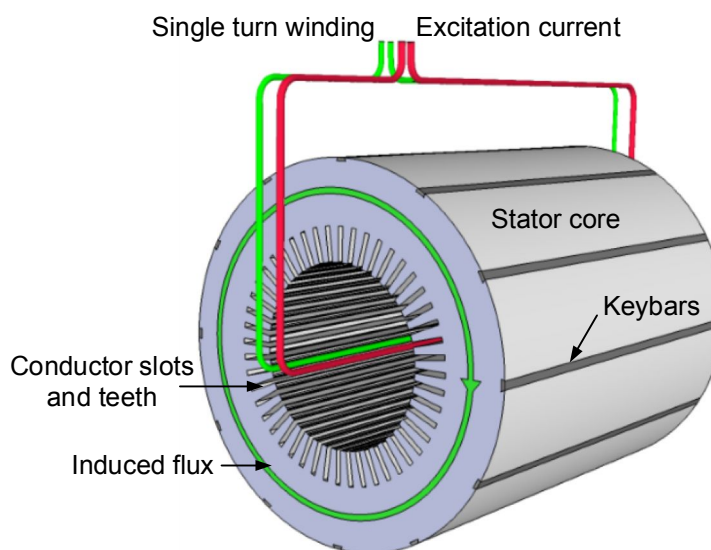


Figure 3.1 Stator core excitation winding and induced flux

The test flux is normally set at 4% of operating flux¹¹. In practice the operating flux is rarely known, so has to be computed back from the machine's rated voltage and winding data. Typical ranges of values of *STV* for 4% flux are given in Table 3.1, expressed as the induced axial voltage field, volts/metre of core length.

¹⁰ The required value can be very variable, in the region of 10–200 A-t.

¹¹ Originally set to give an axial field of 5 V/m for turbo-generators.

Medium to large turbo-generators	4–6 V/m
Typical hydro-generators	1–3 V/m
Medium to large motors	0.7–2 V/m

Table 3.1 Typical STV excitation field levels for 4% flux

3.2. Chattock potentiometer sensor

The fault current induced is determined by measuring the magnetic field strength on the surface of the stator bore teeth with a flexible Chattock magnetic potentiometer shown in Figure 3.2(a), spanning a section of core surface. Since its signal is the line integral of the ac magnetic field strength along its length, it thus records the mpd between its ends. It is placed in the bore of the core across a pair of teeth as shown in Figure 3.2(b) and scanned axially down the core (illustrated in Figure 2.5), recording the detected mpd down the complete length of each slot. The mpd developed across each slot mainly comes from the excitation flux density¹², however over a fault the signal will also include a component from the current in the fault.

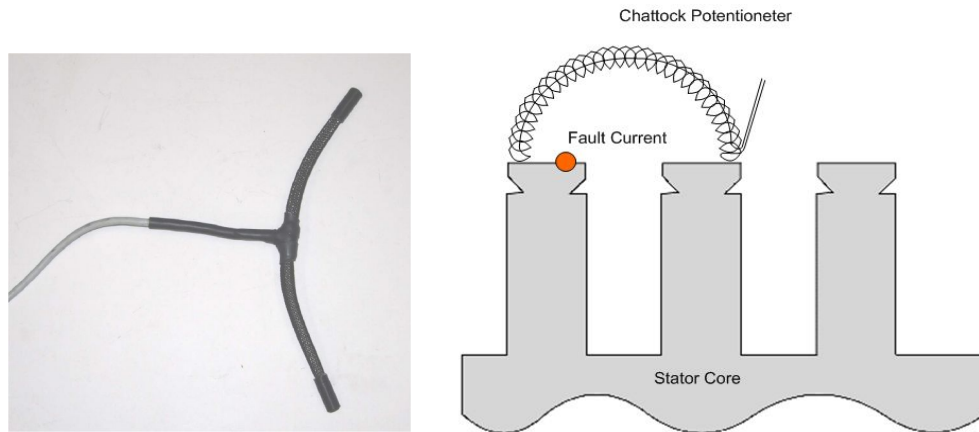


Figure 3.2 (a) 250 mm Chattock potentiometer, (b) Chattock positioned across stator fault

The operation of Chattock [24] and related Rogowski [178] coils has been analysed in detail by many others [72, 179]. These show that for a coil of length l , number of turns n , cross-section area A , a magnetic field strength vector \vec{H} coaxial to the Chattock of frequency ω , will induce the detected voltage signal V_C according to

$$V_C = \mu_0 A \frac{n}{l} \omega \int_{end}^{end} \vec{H} d\vec{l}. \quad (3.1)$$

This shows that the output is frequency dependent, but is independent of length as long as the coil's turns per unit length and area remain constant. It also assumes the field is

¹² This may vary from the ideal pro-rata proportion of the excitation mmf due to non-uniformity of the core steel, core joints and parasitic induced currents in any windings present [66].

substantially uniform across the coil cross-section, which requires Chattock coils to be as small a diameter as possible to minimise this inaccuracy¹³.

3.3. Electromagnetic detection of fault current

If the Chattock is positioned across the fault as modelled in Figure 3.3, it is known that the total magnetic field strength H integrated around a current is equal to the current by *Ampère's law* regardless of the path of integration. In this model the electrical steel of the stator core and air boundaries have infinite extent in the y and z planes and are on the centre-line, with infinite length current assumed to simplify the analysis¹⁴.

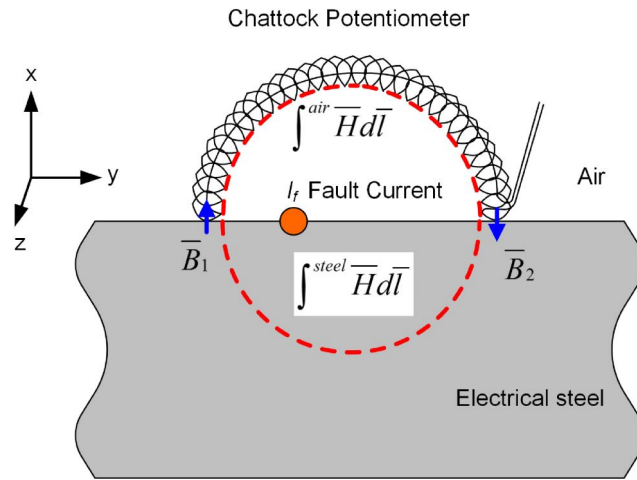


Figure 3.3 Chattock potentiometer fault current detection

It can thus be seen that the magnetic field is composed of two sections, the path in the air and the path in the steel, which can be integrated separately. Despite the fact that the field is inaccessible for measurement within the core, this is conveniently minimised by the high permeability of the steel. The fault current is thus given by

$$I_f = \oint \overline{H} d\overline{l} = \int^{air} \overline{H} d\overline{l} + \int^{steel} \overline{H} d\overline{l}. \quad (3.2)$$

The usual solution to this [158], $I_f \approx \int^{air} \overline{H} d\overline{l}$ is given by the fact that the flux densities \mathbf{B}_1 and \mathbf{B}_2 at the boundaries must be constant across the boundary¹⁵. Consequently for the 2D situation, with a filamentary fault current on a plane boundary, the magnetic field strengths immediately either side of the boundary where μ_r is the relative permeability of the steel must be

$$\overline{H}_{steel} = \frac{1}{\mu_r} \overline{H}_{air}. \quad (3.3)$$

¹³ EL CID Chattocks have a 4 mm coil dia. with nominal signal sensitivity $S_C = 100 \mu\text{V/A} @ 50 \text{ Hz}$.

¹⁴ Such that the return current paths do not affect the model's fields.

¹⁵ This is since from *Maxwell* $\nabla \cdot \overline{B} = 0$, the flux field is conservative.

Since I_f is the only source of magnetic field, by symmetry the two integrations in equation (3.2) must be identical, subject to the scaling of equation (3.3), even with an offset fault current. Since μ_r is >2000 for typical EL CID test flux density levels, equation (3.2) becomes

$$I_f = \left(1 + \frac{1}{\mu_r}\right) \int^{air} \overline{H} d\overline{l} \approx \int^{air} \overline{H} d\overline{l} . \quad (3.4)$$

From equation (3.4) it can be seen the signal detected by the Chattock is $>99\%$ of the fault current, regardless of the position of the fault current within the Chattock's span on the steel surface.

In the more realistic example of a fault on a stator tooth shown in Figure 3.4, the steel is not homogeneous due to the winding slots and the path of integration is longer. Nevertheless since the slot depth will be typically three times the pitch, the effect at most will be to treble the H field proportion in the steel, still negligibly affecting the answer. In addition it can be seen that the detection sensitivity of long faults is essentially identical regardless of their position on the tooth surface (1) or down the slot (2), since the integration path through the low reluctance steel between the Chattock ends always includes the fault current.

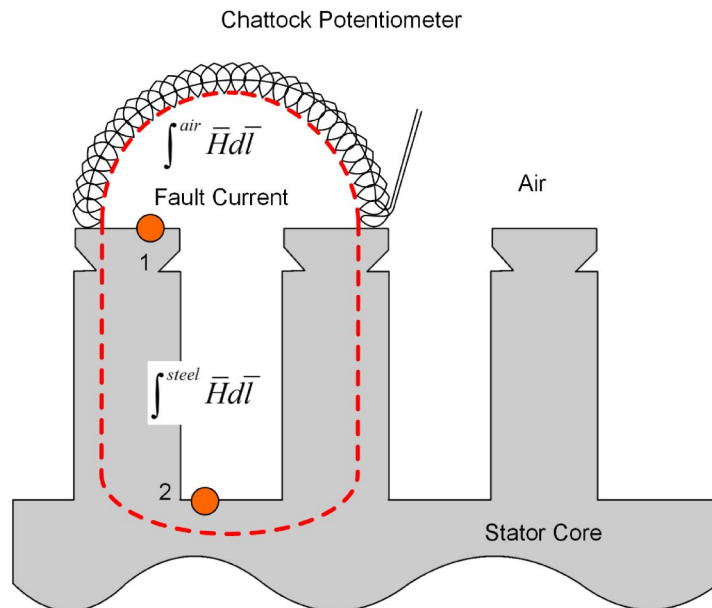


Figure 3.4 Chattock field integration paths in practice

This analysis is strictly true only for Chattock coils that exactly touch the steel surface and infinite length fault currents. The alternating excitation flux will also attempt to induce eddy currents into the plane of the page, though they will be greatly limited by the laminations. For practical reasons the Chattock potentiometer internal coil end will be

inevitably spaced 2–3 mm above the steel surface, but this generally introduces minimal error.

A further modest reduction in detected signal will come from the mpd developed by the flux density induced in the core by the fault current (the ‘Quad recovery’ effect discussed in section 6.1), where for a generator of N slots, the induced core flux from a fault will reduce the detected signal by $1/N$, e.g. 2% on a 48 slot machine.

The main detection error comes from the short length of real faults. Ho [72] studied their attenuation both analytically and experimentally, and showed that a 30 mm surface fault will suffer a 50% attenuation, rising to ~75% by 10 mm. Sutton [158] also showed that while this attenuation due to short length is inevitable, there is only modest further attenuation due to the Chattock being spread so its ends are distant from a short fault current. (It was shown earlier that this has no effect only on an infinite length fault.) This is due to the laminated structure of the steel having a low axial permeability.

This analysis also does not hold for faults that are buried within the core, and thus have a steel flux circuit totally around them. Sutton [158] analysed the detection of these faults, but assumed long fault currents so inevitably obtained high detection predictions. He projected that ~20% of the signal is still detected at 40% depth below bore surface (base of slot). Ho developed a 3D FE model of buried short faults with predictions of much greater attenuation. For a fault 40% back in the core yoke, a 40 mm long fault was only 4% detected at the bore slot, falling to just 1.5% at 10 mm long. These have been verified with corrections by experiment in Chapter 11. Gandshu et al. [97] similarly concluded that faults more than 25% deep in the yoke cannot be detected by EL CID.

The only detection improvement for these buried faults is that the fault signal rises if the measurement spans greater than one slot; spanning three slots can nearly treble a deeply buried fault signal and thus offer some analysis opportunity.

3.4. EL CID phasor analysis

The simple phasor diagram in Figure 3.5 was developed and promulgated in training material and papers from before 1993 [180]. It proposes that the induced fault voltage lags the excitation current and flux by 90° , and the actual fault current has a further lag due to self-inductance. However the theory does not reflect the existence of core loss, nor the observed basic fault signals. These are that, for a fault within the span of the Chattock, a core fault shows as a negative *Quad* signal for a positive *Phase* signal (and vice-versa), both of which increase with fault severity. Previous studies [66, 67, 72, 148, 158] have

described the basic system of detection and considered qualitatively the impact of core loss, without resolving the difficulty. Ridley [148] (§6.4) offered a more rigorous analysis based on transformer theory, but still did not correctly predict the results.

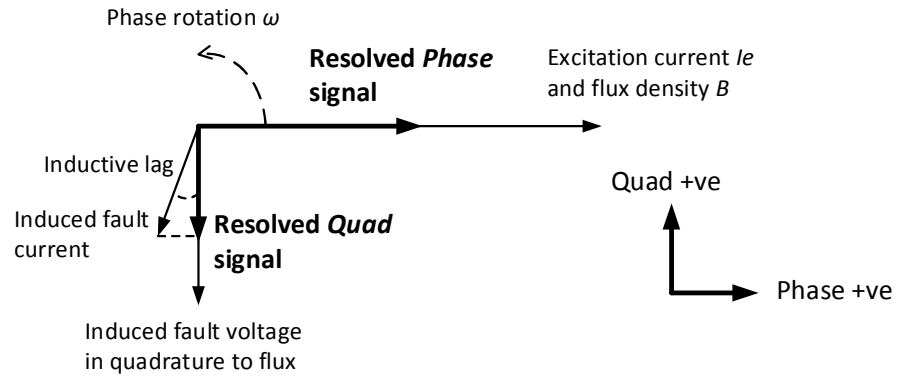


Figure 3.5 Original EL CID phasor diagram with assumed Phase and Quad axes

This was finally resolved in 2006 [66] through recognition of the physical relationship of the Chattock sensor when used to measure fault currents in a core, and the detail operation of the EL CID instrument. This is shown in Figure 3.6 for a homogeneous core, where the mpd measured by the Chattock has contributions from the excitation current and fault current (both into the page) spanned by the Chattock. The magnetic fields are conventionally clockwise for a notation of positive current and induced voltage into the page, with the assumption of long axial current paths and uniform high permeability magnetic core. The fault current is phasor I_f and the excitation current phasor I_e .

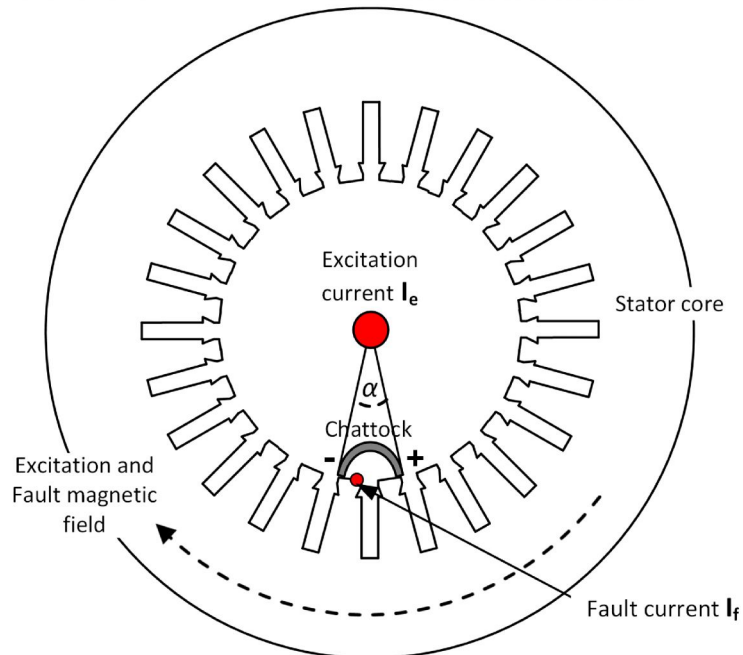


Figure 3.6 Excitation and Chattock relationship

Since the majority of the magnetic field strength from the fault mmf occurs in the air, as analysed in section 3.3, the Chattock signal will be the sum of the fault mmf and the section proportions of the fault and excitation magnetic field strengths developed within the core. Thus the mpd detected by the Chattock at the span angle α is:

$$mpd = \overline{I}_f(1 - \alpha / 2\pi) - \overline{I}_e \alpha / 2\pi . \quad (3.5)$$

Since $\alpha \ll 2\pi$ for single slot Chattock spans,

$$mpd \approx \overline{I}_f - \overline{I}_e \alpha / 2\pi . \quad (3.6)$$

This shows that the Chattock essentially detects all the fault current mmf and the inverse of the circumferential proportion of the excitation current mmf (where the positive direction of each phasor is the same). The sum total of all the mpds detected by the Chattock across each slot around the bore in the air should sum in phase and amplitude to the enclosed current (density \mathbf{J}) from *Ampère's law*

$$\oint \overline{H} dl = \int \overline{J} ds . \quad (3.7)$$

The fault current is outside the area of the bore enclosed by the summation of the Chattock spans across each slot. Thus $\int \overline{J} ds$ can only be the excitation current phasor \mathbf{I}_e which has phase angle ϕ to the EL CID reference. The phasors can be considered in their real and imaginary components. The $\int \overline{H} dl$ values are detected by the Chattock and resolved by EL CID into in-phase (P , *Phase*) and quadrature (Q , *Quad*) components to the Reference, hence equation (3.7) becomes (noting the negation of the Phase signal)

$$\oint (-P + jQ) dl = I_e (\cos \phi + j \sin \phi) . \quad (3.8)$$

The EL CID is set up normally using the phasor diagram shown in Figure 3.8 so that its Phase resolution is in phase with the excitation current \mathbf{I}_e , thus by inspection $\phi = \pi$ and

$$\oint P dl = I_e \quad \text{and} \quad \oint Q dl = 0 . \quad (3.9)$$

The measurement interpretation of equation (3.9) is that the *Quad* values around the core surface must sum to zero, and the *Phase* values sum to the excitation current I_e (as usually expected). This is regardless of the presence or absence of faults. Since the Chattock is normally set to span the opposite sides of the teeth across a slot, there is double-counting of the mpds across each tooth surface. Though small, these give a 10–15% over-estimate, however any fault on a tooth tip is counted twice, and must be more explicitly allowed for in the *Quad* summation. For laminated stator cores, especially with radial vents isolating separate core packets, this also means the phase angle of the

induced flux will vary axially along the core to reflect the fault's flux in any local circumferential region.

In a stator core, the flux significantly lags the excitation mmf due to hysteresis and eddy current losses in the core. This varies with type of the steel and especially the excitation level. As an example from tests on assembled cores, M310-50A electrical steel, Cogent [66, 181] and C.D. Wälzholz (CDW) [182] exhibit the variations of core loss angle (phase lag) with low levels of flux density given in Figure 3.7. This shows that at the usual level of EL CID testing (4% of full flux density) a loss angle of 15–20° would be expected, found to be typical of large turbo-generators¹⁶.

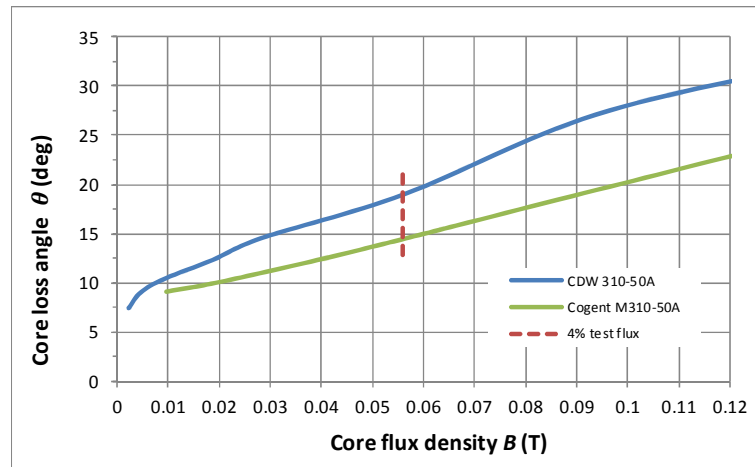


Figure 3.7 Core loss angle variation with excitation for M310-50A electrical steels

There is a further complication in that all EL CID instruments invert the *Phase* signal polarity to convention due to the way they are designed. From this a combined phasor diagram can be drawn showing the addition of the detected Excitation and Induced fault currents, resulting in a combined Chattock signal in Figure 3.8.

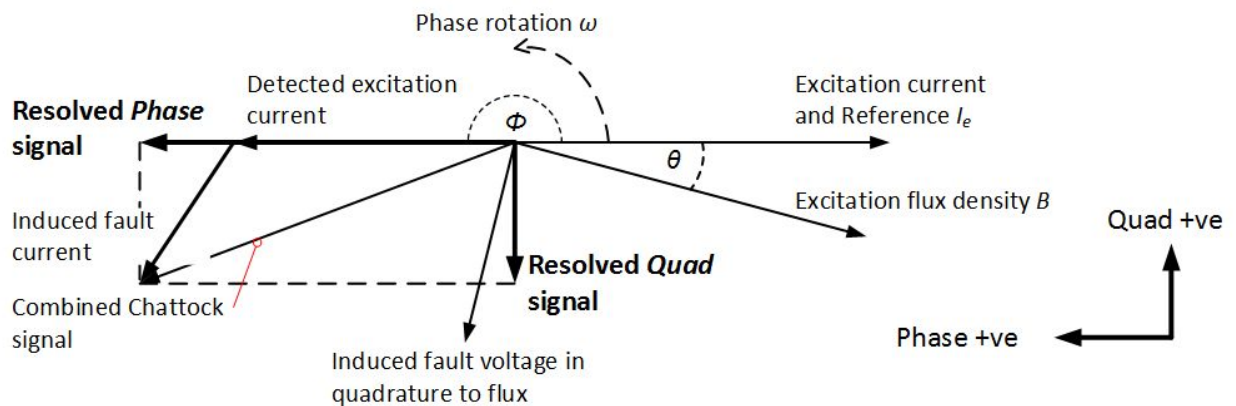


Figure 3.8 Combined phasor diagram and EL CID axes

¹⁶ This phase lag of magnetising current to flux (and hence voltage) is much larger than that commonly experienced in electrical machines such as motors, since their magnetic circuits include the lossless rotor air gap which dominates the reluctance. There is no air gap in the usual toroidal test flux path, and even those that occur in large, jointed-core, hydro-generators contribute only a small proportion of the total reluctance.

The polarity and direction of the resolved EL CID signals are shown where the Phase axis is reversed to reflect the instrument's polarity inversion. The Reference is normally aligned to the excitation current and adjusted [26] such that zero *Quad* signal is developed in a fault-free environment. From this it can be seen that the *Phase* signal mostly consists of the Excitation current plus that proportion of the Fault current in phase with the excitation Reference. The *Quad* signal is solely the induced Fault current resolved to the quadrature axis. This allows the observed detection phenomena to be explained, that for a valid fault the *Quad* signal is -ve for a +ve *Phase* signal, and vice versa.

However there are many other problems that can affect the detected signal. Unbalanced excitation in a stator with windings in place can cause circulating currents in the windings [159, 160], which being situated in the slot under the Chattock will be directly detected. Core construction, especially joints in larger hydro-generators, will substantially affect the excitation field in the core and cause a large standing mpd across each joint [66]. Other issues such as varying core loss and permeability can also potentially cause core fault artefacts, and are studied further in Chapter 7 and Chapter 8.

3.5. Analysis of current and power in stator core faults

A fault is illustrated on a slot base in Figure 3.9 (with teeth omitted for clarity), consisting of a number of laminations joined together with a return path for currents through normal keybars on the core rear. A fault voltage and hence current is induced, which is assumed not to affect the excitation current. The phasor orientation used is also shown in Figure 3.9 with conventional Real and Imaginary Argand dimensions.

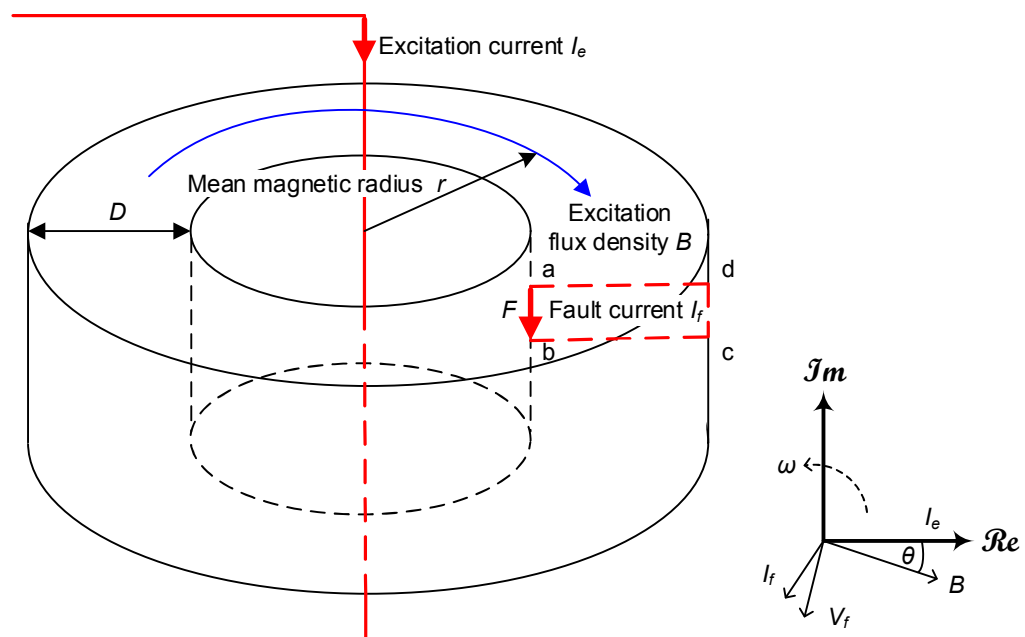


Figure 3.9 Stator core excitation and fault circuit with phase relationships

In this situation, the rms excitation current I_e (instantaneous current i_e), of rotational frequency ω induces a peak toroidal flux density B in core steel of relative permeability μ_r , with a mean magnetic path around the core yoke of radius r . The fault length ab is F , the conducting area of the faulted lamination insulation A , and the steel resistivity ρ . The resistance of the closing circuit bcd through the laminations and the rear keybar is assumed negligible. The flux lags the excitation current by an angle θ due to the core loss.

$$\text{Hence } i_e = \sqrt{2}I_e \sin(\omega t) \text{ and } b = B \sin(\omega t - \theta), \quad (3.10)$$

$$\text{and } B = \frac{\mu_r \mu_0 I_e}{\sqrt{2\pi r}}. \quad (3.11)$$

The fault's total resistance R_f and self-inductance L_f are computed, the latter assuming the flux induced by the fault current remains planar in the core circumference:

$$R_f = \frac{\rho F}{A} \text{ and } L_f = \frac{\mu_r \mu_0 DF}{2\pi r}. \quad (3.12)$$

Assuming the flux is uniformly distributed, the induced rms fault voltage V_f (instantaneous value v_f) and current I_f in the single turn fault is computed using complex notation as

$$v_f = -FD \frac{db}{dt} = -FDB \frac{d(\sin(\omega t - \theta))}{dt}. \quad (3.13)$$

$$\text{Thus } V_f = \frac{-\omega FDB \sin \theta}{\sqrt{2}} - \frac{j\omega FDB \cos \theta}{\sqrt{2}}, \quad (3.14)$$

$$\text{and } I_f = \frac{V_f}{R_f + j\omega L_f} = \frac{V_f (R_f - j\omega L_f)}{R_f^2 + \omega^2 L_f^2}. \quad (3.15)$$

$$\text{Hence: } I_f = \frac{-\omega FDB (R_f \sin \theta + \omega L_f \cos \theta) - j\omega FDB (R_f \cos \theta - \omega L_f \sin \theta)}{\sqrt{2} (R_f^2 + \omega^2 L_f^2)} \quad (3.16)$$

The power developed P_f is $\mathcal{R}_e(V_f I_f^*) = \mathcal{R}_e(V_f) \mathcal{R}_e(I_f) + \mathcal{I}_m(V_f) \mathcal{I}_m(I_f)$, thus

$$P_f = \frac{\omega^2 F^2 D^2 B^2 R_f}{2(R_f^2 + \omega^2 L_f^2)}. \quad (3.17)$$

If the resistance dominates ($R_f \gg \omega L_f$) as is normal for a modest fault, equations (3.12)

and (3.17) give:

$$P_f \approx \frac{\omega^2 AFD^2 B^2}{2\rho}. \quad (3.18)$$

Similarly if the inductance dominates ($R_f \ll \omega L_f$), as may occur for a very severe fault or at high frequencies, from equations (3.11), (3.12) and (3.17)

$$P_f \approx \frac{I_e^2 \rho F}{A} \approx I_e^2 R_f. \quad (3.19)$$

Equation (3.18) shows that the power in a fault dominated by fault resistance is proportional to the fault length and area, and as expected, to the square of the factors that control the fault voltage. It also shows that the fault power is independent of the core loss angle. Equation (3.19) shows that the power in a fault dominated by inductance is still proportional to the fault length, but now inversely proportional to area. It also interestingly reduces to the equivalent of a 1:1 current transformer from excitation current into fault resistance.

The *Quad* signal is detected as that current in quadrature to the excitation current, here the imaginary axis. Hence the *Quad* signal I_Q has no contribution from the excitation current, and is solely the imaginary fault current from equation (3.16), thus (assuming 100% relative detection sensitivity S_R)

$$I_Q = \frac{-\omega FDB(R_f \cos \theta - \omega L_f \sin \theta)}{\sqrt{2}(R_f^2 + \omega^2 L_f^2)}. \quad (3.20)$$

This shows that the amplitude of the *Quad* signal is affected by L_f as well as θ . The effect is explored for a range of core loss angles from 0–30° for fixed L_f and ωFDB (normalised to zero core loss) as R_f is varied as a proportion of ωL_f in Figure 3.10(a). This assumes an electrical steel such as M310-50A [183] with relative permeability of 3000 at test flux density levels and 1000 at service flux density. It shows that for the ideal loss free core, the *Quad* signal reaches a peak at the maximum low flux density power point of $R_f = \omega L_f$, though the full flux density fault power peak is at $R_f = 0.3\omega L_f$. The presence of core loss substantially affects the maximum detected *Quad* signal at this turning point, with the typical core loss of 20° causing a 35% reduction.

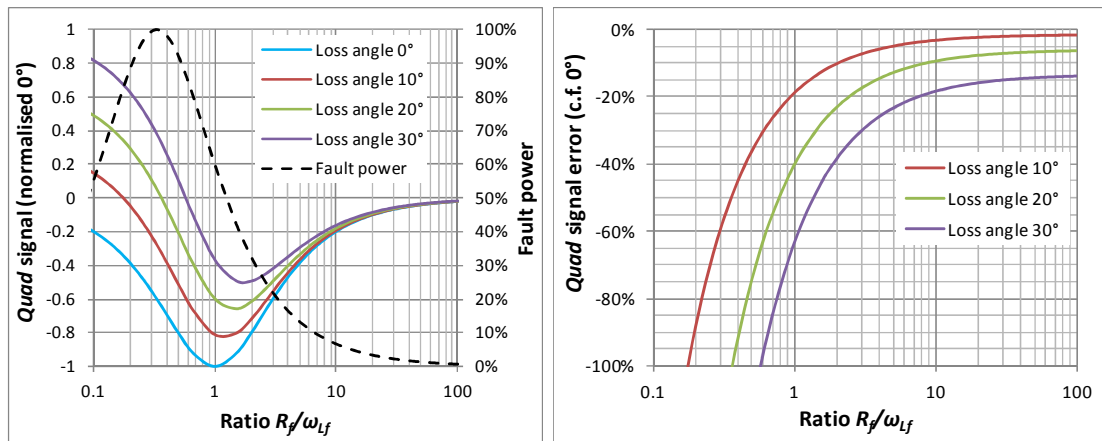


Figure 3.10 (a) Normalised *Quad* signal and service fault power, (b) *Quad* error compared to no core loss, with ratio of $R_f/\omega L_f$ and core loss angle.

Any further core loss causes a window where the *Quad* signal disappears, then suffers polarity inversion as $R_f \ll \omega L_f$. The detection error caused by core loss, compared to the no-loss case, is analysed in Figure 3.10(b), where during early fault development with $R_f \gg \omega L_f$ the error caused by a 20° core loss remains $<10\%$.

For the DAX8 experimental stator described in Chapter 9, the geometry and material parameters give a maximum *Quad* signal sensitivity of -0.35 mA/W/m for full flux fault power/metre where the fault is long and resistance dominated. Ho [72] has shown that the fault current is not totally uniform along the fault path since the lamination resistance and fault inductance cause the return currents to be shared between the end laminations. This will further reduce the detected fault current, as will the fact [184] that a Chattock sensitivity reduces with shorter fault currents. The impact of Chattock sensitivity on interpreted fault power is explored further in Appendix A.1

3.6. Synchronous detection of fault signals

An understanding of the operation of the instrument is needed to determine the response to real stator core faults and fault artefacts, especially harmonics. The basis of the process is the well-known technique of synchronous demodulation, as used for example in lock-in amplifiers.

3.6.1. Square wave synchronous demodulation

The Analogue and Digital EL CID instruments use ‘square wave’ demodulation with the basic block diagram as shown in Figure 3.11. The typical 4 mm dia. Chattock used by EL CID has a nominal 50 Hz sensitivity S_C of $100 \mu\text{V/A}$, so requires a low noise, high gain pre-amplifier to reliably detect mA. Both the Chattock and air-cored excitation current sensor (a Rogowski coil) have a 90° lag on their detected signals, but these cancel each other out so there is no need to account for them.

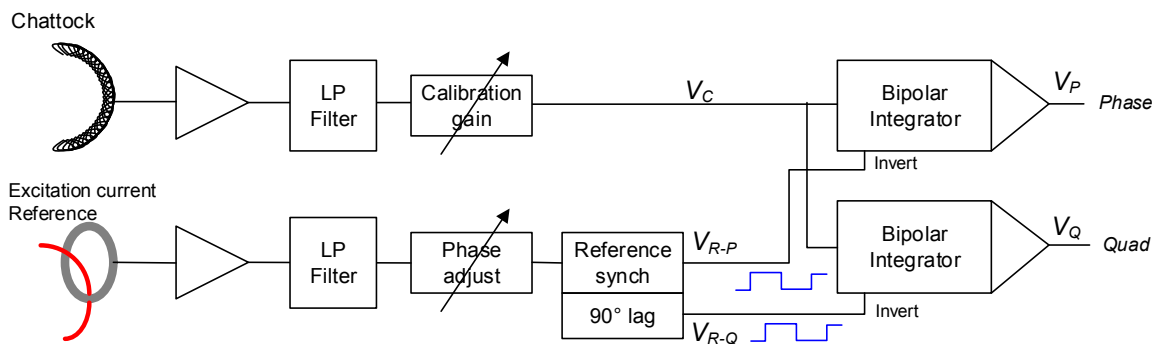


Figure 3.11 EL CID functional block diagram

The Chattock and Reference signals are low pass filtered to remove HF noise, particularly required due to their rising frequency response. The user ‘Phase adjust’ control compensates for instrument and sensor phase errors, and the ‘Calibration gain’ control for varying Chattock and instrument sensitivity. The signal is passed to two controlled full-wave bipolar integrators, while the Reference signal is converted to two square wave signals, one in quadrature to the other, to switch the two integrator polarities and produce the *Phase* and *Quad* signals. Mathematically this is the convolution (and with the integration, demodulation) of the Reference square wave signal and detected Chattock sine wave V_C of unknown leading phase angle ϕ to the I_e Reference, shown in Figure 3.8. (Phase angle ϕ is normally $> \pi$ since the detected dominant excitation mpd is inverted as described in section 3.4)

Considering the Phase demodulation, for V_R Reference square wave ($V_R = +1$ for $0 < t < \pi$, -1 for $\pi < t < 2\pi$) and peak Chattock signal \hat{V}_C at phase angle ϕ to the Reference, the instantaneous *Phase* signal v_p is

$$v_p = V_R \hat{V}_C \sin(\omega t + \phi). \quad (3.21)$$

A square wave can be expanded as a Fourier series of odd harmonics of the fundamental, with V_R described by the square wave sine series given in equation (3.22)

$$v_p = \frac{4\hat{V}_C}{\pi} \sum \left[\sin(\omega t) + \frac{1}{3} \sin(3\omega t) + \frac{1}{5} \sin(5\omega t) \dots \right] \sin(\omega t + \phi). \quad (3.22)$$

Multiplying out the terms in (3.22), with normal trigonometric substitution gives

$$v_p = \frac{2\hat{V}_C}{\pi} \sum \left[\begin{array}{l} \cos(-\phi) - \cos(2\omega t + \phi) + \frac{1}{3} \cos(2\omega t - \phi) - \frac{1}{3} \cos(4\omega t + \phi) \\ + \frac{1}{5} \cos(4\omega t - \phi) - \frac{1}{5} \cos(6\omega t + \phi) \dots \end{array} \right]. \quad (3.23)$$

The integrators operate over one cycle, a period of $2\pi/\omega$, thus for unity gain integration over this period, the mean *Phase* signal V_p is given by

$$V_p = \frac{2\hat{V}_C}{\pi} \frac{\omega}{2\pi} \int_0^{2\pi/\omega} \left[\begin{array}{l} \cos(-\phi) - \cos(2\omega t + \phi) + \frac{1}{3} \cos(2\omega t - \phi) \\ - \frac{1}{3} \cos(4\omega t + \phi) \dots \end{array} \right] dt. \quad (3.24)$$

Integration of $\cos(n\omega t + \phi)dt$ over $2\pi/\omega$ for integer $n > 0$ is always 0, thus all the harmonic terms in equation (3.24) integrate to zero, hence the signal reduces to

$$V_p = \frac{2}{\pi} \hat{V}_C \cos \phi. \quad (3.25)$$

It is recorded in section 3.4 that the Chattock detects the inverse of the excitation current, but the measured *Phase* value is negated, hence the net effect is unchanged. Thus equation (3.25) gives the expected result, a dc *Phase* signal proportional to the Chattock signal and resolved to the Phase axis of 0° to the Reference.

The similar process occurs for the Quad axis detection, achieved by convolution with Quad Reference square wave ($V_R = +1$ for $-\pi/2 < t < \pi/2$, -1 for $\pi/2 < t < 3\pi/2$ resulting in the Fourier square wave cosine series) for V_Q .

$$v_Q = \frac{4\hat{V}_C}{\pi} \sum \left[\cos(\omega t) - \frac{1}{3} \cos(3\omega t) + \frac{1}{5} \cos(5\omega t) - \frac{1}{7} \cos(7\omega t) \dots \right] \sin(\omega t + \phi). \quad (3.26)$$

It can thus be similarly derived that the mean *Quad* signal is given by

$$V_Q = \frac{2}{\pi} \hat{V}_C \sin \phi. \quad (3.27)$$

Equation (3.27) shows that since the current from a fault leads the Reference by $>\pi$, a negative *Quad* signal thus occurs for the positive *Phase* signal. The mean values are scaled to rms for output.

If the Chattock signal contains odd harmonics of the fundamental then these are also demodulated. Since the system is linear, each harmonic can be considered separately. For the *Quad* demodulation, if for example there is a 3rd harmonic signal of instantaneous amplitude $\hat{V}_{C3} \sin(3\omega t + \phi_3)$, where ϕ_3 is the angle the harmonic leads the fundamental, then this will demodulate to:

$$V_{Q3} = \frac{2\hat{V}_{C3}}{\pi} \frac{\omega}{2\pi} \int_0^{2\pi/\omega} \left[\begin{aligned} &\sin(4\omega t + \phi_3) - \sin(-2\omega t - \phi_3) - \frac{1}{3} \sin(6\omega t + \phi_3) + \frac{1}{3} \sin(-\phi_3) \\ &+ \frac{1}{5} \sin(8\omega t + \phi_3) - \frac{1}{5} \sin(2\omega t - \phi_3) \dots \end{aligned} \right] dt, \quad (3.28)$$

hence
$$V_{Q3} = -\frac{2}{3\pi} \hat{V}_{C3} \sin \phi_3. \quad (3.29)$$

Thus any odd harmonic is demodulated in the *Phase* and *Quad* signals with the attenuation and polarity of the related square wave harmonic order (3rd and 7th *Quad* harmonics are inverted) and resolved according to the cosine or sine of its phase angle to the Reference. By inspection, even harmonics always integrate to zero, thus are not demodulated.

3.6.2. Sine wave synchronous demodulation

The later EL CID Evolution uses Digital Signal Processing (DSP) techniques where the convolution Reference signals are pure sine and cosine waves (not square). The *Phase* and *Quad* output signals are still resolved by convolution and integration over $2\pi/\omega$.

Consequently the outputs only respond to the fundamental, any harmonics are converted to another harmonic and integrate to zero.

3.7. Fault interpretation

Each slot of the machine is scanned axially from end to end, with the *Phase* and *Quad* values recorded against position in the core. Inspection of the recorded traces allows visual analysis, such as in the example individual trace in Figure 3.12 with a clear core fault circled. Here the *Phase* polarity is +ve, so the *Quad* signal is swinging correctly –ve for the fault, and the *Phase* signal is also seen to increase slightly at the fault, as expected. In order to determine where a fault might be situated in the tooth or slot or core yoke, scans down adjacent slots are compared.

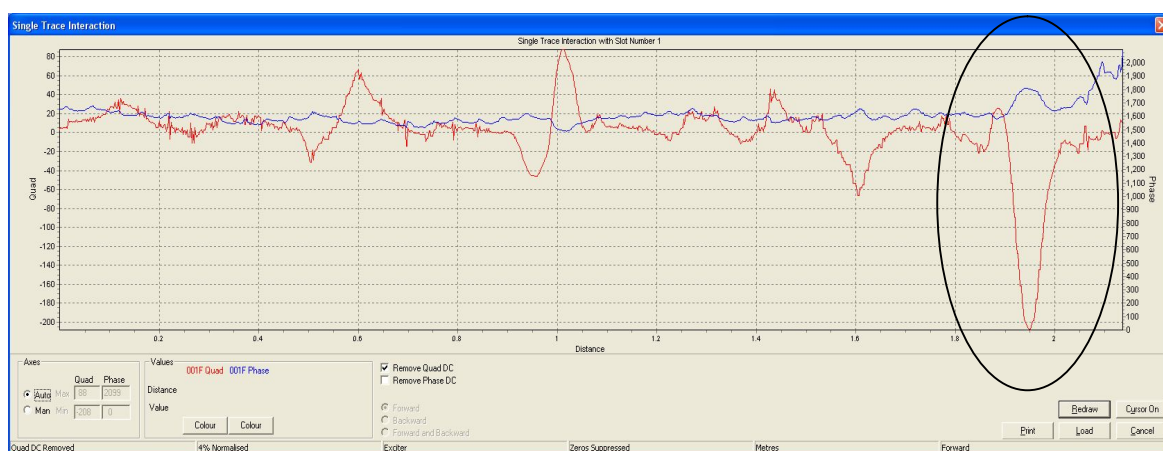


Figure 3.12 Slot trace with fault. Left scale *Quad* (red trace) -200 to +80 mA, right scale *Phase* (blue trace) 0 to 2000 mA, horizontal scale *Distance* 0 to 2 m)

The *Quad* fault signal level considered ‘significant and should be investigated further’ is generally set at 100 mA (at the standard excitation level of 4%) [26], originating from the totally precautionary approach in the CEGB work [68]. It was not chosen as a thermal correlation, which was felt would be impractical, just a level that offered the ‘safest strategy’. This was not yet a level that would indicate dangerous heating but the presence of nascent damaged areas which could usually be repaired. Sutton [61] considered in 1995 that this had served the industry well, with no reports of machine failures from faults <100 mA when returned to service.

Many faults cannot be readily repaired without major work, but there remains no objective evidence of how time-to-failure decreases with increasing fault signal above 100 mA to assist decisions on how quickly to repair. Sutton [61] and Sasic [147] suggest that 300 mA should be treated seriously, while Ridley [148] (§4.1) based on his CIGRE survey [185] thinks 300 mA ‘strongly indicates the need for investigative action’. The hydroAMP consortium [186] (§App. E, T2.S10) considers that the 100–200 mA region is

as dangerous as ‘many loose wedges’, while >200 mA equates in threat to ‘mostly loose wedges’ or massive ozone presence (from Partial Discharge). However there are reports [40, 187, 188] of machines surviving for years with faults of >500 mA due to inability to correct them, so high *Quad* readings are not automatic ‘death sentences’. The correlation of the *Quad* signal with recorded fault temperatures is studied from field data in Chapter 4.

3.8. Discussion and summary

The magnetic field strength developed in the stator bore by the current in a core fault is measured by a Chattock potentiometer as the mpd across the fault. The high permeability of the steel core ensures that the majority of the field from surface faults is detected by the Chattock. A phasor analysis showed the mpd from the fault current which contributes to fault heating is mostly in quadrature to the excitation, allowing this component of the fault current to be separated from the excitation by phase resolution as the *Quad* signal.

An analytic study of fault powers showed the dependencies for modest faults where fault resistance dominates, to be proportional to fault area and length, while once fault inductance dominates, the power is still proportional to length but now inversely proportional to area, and is the equivalent of a 1:1 current transformer from excitation current into fault resistance. The core loss angle affects the accuracy with which the *Quad* signal indicates the fault power; the *Quad* signal can be severely attenuated or even inverted for faults that are becoming inductance limited. At the lower permeability of high flux density levels, this may be before the fault is inductively limited in service, and thus has important connotations for severity interpretation of intense faults where the fault is not visible. The study made the usual assumption that the fault inductance is solely that from toroidal flux circuit, whereas it is shown later that significant additional axial flux linkage may exist and increase the self-inductance, despite the lamination stacking reluctance.

The measurement of the fault-indicating *Quad* signal is achieved by phase sensitive detection that works on the principle of synchronous detection, which can result in the detection of harmonics. Synchronous detection by the common ‘square wave’ detection process results in any odd harmonic being also demodulated into *Phase* and *Quad* signals with the attenuation and polarity of its square wave harmonic order. This is potentially important given the large variation in permeability of electrical steel with test flux density.

Even harmonics are not demodulated. Instruments using DSP demodulation with sinusoidal references are not susceptible to harmonic demodulation.

The *Quad* signal is the prime indicator of a core fault, but must be interpreted with the excitation polarity (*Phase* signal) to ensure it is indicating an increase in core loss (i.e. fault current), where -ve *Quad* with +ve *Phase* (or vice versa) is a valid fault. The *Quad* threshold for investigation is generally set at 100 mA (at 4% flux density), though is not an automatic repair recommendation. However there remains little guidance on the *Quad* level at which repair is mandatory, with several proposals for a >300 mA threshold conflicting with anecdotes of machines surviving years with >500 mA faults.

Chapter 4. Correlation of High Flux and Electromagnetic Tests in the Field

As noted in section 1.2, the main threat of a stator core fault is the local heating effect, and electromagnetic tests on the fault are undertaken on the basis that their results reflect the expected service overheating. There is no known proof of this. This section studies all the available data to better determine the correlation actually occurring on electrical machines in service in the field, between fault heating as perceived by the high flux test (HFT) and the EL CID *Quad* signal, and also the test variables that can affect them. The work was first published in 2011 [189] and in expanded form in 2012 [190]¹⁷.

4.1. The problem of core heating

The only process that can affect the core integrity from interlamination defects is the heating effect of the fault currents. Commercial lamination insulation, for example to ASTM A976 has generally quite high temperature resistance [191]. The common grades C-3 and C-6 have continuous ratings in air of 180 °C, well above the limits of normal winding insulation classes of B / F at 130 / 155 °C. Consequently the risk to the core of a nascent defect (one that is as yet below 180 °C) is that the electro-mechanical degradation process will continue until the core heating from the current becomes severe enough to pyrolise the lamination insulation. At this point thermal damage will contribute to the process, and likely lead to the runaway melt-down effect described by Murray et al. [192] and Tavner and Anderson [18], and illustrated in section 1.2.

However any minor core fault heating that increases the temperature of the HV winding insulation will affect the winding's life, even if it does not cause an over-temperature. Stone et al. [17] (§2.1.1) advises this usually comes from thermal oxidation in which the rate of the reaction is governed by the *Arrhenius rate law*. Here the lifetime of the insulation (t) is related to the temperature (T in °K) where A and B are constants

$$t = Ae^{B/T}. \quad (4.1)$$

Stone et al. report this is often interpreted as indicating that the life of the winding will decrease by 50% for every 10 °C rise in temperature, once temperatures high enough to

¹⁷ Reproduced with permission. Copyright IET.

start chemical decomposition are reached¹⁸. Since electrical insulation is only as sound as its weakest link, any small region that is weakened will result in a reduced life of the whole winding.

4.2. Assumed correlation of the tests

There is a commonplace expectation that the *Quad* signal of a stator core fault detected by the EL CID system is correlated to the temperature rise during a high flux test at 5–10 °C/100mA [26]. There is no known theoretical proof of this. Both the tests were and still are applying the total precautionary approach, in that all core faults are considered problematic and a risk to winding insulation life well before they pose any threat to lamination insulation. Consequently the criterion set for both tests was a threshold sufficiently above normal background variation that a fault is evident, and thus could reasonably benefit from attention. Thus the two test threshold values have become synonymous.

Early field experiments were of course conducted; Gill [193] in 1984 reported ‘good correlation’ with values from 7–44 °C/100 mA, while Rickson [194] in 1986 described a fault displaying 5 °C/100 mA. However no general correlation was publicly proposed until Sutton [61] in 1995 reported an assumption of ‘perhaps’ 10 °C/100 mA. This has now translated to the 5–10 °C/100 mA correlation given by the EL CID manufacturer [26] and echoed by CIGRE [25]. Despite this, there remain industry concerns [16] that the tests appear poorly correlated and that it may be unwise to rely on EL CID alone in case of doubt over the core’s condition.

Though most practitioners and some field reports give support to this unqualified correlation, contrary anecdotes remain [54]. Given the great variety of fault positions, their severity and machine types, it is implausible that all faults assuredly lie within this range, thus the goal of this element of research is to determine the probabilities that attach to the correlation. Confidence in the correlation is important since conducting both tests to ensure all faults are discovered is expensive.

4.3. Field evidence for the correlation

There have been a few reported experiments [57, 195-197] to verify this correlation with variable results. The only previous review of test results is by Ridley [185] on hydro-

¹⁸ Not easily defined, since the insulation will have many molecular constituents each with their own temperature thresholds and precise rates. However the formula has now developed a life of its own in insulation life assessment.

generators which showed that a 10 °C/100mA correlation had some justification. EPRI also reported an ad hoc survey in 2008 [25] on users' comparative experience of the two tests. This subjective feedback provided some support for the expected correlation, but frustration that the relationship is not exact.

Thirteen papers [56, 57, 185, 187, 194-203] (including the EPRI study below) were identified which report details of both an EL CID and high flux test conducted on the same faults. This produced a total of 106 fault results on 23 machine tests to correlate, and included Ridley's work where it does not repeat other source material. The records were rarely complete but generally the results and machine description were given, plus sometimes excitation levels. While this provided the basic data to determine the correlation, a number of adjustments were developed in the survey to improve the analysis.

4.4. EPRI Core Model studies

EPRI obtained the terminally damaged 496 MVA Deely stator in 2001 to study the origin and mechanisms of the many stator core faults that had occurred [200]¹⁹. The results were sufficiently inconclusive to require a follow-up EPRI Core Model study [57] reported in 2004. This used laminations from the now dismantled Deely stator to construct a 0.6 m long model core section with 9 packets, on which a large variety of surface and subsurface artificial faults were applied. There were 12 surface faults on teeth, slot side and base, 4 inside through bolt holes, and 16 embedded in the core in the teeth and core back, a total of 32 with lengths varying from 10–30 laminations. These were tested by HFT, EL CID and DIRIS test systems and the results compared. The disappointing conclusion was 'very little quantitative correlation between any two of these test methods and even less correlation of any of these test methods with the intended severity of the shorts.'

The tests suffered several problems. The keybar connections were ineffective, so these were bridged with just aluminium foil on the rear. The faults were not calibrated, being welds on the lamination surfaces which rarely matched the declared number of shorted laminations. The welds also produced very severe faults, not really typical of service degradation. The embedded faults made poor contact and were mostly abandoned, leaving ultimately only 12 successfully applied surface faults, spread across 3 packets.

The EPRI high flux and EL CID results were analysed in detail and it became clear that a number of problems had accumulated to confound the researchers. These were corrected and a much better correlation was obtained.

¹⁹ Unfortunately their report remains commercial.

4.4.1. Correction of standing test errors

Section 3.4 demonstrates that a true fault *Quad* signal's polarity must always be opposite to the *Phase* signal. In consequence only negative *Quad* signals indicative of a fault within the Chattock span were considered. There was also a standing error, determined from the one packet (H) with no faults applied. This was found to be dependent on the slot's maximum value, giving corrections from -40 to +200 mA.

4.4.2. Correction of Quad recovery errors

The problem of 'Quad recovery' studied in section 6.1 occurred to a considerable degree, where multiple or severe faults on the same core packet interact, partially suppressing each other. In this case there were 4 severe faults on each of 3 packets and with only 27 slots there were consequently substantial interactions between the faults.

The algorithm developed in Appendix C.2 was used to correct and compute the expected true *Quad* fault signals. The Quad recovery mpd is assumed to be evenly distributed around the bore in the axial plane. Q_{in} and Q_n are the measured *Quad* signal and actual *Quad* fault value for slot n at each core axial packet, and ε a global error value from any error in the EL CID phase reference. (In this case ε was already determined from packet H). Each slot signal at an axial position/packet on a core of N slots will thus be

$$Q_{in} = Q_n - \frac{\sum_N^1 Q_n}{N} + \varepsilon. \quad (4.2)$$

Unfaulted slots will carry a positive *Quad* signal averaged as Q_{+max} ²⁰. From equation (4.2) the packet's Quad recovery potential $\sum_N^1 Q_n / N$ for the slots with $Q_n = 0$ is

$$Q_{+max} = -\frac{\sum_N^1 Q_n}{N} + \varepsilon. \quad (4.3)$$

From equations (4.2) and (4.3) the correction and true *Quad* fault signal can be computed

$$Q_n = Q_{in} + \frac{\sum_N^1 Q_n}{N} - \varepsilon = Q_n - Q_{+max}. \quad (4.4)$$

The magnitude of the corrections ranged from -17 to -234 mA.

4.4.3. High flux test anomalies

Compensation for high flux test anomalies was also needed. The high flux test was initially conducted at 103% flux and then due to supply overload reduced to 90% flux for a

²⁰ Each packet's 8 maximum values were ranked to check for errors. The mean then taken of the lowest 7 to reduce any bias from one-off 'spikes', less 10% to allow for double-counting of the Quad potential across teeth.

final period. This produced a bias in the results, plus there was lack of compensation for core body temperature rise. The core ‘ambient’ used to compute the fault temperature differential rise was recorded as increasing by just 3°C, whereas around a 20°C rise would be expected, so corrections were applied. In addition four unexplained sudden changes in temperature were assumed erroneous and adjusted to reflect their preceding trend.

4.5. Normalisation of field data

4.5.1. Selection of results

Some results displayed heat but no sensible *Quad* signal and vice versa, which produced extreme outliers including infinite correlation factors. They were excluded on the basis that they were either untrustworthy due to error, or maybe extremely short faults or faults deeply buried in the core. Such short/deep faults can cause the *Quad* signal or temperature value to be badly attenuated and lost in noise. The 106 total test results are after extreme outlier eliminations.

Repeat fault test results after repair were included as an independent set of results, since they will have either been disturbed faults or possibly fresh faults induced.

4.5.2. Core size correction

The survey results embrace a wide range of machine sizes and construction, from a 40 MW hydro-generator to a 900 MW turbo-generator, which may affect the test result correlation.

During a high flux test, core faults (which mostly afflict stator teeth) are believed to be principally cooled by laminar conduction across and up and down the tooth and normally achieve a steady state temperature before the test end. Thus their final differential temperature rise should be linear with fault power. For a fault of given resistance, the detected fault current will be proportional to coupled core flux Φ , while the heating power in the fault will be proportional to Φ^2 . Since the correlation originally derived from larger turbo-generators, the temperature rise per unit fault current should scale with Φ for smaller machines.

Due to lack of detail, the machines were categorised into two groups using their typical EL CID excitation p.u. length to reflect the flux. Larger turbo-generators (~5 V/m) were unscaled and small turbo-generator/larger hydro-generator (~3 V/m) high flux tests scaled x1.6 to compensate. No machines smaller than these were reported.

4.5.3. Short fault length correction

EL CID has substantial and increasing attenuation for shorter faults and Ho, [72] (Fig. 9.5), has shown this becomes severe at very small lengths. Due to the laminated core an analytical solution is very complex, thus Ho's 3D FE and experimental results were plotted in Figure 4.1 and an interpolated curve of Chattock relative sensitivity S_R fitted to the points, according to equation (4.5) where F is fault length

$$S_{RS} = 0.5(2 - e^{-F/100} - e^{-F/23}). \quad (4.5)$$

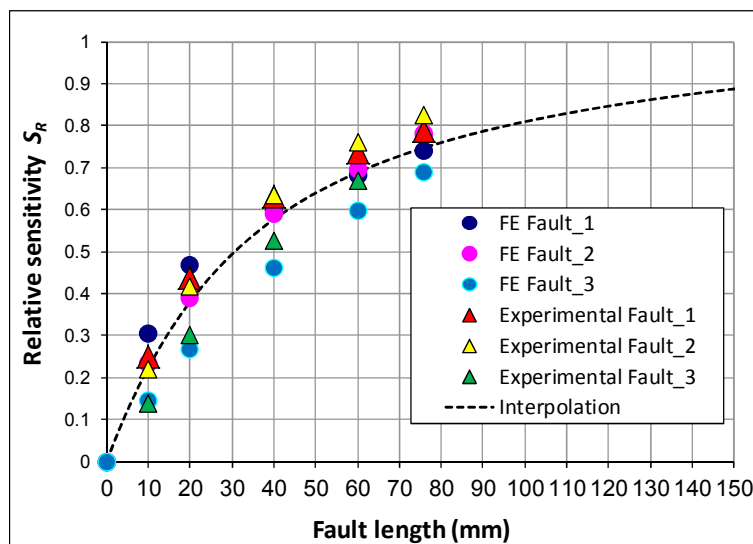


Figure 4.1 Chattock relative sensitivity curve fitted to 3D FE and experimental results

The conventional 5–10°C/100mA correlation is assumed to be based on the Chattock sensitivity for a fault length in the 10–20 mm region, whose mean relative sensitivity is 0.31. The faults had varying lengths so a compensation for the Chattock's relative sensitivity S_R with fault length was applied to normalise shorter faults to the notional length in Table 4.1. Unless recorded, the best estimate of length was taken from any IR picture or textual clue, with clearly short faults ascribed as 10 mm and those described like a 'point' as 5 mm.

Faulted laminations (qty)	Fault length (mm)	S_R	Normal correction factor
10	5	0.12	2.5
20	10	0.22	1.4
30+	15+	0.31	1.0

Table 4.1 Short fault corrections

However examination of the thermal pictures of the EPRI [57] faults showed the rather crude welding gave true lengths often longer than specified. Consequently a 1.4 correction was applied to the 10 as well as 20 lamination fault lengths.

4.5.4. High flux test level correction

The high flux density test level used (B) was not always 100% design flux density (B_D). While IEEE Std 62.2 [48] requires 100%, the custom is to run a little lower, and the commonplace correlation discussed in section 2.2 is thus generally reflecting an 80–100%, i.e. 90% nominal flux density region. Since as shown in section 2.2, the temperature rise in a fault is proportional to B^2 , the rise was corrected by the factor $(0.9B_D / B)^2$, which gives 127% for 80%, and 165% for 70% test flux density levels.

IEEE Std 62.2 recommended test time is ~ 2 hours. A surface fault differential fault temperature rise will have already stabilised within 1 hour and be just slowly following the core body temperature as it rises. However for deep-seated faults this is not so, and the test time (t) will affect the differential temperature rise. Since few faults were identified as to their depth, a weak temperature rise correction of $(60/t)^{0.3}$ was generally applied for tests $t < 60$ mins, which gives for example +23% for 30 mins. There was no precise analytic justification for formula, just a desire to provide some correction for a very poorly identified problem.

4.5.5. Buried faults correction

Buried faults being deep in the tooth root or core yoke, are expected to have differing correlation, since the attenuation of the *Quad* signal is likely to be different to the thermal signature. There is little data on the fault locations so these were simply categorised into surface (default), down slot, and core yoke.

From paper [56] a slot base thermal signal reads just 17% vs. $> 80\%$ for EL CID of the equivalent surface fault, so strictly requires 500% correction. The attenuation would be less for faults only partially down a slot, and more for core yoke faults. Since a precise correction is impossible without accurate fault location, very rarely given, a cautious aggregate fault temperature rise correction for down-slot temperatures of 200% and core yoke temperatures of 400% was chosen, though no core yoke faults were in fact identified.

4.6. Final high flux and EL CID correlation analysis

The data for all the results was collated and the initial uncorrected correlation plotted in Figure 4.2. The Mean Least Squares (MLS) trend line slope was chosen over the statistical mean, since it allows the enforcement of a logical $0\text{ }^\circ\text{C} / 0\text{ mA}$ origin on the trend. Logarithmic scales were used due to the large range of values.

4. Correlation of High Flux and Electromagnetic Tests in the Field

The identified correction factors were then applied to the EL CID *Quad* values and the high flux test results, and the data re-plotted in Figure 4.3. However it was noted that contrary to the expectation of section 4.5.2 the HFT temperature correlations were generally higher in hydro-generators than turbo-generators before the core size correction. This indicated that the correction is probably unsound and was thus not applied. The key result is the 9.6 °C/100mA trend line slope, almost the customary 10 °C/100mA.

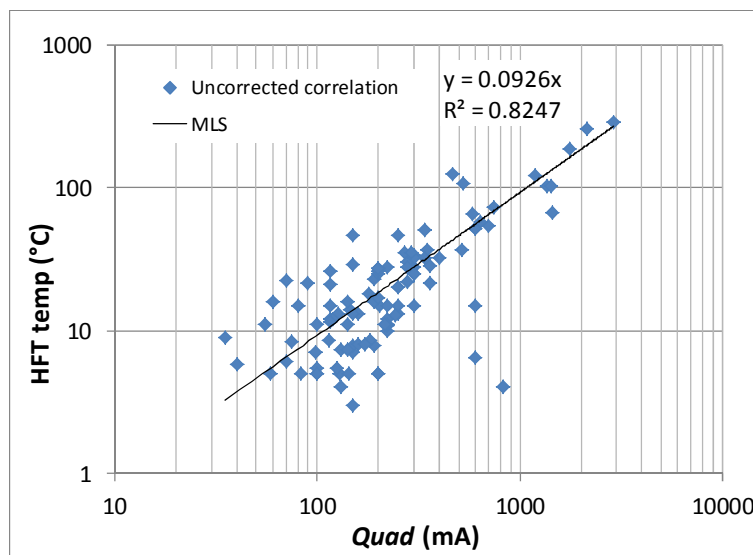


Figure 4.2 *Uncorrected field data correlation with mean*

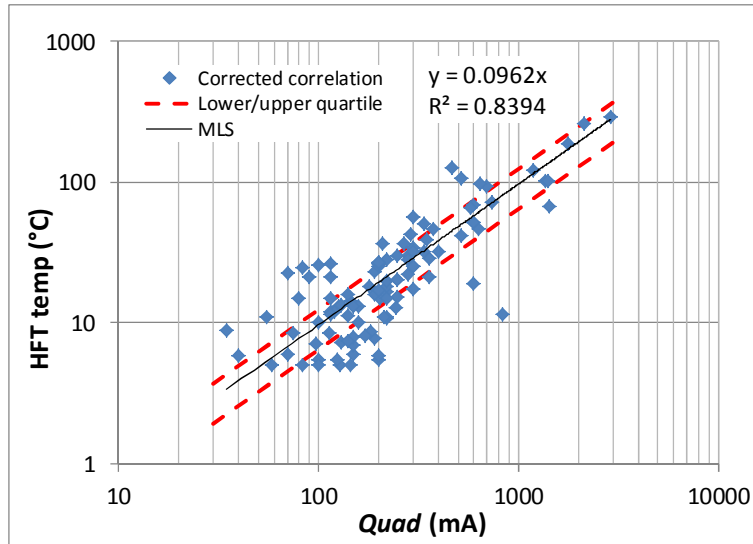


Figure 4.3 *Corrected field data correlation with mean and lower/upper quartiles*

Figure 4.3 shows a visually tighter grouping of the data around the trend line and the lower/upper quartiles, however both the correlation coefficient and standard deviation only improve by about 5%. The correlation coefficient was found to be strongly influenced by the seven very intense (>1000 mA) faults in the EPRI Study. If these are removed, the R^2 coefficient rises from 0.34 for the uncorrected results to 0.51 when corrected, better reflecting the visibly tighter clustering of the results. The resultant trend remained almost

unchanged at 9.8 °C/100mA. There was a modest difference in the correlation and spread between the separate corrected turbo-generator and hydro-generator results shown in Figure 4.4

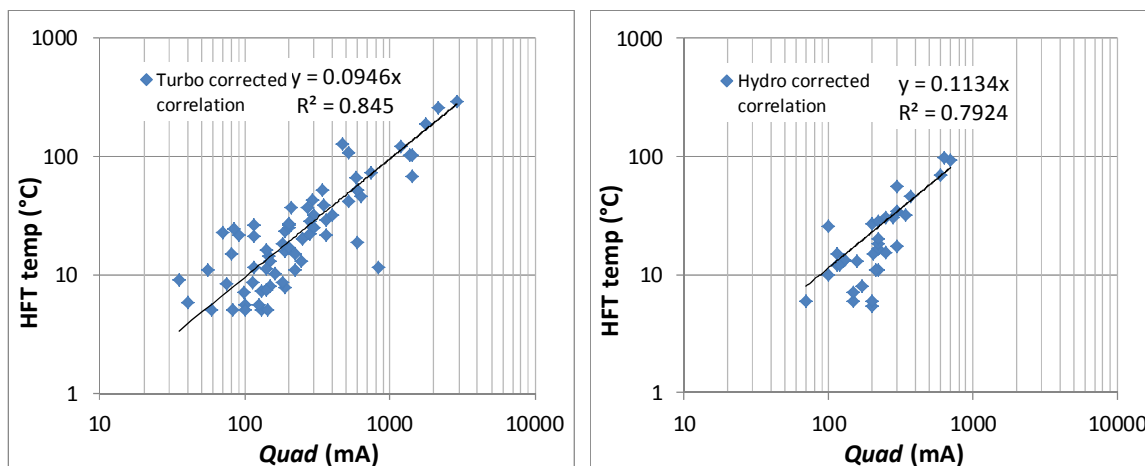


Figure 4.4 (a) Turbo-generator corrected correlation, (b) hydro-generator corrected correlation

4.7. Results statistical study

4.7.1. Test for normal distribution

The analysis assumes a normal population distribution as the null hypothesis, so this was examined to determine the probability that this is true. The corrected data for all tests was collected in 2 °C/100mA bins to reduce granularity, and the frequency of occurrence plotted. Normal distributions are overlaid for comparison in Figure 4.5.

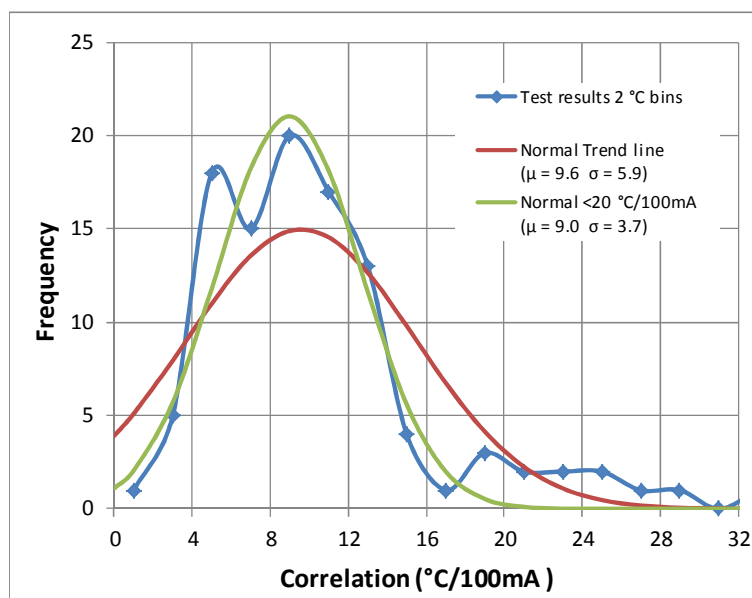


Figure 4.5 Test and Normal correlation distributions

It can be seen that the test correlation distribution has a clear normal tendency, with a modest skew to the right tail. The red solid line shows the normal distribution for the Trend

line Mean (μ) and Standard Deviation (SD, σ) of the full test results. The green line shows the normal distribution that would result if only test results ≤ 20 °C/100mA are considered.

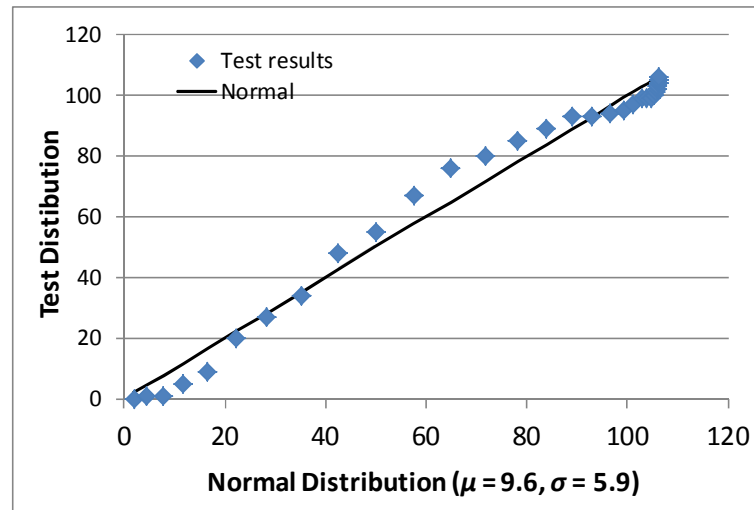


Figure 4.6 Probability plot test

As a more visually clear test of normality, a probability plot test was conducted. This plots the cumulative Test results (here collected in 1 °C/100mA bins) against the assumed full normal distribution, shown in Figure 4.6. This also indicates a close alignment between the two distributions, justifying the assumption. A Chi-square²¹ test of normality (the red line in Figure 4.5) on the full data set failed ($p = 0.005$), but just the values ≤ 20 °C/100mA (the green line in Figure 4.5) returned $p = 0.59$, strongly supporting the null hypothesis for this region.

4.7.2. Data analysis

On the basis that data has a distribution that is approximately normal, the SD of the sample (quantity 106) can be used to derive confidence limits for the population mean. The analysis is listed in Table 4.2 .

It can be seen from this study that the trend line population mean for the test correlation is between 8.5–10.7 °C/100mA to a 95% confidence, essentially within the industry expectation of 5–10 °C/100mA. In data sets with extreme outliers such as this, using the central quartiles can provide a better indicator of the commonplace result which here embrace the 6–12 °C/100mA range, again close to the industry expectation. There is also an indication that the populations of hydro-generators and turbo-generators have slightly different correlations, as their 95% trend confidence limits have only a modest overlap, though the evidence is not statistically reliable ($p < 0.05$).

²¹ The test results were collected in $\Rightarrow 2$ °C/100mA bins to ensure >5 class frequency.

4. Correlation of High Flux and Electromagnetic Tests in the Field

* ($^{\circ}\text{C}/100\text{mA}$)	Original All tests	Corrected All test	Turbos	Hydros	Real Faults
Number of samples	106	106	73	33	81
Mean correlation *	9.8	10.4	10.6	9.7	10.2
MLS trend correlation *	9.3	9.6	9.5	11.3	8.7
Correlation coefficient R^2	0.82	0.84	0.85	0.79	0.50
SD of population *	6.15	5.84	6.30	4.67	5.74
SD of population mean *	0.60	0.57	0.74	0.81	0.74
95% confidence trend line correlation *	8.1–10.4	8.5–10.7	8.0–10.9	9.8–12.9	7.3–10.2
Lower – upper quartiles *	5.3–11.4	6.4–12.2	6.7–12.5	6.1–12.9	6.33–12.5
95% confidence population limit *	18.2	18.1	18.6	18.1	18.3
Absolute minimum – maximum *	0.5–32.1	1.4–32.1	1.2–32.1	2.6–22.9	1.4–32.1

Table 4.2 Statistical analysis of original and corrected correlations

The effect of enabling each of the correction factors described in sections 4.5 was studied. Most made some improvement, albeit small, in the correlation coefficient R^2 shown in Table 4.3.

Correlation ($^{\circ}\text{C}/100\text{mA}$)	Uncor rected	Core size	Short Faults	Flux density level	Test time	Buried faults	Total corrections exc. Core size
Qty affected tests	106	44	4	14	7	9	34
Mean correlation	9.8	11.9	9.4	10.2	10.0	10.2	10.4
Trend line slope	9.2	9.7	9.2	9.4	9.4	9.4	9.6
Correlation R^2	0.82	0.79	0.83	0.83	0.82	0.83	0.84
SD of population	6.15	7.18	5.51	6.43	6.16	6.19	5.86

Table 4.3 Effect of correlation corrections

4.7.3. Correlation improvement in EPRI study

The original measurements supported the very pessimistic EPRI conclusion, with an apparent mean $22\text{ }^{\circ}\text{C}/100\text{ mA}$ correlation and very poor $R^2 = 0.13$ correlation coefficient in Figure 4.7(a).

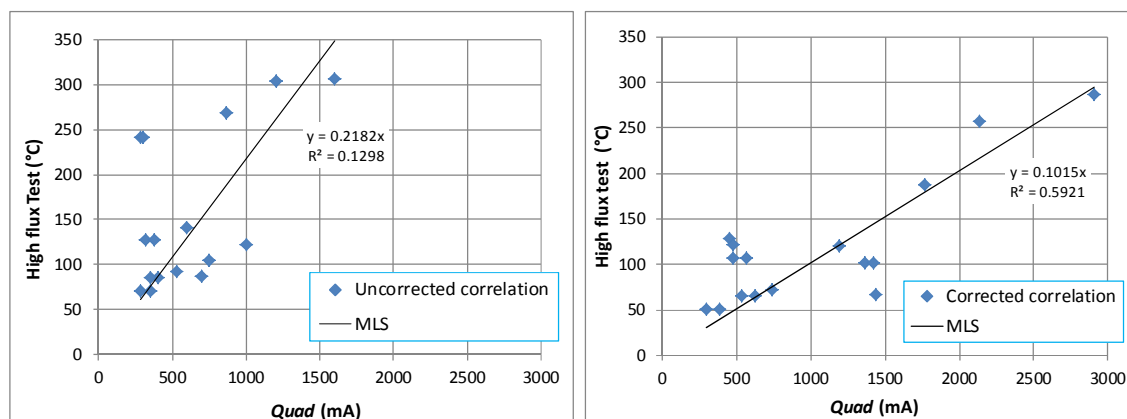


Figure 4.7 (a) Original EPRI study correlation, (b) corrected EPRI study correlation

4. Correlation of High Flux and Electromagnetic Tests in the Field

After the adjustments in section 4.4, together with the short fault correction, the mean correlation dropped to 10 °C/100mA, with a stronger R^2 coefficient of 0.59, shown in Figure 4.7(b).

The values were statistically analysed to determine the standard deviation of the sample, used to derive the confidence limits for the EPRI population (12 samples) correlation mean listed in Table 4.4. It can be seen that there is a 95% confidence that the population mean for the EPRI surface faults has a correlation between 6.3–14.0 °C/100mA, close to the industry expectation of 5–10 °C/100mA.

Measure	Original correlation	Corrected correlation
Origin trend line slope	21.8 °C/100mA	10.2 °C/100mA
Correlation coefficient (R^2)	0.13	0.59
SD of population (N = 12)	19.9 °C/100mA	6.8 °C/100mA
SD of mean	5.8 °C/100mA	2.0 °C/100mA
95% confidence mean correlation trend line limits	10.5–33.1 °C/100mA	6.3–14.0 °C/100mA

Table 4.4 Statistical analysis of original and corrected EPRI study correlations

4.7.4. Influence of artificial faults

The number of test results which used artificially applied faults was 25 out of the 106 total. It might be considered that these could skew the results, on the basis that the application of artificial faults, by for example the welding of the very severe EPRI faults, may give a different correlation to genuine core degradation. If the correlation is restricted to only the real faults as shown in the last column in Table 4.2, it is seen that there is little difference, with the trend line mean falling to just 8.7 °C/100mA.

4.8. Discussion and summary of correlation results

The result is encouraging evidence that the HFT and EL CID tests are in practice quite strongly correlated, that the commonplace expectation of 5–10 °C/100mA is supported with central quartiles of 6–12 °C/100mA, and furthermore that 95% of tests will correlate under 18 °C/100mA. However there remain several outlying results that appear to severely buck the trend in both directions, for which no explanation can be offered. In addition, even though five types of correction were identified that could be applied to each sample, only 34 total corrections could be made to the 106 samples so the bulk of the data remains uncorrected. This might explain some of the still substantial spread in the data, in addition to the possibility of test or reporting error. There are also other variances that can affect the results of the two tests differently, such as the resolution of any IR camera used and the competence of its operator, and the proximity of the Chattock winding to the core and its linearity.

In analysing the data, while the zero-origin MLS trend line would seem best, its sensitivity to extreme outliers can distort it as a predictor and give no information on variance. Using the two central quartiles can provide a better indicator of the commonplace result, which here embrace the 6–12 °C/100mA range, close to the expected rate. It was found that 55% of the sample tests lay in the expected 5–10 °C/100mA range.

There is an indication that the populations of hydro-generators and turbo-generators have slightly different mean correlations. However their population variances are sufficiently large that one would not perceive the difference in individual tests. Further, the theoretical expectation that there would be a substantially lower correlation ratio in hydro-generators due to lower fault voltages is not found in practice. It is hypothesised that the generally much narrower core teeth in hydro-generators results in less effective laminar conductive cooling, offsetting the lower test voltage and hence fault power. This is supporting evidence for the same hypothesis made in section 2.4.5 studying the EMK test metrics compared to EL CID with varying core geometry.

The very large test values all come from the EPRI study, where the welded faults were in the main very severe, with 7 out of 12 ranging from 1,000–2,906 mA. Several of their outlying results appear to severely buck the trend with values >25 °C/100mA for no further reasons that can be ascribed. Experience is limited to just the EPRI study for such intense faults, and it may be that the faults were approaching inductive limitation as described in section 3.5, where *Quad* signal sensitivity falls rapidly due to core loss. It is also possible that the temperature signal displayed from a welded fault will be higher than that from a genuine core fault since all the current flows on the surface. In addition very severe faults will have differing current profiles than more modest ‘normal’ faults, due to fault inductance and lamination impedance, thus their Chattock detection efficiency may be different to the standard model. However it is encouraging that even in EPRI’s very unrepresentative examples, once known corrections are applied for the test errors or compromises, the commonplace correlation becomes quite apparent.

It might be argued that a field technician wishing to correct an EL CID reading will not be able to apply an extensive set of corrections, and thus will be doomed to obtain a poor correlation. However relatively few corrections were made, and those done were a simple scaling which should be quite practical in the field.

The root cause of the concern that EL CID often does not detect very short surface faults is also evident. A 10 °C fault affecting say 5 laminations (2.5 mm) would be clearly evident on an thermal camera close up, but lost in the background at <30 mA *Quad* level

4. Correlation of High Flux and Electromagnetic Tests in the Field

when measured with EL CID. However the risk to the machine from such a short surface fault is low.

Chapter 5. Electromagnetic FE Models

A number of studies in this thesis have used electromagnetic Finite Element (FE) models to determine the expected fault signals for particular core constructions and/or fault locations. These have all used the 2D software package FEMM [204]. This uses the A-V electromagnetic formulation, whose theory and implementation is well known [205] (§3.3) and was used without alteration.

In summary, the computation uses the magnetic vector potential \mathbf{A} defined such that the curl of \mathbf{A} is the flux density vector \mathbf{B} .

$$\nabla \times \bar{A} = \bar{B}. \quad (5.1)$$

Ampère's law similarly relates the magnetic field strength vector \mathbf{H} and current density vector \mathbf{J} (which includes both imposed and induced currents)

$$\nabla \times \bar{H} = \bar{J}. \quad (5.2)$$

Substituting $\mathbf{B} = \mu\mathbf{H}$ and assuming μ is constant in equations (5.1) and (5.2) gives

$$\nabla \times (\nabla \times \bar{A}) = \mu \bar{J}. \quad (5.3)$$

Equation (5.3) can be expanded by normal vector relationship [206] (§10.8.2) to give

$$\nabla(\nabla \cdot \bar{A}) - \nabla^2 \bar{A} = \mu \bar{J}. \quad (5.4)$$

The vector potential \mathbf{A} needs to be constrained to allow a solution, and the usual constraint is to impose the *Coulomb gauge* [207] (§12.5.1) where $\nabla \cdot \bar{A} = 0$. Thus equation (5.4) reduces to *Poisson's equation* in equation (5.5).

$$\nabla^2 \bar{A} = -\mu \bar{J}. \quad (5.5)$$

(The *Coulomb gauge* is automatically applied in the 2D situation where only A_z exists.)

In the 2D case current is assumed to only exist in the z dimension hence $A_x = A_y = 0$ and A_z is constant along the z axis, thus equation (5.5) reduces to

$$\frac{\partial^2 A_z}{\partial x^2} + \frac{\partial^2 A_z}{\partial y^2} = -\mu J_z, \quad (5.6)$$

and, where $\hat{\mathbf{x}}$ and $\hat{\mathbf{y}}$ are unit vectors, equation (5.1) expands to

$$\hat{\mathbf{x}} \frac{\partial A_z}{\partial y} - \hat{\mathbf{y}} \frac{\partial A_z}{\partial x} = \bar{B}. \quad (5.7)$$

Boundary conditions need to be established to obtain a unique solution to equation (5.6). These are set to reflect the physical nature of the problem. They are normally:

- i. Neumann boundary. Here the derivative $\partial A / \partial n = 0$ is established along the normal n to the boundary to enforce magnetic flux to be normal to the boundary. It is the natural boundary condition for the A-V model, and establishes symmetry along a flux axis.
- ii. Dirichlet boundary. Here the vector potential A is set equal to a value. If constant along a boundary, it prevents any flux flow across it (acts as a screen). It may be used to establish an outer boundary to a problem, a plane of symmetry or a gradient used to impose a flux density. Normally \mathbf{A} has to be set to an reference value at some point in the problem to enable a solution.
- iii. Other boundary conditions are possible to define an impedance or anti-periodic boundary.

The 2D FE elements in FEMM are triangular with the vector potentials defined at the vertices, and intermediate values obtained by linear interpolation. Uniform current density giving total current I is assumed in each element, while the linear variation of \mathbf{A}_z within each element leads to a constant value of \mathbf{B} for the whole element. Non-linear material permeability with flux density is accommodated by use of a step-wise interpolated table of B/H values for the material.

FEMM uses the variational formulation based on minimising the 2D energy $(J \cdot Area - \int_0^B H dB)$ in each element [205] (§4.5) to derive a solution to equation (5.6), as described by Allaire [208] (§9.1). This allows the generation of a large matrix relating the node potentials to the element currents, with the constant value of \mathbf{B} within each element from equation (5.7) now a linear function of the node potentials. The overall matrix solver is based on the iterative Conjugate Gradient solver [204], with the iteration stopping criteria being the proportion of the step change to the net variational energy (default setting 1 in 10^{-8}).

In use, FEMM provides a pre-processing interface to define geometry, meshing, currents and materials, with ability to adjust meshing density in different regions. Both magnetostatic and time harmonic (assuming sinusoidal variables) analysis is possible. After solution, post-processing allows extraction of flux density, current and magnetic field strength distribution data as well as normal visualisations. The constant value of \mathbf{B} and I in each element is normally smoothed out by interpolation between adjacent elements in the display and analysis.

Chapter 6. Interaction of Multiple Faults

In the majority of cases of electromagnetic stator core testing, the stator has either no significant faults, a few of modest amplitude (i.e. 100–300 mA *Quad*), or one serious fault. In these situations the interpretation of the fault signals is conventional. However if multiple faults occur at the same axial distance down the core, such that there is circumferential alignment, and especially if any are severe faults, the *Quad* signals can interact and cause reduction of their detected values. This has led to under-recording of the severity of faults in field examples. The cause of this effect termed ‘Quad recovery’ is researched in this section and interpretation methods proposed. The work was published in 2009 [203].

6.1. The phenomenon of Quad recovery

It was shown in section 3.4 for long current paths that the flux from the fault induced in the core will establish a magnetic field around the core, and that this field would be detected by the Chattock away from the fault. From equation (3.5) the detected mpd away from the fault will be the sum of the excitation current and fault current, proportioned by the slot and Chattock span angle.

$$\text{Detected mpd} = -\overline{I}_f \alpha / 2\pi - \overline{I}_e \alpha / 2\pi . \quad (6.1)$$

The *Quad* component of the $-\overline{I}_f \alpha / 2\pi$ fault signal element is the Quad recovery signal, and is thus the opposite polarity to the usual detected fault current signal. As shown in equation (3.9), from *Ampère's law* the *Quad* values around the core surface must sum to zero for the nominal case where the Chattock is set at exactly the slot pitch. However since the Chattock is normally set to span the opposite sides of the teeth across a slot, there is double-counting of the potentials across each tooth surface, and thus magnetic potentials around the machine may not sum to zero. For the Quad recovery potential deriving from the circulating fault flux, this is a small potential referred to the tooth surface and may be ignored (or a notional 10–15% allowed). However any fault on a tooth tip is counted twice, and must be fully considered in the summation.

Normally Quad recovery is a very small effect. Figure 6.1 shows Ho's [72] 2D FE models for the *Quad* signal, where it can be seen that a single tooth tip fault gave the expected $780 / 48 = 16$ mA Quad recovery signal on all other slots. However if the fault is large, or there are multiple substantial faults in the same axial region (core packets), the

Quad recovery signal may become significant in the other slots. This can cause concern to a tester who may think this indicates further faults (forgetting the importance of polarity), or even act to depress or mask an actual further fault further round the core in the same axial region.

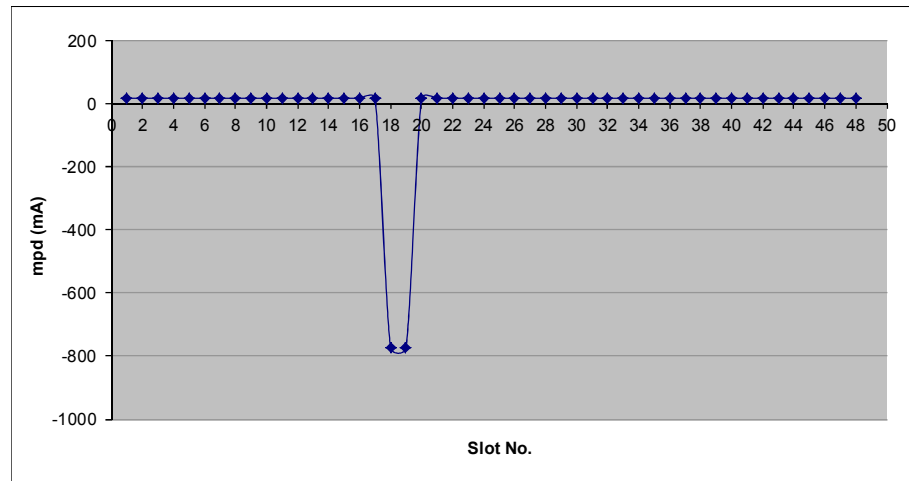


Figure 6.1 Plot of Quad mpd obtained from 2D FE (© C. W. Ho [72])

6.2. Practical effect of Quad recovery

The application of a correction for this effect might seem simple, however determining the correct fault current can be challenging. A fault current on a tooth tip and often a severe one down a slot will show a *Quad* fault signal on more than one slot, and due to its depth, will have some permeable steel fully surrounding it. In consequence the simple assumption in section 3.3 will not be true, and not all the mmf will appear between the teeth. Some of this mmf will now partially appear on other adjacent slots as illustrated in Figure 6.2. With some mmf double detected and some undetected, summing all the slot contributions will generally be a ‘fair’ contribution in the estimate of the total fault current.

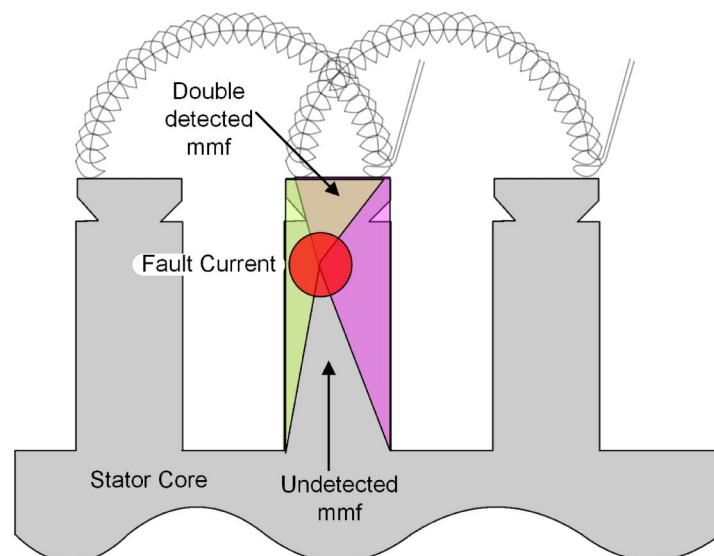


Figure 6.2 Detection of buried tooth fault on multiple slots

While apparently uniform in 2D, it is expected that the 3D reality of faults that are not long in relation to the core or packet will display a poorer circumferential uniformity. In addition is it going to be so rare that users need not worry? Three situations have been identified where field results were seriously affected by this phenomenon, described in Appendix C.1. In all of these, correction for the effect of Quad recovery allowed a more rational interpretation of the stator core condition.

Knowledge of the uniformity of the Quad recovery around the core is important to allow accurate compensation. In Appendix C.3 two examples illustrated cases where the recovery was fairly uniform, varying from a 30% to 50% reduction around the circumference. However a third example displayed greater non-uniformity, exceeding 5:1, with no apparent reason for the difference.

6.3. Transverse FE models

The development of the magnetic potentials around the core from a fault was investigated in a series of FE models, to better ascertain the expected distribution. In reality the flux from the fault may not be totally constrained to that part of the core packet, or the whole packet, due to the relatively small packet air gaps (also some stators do not have radial cooling gaps) which may allow significant axial flux leakage. The purpose of this study is to consider the degree to which this leakage occurs, and thus how the recovery potential may be distributed in practice.

The study does not attempt a full 3D analysis due to the difficulty of modelling actual laminations in a full-size model and lack of tools, and instead used the 2D package FEMM [204], discussed in Chapter 5. The models are transverse to the plane of the laminations, rather than the more usual transverse to the machine windings. While this 2D model does not fully model the laminations, it enables the axial flux constraints imposed by interlamination insulation reluctance to be modelled, and in addition in some models, the effect of eddy currents within each lamination.

6.4. Transverse lamination magnetostatic 2D FE model

The magnetostatic model developed is that of a stator core with five 40 mm high core packets separated by 8 mm air gaps, with 50 mm outer air boundaries either side. The core is viewed on the edge of the laminations as shown in Figure 6.3, as if from within the bore (red arrow), and is effectively unrolled along the mean magnetic path of the core yoke. In consequence the normal polar co-ordinates of radius (r), subtended angle from axis (θ) and length (l) are approximated in the case of the large diameter stator core to the Cartesian

dimensions x = circumferential direction at magnetic mean radius (r), y = radius (r) and z = axial length (l).

The model provides for radial lamination fault currents (shown in red in Figure 1.1) to be set in the y -axis in lamination positions at either end of the fault's extent, then computes flux density B and magnetic field strength H in the model's x/z plane. Since the Chattock detects the mpd on the surface of the core lamination edges, these are in the x/z plane. Thus by integration of $H \cdot dx$ between points on this plane, this model will present the mpd a Chattock detects placed conventionally on the core's inner surface.

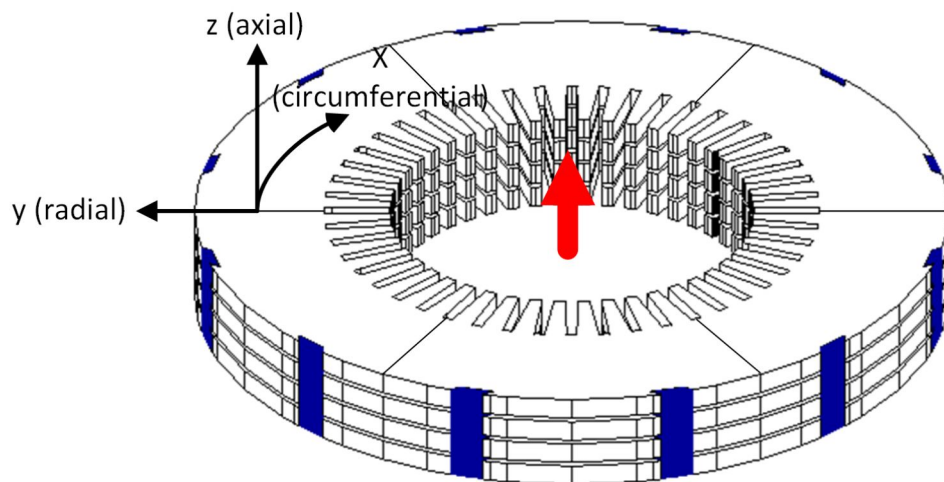


Figure 6.3 Model orientation and axes (© C. W. Ho [72])

The interlamination insulation is simulated with asymmetric permeability. The segment gaps are modelled as 1 mm air gaps on a 1 mm pitch at the segmentation positions, to ensure that the flux is funnelled through their grid structures. The model dimensions were chosen from the proportions of a ~100 MVA turbo-generator, derived from the 'TCS' DAX7 core modelled by Ho [72]. The values are summarised in Table 6.1.

The typical permeabilities of low loss electrical steels were modelled from published Cogent data [183], shown in Figure 8.8. From this a relative permeability at ~0.05 T (4% test flux density) was estimated as 2000. The stacking factor (SF) was used for establishing the z -axis permeability, and in Chapter 9 a maximum value of $SF = 0.97$ was predicted, so $\mu_z = 1/(1-SF) = 33$.

Packet height	40 mm
Radial vent gap height	8 mm
Mean circumference	4.8 m
Segmentation	6/circle, 50% overlap, 1 mm gaps
Fault lengths	10, 20, 40, 88, 96, 136 & 224 mm (up to full 5 packets)
Relative permeability	2000(x), 33(z)

Table 6.1 Stator core model data

The radial fault currents were modelled as 1 mm thick, and as if from a 40 mm wide tooth (20 mm half width in actual model) with ± 1 A total fault current imposed in the conductive circuit end regions. While the fault itself will likely be from a constrained region, the laminar current flow will soon spread out in the yoke, so the fault width provides some simulation of this (as much as is possible to model in 2D). The model is magnetostatic so there is no induction of eddy current in the model, and for simplicity no variation in permeability with flux density. The teeth are not modelled and the core is assumed homogenous in the x-axis for the length of each lamination segment in Figure 6.5. Only 180° of the circumference (x-axis) is modelled, shown before meshing in Figure 6.6.

Symmetry was assumed at the ends where Neumann boundaries were applied. Neumann boundaries were also applied at the top and bottom to avoid forcing any particular flux field, relying on the air outer boundaries to minimise the effect this region would have on the flux developed by the fault currents. The mesh required 165,511 nodes. The fault was placed midway between segmentation positions, as shown in Figure 6.4.



Figure 6.4 Segmentation layout with fault axis (red line)

The typical fault current has been shown to be quite ‘rectangular’ (radial current flow is predominantly in the end laminations) by analytic analysis [72], so establishing a current only at the boundaries of the fault is a reasonable approximation. There is of course no modelling of the fault current in the direction of the actual fault, the z-axis, however the current is forced in this 2D FE model thus does occur in terms of induction of flux.

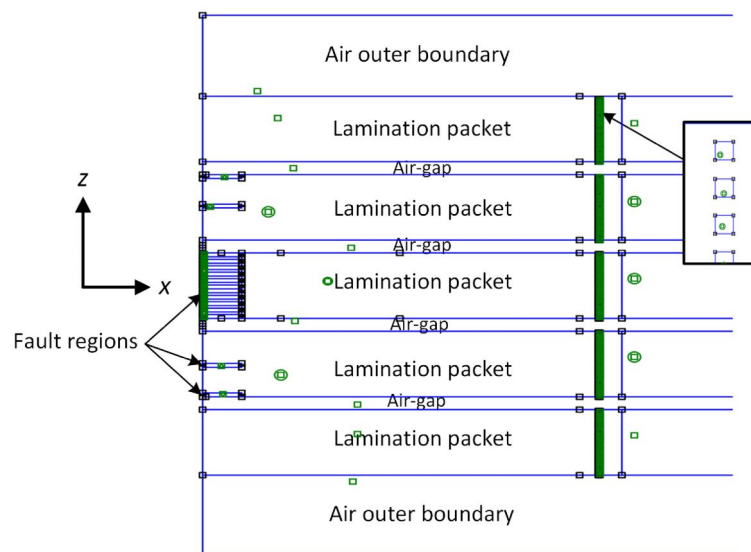


Figure 6.5 Magnetostatic FE model fault regions and axes for all models. View on edge of laminations inside bore (lamination joint air gaps inset).

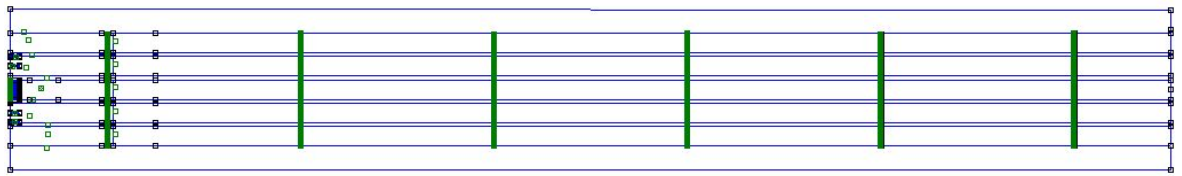


Figure 6.6 Magnetostatic FE model — whole 180° model (axes as Figure 6.5)

The result was a foregone conclusion; despite the low μ_z value, the reluctance of the long circumferential core path (equivalent to ~ 40 mm of the z-axis reluctance) ensured that most flux either circulated around the fault currents or leaked away to adjacent steel. Figure 6.7 shows how the induced flux rapidly decayed, with most circulating back around the fault before the first segmentation section. The model was re-run with no segmentation barriers (segment gap property changed from air to steel) with negligible effect on the central flux density results for 10 and 20 mm faults.

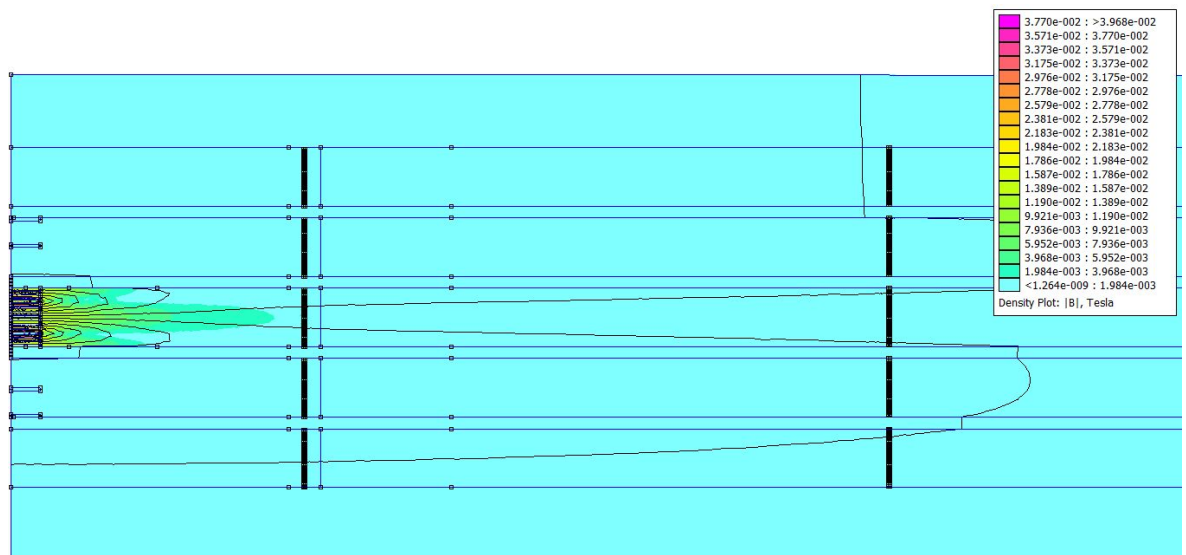


Figure 6.7 20 mm fault magnetostatic FE flux distribution model (axes as Figure 6.5)

Finally the simulated *Quad* recovery potentials which would occur for a 100 mm Chattock span were computed from the $H \cdot dx$ values integrated circumferentially (x-axis in model), shown in Figure 6.8. Here clearly uniformity around the core occurs only for particularly long magnetostatic faults. A better simulation needs to include the bounding effects of eddy currents in a time-harmonic magnetic model.

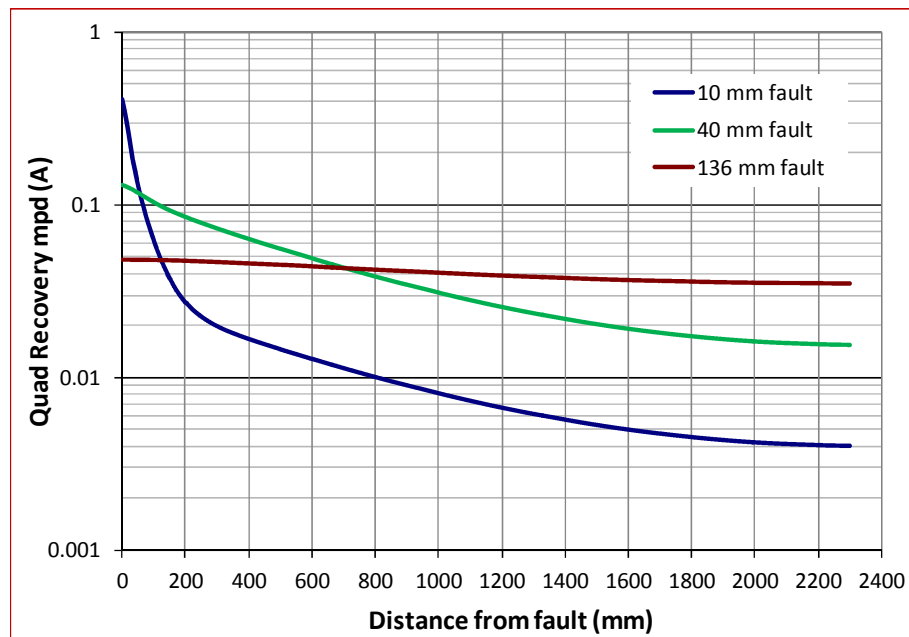


Figure 6.8 10, 40 and 136 mm fault length Quad recovery potentials around half-circumference

6.5. Transverse lamination time-harmonic 2D FE model

There are several problems with a time-harmonic 2D FE model in terms of real-world comparisons. Firstly the connection of the lamination planes at $\pm\infty$ has no resistance, only the resistance in the y-axis (the declared steel conductivity) limits the development of eddy currents. There is no ready means to simulate this in normal 2D FE, though segmentation will also limit the extent of these eddy currents. It was thus assumed initially that the resistance in the x-axis (in this model) has little effect, with current effectively controlled by the y-axis resistance.

Secondly, while the interlamination insulation is not explicitly modelled (a reduced μ_z is applied) a laminated model structure is still needed to provide eddy current constraint within each lamination. This to ensure that the overlapping and finite length of the laminations is effectively modelled.

Thirdly modelling actual 0.5 mm laminations for a whole semi-circumference was a problem due to model size. Two initial smaller models were constructed using 0.5 mm and 1.0 mm thick laminations to determine if thicker laminations could be used for modelling economy. From plotting the magnetic field strength H_x down the centre of the model the results were found equivalent. It was thus concluded as satisfactory to use 1.0 mm laminations with 0.3 mm meshing at the segment gaps, 0.5 mm meshing near the fault where the gradients are severe, and 1.0 mm meshing in the laminations elsewhere. This also assumes the x-y planar eddy currents are uniform across the lamination thickness (z). Another initial model with a laminated guard packet alongside the faulted packet was

constructed, but demonstrated that this made no difference over one with a simple air-spaced iron boundary region.

The final time-harmonic 2D FE model was of a 40 mm wide core packet completed with 1.0 mm laminations, 2400 mm x-axis length (being 180° of mean circumference) for longitudinal symmetry, with Neumann end boundaries. Only one half of the z-axis (i.e. 20 mm) was modelled using mirror symmetry with a Dirichlet central x-axis boundary, as shown in Figure 6.9. Segmentation was modelled with 1.0 mm air gaps between lamination ends. To improve model accuracy, the segmentation air gaps were meshed at 0.2 mm and the faulted laminations were meshed at 0.5 mm for their length to improve current modelling fidelity.

A fault current of +1 A was imposed on the fault region shared equally between the two laminations at the fault end, with the fault width modelled for 10, 20, 30 and 40 mm full width faults. Each lamination was defined as a separate circuit set to zero net current except for the fault region.

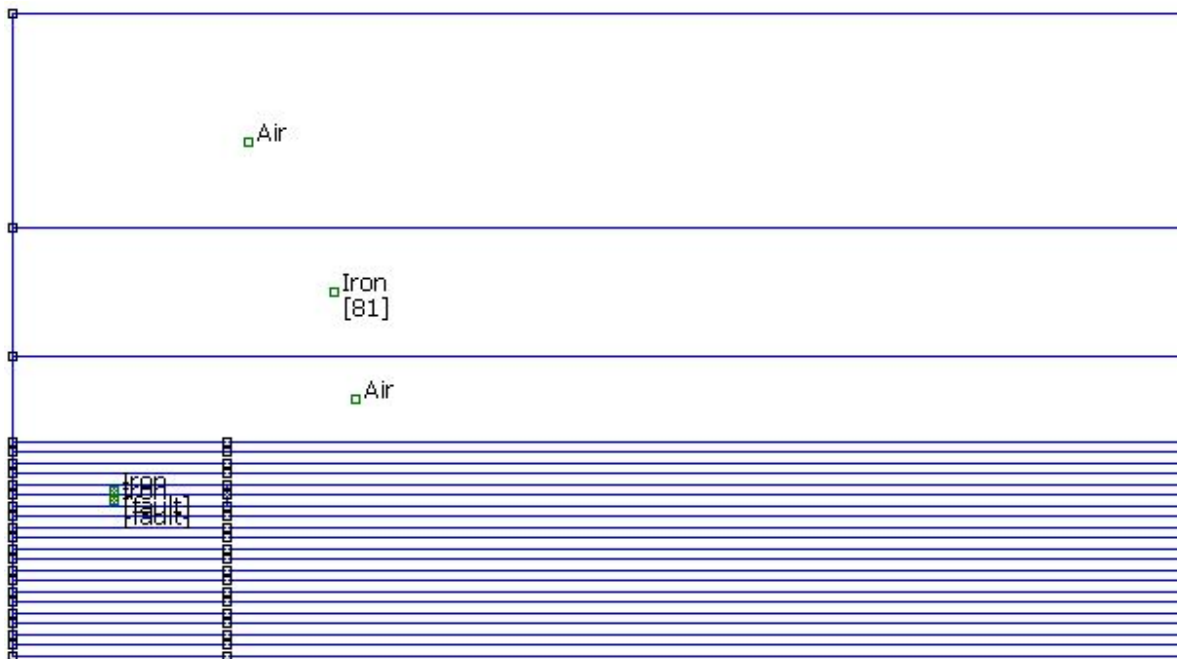


Figure 6.9 30 mm fault length half-packet ac model (axes as Figure 6.5)

Since the results from all models showed an almost total constraint of the flux within the packet, no attempt was made to model any longer fault, as clearly this will be similarly fully constrained. For the 40 mm model (full packet width), a set of 8 laminations were added to the outer guard packet to provide an eddy current region, as clearly some flux escapes when the fault is on the extremity of the packet. The results clearly show almost totally uniform constraint of the induced flux in Figure 6.10 to Figure 6.13.

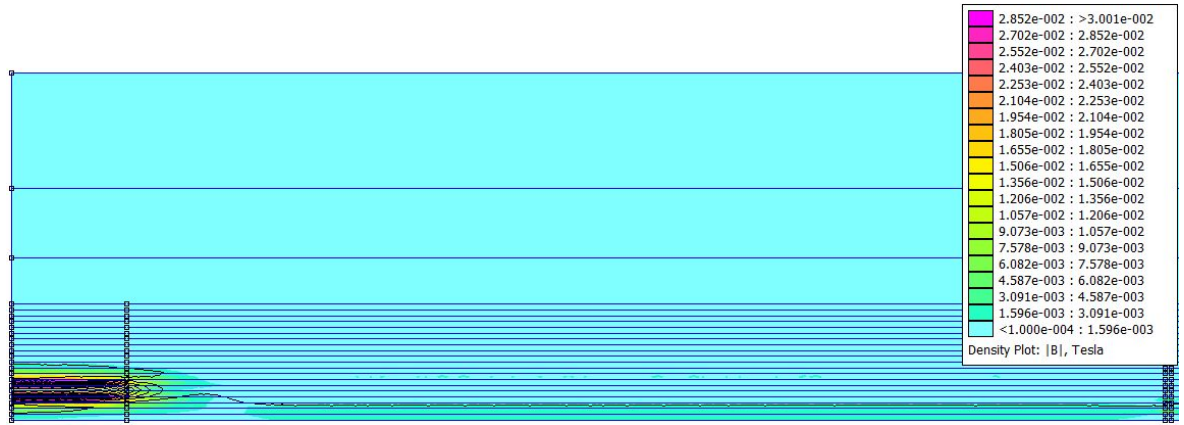


Figure 6.10 10 mm model flux distribution for first 200 mm x-axis (axes as Figure 6.5)

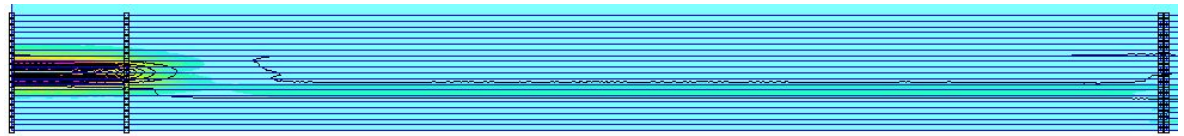


Figure 6.11 20 mm model flux distribution (flux density as Figure 6.10)



Figure 6.12 30 mm model flux distribution (flux density as Figure 6.10)

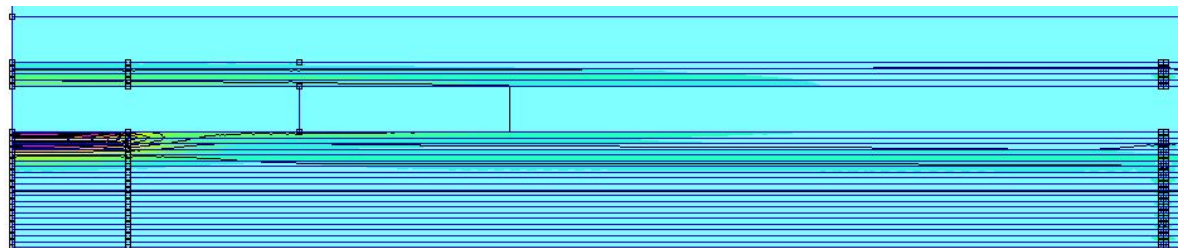


Figure 6.13 40 mm model flux distribution (flux density as Figure 6.10)

The variation in magnetic field strength down the packet centre was measured, as this is the value of prime concern. H_x field values circumferential along the centre x-axis of the first and second (y-axis) laminations were recorded and averaged, reflecting the fact that Chattock sensors have a sensing area of >4 mm dia. The mpd that a 100 mm Chattock span would detect was then computed by 100 mm integration of the averaged H_x field. The high spot mpd occurring at the 1 mm segmentation gaps has been deleted to avoid showing meaningless small steps when these spots are included in the span. They were seen to be equal along the model x-axis so do not reflect any difference in Quad recovery with circumference and in total only represent $\sim 5\%$ of the mpd.

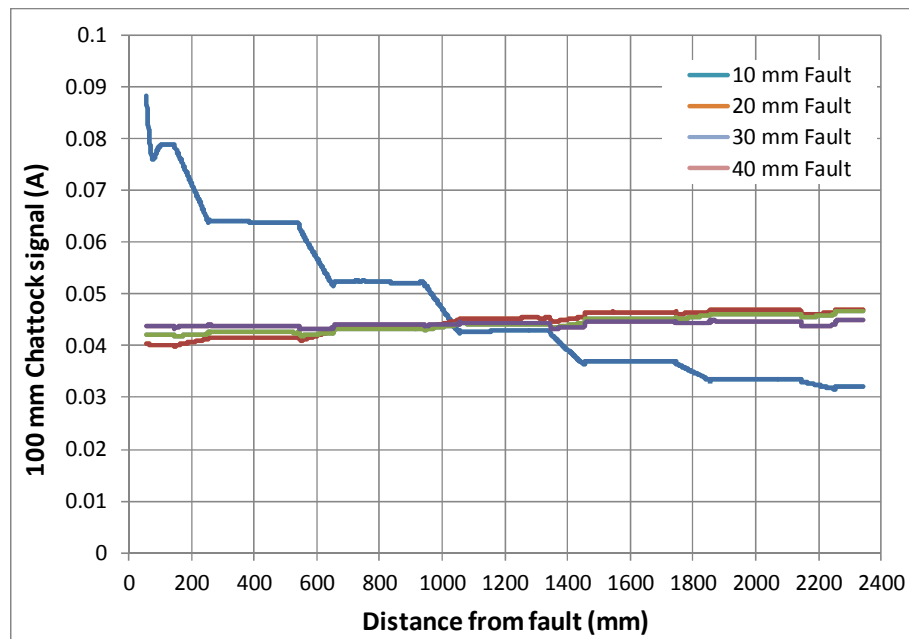


Figure 6.14 Plot of detected 100 mm Chattock mpd along x-axis for modelled faults

The results in Figure 6.14 show that for a very short fault of 10 mm the Quad recovery is skewed towards the source somewhat, however once the fault reaches 20 mm and above the recovery is virtually uniform, and even rises slightly. The average modelled Chattock signal value of ~ 0.043 A is rational; the induced current is 1 A over 2.4 m model length, and a linear distribution with a 100 mm Chattock span gives $1.0 / 2.4 \times 0.1 = 0.042$ A.

However the measure of H_x on the model is on the inner surface of the core yoke, essentially at the slot base of the bore, while the Chattock detection is on the tooth tip. Studies in Chapter 11 show that the high reluctance of the tooth tip to magnetic potentials developed across the slot, results in substantial spreading of the flux between laminations. It is thus assumed that the magnetic field strength developed by the flux density from a 20–40 mm fault is homogenised at the tip of a >100 mm long tooth whose centre is measured by the Chattock. From this the total local flux induced in the packet (flux density) is used as a measure of the developed magnetic field strength. The result is shown in Figure 6.15, which shows that the flux developed circumferentially around the packet from the fault is essentially unvaried for the 20 mm fault, however it does suffer a $\sim 19\%$ loss between 100 mm and 2400 mm away from the fault for the 40 mm fault (with 2.3 MS lamination conductivity).

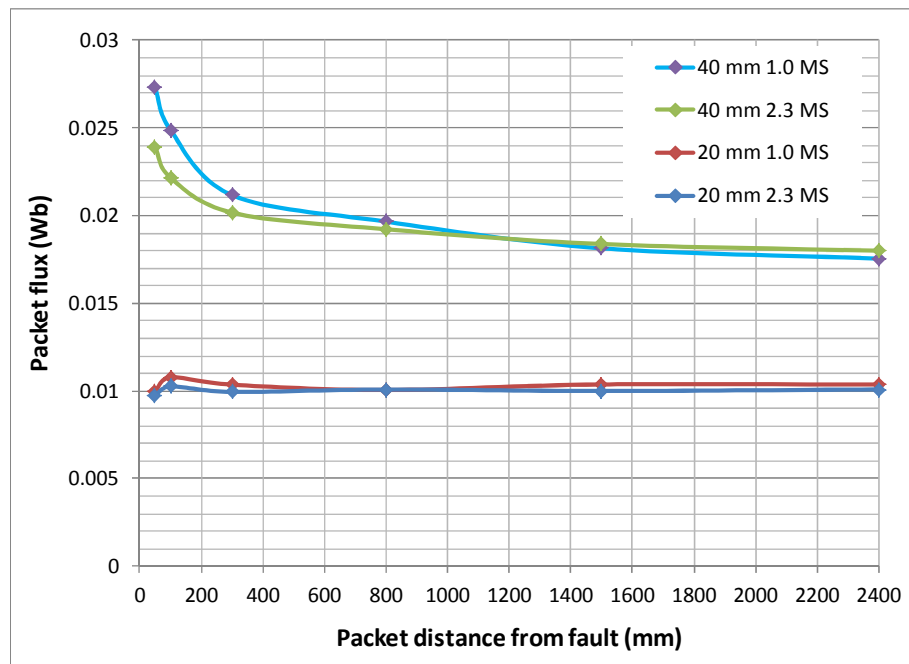


Figure 6.15 Plot of total fault flux along x-axis for modelled faults.

A further concern remained that the 2.3 MS lamination conductivity did not reflect the extra resistance caused by the x-axis current flow needed to join the eddy current circuits. On the assumption that the x-axis currents are at least as long as the z-axis currents in real life, the models were re-run using a 1.0 MS conductivity to determine if this affected the constraints, for the 20 mm and 40 mm faults. Figure 6.15 shows that this had negligible effect on the shorter 20 mm fault, whereas on the longer 40 mm fault the drop from 100–2400 mm increased to 22%.

6.6. Modelled eddy currents

The flux constraint and hence great uniformity of fault H field is of course due to the induced eddy currents. The eddy currents (Real component since the applied FE fault current and induced fault flux are in the Real phasor direction) were plotted down the centre of each lamination for the 30 mm fault and plotted in Figure 6.16 near the fault. The first observation was that the flux circulating around the positive fault current induces a large negative eddy current directly adjacent to the fault on all nearby laminations. It can be seen that the current has a balancing positive current in the remainder of the lamination which terminates at the 200 mm segmentation position. However those laminations extending further maintain the negative current until the adjacent segmentation gap where the current inverts to positive, again to obtain a net zero lamination current.

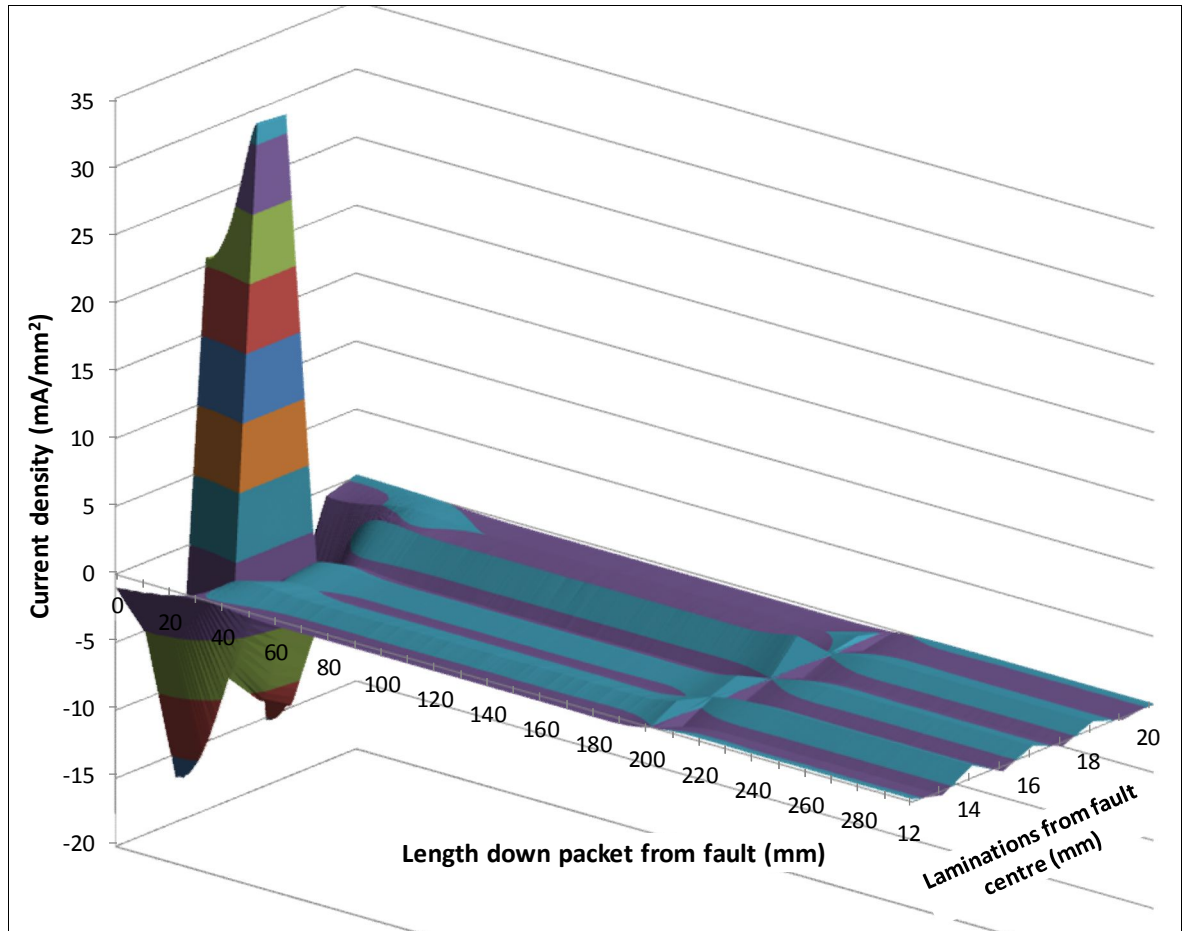


Figure 6.16 Fault and eddy current density distribution in 30 mm fault model near fault

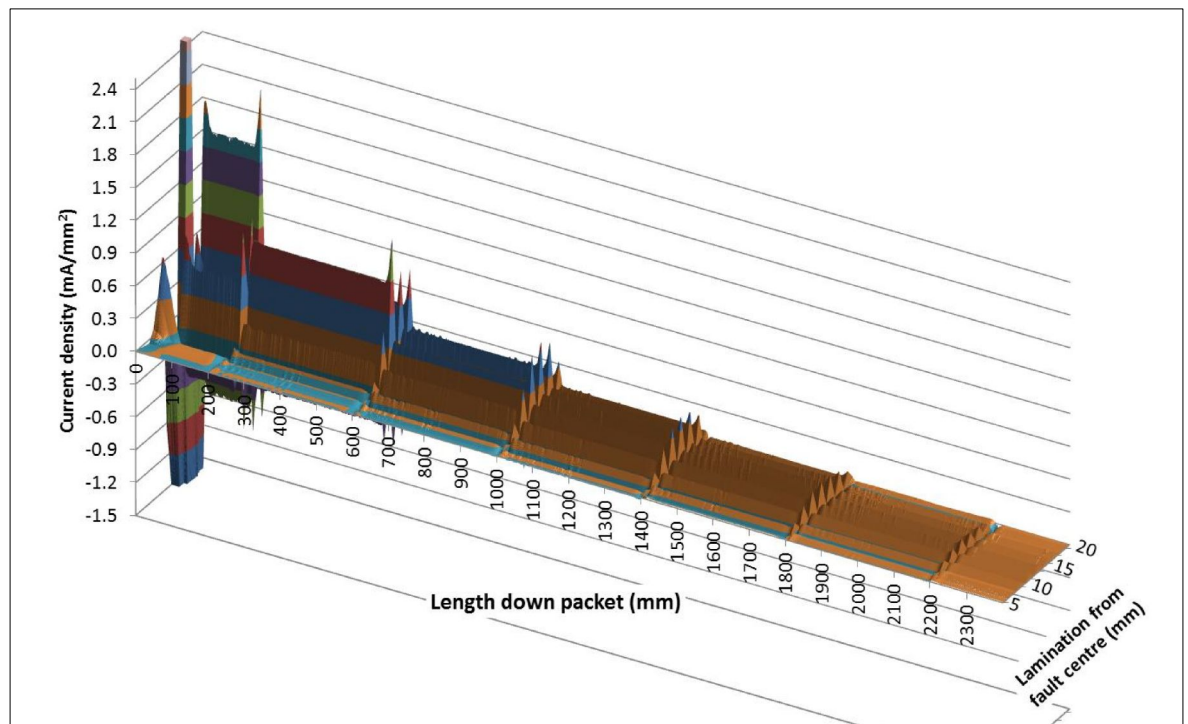


Figure 6.17 Eddy current density distribution in 30 mm fault model around half-core

Further around the core after the direct influence of the fault has ceased, the alternating positive/negative current in the laminations continues to be induced, as shown in Figure 6.17, with steadily reducing currents. While only the positive profile is visible, the negative profile is comparable, though always with a slightly lower current density. In this manner the eddy current pattern with slight positive bias of 0.0209 mA/mm^2 is handed down the packet from segment to segment, decreasing and broadening at each stage but retaining its effect. It is remarkably constant as shown in the Figure 6.17 plot of the average current density over the modelled half-packet around the half-circumference.

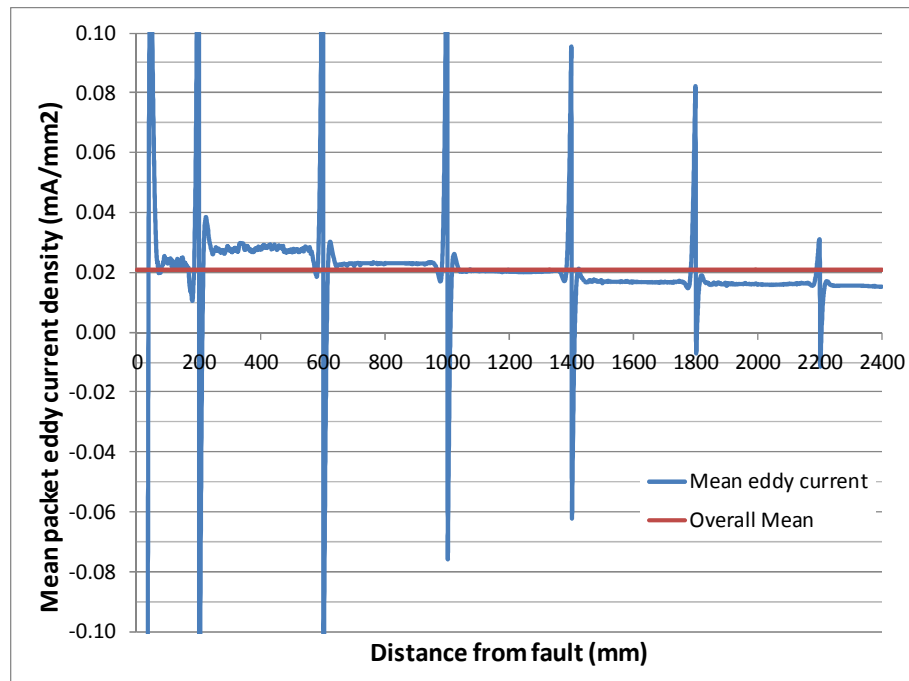


Figure 6.18 Mean eddy current density around packet for positive half modelled 30 mm fault

To check it is sufficient current to provide the constraining solenoidal field needed, the mean current from 80 mm onwards, averaged over 20 mm for the 2.4 m length of packet, gives $0.0209 \times 20 \times 1000 / 1000 = 0.418 \text{ A/m}$ total solenoidal field along the centre. The mean magnetic field strength from the fault mmf is similarly $1.0 / 2.4 = 0.417 \text{ A/m}$. Thus this induced eddy current field is clearly sufficient current to provide the total constraint that faults of less than one packet width experience.

6.7. Discussion of transverse 2D FE model results

The FE models were developed initially to investigate the likely distribution of the Quad recovery effect. Despite shortcomings, the time-harmonic model has shown some intriguing results. The clear evidence from this study is that the laminated structure alone provides a very limited restraint to flux divergence around the core (x-axis). However once induced eddy currents develop, these form a very effective constraint, except when the

fault extends to a packet boundary where there is limited bounding steel to develop the currents. Even in this case, substantial constraint still occurs.

The conclusion is that faults which are sufficiently severe to warrant this concern, are likely to reach or exceed one packet length. Their Quad recovery magnetic fields will thus be quite constrained, with only up to around 20–30% attenuation around the core. This appears generally in accord with the field experience described in section 6.2.

The effect of a 2D FE model is that there is no modelling of the fault or eddy currents in the x and y-axes, hence the resistance of the x-axis to eddy current is not modelled. However an investigation of the likely effect of this by reduction of the total conductivity showed that this only affects faults extending to the edge of packets; those shorter than the packet remain fully constrained.

It was also observed in both models that flux restrained from diverting between laminations until very close to the joint. This developed a high mpd across the joint due to the reluctance from the asymmetric permeability, in addition to the doubled flux density in the flanking laminations at the joint. This caused a high spot H field to be recorded in the x-axis axial plots, locally affecting the measured mpd. These are not seen in practice due to the fact that the Chattock sensors detect the mpd that propagates to the tooth tips, which thus have a wide region to integrate the potential over.

The model had to be compromised in fidelity with 1 mm laminations and coarse meshing to achieve a soluble problem. Finer mesh models with more substantial computing resource may be required to explore longer faults with fault current profiles more realistic for severe faults. The fault current here was applied rather than induced, due to the problem of inducing the required uniform excitation flux density. However if excitation flux could be modelled, then the fault could be simulated as a continuous conducting region, and hence create a more realistic model of the current in a faulted region. The model also did not include the effect of core loss causing a phase lag between current and induced flux. The model was based on the 100 MVA stator core modelled by Ho [72] with just 6 lamination segments/circle. Larger machines can have up to 18 segments/circle and are thus likely to develop less constraining eddy currents.

The pattern of the eddy currents is very distinct, being essentially equal and opposite either side of the segmentation joint. This pattern of an almost uniform circulation of currents around each lamination centre, peaking at the edges, was predicted by Mecrow and Jack [209] while investigating the impact of axial flux on half-overlapped stator laminations, reproduced in Figure 6.19.

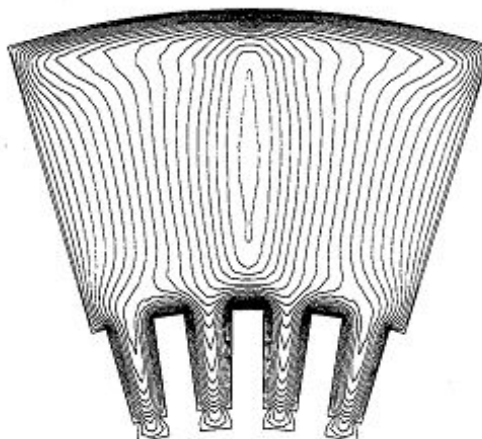


Figure 6.19 *Half-overlap eddy currents from axial flux (© IEEE [209])*

The model shows that a significant amount of induced fault flux also circulates locally around the radial fault current path. In section 3.5 and previous analytic models [72] this has been assumed negligible due to lamination stacking factor, but is clearly not the case, even when the additional opposition of eddy currents is included. Other investigators considering fault inductance in the study of destructive faults [18, 19] have also only considered the inductance from the torroidal flux, ignoring the flux locally linking the radial fault currents. This insight may substantially affect the modelling of the inductive limiting of severe fault currents, and their ability to develop thermal runaway.

An algorithm to assist in the field compensation of the effect of Quad recovery was developed and is described in Appendix C.1.

6.8. Summary

If there is axial alignment of multiple faults, their *Quad* signals can interact and cause misleading reduction of their maximum values, since an opposite fault signal occurs proportioned around the unfaulted slots in the same axial position as the fault. This phenomenon, called Quad recovery, is shown to be a natural result of *Ampère's law* with the use of the excitation current as test reference, in a laminated structure. However knowledge of the distribution of the Quad recovery mpd is desired to allow more reliable fault determination.

A stator core was studied in a transverse 2D FE magnetostatic model with the lamination segment joints and packet air gap structure explicitly modelled, and axial permeability controlled by the stacking factor, including packet air gaps. A complete 180° stator core half-segment was modelled. The Quad recovery of the imposed fault current was shown to remain very biased towards the fault region, unless the fault was exceptionally long and encompassed several core packets.

The transverse 2D FE segmented model was developed into a time-harmonic model to allow eddy current formation constrained to individual laminations. Fault currents were imposed and the magnetic field developed by them around the core determined. The constraining eddy currents were shown to be initiated at the fault region, but continue alternating between the segmented laminations around the core, maintaining an almost constant solenoidal field. It was shown that the resultant Quad recovery potential is very uniform for faults =>20 mm long.

An investigation to simulate the un-modelled x-axis eddy current resistance by a nominal 50% reduction in steel conductivity, showed that for faults reaching the packet boundaries (where there is limited bounding steel to develop the currents), a ~22% Quad recovery bias towards the fault region can develop, in line with some field experience.

Chapter 7. Impact of Varying Stator Core Loss and Permeability on Electromagnetic Tests

The standard model for the EMT assumes that the stator core is composed of electrical steel with uniform magnetic properties. However variances in core loss and permeability caused by non-uniform steel have been shown to occasionally give rise to substantial fault signal artefacts not due to actual interlamination insulation defects, in particular due to the use of circumferentially differing steels in manufacture. A new theory was derived to support and quantify this with interpretation techniques, validated on a field example. The work was published in 2011 [210]²² with a field example.

7.1. Potential scale of core loss variation

Electrical steel has considerable variation in its loss and permeability. This is due to the manufacturing need to balance losses against magnetising performance through control of additives and impurities in the melt and subsequent cold processing [33] (§4.1-2). The outcome is a range of steels compliant with commercial standards, but inevitably varying within the prescribed limits between lots and even within the lot. The grades in EN10106 [211] at the lower loss regions have maximum loss steps of 2.9 / 3.1 / 3.3 W/kg losses at 1.5 T for M290 / M310 / M330 grades, being only ~6% steps. However these are maximums, and for example Cogent M310-50A material [183] is typically 2.83 W/kg at 1.5 T, i.e. 9% under the limit. On the assumption that the production quality scheme ensures the worst case loss just does not exceed 3.1 W/kg, and the manufacturing process distribution is symmetric, the total variance is likely to be 2.6–3.1 W/kg, about +/-9%.

However while typical losses are given down to 0.1 T, there is no grade specification under 1.5 T. Further, at 4% service flux density typically used by EMT systems (~0.05 T), there is no control of the core loss (or permeability). Field data [210] shows that this can be much more variable, exceeding +/-50%, thus making the EMT much more exposed to steel magnetic parameter variance than the stator core design experiences in service. The worst case occurs when the stator core is assembled with differing electrical steel around the circumference, thus the toroidal flux for each core packet/axial region passes through the

²² Reproduced with permission © IEEE 2011.

differing steels, developing differing magnetic field strengths. This situation is studied below.

7.2. Analytic study of core loss and permeability variation on EL CID

In the EL CID test described in section 3.4 where the analysis reference is taken from the excitation current, variation in the core loss and hence core loss angle in the absence of actual core faults does not affect the *Quad* signal if the loss is uniform around the core circumference. Similarly overall variations in permeability will only affect the magnetic field strength (hence excitation current) required to induce the flux, thus only vary the *Phase* signal.

However when these variations are not uniform in the core these conclusions are not true, and a more complete analysis must respect the following electromagnetic constraints. Firstly, due to low axial permeability from the stacking, the flux around the core in each lamination plane will remain mostly constrained to that plane, and thus approximately circumferentially constant in amplitude and phase angle to the excitation current. The development of eddy currents in the lamination planes will also limit axial flux divergence as shown in section 6.5. The presence of radial vents/packet air gaps provides a further very substantial axial flux constraint. Secondly, equation (3.9) showed that since the *Phase* reference is taken from the excitation current, the *Quad* values around the core must sum to zero, with the *Phase* values summing to the total excitation current.

The change in energy density ΔW_M in an induced spatially uniform magnetic field where varying magnetic field strength \mathbf{H} induces a change in flux density $d\mathbf{B}$ is $\Delta W_M = \int \overline{H}d\overline{B}$ [212] (§16.3). By integrating over an ac cycle it is shown in Appendix D that for a sinusoidal flux density phasor \mathbf{B} of rotational frequency ω , with lagging phase angle θ , induced by co-axial magnetic field strength phasor \mathbf{H} , the net absorbed power density P_L (being the core loss spatial density) is given as

$$P_L = \omega HB \sin \theta, \quad (7.1)$$

where B and H represent the fundamental rms values of \mathbf{B} and \mathbf{H} . The study in Chapter 8 shows that the \mathbf{H} field harmonics do not exceed 6%, consequently using the total measured rms value for \mathbf{H} will result in errors <1%.

A *Quad* signal is developed when the magnetic potential across a slot is not in phase with the excitation mmf I_e . To determine how both a variation in core loss and permeability can develop *Quad* signals, the locally developed rms magnetic field strength \mathbf{H} is resolved into components $H_{inductive}$ in phase and H_{real} in quadrature to the flux density

B. The resultant phasor diagram around a simple 4 slot core is shown in Figure 7.1. Since for slot n $H_{real} = H_n \sin \theta_n$, it can be seen that the core loss power is wholly transferred in the H_{real} component, the component $H_{inductive}$ in phase with the flux density carries no net power.

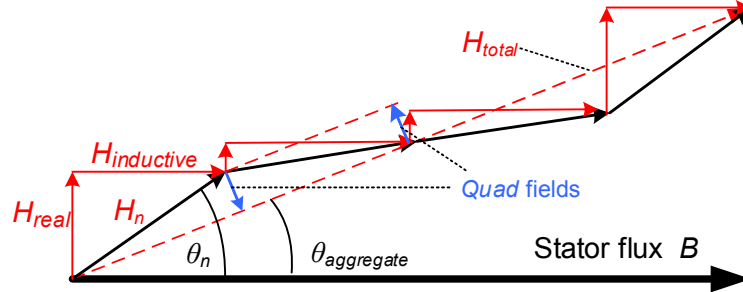


Figure 7.1 Varying core loss phasor diagram around core

The local and aggregate core loss angles θ_n and $\theta_{aggregate}$ are given for slot n with N slots

$$\theta_n = \tan^{-1}(H_{n-real} / H_{n-inductive}) \quad \text{and} \quad (7.2)$$

$$\theta_{aggregate} = \tan^{-1}(\sum_1^N H_{n-real} / \sum_1^N H_{n-inductive}).$$

The total magnetic field strength equating to the excitation mmf I_e will be

$$I_e = H_{total} = \sqrt{(\sum_1^N H_{n-inductive})^2 + (\sum_1^N H_{n-real})^2}. \quad (7.3)$$

Thus from equations (7.2) the local *Quad* field Q_n developed for slot n shown in Figure 7.1 can be computed in equation (7.4)

$$Q_n = -\sqrt{H_{n-real}^2 + H_{n-inductive}^2} \sin(\theta_n - \theta_{aggregate}). \quad (7.4)$$

7.3. Numeric example of core loss and permeability variation on Quad signals

To study the practical scale of these phenomena, a model is considered of a stator core yoke of density ρ and unit depth illustrated in Figure 7.2 (without teeth), where the central excitation current I_e of angular frequency ω induces rms core flux density B . Flux density B is assumed approximately constant with radius due to the large radius (shown in Figure 11.5). It is also assumed constant axially, being limited by the stacked laminations, packet gaps and induced lamination eddy currents (shown in Chapter 6).

In the normal region the specific mass core loss (W/kg) and permeability are W and μ , while in a variance region of proportion a of the circumference, the variance specific core loss and permeability are W_a and μ_a . The flux density develops an rms magnetic field strength H in the normal region and rms magnetic field strength H_a in the variance region. The phase angle (core loss angle) between flux density and magnetic field strength is θ in

the normal core and θ_a for the variance region. The induced rms flux density B is assumed constant.

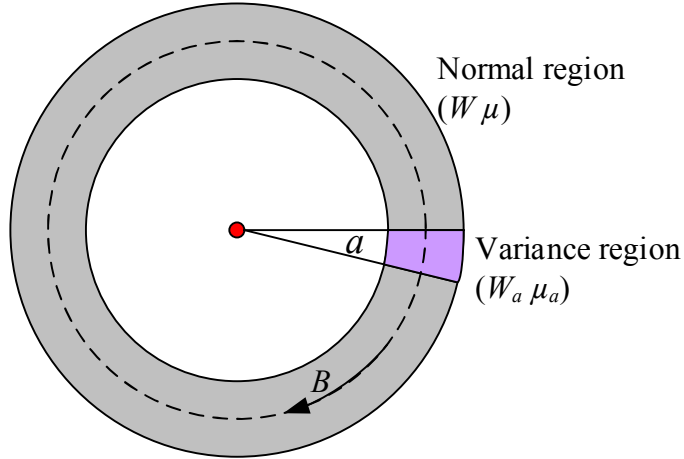


Figure 7.2 Stator core normal and variance regions

Factors X_w and X_μ proportion the variances such that

$$W_a = W(1 + X_w) \quad \text{and} \quad \mu_a = \mu(1 + X_\mu). \quad (7.5)$$

The power densities are given by both the electromagnetic power from equation (7.1) and core loss in the normal and variance core regions as

$$\omega BH \sin \theta = W \rho \quad (\text{normal}) \quad \text{and} \quad (7.6)$$

$$\omega BH_a \sin \theta_a = W_a \rho \quad (\text{variance}). \quad (7.7)$$

Since $B = \mu H$, equations (7.6) and (7.7) give for the normal and variance core regions

$$\sin \theta = \frac{W \rho \mu}{\omega B^2} \quad \text{and} \quad (7.8)$$

$$\sin \theta_a = \frac{W \rho \mu}{\omega B^2} (1 + X_w)(1 + X_\mu). \quad (7.9)$$

From Figure 7.1 the full core H field real and inductive components and scalar total are given by

$$H_{real} = (1 - a)H \sin \theta + aH_a \sin \theta_a, \quad \text{thus} \quad (7.10)$$

$$H_{real} = \frac{B}{\mu} \left[(1 - a) \sin \theta + \frac{a}{(1 + X_\mu)} \sin \theta_a \right],$$

and

$$H_{inductive} = (1 - a)H \cos \theta + aH_a \cos \theta_a, \quad \text{thus} \quad (7.11)$$

$$H_{inductive} = \frac{B}{\mu} \left[(1 - a) \cos \theta + \frac{a}{(1 + X_\mu)} \cos \theta_a \right],$$

hence

7. Impact of Varying Stator Core Loss and Permeability on Electromagnetic Tests

$$H_{total} = \sqrt{H_{real}^2 + H_{inductive}^2} \quad \text{and} \quad (7.12)$$

$$\sin \theta_{aggregate} = \frac{H_{real}}{H_{total}}. \quad (7.13)$$

Thus from equation (7.4) the *Quad* magnetic field strength Q is given by

$$Q = -H_a \sin(\theta_a - \theta_{aggregate}) = -\frac{B}{\mu(1 + X_\mu)} \sin(\theta_a - \theta_{aggregate}). \quad (7.14)$$

Expanding equation (7.14) from equations (7.9) and (7.13) only produces a complex expression which does not provide any better insight into the effects of the variance. A numeric example provides a case specific illustration of the scale of the effect. Equation (7.14) describes the *Quad* field (A/m), however the *Quad* signal is detected as a mpd developed across a slot pitch. Table 7.1 illustrates examples of the turbo-generator slot pitches that can be experienced.

Machine	Power and slot count	Slot pitch
Large nuclear (4 pole)	1000 MW, 48 slot	179 mm
Medium turbo (2 pole DAX8)	100 MW, 48 slot	110 mm
Small turbo (4 pole Brush)	35 MW, 84 slot	60 mm

Table 7.1 Typical stator tooth pitches

Using the DAX8 core example (described in section Chapter 9), its magnetic and geometric parameters were used to predict the expected *Quad* signal that would develop in the core variance region due to varying core loss and permeability at constant flux density, depending on proportion (a) of variance core. The curves in Figure 7.3 illustrate the *Quad* signals that are developed with the variance region a of the core modelled at 10% and 50%, for up to +/-50% variation in core loss and permeability.

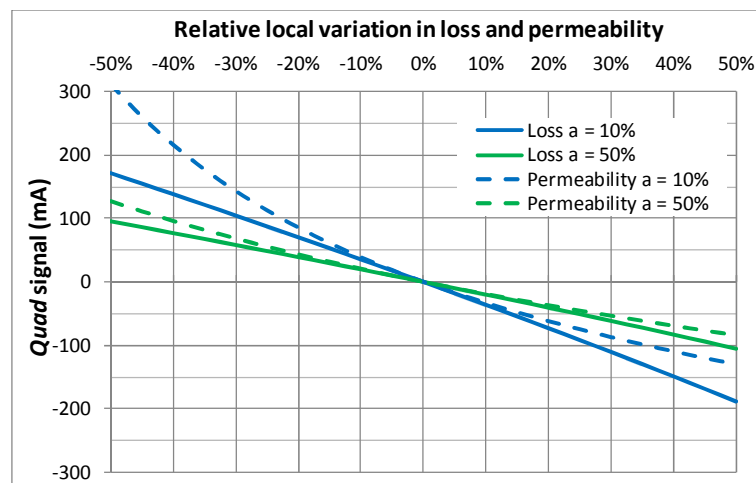


Figure 7.3 DAX8 Quad signal from local variation in core loss and permeability, for 10 & 50% proportion of affected core at constant 4% flux density

This shows that significant *Quad* signals above the -100 mA warning threshold can be developed in stator cores with quite modest magnetic non-uniformity. The *Quad* signals from the two parameter variances may accumulate or offset each other depending on polarities, but the combination is not linear.

In practice a more complex numerical model would normally be needed to evaluate the particular effects of any variance in an actual machine study. This must take account of both axial and circumferential variance, and consider the balance of fluxes in the core since it is only the aggregate core flux level that is maintained at 4%. Such an example is given below.

7.4. Field confirmation of core loss and permeability variation

A major set of apparent faults were recorded on core sections from a new 1000 MW generator at a nuclear power plant. These presented *Quad* signals sampled in the false colour map in Figure 7.4, significantly exceeding -100 mA and thus a serious technical and commercial concern on a new stator.

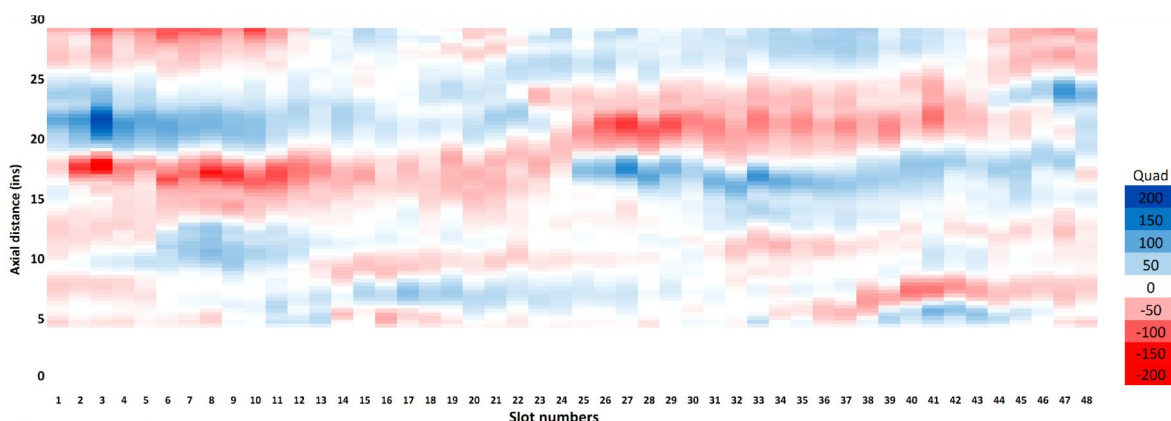


Figure 7.4 False colour map of *Quad* signals for 30 inches of stator length

The manufacturing practice used dual robotic stacking of the laminations [213] into core sections termed ‘donuts’ illustrated in Figure 7.5, where each robot of the pair used a separate source of material, potentially from a different batch or even supplier. If mixed during stacking, material variances normally disappear in aggregate, but in this case the robotic stacking resulted in 180° segments of each core donut having consistently differing material.



Figure 7.5 Robotic stator core stacking (© Siemens 2010)

When measured, the M270-50A lamination steel properties at low flux density were found to have large variations of relative permeability of 2000–2800 and core loss of 0.004–0.01 W/kg, with little correlation between them as shown in Figure 7.6.

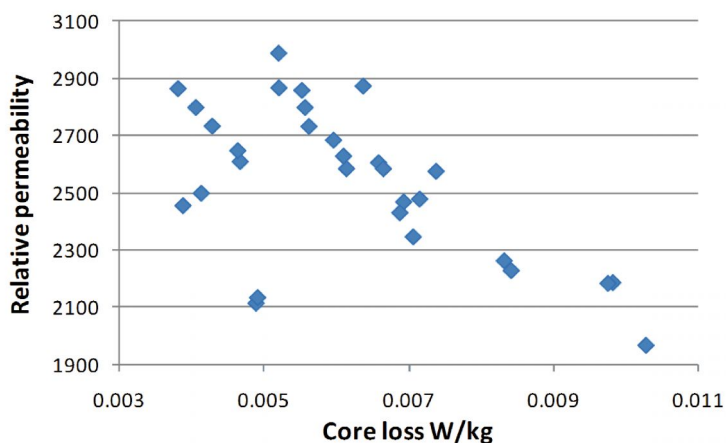


Figure 7.6 Spread of core loss and relative permeability at 0.05 T

Using the analytical approach above, a numerical model was constructed to match the core and to maintain aggregate flux levels, in which the variances from the opposed systematic stacking process were analysed. This showed that the local variance in core loss in one half of a donut could cause up to 368 mA *Quad* signal to appear, and up to 111 mA from the same maximum spread in permeability. These would appear as negative (fault indicating) in the sector of the core with the increases, with balancing positive signals in the opposite sector, significantly exceeding the discovered worst case values of ~200 mA.

The forecast *Quad* signal patterns matched the test results sampled in Figure 7.4. In conjunction with other analysis and tests, it was concluded that there was no actual interlamination insulation damage, and the generator was successfully commissioned. Full details are given in paper [210].

7.5. Discussion and summary on the problem of testability

It has been assumed in all the preceding literature that the sole source of significant electromagnetic fault signals (esp. EL CID *Quad*) is interlamination current flow through fault circuits. This research has shown that artefact *Quad* signals can arise from circumferential variations in the laminations' core loss and even core permeability. It is also shown that at the low flux density region used for electromagnetic testing there is no control of the lamination magnetic properties, which can be much more variable at low flux density levels than at specification flux density level of 1.5 T.

The use of multiple batches of electrical steel, possibly even from differing vendors is to be expected in commercial stator core manufacture simply due to the volume of steel used. Normally the laminated structure will homogenise variations in material properties (a 4 mm Chattock aperture spans >8 laminations) providing there is some mixing of material batches in the stacking. Lots from the same roll, thus from the same melt, would also expect to result in much greater uniformity. The magnetic properties may vary axially by a substantial amount as the material lots are consumed while the core is stacked, however no measurement is made of axial magnetic potentials so there is little EMT impact. The worst case is when opposing sides of the core are stacked from two different sources of material in axial alignment. Fortunately this seems to be a rare occurrence.

The results of these studies is that up to +/-50% variation in core loss or permeability is possible at test flux density levels, and shows that significant *Quad* signals above the 100 mA warning threshold can be developed in stator cores with significant magnetic non-uniformity. Unfortunately the artefact signals are not electrically separable from actual fault signals, since a core fault is simply a local increase in eddy current loss, one source of the artefacts. However the shape and distribution of the artefact signals can be expected to differ substantially from actual faults, since the artefact signals appear in circumferential bands and display mirror symmetry around the core packets. Thus knowledge of this analysis should allow an experienced engineer to distinguish faults from artefacts. If doubt remains, supplementary high flux testing (section 2.2) can provide further confirmation of the presence of actual faults (though a less reliable proof of absence of fault).

Fortunately any actual core fault *Quad* signals are linearly superimposed on these artefacts [210] and being derived from material properties, likely to remain constant with service. This allows the detection of any genuine *Quad* fault signal in service by simple difference from a pre-recorded, no-fault template test level rather than zero.

Chapter 8. Impact of Non-linear Permeability on Electromagnetic Tests

The assumption in all EMT systems is that the system is linear. The permeability and loss of electrical steel is however known to vary substantially with flux density, including the low EMT flux density levels. It has been shown in Chapter 7 that localised stator core loss or permeability variation of >40% at constant flux density can cause diagnosis errors. This raises the possibility that variations and non-linearities in permeability with flux density, may similarly impact results through varying levels of harmonic generation. The principle source of variation is identified as Rayleigh hysteresis. The effect on the EL CID is modelled and compared to measurements made from the DAX8 experimental stator core described in Chapter 9. The work was published in 2014 [214].

8.1. Source and scale of non-linearity

The induced excitation flux for the EMT is normally sinusoidal, however a number of factors are non-linear with flux density. Firstly Figure 8.1 shows that the relative permeability of the CDW M310-50A steel [182], assembled in the DAX8 stator, varies by 4:1 up to the peak magnetic field strength used in the EL CID test (12 A/m at 0.056 T).

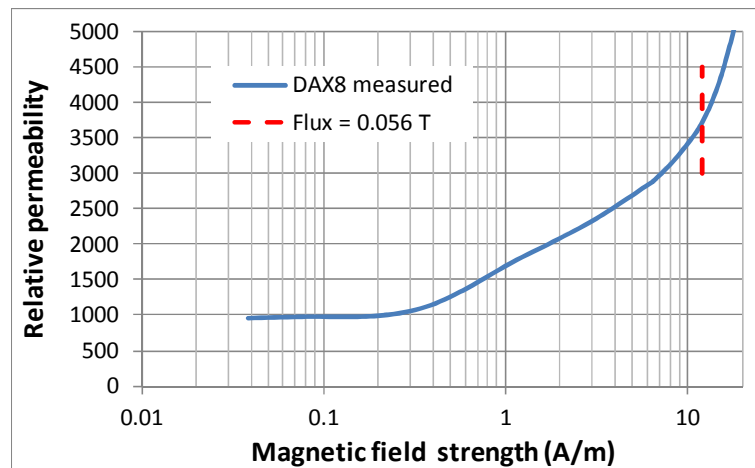


Figure 8.1 50 Hz relative permeability variation with magnetic field strength of DAX8 stator

Secondly the induced flux exhibits a phase lag relative to the magnetic field due to core losses, consisting of hysteresis loss²³ W_H , eddy current loss W_E and anomalous loss W_A [216] (§12.1.5). The losses increase with frequency ω and flux density B where typically

$$W_H \propto B^{1.6} \omega, \quad W_E \propto B^2 \omega^2 \quad \text{and} \quad W_A \propto B^{1.5} \omega^{1.5}. \quad (8.1)$$

²³ The hysteresis loss factor of typically 1.6. is originally attributed to Steinmetz [215] though is found to vary widely.

The sinusoidal excitation flux density is normally generated by a low impedance voltage drive. The rising permeability characteristic and ferromagnetic hysteresis give the non-linear, slightly asymmetric, magnetic field strength waveform shown in Figure 8.2. This was computed using the Rayleigh parameters determined in section 8.3 for the DAX8 stator test core. It may be compared to the performance of the test core in Figure 9.7.

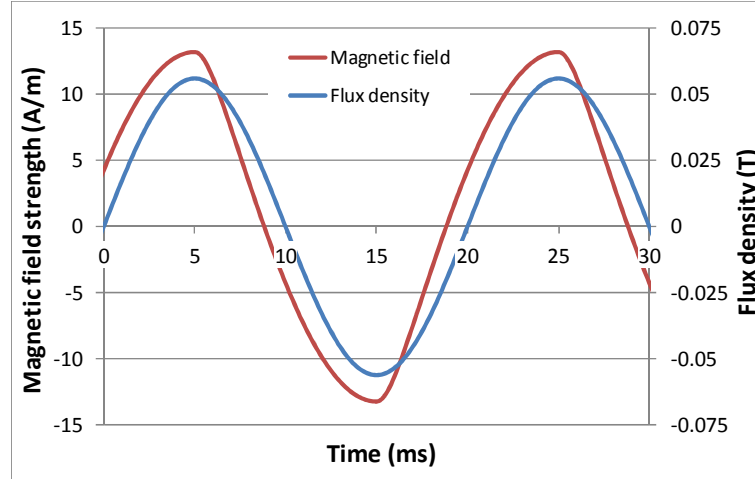


Figure 8.2 Computed magnetic field strength and flux density waveforms for DAX8 Rayleigh hysteresis

Classic eddy current loss is assumed linear, being due to induced currents in the bulk resistance from the sinusoidal flux, and thus does not contribute to harmonic generation. Anomalous loss is potentially also a source of magnetic non-linearity, however is shown below to be effectively absent at EMT flux density levels.

8.2. Relative proportions of loss components at EMT flux density levels

The DAX8 core loss was measured at sinusoidal flux density levels of 0.03 / 0.056 / 0.1 T and at frequencies of 25 / 50 / 75 / 100 Hz. The loss was directly measured by integration of the excitation current and core induced emf from a flux sense winding. The core remained at room temperature ($\sim 20^\circ\text{C}$). The core's total loss W_T for flux density B at radial frequency ω was assumed to be controlled by equation (8.2), with loss coefficients²⁴ k_H , k_S , k_E & k_A (ref. Table 8.1).

$$W_T = k_H B^{k_S} \omega + k_E B^2 \omega^2 + k_A B^{1.5} \omega^{1.5}. \quad (8.2)$$

The 12 measurements allowed a minimum rms error solution in W_T to be determined for the 4 loss coefficients. The error sum was weighted 200% in favour of the 0.056 T measurements since that is the test flux density level, with the results for coefficients and resultant proportional losses at 0.056 T given in Table 8.1. From this it can be seen that

²⁴ Core loss only occurs in the magnetically active yoke region for toroidal excitation. The coefficients only include this mass.

there is no anomalous loss component detected at low flux density levels. Of further note is the Steinmetz coefficient k_s evaluated at 2.17 rather than the conventional 1.6. This value is supported by the experimental observation of Bozorth [217] (§11), that as flux density increases from 0.002 T to 0.1 T this coefficient for iron reduces from an initial 3 to 1.6.

Coefficient		Value	Total core loss at 0.056 T, 50 Hz	
Hysteresis coefficient	k_H	6.62	3.98 W	65.7%
Hysteresis exponent	k_S	2.17		
Eddy coefficient	k_E	0.00672	2.08 W	34.3%
Anomalous coefficient	k_A	0		
Weighted rms loss error		0.67%		

Table 8.1 DAX8 magnetic loss coefficients between 0.03–0.1 T and 25–100 Hz.

A method was also needed to remove the effect of eddy current loss from the magnetic field strength data in order to assess hysteresis loss from generic data. The eddy current and hysteresis magnetic field strengths H_E and H_H that solely generate their related losses are in quadrature (leading phase) to the flux density B . They are shown together with the total magnetic field strength H that has a core loss angle of θ to flux density B in the overall phasor diagram in Figure 8.3.

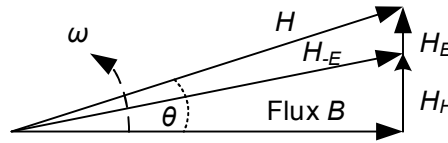


Figure 8.3 Hysteresis and eddy current magnetic field strength phasors

The hysteresis loss is a known proportion K_H of the total loss at a particular flux density B , hence $K_H = H_H / (H_H + H_E)$. If the resultant magnetic field strength after removal of the eddy loss is H_{-E} , the proportional reduction in the magnetic field strength that occurs by removal of eddy current loss is given by equation (8.3).

$$\frac{H - H_{-E}}{H} = 1 - \frac{K_H \sin \theta}{\sin(\arctan(K_H \tan \theta))} \tag{8.3}$$

From field experience and as shown for the DAX8 core, angle θ typically varies from 12–25°, thus the proportional reduction in magnetic field strength for even 66% hysteresis loss is small at ~3%, as shown by the plot of equation (8.3) in Figure 8.4. Given the uncertainty in the data, the above analysis indicates that ascribing 66% of losses to hysteresis and a 3% reduction to the total H field, is sufficient to remove eddy current loss from the data where no better metric exists.

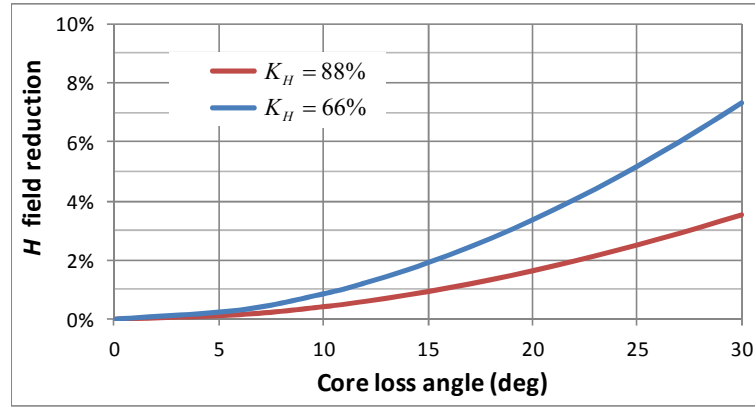


Figure 8.4 Magnetic field strength reduction to eliminate eddy current loss with varying core loss

8.3. Rayleigh hysteresis and magnetic field

The variation of permeability with magnetic flux density in conjunction with ferromagnetic coercivity gives rise to Rayleigh hysteresis [216] (§5.1.7) and the related hysteresis loss. The characterisation of ferromagnetic hysteresis has long been investigated, with Rayleigh [218] first identifying the basic parabolic relationship between ac magnetising field strength H and induced flux density B at low flux density levels. Assuming no residual magnetisation, where μ_i is the initial permeability at zero flux and γ the ‘Rayleigh constant’ for the material, B is given by

$$B = \mu_i H + \gamma H^2. \quad (8.4)$$

Rayleigh noted the induction from the term γH^2 is irreversible, thus equation (8.4) can be expanded to describe the instantaneous cyclic relationship where \hat{H} is the bipolar peak value reached by H

$$B = (\mu_i + \gamma \hat{H})H \pm \frac{\gamma}{2}(\hat{H}^2 - H^2) \quad (8.5)$$

(The \pm operator is + for decreasing and – for increasing H).

Equation (8.5) can be integrated [219] (§9.13) to determine the hysteresis energy density dissipated in each cycle, giving the specific hysteresis core loss W_H (W/kg) for angular frequency ω and steel density ρ in equation (8.6).

$$W_H = \frac{2\omega}{3\pi\rho} \gamma \hat{H}^3. \quad (8.6)$$

There remains uncertainty regarding the range of low flux densities, termed the ‘Rayleigh region’, where the above relationships apply²⁵. This inevitably also varies with the material. Bozorth [217] suggests it is applicable up to about 10% of saturation flux

²⁵ Rayleigh investigated with fields in iron up to ~100 A/m.

density (hence ~ 0.2 T) for ferromagnetic materials, while Bertotti [220] (§10.1.3) considers the validity is restricted to regions where the fields are ‘much smaller’ than the coercivity (~ 0.17 T for M310-50A). Published experimental data is also generally from lower flux density levels, where Ellwood [221] does not exceed 0.01 T and Dietzmann and Schaefer [222] limit themselves to 0.1 T. Thus, subject to validation with sample measurement, electrical silicon steel may be expected to exhibit Rayleigh hysteretic behaviour up to the typical EMT flux density of 0.056 T.

A sinusoidal flux density B induced by the magnetising field strength H can be defined as a cosine wave $B = \hat{B} \cos \omega t$ of angular frequency ω . By inspection of equation (8.5) \hat{B} occurs at the same time as H reaches \hat{H} , hence

$$\hat{B} = \mu_i \hat{H} + \gamma \hat{H}^2. \quad (8.7)$$

Rearranging equation (8.5) with (8.7), where $Z = +1$ for decreasing H and $Z = -1$ for increasing H , gives for H (where \hat{H} and \hat{B} are bipolar)

$$-Z \frac{\gamma}{2} H^2 + (\mu_i + \gamma \hat{H}) H + Z \frac{\gamma}{2} \hat{H}^2 - \hat{B} \cos \omega t = 0. \quad (8.8)$$

The positive root of equation (8.8) for H can be arranged as

$$H = Z \left(\frac{\mu_i}{\gamma} + \hat{H} \right) - \frac{Z}{\gamma} \sqrt{\mu_i^2 + 2\mu_i \gamma \hat{H} + 2\gamma^2 \hat{H}^2 - 2Z \gamma \hat{B} \cos \omega t}. \quad (8.9)$$

This is of the form given in equation (8.10), with constants K_{1-3} replacing the expressions of μ_i , γ and \hat{H} .

$$H(t) = ZK_1 - ZK_2 \sqrt{K_3 - Z \cos \omega t}. \quad (8.10)$$

To determine the harmonics in the H waveform, equation (8.10) can be expanded into the Fourier series for period $2\pi/\omega$, with sine and cosine coefficients S_n and C_n

$$H(t) = \frac{1}{2} C_0 + \sum_{n=1}^{\infty} [S_n \sin n\omega t + C_n \cos n\omega t] \quad \text{where}$$

$$S_n = \frac{\omega}{\pi} \int_{-\frac{\pi}{\omega}}^{\frac{\pi}{\omega}} H(t) \sin n\omega t dt \quad (8.11)$$

$$C_n = \frac{\omega}{\pi} \int_{-\frac{\pi}{\omega}}^{\frac{\pi}{\omega}} H(t) \cos n\omega t dt.$$

The example harmonic coefficient C_n can be evaluated by integrating over one cycle for the increasing and decreasing waves separately ($Z = -1$ for $-\pi < \omega t < 0$ and $+1$ for $0 < \omega t < \pi$). If $\omega t = 2\theta$ and $\cos 2\theta$ is replaced with $1 - 2\sin^2 \theta$, C_n is given by

$$\begin{aligned}
C_n = & \frac{2}{\pi} \int_{-\frac{\pi}{2}}^0 -K_1 \cos 2n\theta + K_2 \cos 2n\theta \sqrt{K_3 - 1 + \sin^2 \theta} d\theta \\
& + \frac{2}{\pi} \int_0^{\frac{\pi}{2}} K_1 \cos 2n\theta - K_2 \cos 2n\theta \sqrt{K_3 + 1 - \sin^2 \theta} d\theta.
\end{aligned} \tag{8.12}$$

The square root parts of equation (8.12) indicate that the harmonic coefficients contain elliptic integrals of the second kind [223] (§11.1), for which no analytic solution exists. In the literature the usual analytic solution of the Rayleigh hysteresis equation is for sinusoidal magnetic field strength (e.g. [224]), which yields a simple result. Dietzmann and Schaefer [222] attempted to solve the equation for sinusoidal flux density, but similarly encountered the elliptic integral and used a power series in a numeric approximation. Baldwin [225] solved an amended Rayleigh loop function but only developed a solution expressed in modified Bessel functions, while Saito et al. [226] only developed a parametric model for numerical FE solution. In consequence numeric integration of the Fourier series coefficients was necessary to evaluate the data and models.

8.4. Determination of Rayleigh parameters

In order to evaluate the likely extent of any test artefacts from varying permeability, it is necessary to determine the range of hysteresis characteristics that may occur in practice. Measured data was available from the DAX8 core described in Chapter 9 for both magnetic characteristics and harmonics. The mean magnetic path length determined in section 11.4 was used to compute mean magnetic field strength. Low flux density magnetic characteristics were also available from steel samples of a generator in service for comparison. These were then complemented with analysis of published data for three generic electrical steels across the expected spread of steel grades in use.

The parameters μ_i and γ are very material specific. For example Both [227] showed that the relative initial permeability μ_{ri} of 3.25% silicon steel (SiFe) can vary from 770–1950 depending only on the annealing temperature. Wohlfarth [228] (§5.7.2) records a μ_{ri} of 400 for 4% SiFe, with ~450 reported by Bozorth [217] (§11) for 3% SiFe, while Zurek et al. [229] measured 900 for a typical non-oriented SiFe of ~M400 grade [230]. Typical values for γ are not reported in the literature, but since it is directly related to the hysteresis loss, differing loss grade steels will cause both parameters to vary substantially. Manufacturers also do not specify these parameters nor magnetisation data <0.1 T, thus estimation methods are required to determine their likely values.

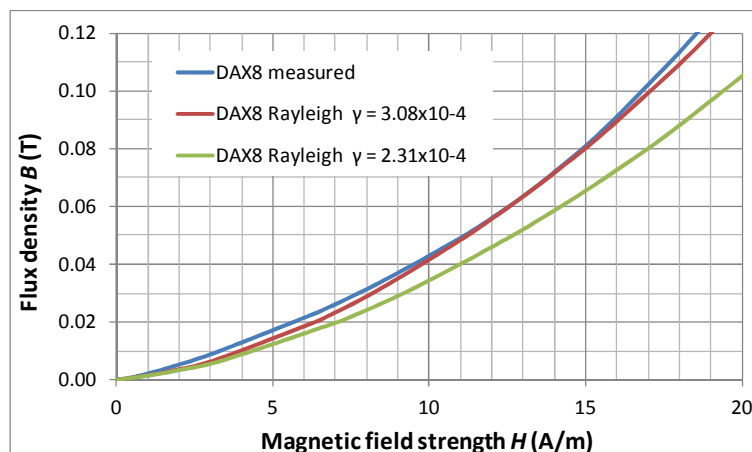


Figure 8.5 DAX8 low flux density measured and Rayleigh predicted B/H curves

To determine the Rayleigh parameters of the assembled DAX8 experimental stator core, the relative permeability was plotted at flux density from 0.02 T down to 0.05 mT in Figure 8.1 where the relative initial permeability μ_{ri} is asymptoting to ~ 950 . The parameter γ was determined from the hysteresis loss in Table 8.1 by equation (8.6), which gave a value of $2.31 \times 10^{-4} \text{ Wb/A}^2$. It was alternately evaluated at 0.056 T according to equation (8.7) as $3.08 \times 10^{-4} \text{ Wb/A}^2$ which would increase the hysteresis loss proportion in Table 8.1 to 88%. These values were used to plot predicted Rayleigh peak B/H curves compared with the measured data in Figure 8.5, and the much closer match to measured values of 3.08×10^{-4} indicated this is the more reliable value.

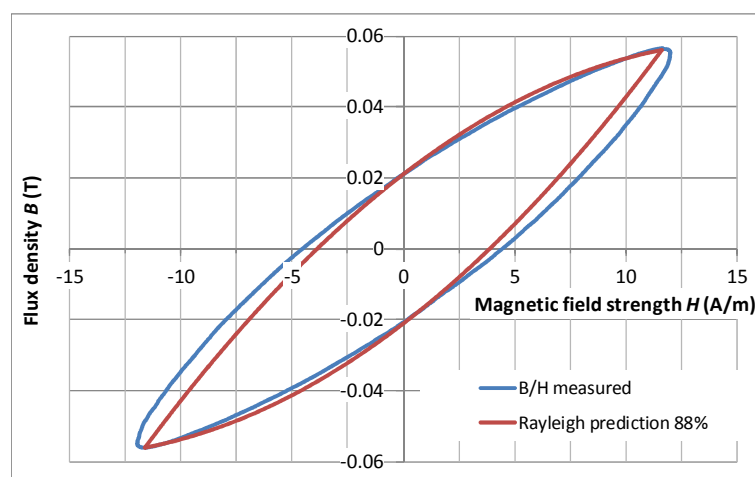


Figure 8.6 Measured and predicted DAX8 Rayleigh hysteresis loops

The difference in the above values for γ is assumed to lie in the simplistic model of the eddy current field and the effect of assembly of the steel into a laminated structure. Given the great variation in the measured and estimated values of γ , the difference is not large. The DAX8 values of $\gamma = 3.08 \times 10^{-4}$ and $\mu_{ri} = 950$ were used in the models, as better reflecting the B/H curve and representing the worst case of the non-linear component for later analysis. The DAX8 B/H loop was plotted both for the measured values at 0.056 T

and also for the loop predicted by the above Rayleigh parameters in Figure 8.6. The calculated power difference of 11% between the two loops reflects the absence of eddy loss.

Low flux density magnetic measurement data from other electrical steel was only available for M270-50A at 0.05 T, from the 1000 MW generator analysed in section 7.4. The hysteresis loss component was estimated at 65% from the measured value for M310-50A, then γ and μ_{ri} were determined from equations (8.6) and (8.7), giving the values in Table 8.3.

Published Cogent data for three electrical steels, M270-50A, M400-50A and M600-50A [183] was used to investigate the expected generic spread in values. To determine their Rayleigh parameters (μ_i , γ), substitution of $B = \mu H$ in equation (8.4) gives

$$\mu = \mu_i + \gamma H . \quad (8.13)$$

This is classically used to permit parameter determination by linearly extrapolating μ as $H \rightarrow 0$ [231] (§3.2.4). However the result for the Cogent steels in Figure 8.7, from published data points nearest the low flux density region, always gives a negative extrapolated initial relative permeability. This is illogical and results from lack of sufficiently low magnetic field data. Bozorth [217] (§11) shows that for 3% SiFe the rate of decline of permeability with field deviates from Raleigh's law between 20 and 3 A/m, a view supported by Heck [231] (§3.2.4) who states extrapolation needs to be from a 'few A/m'.

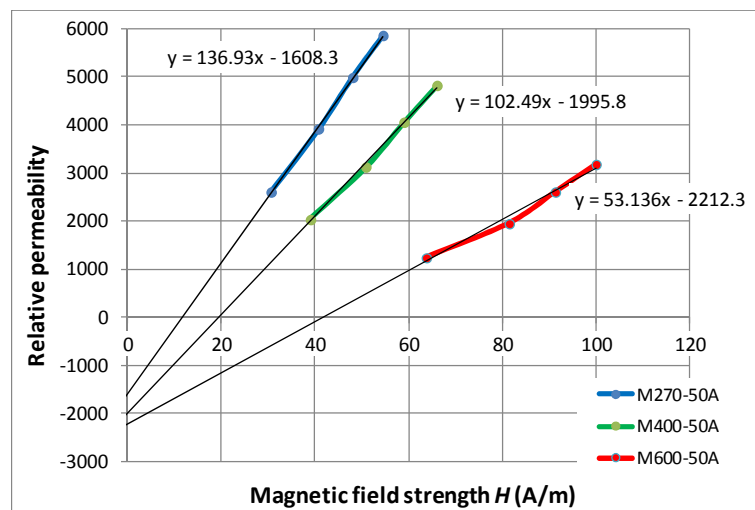


Figure 8.7 50 Hz magnetic field strength estimation of μ_{ri} from Cogent steel data

To investigate a more reliable approach to predicting the Rayleigh parameters, the substitution of $B = \mu H$ in equation (8.13) gives the positive root solution for μ

$$\mu = \frac{1}{2} \left(\mu_i + \sqrt{\mu_i^2 + 4\gamma B} \right). \quad (8.14)$$

The parameters μ_{ri} and γ can thus be derived from flux density by extrapolating their values as $B \rightarrow 0$. Since permeability is now a weaker function of B in equation (8.14) than H in (8.13), sensitivity to error in any extrapolation will be less. A square root can be expanded in a power series, thus a polynomial approximation was used to determine the initial relative permeability μ_{ri} using flux density data. The permeability curves were extrapolated to zero flux with 2nd order best fit polynomials in Figure 8.8.²⁶

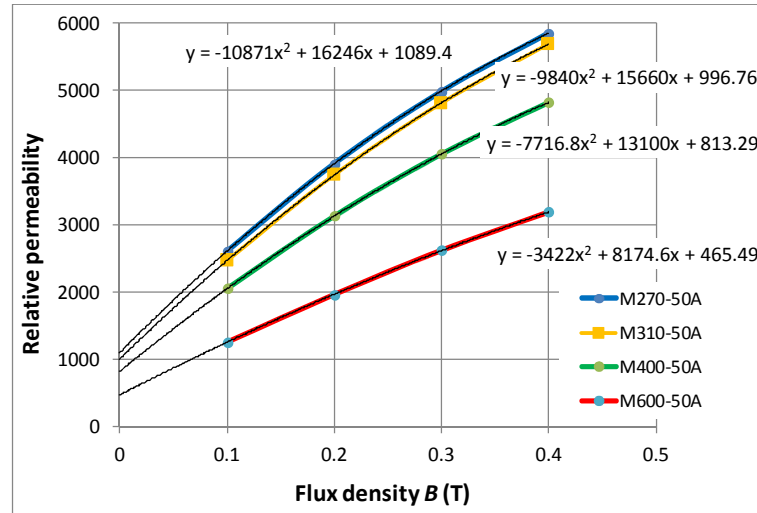


Figure 8.8 Flux density estimation of μ_{ri} and γ from Cogent steel data

From this it can be seen that rational results in the expected range are obtained, with the predicted μ_{ri} varying from 465–1089. In addition in Figure 8.8 the predicted μ_{ri} at 997 of Cogent M310-50A steel was only 4.9% greater than the measured DAX8 value of 950 of the same grade of CDW steel. Similarly the predicted μ_{ri} at 813 of M400 is only 9.7% under the measured value by Zurek. To determine Rayleigh constant γ , equation (8.15) was derived from equation (8.7)

$$\gamma = (\hat{B} - \mu_i \hat{H}) / \hat{H}^2. \quad (8.15)$$

This allows γ for the three Cogent steels to be determined from the B/H values of the permeability extrapolation polynomials at 0.05 T, given in Table 8.3.

²⁶ It is commonly expected that the higher silicon content of lower loss electrical steels reduces their permeability. However this effect only occurs for flux densities >1.3 T where the dissolved silicon reduces the saturation polarisation of the iron [33] (§3.1). At lower flux densities commercial NGO steels from for example Cogent [183] and ThyssenKrupp [181] show strongly increased permeabilities for lower loss grades at 0.1 T flux density.

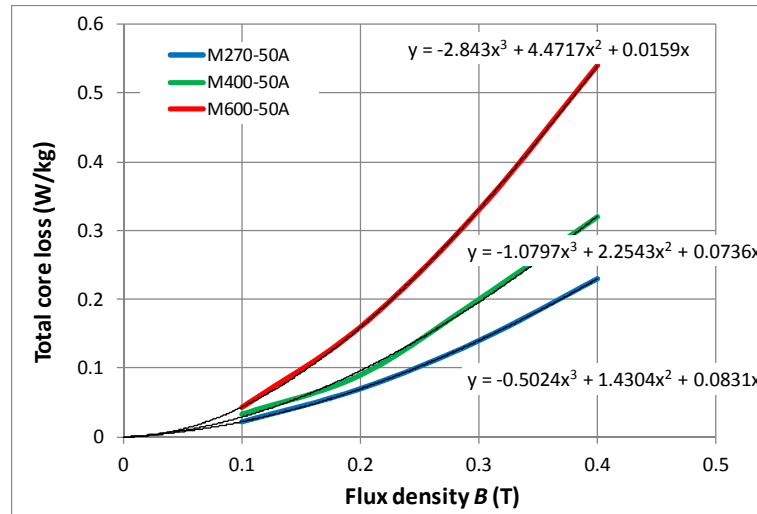


Figure 8.9 Core loss extrapolation to 0.05 T from Cogent steel data

The core loss at EMT flux density levels was determined by extrapolating the total losses in the three steels down to 0.05 T, using best fitting 3rd order polynomials as shown in Figure 8.9. The estimated values for γ from the extrapolations in Figure 8.8 were then used with equation (8.6) to compute the hysteresis loss and hence its proportion of total loss shown in Table 8.3, where it can be seen to vary from 51–82%.

8.5. Harmonic analysis and impact on measurements

The induced flux and hence fault voltage is sinusoidal, and for modest faults the fault resistance dominates as shown in section 3.5, thus the detected fault current in any fault will also be sinusoidal with no harmonic content. However the excitation magnetic field in the core with its harmonics is also detected by the Chattock sensor. While the dominant fundamental is resolved as the *Phase* signal, harmonics not in phase with the fundamental may appear in the *Quad* signal, affecting fault detection.

The impact on common EMT systems depends on their method of synchronising to the flux or magnetic field strength and demodulation of the *Phase* and *Quad* signals. The normal method of detection is by synchronous demodulation analysed in section 3.6. This demodulation may be by the simpler method of square-wave switching and integration which also causes demodulation of harmonics, or the more complex convolution with sinusoidal references which does not. The EL CID systems in service use both methods²⁷, hence this analysis considers the worst case square wave demodulation.

²⁷ Other electromagnetic tests have not disclosed their method of demodulation of the fault signal, except the PROFIM system which uses a zero-cross measure of the phase angle, and will thus be sensitive to harmonics. The multi-frequency Siemens SMCAS must use sinusoidal demodulation and thus be insensitive to harmonics.

As concluded in section 8.3, the harmonics can only be computed numerically from a Fourier series expansion of the Rayleigh loop in equation (8.10). This was completed for the Rayleigh models of the five steels with a 200 step trapezoidal integration of the magnetic field strength over one 50 Hz cycle of a 0.056 T flux density cosine wave. The amplitude and phase angle of each harmonic was determined from sine and cosine coefficients with respect to the flux density (B) reference, with leading angles positive (hence the fundamental field component leads the flux density).

The harmonics in the detected magnetic field strength are also affected by the rising ($\propto \omega$) frequency response of the Chattock, and the frequency response of the signal and reference instrument inputs, both assumed to be 50 Hz first order low pass filters²⁸. Section 3.4 shows that the detection of the excitation field is inverted which, together with the conventional negation of *Phase* signals, will also apply to the excitation harmonics. This gives overall detection relative sensitivities and signal phase leads compared to the fundamental current given in Table 8.2, including demodulation polarities. From this it can be seen in Figure 8.10 that lagging harmonics ($0 > \psi_n > -\pi$) will give rise to a positive *Quad* signal for conventional positive *Phase* signal.

Harmonic order (n)	1	3	5	7
<i>Phase</i> signal relative detection sensitivity (G_{Pn})	100%	132%	137%	140%
<i>Quad</i> signal relative detection sensitivity (G_{Qn})	-100%	132%	-137%	140%
Phase lead of filtered signal (ψ_n)	-45.6°	-72.0°	-78.9°	-81.9°

Table 8.2 Detection sensitivity and phase lead of harmonics relative to fundamental

The fundamental and harmonic magnetic field strength phase angles are computed with respect to the flux density B . However the convention and calibration in EL CID is that the *Quad* signals are resolved with respect to the excitation current (to ensure that for no fault the *Quad* signal is zero). Internally the EL CID has a true Reference phase axis delayed due to the filters on the Reference signal, and knowledge of this delay is needed to resolve the differing phase angle harmonics. All phase angles are positive for leading.

²⁸ The combined response of the Chattock and instrument at 60 Hz is usually 6-8% above the 50 Hz level, which corresponds to a 50 Hz first order low pass filter.

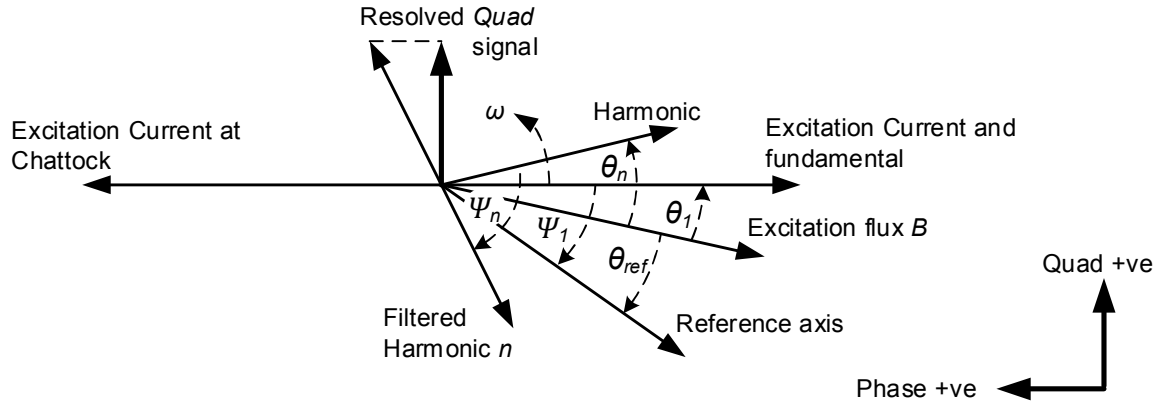


Figure 8.10 EL CID phasor diagram of detected harmonic signals

The angle θ_n is the computed phase angle lead of harmonic n on the flux density wave shown in Figure 8.10. The harmonics are detected by the Chattock and filtered as given in Table 8.2, with phase leads of ψ_n on the computed phase angle of the harmonic. They are then resolved into *Phase* and *Quad* components against the internal Reference axis. Since the fundamental can be assumed to be dominant and is resolved to give zero *Quad* in calibration, the Reference axis filter lead on the fundamental component must thus be ψ_1 . The offset θ_{ref} of the Reference axis to flux density is thus given by

$$\theta_{ref} = \psi_1 + \theta_1. \quad (8.16)$$

The effect of resolution of harmonics to the leading Reference axis of θ_{ref} (rather than their origin of B) is to add a constant time delay, and thus a phase lag in proportion to the harmonic order of the harmonic signal. In consequence the effective phase angle lead ϕ_n of the harmonic n on the Reference axis is given by

$$\phi_n = \psi_n + \theta_n + n\theta_{ref}. \quad (8.17)$$

The harmonics have amplitude H_n given in Table 8.3 for the selected steels and filter/signal detection sensitivities G_{Pn} and G_{Qn} given in Table 8.2, and demodulated with respect to the Reference axis in accordance with equations (3.25) and (3.29). The net *Phase* and *Quad* signals are then given by equations (8.18)

$$Phase = \sum_{n=1}^7 \frac{1}{n} H_n G_{Pn} \cos \phi_n \quad \text{and} \quad Quad = \sum_{n=1}^7 \frac{1}{n} H_n G_{Qn} \sin \phi_n. \quad (8.18)$$

The harmonics of the DAX8 core test current, representing the magnetic field strength at a sinusoidal flux density of 0.056 T, were also analysed by a 1024 point FFT of the recorded excitation current. These measured harmonics are shown in Table 8.3 where it can be seen that the Rayleigh model predicts about twice the harmonic content of the measured results.

The *Phase* and *Quad* signal detection is also affected by the impact of the harmonics on the EMT Reference signal. Reference detection is normally from a Rogowski coil on the excitation current and thus has a rising frequency response. In addition Reference synchronisation is commonly by zero-crossing detection rather than measuring the fundamental phase angle, thus excitation current harmonics may further impact the *Quad* demodulation. A study of the filtering and zero-cross impact of the harmonics, assuming the same filtering as the Chattock signal with zero-cross detection, showed that the harmonics cause the Reference to have a small phase difference to the fundamental (e.g. -0.54° lead for M310-50A steel). The *Quad* signal is strongly affected by any change in the Reference phase angle, since it affects the proportion of the excitation mmf (the *Phase* signal) also included. The expected Reference phase error for each case was computed, and the resultant total *Quad* error signal expected given in the final row of Table 8.3.

	Measured		Modelled			
	DAX8 M310-50A	M270-0A	DAX8 M310-50A	M270-50A	M400-50A	M600-50A
Electrical steel grade						
Initial relative permeability (μ_{ri})	950	1035	950	1089	813	456
Rayleigh constant (γ)	2.31×10^{-4}	1.31×10^{-4}	3.08×10^{-4}	5.14×10^{-5}	3.21×10^{-5}	1.19×10^{-5}
Hysteresis loss prop.	66%	n/a	88%	51%	58%	82%
Hysteresis loss (mW/kg)	3.22	4.03	4.32	3.91	5.32	9.53
<i>H</i> field 3 rd Harmonic	2.95%	5.20%	6.22%	3.84%	4.00%	4.23%
<i>H</i> field 5 th Harmonic	0.34%	1.31%	1.79%	0.80%	0.85%	0.93%
<i>H</i> field 7 th Harmonic	0.07%	0.49%	0.74%	0.27%	0.29%	0.32%
Fundamental angle	20.3°	15.5°	19.0°	11.2°	11.7°	12.4°
3 rd Harmonic angle	-48.4°	-35.1°	-21.9°	-50.6°	-48.9°	-46.4°
5 th Harmonic angle	-44.0°	-57.9°	-41.3°	-74.2°	-72.6°	-70.2°
7 th Harmonic angle	-36.8°	-71.4°	-54.5°	-84.3°	-83.3°	-81.6°
(angles are leading)						
Harmonic <i>Quad</i> per 1 A <i>Phase</i> (mA rms)	-6.6	-6.5	-6.5	-5.8	-5.9	-6.1
Harmonic <i>Quad</i> per 1 A <i>Phase</i> inc. Ref. (°)	-15.2	-12.3	-15.1	-10.2	-10.3	-10.5

Table 8.3 Rayleigh parameters and harmonics as % fundamental at 0.056 T

The harmonics are developed in the core's excitation mmf, and for uniform core material will appear as a constant mpd across all the core slots. It is normal as shown in section 3.4 to rotate the Reference phase angle in calibration to annul any contribution of the excitation field to the *Quad* signal. In consequence this rotation, or similar 'DC removal' [26] to achieve a zero standing *Quad* signal, should also annul any constant harmonic contribution to the *Quad* signal. However non-uniformity of material will cause negative *Quad* signals (apparent fault) in a region of increased harmonics. While the

impact of core loss variation has been studied in Chapter 7, Appendix D shows that for the normal sinusoidal flux (discussed in section 9.3) there is no power carried in any magnetic field strength harmonics. Thus local variation of the Rayleigh parameters, even if they do not affect core loss, could still result in small *Quad* signal artefacts.

8.6. Discussion on impact of varying and non-linear permeability

Even a linear variation of permeability with flux density results in a non-linear B/H transfer function, and would thus be expected to generate harmonics. However Rayleigh hysteresis results in a non-linear variation in permeability with flux density, potentially exacerbating harmonic generation. The results show that the Rayleigh hysteresis generates harmonics in the excitation current whose effect is thus proportional to the per-slot excitation (*Phase* signal). They generate a small *Quad* signal in the region of -6 mA/A Phase which is very constant regardless of the grade of steel used. In consequence if local hysteresis loss variance of as much as $\pm 50\%$ occurred circumferentially and uniformly around a worst case 4 A *Phase* machine²⁹, the local *Quad* signal change indications due to harmonics of just $\pm 12 \text{ mA}$ are much less than the classic threshold of concern of -100 mA , thus would not adversely impact field measurements. Even if one polarity of the variance was concentrated in a small area, the maximum would still only reach $\sim 20 \text{ mA}$.

The effect of the harmonics on the phase accuracy of the Reference signal can exacerbate this, increasing it up to $\sim 15 \text{ mA/A Phase}$. However the effect on the Reference is readily offset, thus would not cause a high localised *Quad* signal that might be interpreted as a defect. The impact when the phase Reference is preset to the excitation fundamental does cause a modest standing negative *Quad* signal in typical turbo-generator stator cores, with $20\text{--}30 \text{ mA}$ seen in practice³⁰.

The predicted *Quad* signals are surprisingly low and constant given the 4–6% third harmonic amplitudes. Further analysis of the data shows that the effect of the phase lags in the filters causes the third and fifth harmonics to remain within $10\text{--}20^\circ$ of the *Phase* axis, thus their contribution to the *Quad* signal remains low. If this fortuitous effect was absent, the potential effect of harmonics on the above illustrated 4 A *Phase* machine could reach

²⁹ Typical *Phase* signals are in the 1–3 A range.

³⁰ A test example was obtained from a 660 MW GEC-Alstom generator. The EL CID test system had its reference phase angle calibrated to match the fundamental current and was unchanged during test. The aggregate standing *Quad* signal was -35 mA for an average *Phase* signal of 1.4 A, giving -21 mA/1 A Phase .

-65 mA, an amount that would be significant in affecting interpretation of modest defects. However this should not occur in practice.

This study has assumed that electrical steel of various grades will behave according to the Rayleigh hysteresis model at flux density levels up to 0.056 T, which literature and measurements indicate is an imperfect assumption. The DAX8 modelled Rayleigh hysteresis loss proportion is 33% greater than that measured by separation into the standard loss model components of equation (8.2), due to the Rayleigh values necessary to match μ_i at $B = 0$ and γ at 0.056 T. This also gives a B/H curve with greater inflection than is seen from measurement. If values for μ_{ri} and γ are chosen that give a best fit to the measured B/H curve up to 0.056 T ($\mu_{ri} = 1910$ and $\gamma = 1.7 \times 10^{-4}$), then closer matching values of the modelled harmonics occur (e.g. 3rd harmonic = 4.0%). However the poor μ_{ri} match indicates a more complex process than the basic Rayleigh model.

The absence of anomalous loss at flux density levels < 0.1 T ($k_A = 0$) did not prove that anomalous loss did not exist, just that there was no component of the loss in the 0.03-0.1 T range that had a best fit to both $B^{1.5}$ and $\omega^{1.5}$. Cullity and Graham [219] (§13.3.1) (supported by Wohlfarth [228] §3.5.8) consider anomalous loss a ‘fiction’ to resolve the difference between classic eddy current loss and that measured. This difference is due to the interaction of the eddy currents with the domain size and wall movement, which they indicate (their Fig. 13.4) increases with flux density. Thus it is reasonable to conclude that at these low flux density levels, and thus low domain wall velocities, this extra anomalous loss both reduces and becomes mostly proportional to B^2 and ω^2 , thus is included into the eddy current value. The issue is anyway of little concern to this study, since the purpose was to solely determine the proportion of loss attributable to hysteresis.

It is also likely the eddy current loss is affecting the detail hysteresis estimations, while the laminated stator core with segmented joints introduces extra complexity as the flux alternates between laminations and doubles in density at the joints. This latter effect is problematic only at high flux density levels as analysed in Chapter 10. However it is possible that the lower than expected harmonic measurement of the DAX8 core (compared to the Rayleigh hysteresis harmonic prediction) derives from the linear axial permeability experienced by the interlaminar flux transfer at the joints.

A further consideration arises in the degree to which local changes in B/H non-linearity could in fact arise without also affecting the local net permeability or core loss studied in Chapter 7. It is most likely that an electrical steel non-uniformity around the core would affect the net permeability, as well as hysteresis loss parameters and hence harmonic

content. From this it is expected that the effects of all three variances would act together in reality, and may augment or offset each other, depending on their polarities.

While the above discussion indicates the areas of uncertainty in the study, the worst case of the errors identified has been assumed. In consequence the conclusion that the studied phenomenon alone is not a significant source of test error remains unaffected. In addition, the effect is restricted to EMT systems using square wave demodulation, which are expected to be a reducing proportion of the EL CID systems in the future.

As a consequence of the study, a new method of initial permeability extrapolation from flux density measurements has been shown to be a more reliable means of estimating the Rayleigh parameters from published electrical steel data than normal magnetic field strength extrapolation.

8.7. Summary

The assumption in the EMT is that the electromagnetic system is linear. However the permeability and hysteresis of electrical steel varies substantially with flux density at the low flux levels used for testing. This causes harmonics to be developed in the excitation field due to Rayleigh hysteresis, which may be interpreted as fault signals depending on their circumferential non-uniformity and the test instrumentation. This was studied for measured data from steel samples as well as published data from a range of commercial steel grades. An improved method to more reliably determine the initial permeability and hysteresis parameters from published commercial steel data was developed.

The use of sinusoidal flux density was shown to prevent an analytic solution of the magnetic field strength, thus a numeric integration method was required to compute the resultant harmonics. These were then used to determine the magnetic field strength harmonics detected within the *Quad* signal due to both harmonic signal demodulation and Reference error. The impact of these was analysed in EMT systems that use simple square-wave demodulation. This showed that due to the tendency for the harmonics to mostly resolve in the Phase axis, the effects will be minor for all grades of electrical steel.

Chapter 9. Construction and Validation of an Experimental Stator Core

A representative stator core is required for experimental validation of 3D FE buried fault detection models developed by Ho. The original stator core modelled by Ho was not available, and in consequence an alternate slightly larger experimental core was constructed. This was proven as a fault-free and scalable test bed on which to validate the buried fault models. In all construction, verification and experimental work on the stator core, the test equipment identified in Appendix E was used.

9.1. Design and construction

The faults being considered are generally shorter than a typical core packet. The flux induced by a fault is shown to not extend far beyond the fault circuit in section 6.5 and be constrained by the packet vents. Similarly the magnetic field in the bore from a 40 mm long fault has subsided to <20% of its central value by 50 mm axially from the fault centre [72]. In consequence a test core does not need to be a full length of a typical generator, and one that is ~2x the maximum projected fault length of 50 mm was considered adequate for experimentation. It also fits the constraint of not exceeding a weight that can be handled in the workshop (<2 t).

The original ‘TCS’ core constructed by Ho was not available, nor the Brush DAX7 laminations (100 MVA machine) used, thus surplus laminations from a Brush DAX8-445 machine [232] (125 MVA machine) were purchased, illustrated in Figure 9.1. These construct a 2032 mm (80”) dia. core rather than the 1780 mm (70”) of the DAX7 (both with 48 slots), so there is a linear scale increase of 14%. The packet sizes were varied to achieve a stack of four packets of (bottom to top) 5/50/25/13 mm shown in Figure 9.3, giving an overall core height of 118 mm including spacers.

The laminations are stacked on a 36 mm thick plywood table and supported on timber trestle beams as designed in 3D in Figure 9.2(a). The table and support structure was analysed for safety, and a minimum Factor of Safety (FoS) of 9 achieved³¹. The laminations were stacked with the table horizontal using machined guides in the lamination slots as well as the 12 keybars. The keybars were cemented into the table to prevent movement after erection and electrically interlinked to simulate frame conductivity.

³¹ Public building standards [233] only require FoS >3 for wooden structures.

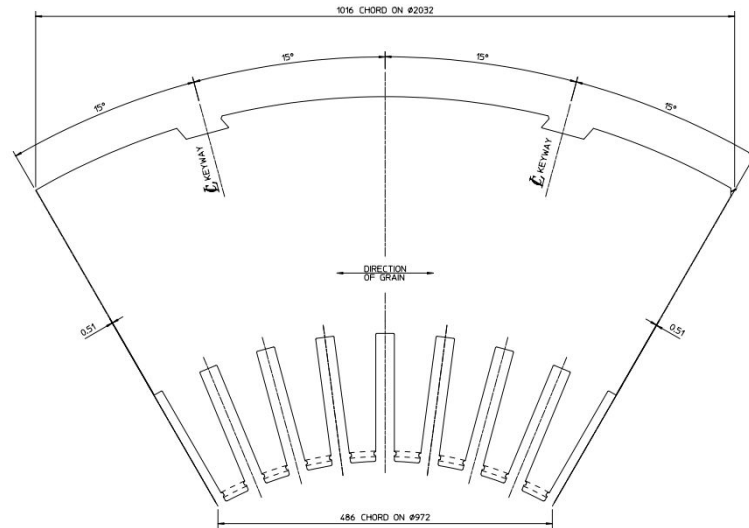


Figure 9.1 DAX8 lamination drawing

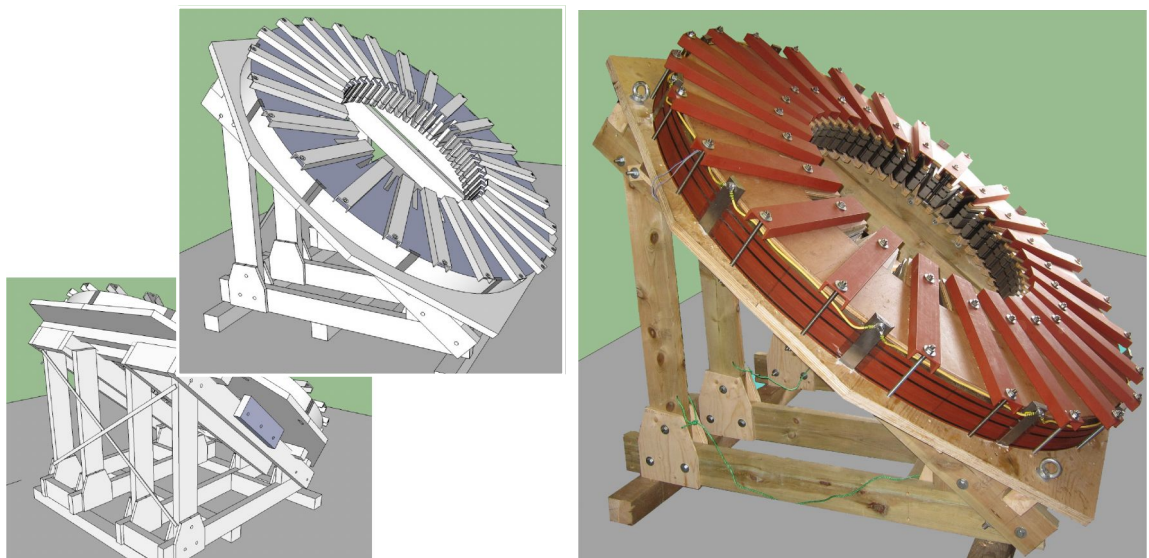


Figure 9.2 (a) Stator 3D design models, (b) assembled experimental stator core

The stator top is held compressed by 19 mm plywood panels, clamped by 24 off 75 x 38 x 5 mm mild steel channels bolted through with M12 austenitic stainless steel studs to maintain pressure. Stainless steel was used to minimise the effect of the studs partially magnetically bridging the stator slots. After construction and test, the table with core was erected at an angle of 40° to enable it to be more easily accessed and accommodated, shown in Figure 9.2(b). It was identified as the ‘DAX8’ stator core.

9.1.1. Lamination keybar contact

Reliable rear keybar-lamination contact was achieved by driving the keybars over tightly packed copper braid against prepared and greased lamination steel edges shown in

Figure 9.3 with the keybar part driven home³². This was proved by <50 mΩ electrical continuity test for all 1116 laminations.



Figure 9.3 Conductive packing between laminations and part inserted keybar

A Kelvin resistance measure was also made between keybars and sampled lamination tooth edges and slot bases. The test results are given in Table 9.1, where it can be seen that the lamination tooth tip resistances average 6.1 mΩ and slot bases average 2.5 mΩ. For the slot base it is clear that at the end of the laminations by the segmentation joint, the resistance rises by ~50% over the mid-point. The tooth tips are much less affected by this variance.

Tooth tip	Packet	Resistance (mΩ)	Slot base	Packet	Resistance (mΩ)
22–23	top	6.3	23	second	2.2
22–23	third	6.0	25	second	2.1
25–26	second	6.6	21*	third	3.3
25–26	base	5.8	21	third	2.3
7–8	second	6.3	7	top	2.4
7–8	base	6.2	7	third	2.2
5–6	top	6.1	9	second	2.1
5–6	base	5.8	9*	base	3.4
Average		6.1			2.5
Lamination temp. 17 °C			* Segmented lamination ends		

Table 9.1 Lamination resistance measurements

9.1.2. Lamination clamping pressure

There is no specification for the preferred Stacking Factor (SF) for assembled stator cores. The standard for fully finished electrical steel EN10106 [211] requires that M310-50A grade without insulation shall be capable of an SF of at least 0.97 when tested to EN60404-13 [234] at 1 MPa pressure. However neither standard offer guidelines on acceptable final results or expectations at lower pressures. Klemptner & Kerszenbaum [8]

³² The tight fit of the keybars caused minor distortion of the lamination rear edges when driven home, which was not an problem.

(§2.1) state pressures for turbo cores are up to 250 psi (1.7 MPa), but that after relaxation 100–150 psi (0.7–1.0 MPa) is more realistic for in-service cores [173]. Znidarich [235] and Walker [43] (§4.6) report 1.0–1.4 MPa as the range for hydro-generator pressure when considering shrinkage and re-tightening requirements. However these massive pressures are required for service robustness, much less is needed to achieve adequate core compression. Walker [236] reports that the majority of core compression is achieved by 40 psi (270 kPa) and shows that for the classic ‘penknife insertion’ field test for tightness [8] (§11.1.1), a core is impenetrable by 15 psi (103 kPa). This supports the conclusion that low pressures are sufficient to obtain the magnetic benefits of a ‘tight’ core. An experiment was thus conducted to determine the pressure for an acceptable SF for the experimental core.

Measurement of the steel thickness and overall insulated thickness was conducted on a number of lamination positions, from which the theoretical maximum SF was computed at 0.969 due to insulation. A section of the core was then progressively compressed under a pair of clamp rails with the pressure determined by selected DIN2093 Bellville washers. The SF was then computed from the degree to which the compressed region total stack height reduced from uncompressed (self-weight only) to theoretical minimum height.

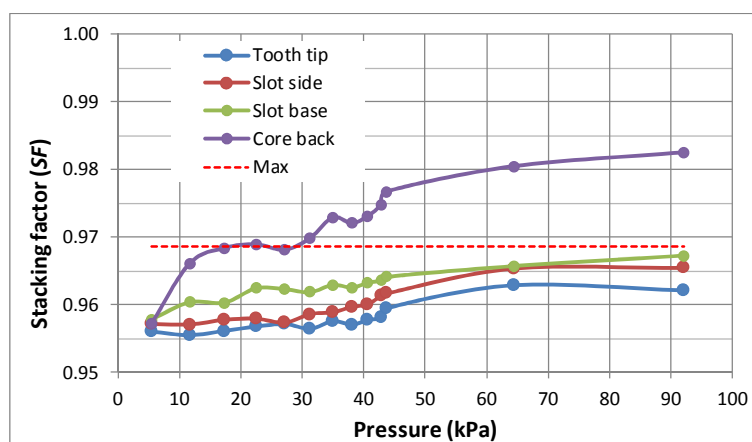


Figure 9.4 Core stacking factor with compression pressure

The results are shown in Figure 9.4, where SF is seen to be stabilising at a core pressure of ~ 70 kPa (10 psi), from which it is considered that the aggregate SF in the core is at least 0.96. The measure at the core back which appeared to exceed the theoretical maximum was found to be due to distortion of the reference plane, but still indicated by its slope that it was stabilising by ~ 70 kPa. This pressure was established around the whole core using 3.3 kN Bellville washers under the 48 channel clamp stud nuts.

9.1.3. Model excitation level

There is no standardised level of service flux density to determine the test core flux density level, thus some field data was surveyed in Table 9.2 to investigate typical turbo-generator peak flux densities. From this it was decided to set a model service flux density of 1.4 T. It was noted that hydro-generators typically operate at significantly lower flux density levels, where Walker [43] (§6.1) advises levels of 0.85–1.0 T, while Milano [237] proposes a maximum of 1.15 T to limit losses.

Site/Machine	Power (MW)	Voltage (kV)	Service flux density (T)
UK, Parsons	660	23.5	1.51
Spain, Siemens	1000	21.0	1.15
Abu Dhabi, ABB	86	13.8	1.35
UK, Alstom	242	15.5	1.48
USA, Westinghouse	530	24.0	1.22
Brush, DAX8-445	106	10.5	1.47
Average			1.36

Table 9.2 Turbo-generator flux density field survey

The final DAX8 stator core has the parameters in Table 9.3.

Originating machine data	Brush DAX8-445, 125 MVA, 0.8 PF, 50 Hz, length 4.45 m	
Lamination material	M310-50A, pre-coated and deburred, CDW	
Lamination thickness	0.5 mm	
Outside radius	1016 mm	
Bore radius	486 mm	
Slot width	27 mm	
Slot depth	186 mm	
Yoke depth	344 mm	
Segmentation	6/circle, 50% overlap, 1.02 mm gap	
No. slots	48	
Packet heights	base = 5 mm, second = 50 mm, third = 25 mm, top = 13 mm	
Packet spacers	7.8 mm	
Yoke geometric mean circumference	5305 mm	
Yoke magnetic mean circumference at 0.056 T	5108 mm	
Computed mass of laminations	1596 kg	
Mass of yoke region	1238 kg	
Weight of complete assembly	1794 kg	
Stacking Factor (<i>SF</i>)	>0.96	
Model service flux density	1.4 T	
Test flux density 4%	0.056 T	
<i>STV</i> for 4% flux density	0.398 V	

Table 9.3 DAX8 experimental stator core parameters

9.2. DAX8 experimental stator verification tests

There is a need to ensure that as constructed, the stator core does not contain any interlamination insulation fault, such that all detected fault signals derive solely from applied faults. The EMT used a measurement system of an EG&G 5210 Lock-in amplifier with a 100 μ V/A Chattock, equivalent to EL CID and scaled to the same *Phase* and *Quad*

signals. Chattock calibration was completed by the standard EL CID method [26] of a standardised mmf source across a steel channel. After demagnetisation by ac induction to 0.5 T, the 4% excitation flux density level of 0.056 T required 44 A-t excitation. The most -ve *Quad* readings for each slot shown in Figure 9.5 ranged from +26 to -37 mA, well within the industry acceptance limit of -100 mA.

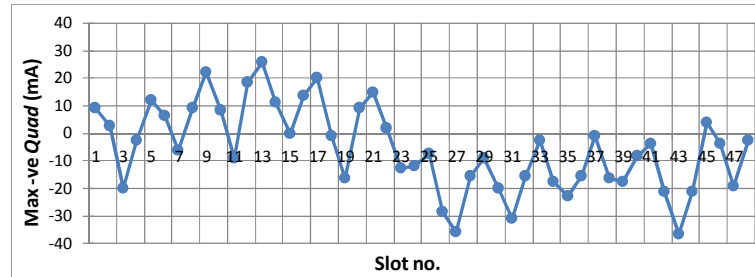


Figure 9.5 Electromagnetic verification test results maximum -ve *Quad* signal

A test wire loop fault 25 mm long around a tooth tip, whose current was directly measured at 363 mA, gave a *Quad* signal of -166 mA indicating a 45.7% relative sensitivity. From previous research [189] a 25 mm long tooth fault has a ~45% Chattock relative sensitivity which confirms the measurement system is performing as expected.

Since the EL CID test has poor sensitivity to very short faults (<10 mm), an HFT was also completed at the maximum power available (240 V, 35 A) inducing 1.06 T at 980 A-t. This is 76% of model flux density level thus the temperature hot spot threshold for acceptance in this test, as discussed in section 4.5.4, is $10 \times (0.76 / 0.9)^2 = 7.1$ °C. After 2 hours excitation the IR images for the whole core showed the comparative core surfaces to be consistent within 2 °C, indicating no significant core fault. The example of slot 9 is illustrated in Figure 9.6(a). The temperatures of a sample slot base (slot 3) and tooth tip (slot3-4) were monitored as plotted in Figure 9.6(b). It can be seen that the differential temperature rise between the slot base and tooth tip stabilised to ~6 °C after the 2 hours.

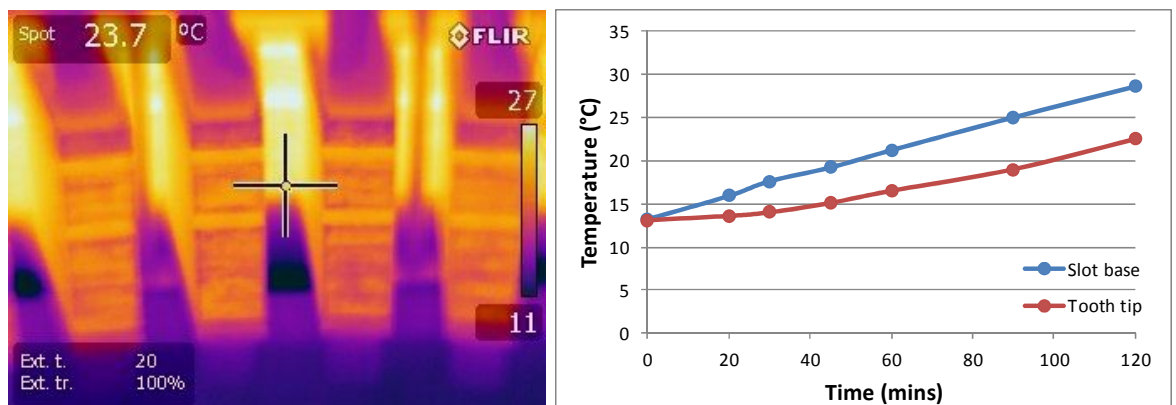


Figure 9.6 (a) Slot 9 HFT test results after 120 mins, (b) HFT temperature rises with time

9.3. Sinusoidal flux excitation drive

At the low flux density levels in the EMT, the relative permeability of the core is not constant, and rises from 1000 to 3800 as shown from measurements in Figure 8.1. This non-uniformity results in harmonics in the excitation current needed to induce a sinusoidal flux, a phenomenon analysed in Chapter 8.

For an EMT in the field the full core length is excited and consequently the excitation flux density closely follows the sinusoidal excitation voltage due to the dominance of the inductive back emf. However in this short experimental core the back emf is small (0.4 V/turn), while resistance of the 1.5 mm² excitation winding is relatively larger (0.48 V/turn) due to the length needed to ensure the excitation winding remains well away from the core ends³³. In consequence the induced flux waveform will contain some of the harmonics from the current, not normally present in field tests or FE models. These harmonics could affect the measurement of experimental faults.

The proportion the core back emf is reduced over the drive source voltage, expressed as the excitation error K_E , is 44.5%. Reducing the winding resistance to a low enough value would require very heavy conductors. Instead a negative feedback excitation drive was developed to reduce the excitation error K_E to match the <4% typical field experience. Together with a synthesised sine-wave source to avoid mains waveform distortion, this reduced the Total Harmonic Distortion (*THD*) of the flux wave from 3.5% to 0.12%, with maximum harmonic of -60 dB. Details of the analysis and design are given in Appendix F.

9.4. Core magnetic tests

9.4.1. Core loss phase angle

The core loss phase angle (between flux and excitation current) variation with varying flux density was measured using the 5210 Lock-in amp in Bandpass/Walsh mode which analyses fundamental frequency components only. It was referenced to the core flux with the feed-back linearised sinusoidal flux driven at 50 Hz, the flux density sensed from a flux sense winding, and the current by a Chattock around the excitation cable to ensure no sensor phase error. The measured loss angle is plotted in Figure 3.7 at 19.0° at the model 4% test level of 0.056 T. A confirmation test was also performed at just 0.056 T by recording the flux density sense signal and current detected by a 0.025 Ω shunt on a digital oscilloscope. The flux density and current signals were convolved with synthetic sine and cosine 50 Hz waveforms, which gave the phase angle of the fundamental as 18.8°, very

³³ The winding needs to loop back around the core well away (>0.5 m) from the core ends to prevent increased flux density being induced in the core ends by the radial segments of the winding.

close to the directly measured results. The normalised flux and current waveforms are shown in Figure 9.7.

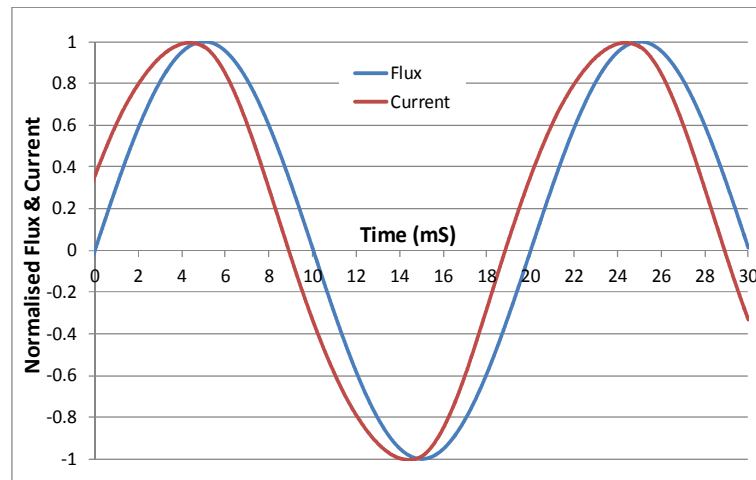


Figure 9.7 Normalised DAX8 flux and current waveforms at 0.056 T flux density

9.4.2. Epstein material tests

In order to be able to predict and interpret stator core magnetisation characteristics, the AC magnetisation curve prescribed by standards [211], of peak flux density against peak magnetic field strength of the core electrical steel (aka B/H curve), needs to be known. The stated steel vendor used was C.D. Wälzholz (CDW) whose sole published M310-50A data [182] included in Figure 9.8 is very sparse and difficult to believe, especially against comparable electrical steel data from Cogent [183] and ThyssenKrupp (TK) [181]. In addition the effect of laminated stacking is unknown.

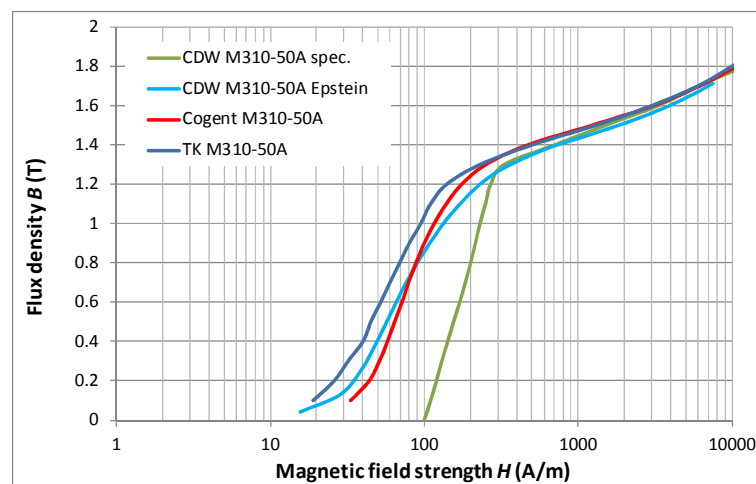


Figure 9.8 CDW M310-50A B/H datasheet curve and comparators

To characterise the CDW lamination material more reliably, a 25 cm Epstein Frame test system was constructed in accordance with EN 60404-2 [238]. Sample laminations were sheared along rolling (RD) and transverse (TD) directions, and tested in the specified 50%/50% RD/TD combination, and also in solely RD and TD directions to determine the

anisotropy. The sheared material samples were not annealed due the practical difficulty, however it is known that the supplied laminations were also not annealed after stamping.

The result is also shown in Figure 9.8 ('CDW M310-50A Epstein') where it can be seen that the material permeability is compliant to or much better than the published CDW data, with the lower flux density values following the typical curves of Cogent and TK.

9.4.3. DAX8 experimental core B/H curves

The stator core B/H curves were expected to differ from the CDW material specification due to the implausible data, plus the toroidal flux path and the effect of lamination stacking. The permeability anisotropy of the CDW steel was determined from the Epstein tests, and the expected toroidal permeability computed using the methodology derived in section 10.2 to give a final response termed 'CDW Toroidal model'.

The core's B/H curve was experimentally determined to ensure assembly had not inadvertently introduced some error or deficiency and to validate the modelled toroidal permeability. Feedback stabilised, sinusoidal flux density excitation was possible up to 0.5 T. Higher flux density levels required direct induction from the mains supply up to a maximum of 1.05 T for the whole core, with levels from 1.1–1.4 T from a test of solely the 13 mm top packet due to power limitations. The comparator Cogent data curves were also compensated for toroidal permeability as described in section 10.2. All B/H curves used the mean core back length to compute the magnetic field strength H . The waveforms for flux density and especially current at higher fluxes were substantially non-sinusoidal, thus digital oscilloscope records were used to determine the crest factors to adjust rms measurements.

The results are plotted in Figure 9.9. It can be seen that the DAX8 stator core's measured B/H characteristic is very comparable to the CDW Toroidal model and Cogent comparator steel toroidal performance up to 0.6 T flux density, then the core's permeability reduces to well under the expected values at higher flux density. The reason for the reduction in the core's permeability is analysed in Chapter 10 and shown to be ferromagnetic saturation at the lamination segment joints, where the joint air gap causes the lamination flux density to double in the flanking laminations. The very small joint regions might be assumed to be negligible in the scale of the complete core. However it is seen that at core flux densities above 0.6 T the assembled core starts to suffer the reduction of electrical steel permeability that occurs above 1.2 T at the joints. It was shown that this phenomena is inevitable and normal (though rarely recorded), and not an indicator of any core construction or interlamination insulation fault.

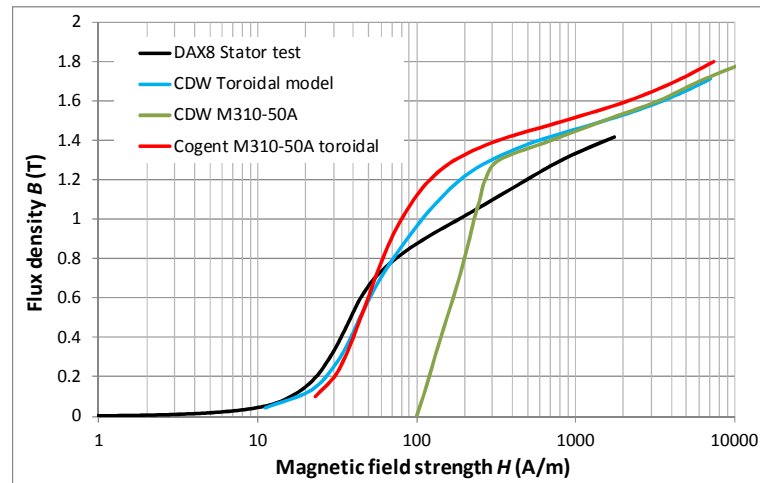


Figure 9.9 DAX8 B/H stator core test with CDW Toroidal model and Cogent M310-50A toroidally corrected steel.

9.5. Artificial fault application

In order to experimentally assess the impact of core faults, a number of surface fault sites were prepared around slots 10–11 as shown in Figure 9.10(a). The lamination edges were machined smooth to permit electrical contact, then dc electro-etched in the normal manner for core repairs [15] until all signs of fault due to machining burrs ceased ($Quad < 20$ mA). The prepared steel edges shown in Figure 9.10(b) were coated in a corrosion inhibitor, then temporarily degreased and lightly abraded clean for each test.

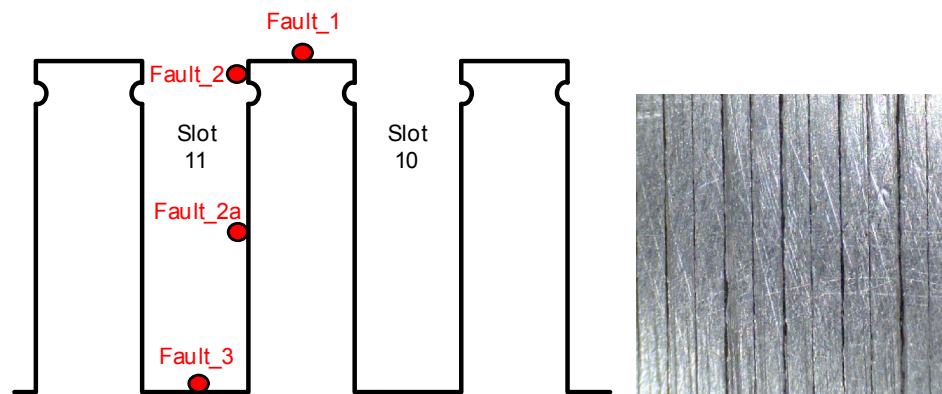


Figure 9.10 (a) Surface fault locations, (b) microscope image of etched fault surface

Screw tensioned application clamps and slot side wedges were fabricated to apply varying length and gauge Nichrome (NiCr) wires to the surface to simulate interlamination faults, illustrated in Figure 9.11(a) for Fault_1. NiCr wires have sufficient resistivity to develop rational fault currents (50–500 mA) for manageable wire sizes from 0.2–1.2 mm dia. The fault wire was retained by an adhesive rubber backing (to provide compliance such that contact is made to all laminations) on a fibre-glass pad shown in Figure 9.11(b), and contact made by tightening the clamp with pad against the prepared fault position.

Tests using a known rate spring washer showed the achieved fault application force was >400 N, more than sufficient to ensure the NiCr wire conforms to the test surface.



Figure 9.11 (a) Fault clamp for Fault_1, (b) fault wire application

9.6. DAX8 scaling factor to TCS core results

The smaller TCS core used in Ho's research [72] defined the geometry used in the FE models, requiring a scaling factor for DAX8 comparison. The DAX8 core yoke height and depth was used to determine the 4% *STV* value for the nominal service flux established in 9.1.3. This was then used to compute the axial test voltage field, and given equal fault wire resistivity, the ratio of these fields gave the scaling factor from TCS to DAX8 fault current signal results of 112.3%, as shown in Table 9.4.

	TCS	DAX8
Test core nominal service flux density	1.38 T	1.4 T
Test core <i>STV</i> for notional 4% flux density test voltage at 50 Hz	0.291 V	0.400 V
Core steel height (for <i>STV</i> loop)	76 mm	93 mm
Core yoke depth	309 mm	344 mm
Induced axial test voltage field (at 4% flux density)	3.829 V/m	4.301 V/m
Resistivity of 0.45 mm dia. NiCr wire	1.08 $\mu\Omega\text{m}$	1.08 $\mu\Omega\text{m}$
Scaling of fault current results from TCS \rightarrow DAX8		112.3%

Table 9.4 DAX8 to TCS scaling

To complete the proving of the DAX8 core and validate the above theoretical scaling factor, Ho's tests on surface faults were repeated. In this case the excitation flux was not feedback stabilised, so as to match any harmonics that would have occurred in Ho's tests (which used mains excitation). The tests were also conducted as Ho's tests using the flux as reference rather than excitation current, to eliminate the core loss phasor error ($\cos 19^\circ \approx 5\%$) described in section 3.5.

Tests on tooth tip, tip side, slot side and slot base were conducted with 10, 20 & 40 mm long faults on the 50 mm packet using the same 0.45 mm dia. NiCr wire gauge as used by Ho, at fault positions Fault_1–3, a total of 12 tests, recording peak values. Example Fault_1 scan results for 10 and 20 mm faults are shown in Figure 9.12.

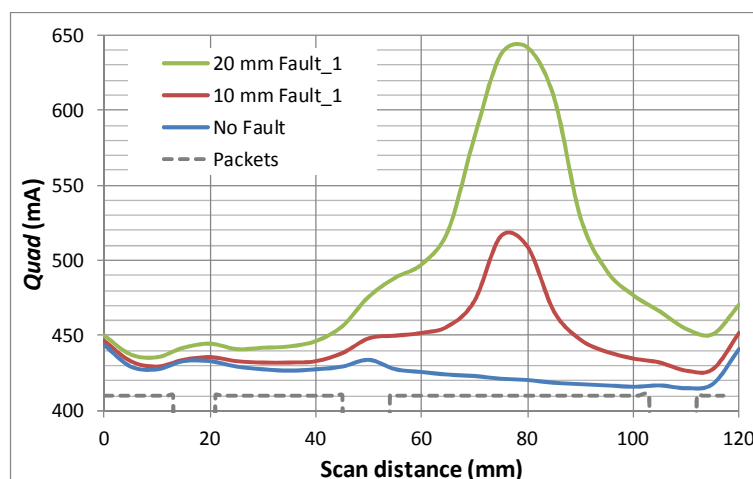


Figure 9.12 Scans of *Quad* values for *Fault_1* faults (top to base)

The maximum fault *Quad* current was determined from the difference between no-fault and fault tests for both sources. Ho's TCS no-fault and fault test results were accessed ('UoM2.dec' and 'UoM3.dec'), scaled 112.3%, and compared to the DAX8 results in Table 9.5.

Fault position	NiCr wire 0.45 mm dia.	Scaled TCS <i>Quad</i> (mA)	DAX8 <i>Quad</i> (mA)	DAX8 error
Tooth tip – <i>Fault_1</i>	10 mm	141	126	-10.2%
	20 mm	279	234	-16.1%
	40 mm	404	357	-11.6%
Tooth tip side – <i>Fault_2</i>	10 mm	123	127	3.7%
	20 mm	264	244	-7.7%
	40 mm	427	379	-11.2%
Slot mid side – <i>Fault_2a</i>	10 mm	74	87	16.8%
	20 mm	207	187	-9.5%
	40 mm	355	350	-1.6%
Slot base – <i>Fault_3</i>	10 mm	94	83	-10.9%
	20 mm	197	180	-8.6%
	40 mm	344	351	2.1%
DAX8 mean error				-5.4%
SD population error				9.1%
SD mean error				2.6%
95% confidence range of mean error				-0.2% >> -10.6%

Table 9.5 Test result of DAX8 – TCS comparison

From this test the results on the DAX8 core are on average 5.4% less than achieved on the TCS core after scaling. The standard deviation of the mean error is 2.6%, thus the actual mean error to 95% confidence is expected to lie between -0.2% and -10.6%, assuming a normal error distribution.

9.7. Discussion and summary

The conclusion of the construction and testing is that the DAX8 experimental stator core provides a fault-free and representative test bed for experimental comparison of stator

core faults originally modelled on the TCS core. The integrity of the core was proved with EMT and HFT surveys.

In the course of the construction and validation of the experimental stator core, a number of issues had to be resolved. Firstly the inability to achieve high clamping pressures required investigation of the effect of pressure on stacking factor (SF). The expected variance in the standardised EN60404-13 [234] SF measurement means that the measured SF = 0.96 would have a 95% confidence range of over 0.95–0.97, thus including the theoretical full lamination compression SF of 0.969, as well as the uninsulated steel requirement of just 0.97. This indicates that attempting higher precision is probably fruitless, that the SF achieved was representative of manufactured stator cores, and was thus acceptable at just 70 kPa core pressure.

A second complication was the problem in achieving a sinusoidal flux density caused by the very short core section. It was shown that the varying permeability can generate over 3% of 3rd harmonic flux content in a manner not comparable to field tests. Since the Chattock is frequency sensitive this would appear as a 9% Chattock signal, potentially causing measurement error. The problem was successfully resolved by feedback stabilised excitation which reduced the worst case flux harmonics to -60 dB.

An unexpected issue was the discovery of the substantial difference in the high flux density magnetic performance of the assembled stator core compared to its lamination material Epstein test results, with excitation levels reaching ~260% of that expected at 1.2 T. This was determined to be due to both anisotropy of the steel's permeability and ferromagnetic flux saturation at the lamination segment joints, which are investigated in Chapter 10. The effect is absent at EMT flux density levels.

The differing sizes of the experimental test stator core and the Ho models required investigation to ensure that the result scaling was reliable. The investigation resulted in a small extra scale mean error of -5.4%, a very reasonable match given the uncertainty with which surface applied faults make contact at very low contact voltages (<20 mV at each end of a 10 mm fault). Further the variance in the measurements indicates that this could just have occurred by chance at the 95% confidence level. Since the inaccuracy of the fault application and measurement process is also considered to be at least 5%, the -5.4% difference was not considered a reliable correction to apply.

Chapter 10. Lamination Joint Reluctance in Stator Cores

In validating the DAX8 experimental stator core, the high flux density excitation requirements were found to greatly exceed values expected from material parameters or published guides to electrical steels, machine design and test. To ensure that the DAX8 core was free of material or construction defect, the cause was investigated. It was established as being both lamination magnetic anisotropy and saturation in the region of the joints at service flux density levels. These phenomena were researched, and their net effect on the toroidal B/H response of a stator core predicted with FE models and validated by test at low and high flux densities. The work was published in 2014 [239].

10.1. The problem of lamination joint reluctance

Stator cores of large electrical machines use segmented laminations stacked in a variety of manners, with the half-overlap lamination joint illustrated in Figure 10.6 the most common. The large air gap reluctance at the lamination butt joints causes the flux to locally divert into the flanking laminations, where the now doubled flux density can reach magnetic saturation at service flux density levels. The increased magnetic field strength at the joints can be sufficient to make a large difference to the overall excitation requirement. Where the joint is more complex with third or even quarter-overlapped joints multiple flanking laminations share diverted flux and the saturation problem is less significant. This study considers the most common and worst case half-overlap joint, used in the DAX8 experimental core.

Magnetic anisotropy can conversely reduce the toroidal reluctance over that expected. Further the high excitation current crest factors caused by the joint magnetic saturation also reduces the total rms current required compared to that expected (assuming sinusoidal current) using peak values derived from B/H data. While long predicted, the impact of these factors on magnetic circuit design, and especially high flux stator core testing, remain apparently unrecognized in the normal guides to electrical steels and their application (e.g. Beckley [33]). Both phenomena were experienced in the validation study of the DAX8 experimental stator core described in section 9.4.3.

10.1.1. Literature research

The problem of lamination joint saturation is long known, with Bohle [240] writing in 1908 that the reluctance of overlapping lamination joints is ‘by no means a negligible quantity, especially for high flux densities’. While studying the effect of lamination joints on shaft voltages in 1924, Alger and Samson [241] showed that at core flux densities of 0.8 T each joint caused a 250 mm equivalent extension of the core circumference. A 1932 paper from Phear and Mallock [242] also showed that for Stalloy³⁴ as the core flux density passes 0.6 T the equivalent joint length rises rapidly, though the analysis was limited to half the saturation value. In 1947 Butler [243] extended Phear and Mallock’s work for tightly packed transformer core joints, and predicted large increases in the joint mpd at core flux density values above 50% of saturation.

The issue then appeared to fall dormant until 1976 when, while also studying shaft voltages, Stoll [244] suggested that at a core flux density of 1.3 T a 0.84 mm joint equates to ~1.3 m of normal core circumference. A 1980 IEE Discussion [245] by Howe, Jack and Bennett on unpublished work analysing axial fluxes reported ‘a large proportion of the circumferential reluctance is introduced at the joints’. This was followed by Jack and Mecrow in 1986 [246] similarly computing that segment joints added ~50% to the circumferential mpd in their study at ~1.0 T. Finally Nakata and Kawase in 1982 [247] studied the effect in transformer cores, predicting that a joint gap of 1.0 mm was equivalent reluctance to ~1200 mm of S30 silicon steel³⁵ at 1.4 T.

10.1.2. Design advice

While the research evidence for the development of high lamination joint reluctance at high flux densities is clear, this knowledge does not appear to have been transferred to any texts advising on stator design or test. Barr and Archibold [248] (§XII) simply compute the yoke magnetising mmf for segmented laminations from the basic B/H curve in their extensive 1913 treatise. Moullin [249] in 1955 (§III.ii.7) does note that flux diversion at joints will increase local magnetic fields, but assumes constant permeability thus the net effect is trivial. Even by 1980, Walker [43] (§6.1) just advises computation of a hydro-generator’s core yoke reluctance from the material data with an allowance only for stacking factor, as does Shima et al.[250] from Hitachi large machines R&D in 2003.

Other general books on machines and electrical steel from 1958 to 2002 (Say [251], Edwards [252] and Beckley [33]) are also silent. Very recently Boldea [253] (§7.6) in 2006

³⁴ 3-4% SiFe steel.

³⁵ Japanese specification comparable to M700-50A steel

and Pyrhonen et al.[254] (§3.4) in 2008 continue to ignore the effect of lamination joints and stacking factor. Both in fact propose reducing the net core yoke mpd in the magnetic circuit as flux densities rise, to accommodate the effect that the flux density is not uniformly high from pole centre to pole centre, and that the flux lines tend to crowd towards the shortest route between poles. A reduction factor down to 0.5 is proposed by Boldea, while Pyrhonen uses a similar factor that can fall to <0.2.

10.1.3. Test advice

Lamination joint reluctance may not be a substantial issue for normal machine field excitation since the stator core is not uniformly at full flux density, and the pole air gaps dominate the reluctance. However in the high flux test (HFT) the situation is reversed and the core is uniformly at full flux density with no air gap.

Despite this, IEEE Std 62.2 [48] simply instructs ‘use the manufacturer’s B/H curves’ to compute the excitation needed. Klemptner & Kerszenbaum [8] (§11.2.2) also propose use of the steel’s specification B/H curve (or the actual machine B/H curves if available, which is rare). To show the disparity, both above sources also give a typical B/H curve that the excitation may follow, as did the now obsolete IEEE Std 432 [47]. However their published typical magnetic field strength figures appear to be considered as rms in the associated texts, and in test advice by Kumar [255] from BHEL, Stols [256] from Eskom and Milano formerly from US Bureau of Reclamation [237]. These were thus converted to peak levels using measured crest factors (1.4 to 2.1) for flux density levels >0.6 T. It appears that these sources do not appreciate that in the EN10106 [211] and ASTM A677 [257] test standards the specified magnetic field strength is the ac peak value.

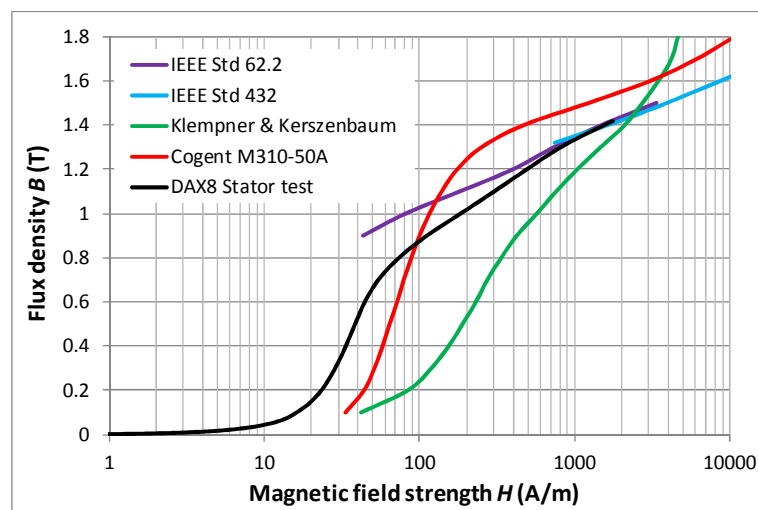


Figure 10.1 Typical and actual B/H curves for high flux tests

The three curves are shown in Figure 10.1 as conventional ac peak B/H values, compared to published data for Cogent M310-50A steel [183] as example, and the

measured B/H curve for the DAX8 test core. It can be seen that the Klemptner & Kerszenbaum and IEEE typical curves converge to the same ~ 2000 A/m magnetic field strength as the DAX8 test result for the typical service flux density level of 1.4 T. They are however very different at differing flux density levels. Interestingly in 1952, Tomlinson [20] proposed 300 A-t/ft (assumed rms) as the nominal excitation for turbo-generators, equating (assuming crest factor of 2) to the same ~ 2000 A/m magnetic field strength. The only other published HFT standard RD 34.45-51.300-97 [50] is silent on the excitation requirement.

10.2. Electrical steel anisotropy and the Toroidal model

The anisotropy of non-grain oriented electrical steel is normally only specified for loss at 1.5 T, where EN10106 requires $\leq 14\%$ for M310-50A, a value matched by CDW [182], whereas Cogent quotes $\leq 10\%$ [258]. While TK [181] and Cogent data sheets also offer separate B/H curves for the rolling and transverse directions, this anisotropy is not a controlled parameter. Epstein Frame tests as described in section 9.4.2 were completed of the CDW lamination steel in both the rolling direction (RD) and transverse direction (TD), in addition to the normal 50% RD : 50% TD mix to measure its magnetic anisotropy. If the permeability anisotropy K_A in equation (10.1) is measured in the same manner as the loss anisotropy, where μ_{RD} and μ_{TD} are the RD and TD axis permeabilities, then

$$K_A = \frac{(\mu_{RD} - \mu_{TD})}{(\mu_{RD} + \mu_{TD})}. \quad (10.1)$$

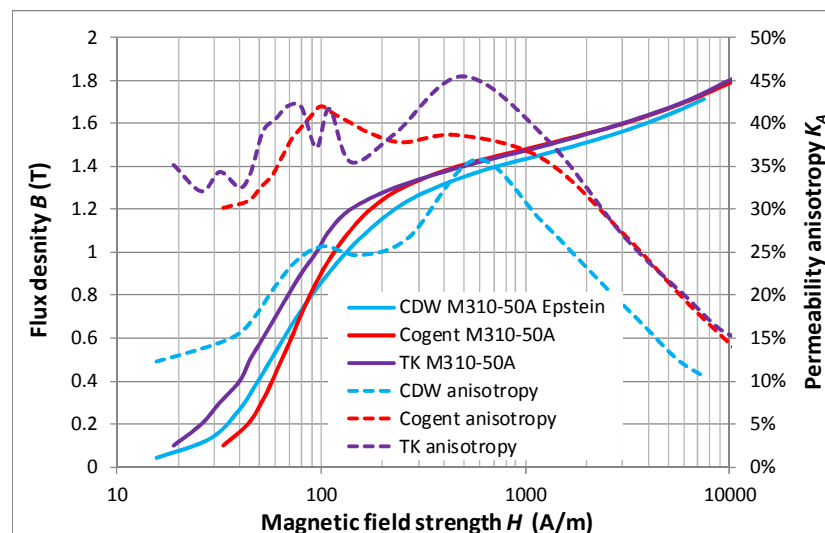


Figure 10.2 Variation of flux density and permeability anisotropy K_A with magnetic field

Figure 10.2 shows the variation of K_A for Cogent and TK M310-50A steels with variation in magnetic field (B and H) and also the Epstein measured results for the CDW

M310-50A steel. It can be seen that permeability anisotropy can vary widely, considerably greater than might be expected from the 1.5 T loss anisotropy. Permeability anisotropy will affect the net permeability of laminations where the toroidal flux flows predominantly in the RD direction. Electrical steel magnetic anisotropy is not normally a regular circular function [259]. However since the intermediate values are not known, a simple vector RD/TD resolution was used assuming uniform circumferential flux density distribution.

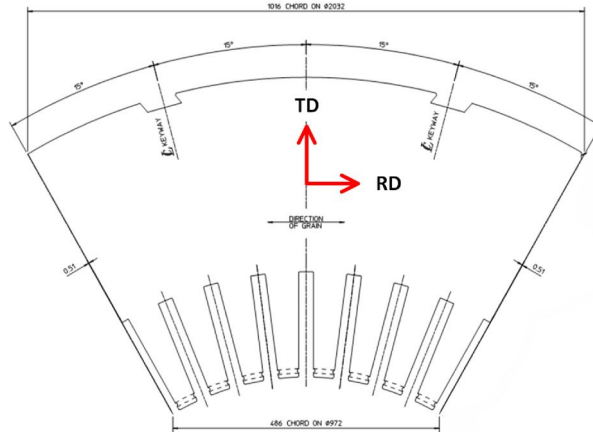


Figure 10.3 Rolling (RD) and transverse (TD) lamination directions

The lamination segment has its RD normal to the radial midline as shown in Figure 10.3, thus the segment can be modelled as a single $\pi/6$ half-section, where the normal Epstein (50:50 TD:RD) measured relative permeability is μ_r . By integrating the magnetic field strength for constant flux density along the mean flux path, the net toroidal relative permeability μ_{net} for the magnetic axes shown in Figure 10.3 is derived in Appendix G, and given by

$$\frac{1}{\mu_{net}} = \frac{1}{\mu_r} \left[1 - \frac{nK_A \sin(2\pi/n)}{2\pi} \right]. \quad (10.2)$$

For the CDW M310-50A steel, over flux densities of 0.1–1.5 T the measured mean value of $K_A = 22\%$, thus equation (10.2) evaluates $\mu_{net} = 1.23 \mu_r$. The measured CDW steel permeability from the Epstein tests was adjusted according to equation (10.2) to compute the CDW Toroidal Model predicted stator B/H curve. Cogent and TK data both gave mean values for K_A of 31% ($\mu_{net} = 1.45 \mu_r$), indicating that significant anisotropy is normal.

These show the net toroidal reluctance is 19% (CDW) to 31% (Cogent/TK) lower than expected from published data in a 6 segment core, since published data is normally only for 50:50 material average μ_r . In a 12–18 segment core as might be used in a much larger turbo-generator, the net toroidal reluctance would be 22–37% lower than expected from published data.

10.3. Development of a saturated steel B/H model

The 50 Hz B/H test curve of the DAX8 stator core above 0.6 T flux density was found to deviate substantially from the CDW Toroidal model predicted by the Epstein measurements above. Figure 9.9 shows the magnetic field strength required to be ~260% of that modelled at 1.2 T. It was expected that saturation at the lamination joints caused the increased reluctance. It was also noted that the predicted performance of the CDW Toroidal model steel in Figure 9.9 is fairly comparable to Cogent M310-50A steel, toroidally compensated for the specified anisotropy.

As expected, sinusoidal flux excitation caused rising excitation current crest factors (peak/rms) with flux density, from 1.4 at 0.6 T, to 2.0 at 1.2 T, and 2.2 at 1.4T. The high crest factor is evident from the excitation current and flux density waveforms at 1.2 T shown in Figure 10.4 for the DAX8 assembled core.

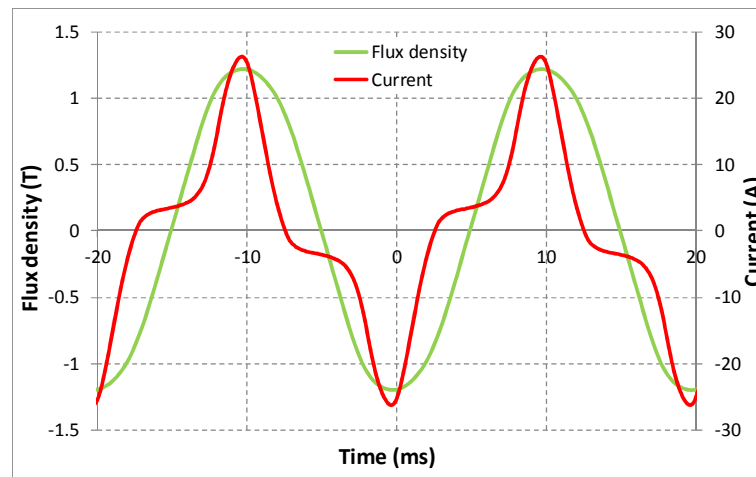


Figure 10.4 Flux density and excitation current waveforms at 1.2 T for DAX8 core

The root cause of the greatly increased toroidal reluctance at high flux densities was investigated using a 2D FE model [204] of the lamination joint, to examine the magnetic fields in the lamination joint. However no manufacturers' B/H data exists above flux densities of 1.8 T, which appears to be only determinable by empirical means. Umenei et al. [260] in 2011 studied three alternate extrapolation techniques that attempt to improve on simple linear extrapolation of the final differential permeability, and recommended both a simplified 'Law of Approach to Saturation' and 'Exponential Law Extrapolation'. Tang et al. [261] drew attention to the problem again in 2012, but only suggested a modified Epstein tester³⁶ to try to reach 1.9–2.0 T.

³⁶ The standard method of measurement of laminated electrical steel, the Epstein test [238] has a maximum magnetic field strength of ~10,000 A/m (~1.8 T in M310-50A steel) due to current limitations.

‘Technical saturation’ ([216] §6.2.5) is seen to occur in comparable electrical steels at 2.0 T (M300-35A [262]) and 1.98 T (M22 [228]) (§3.5.3), however the transition into the saturated region is unspecified by the steel manufacturers. Despite this, electrical steels are frequently driven into saturation in the teeth of both ac and dc electrical machines [253] (§7.6) with apparently little knowledge of their performance in this region. There is a similar problem with modelling large transformers, where the core can be saturated due to transients, geo-magnetic sources or quadrature boosters³⁷.

Both Umenei et al’s recommended extrapolations are comparable to the original Fröhlich-Kennelley equation for anhysteretic approach to saturation [216] (§5.1.5), if this relation is converted to a power series as shown by Bozorth [217] (§11)³⁸. In consequence a B/H model for steel approaching and in saturation was developed using the Fröhlich-Kennelley relation. This method also improves on the method of Stoll [244] which only used the Fröhlich-Kennelley relationship between the maximum measured values and saturation, setting susceptibility $\chi = 0$ above this value.

From Fröhlich-Kennelley, the ferromagnetic magnetisation³⁹ M approaching saturation is given from the magnetic field strength H with α and β parameters by

$$M = \frac{\alpha H}{1 + \beta H}, \quad (10.3)$$

where magnetisation and flux density are related by

$$B = \mu_0(H + M). \quad (10.4)$$

Hence saturation magnetisation M_S and saturation polarisation in the steel J_S are given by

$$M_S = \lim_{H \rightarrow \infty} M = \frac{\alpha}{\beta} \quad \text{thus} \quad J_S = \frac{\alpha}{\beta} \mu_0. \quad (10.5)$$

Substituting equation (10.3) and (10.4) in (10.5) gives

$$\beta = \frac{B - \mu_0 H}{\mu_0 H^2 + \mu_0 J_S H - BH}. \quad (10.6)$$

The steel’s magnetisation is proportional to the susceptibility χ and field H , hence

$$M = \chi H \quad \text{thus} \quad B = \mu_0(1 + \chi)H. \quad (10.7)$$

Equations (10.3) and (10.7) can be combined to give the value of H for total flux density B in

$$\mu_0 \beta H^2 + (\mu_0 + \mu_0 \alpha - \beta B)H - B = 0. \quad (10.8)$$

³⁷ Phase shifting transformers used to manage power flow.

³⁸ This also explains their very similar results.

³⁹ Sommerfeld convention

The α and β parameters were computed from steel saturation J_S and the B/H Epstein values at 1.7 T, after toroidal correction for anisotropy ($\alpha = 1.363 \times 10^{+3}$, $\beta = 8.566 \times 10^{-4}$). From this the positive roots of equation (10.8) gave the Fröhlich-Kennelley curve in Figure 10.5.

Differential susceptibility χ' was used to give a clearer view of the development of saturation than relative permeability. This was computed discretely in 0.1 T steps of B up to 2.8 T, using the relationship in equation (10.9) derived from equation (10.4).

$$\chi' = \frac{\delta M}{\delta H} = \frac{\delta B}{\mu_0 \delta H} - 1. \quad (10.9)$$

This result was combined with the CDW Toroidal model and Cogent M310-50A toroidally compensated data, plus M22 [204] steel⁴⁰ data, to extrapolate a best estimate differential susceptibility curve from 1.7–2.8 T for the Toroidal Model steel, shown in Figure 10.5(a). This gave the final CDW Toroidal model B/H relationship in Figure 10.5(b).

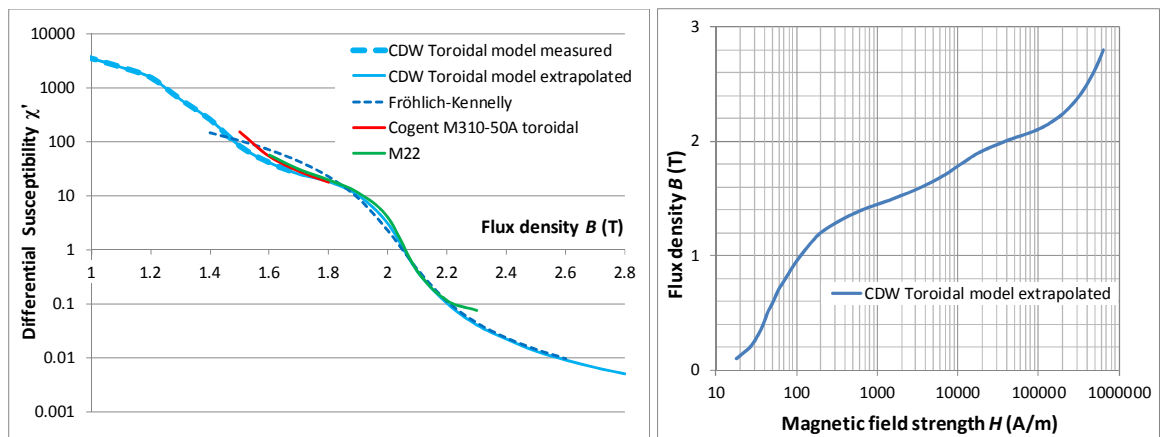


Figure 10.5 (a) Extrapolated differential susceptibility to 2.8 T, (b) resultant B/H curve

10.4. Lamination joint magnetostatic FE analysis

The model is that of the DAX8 laminated core viewed on the edge of the laminations as illustrated in Figure 6.3, with as-designed 1.02 mm butt joint gaps, 0.5 mm thick laminations and 442 mm long mean flux path between joints. From symmetry only one half of the width between the joints needs to be modelled, against half of the thickness of the joint and flanking laminations. The FE modelled region is shown shaded on the stacked laminations with the expected flux streamlines in Figure 10.6. The study was magnetostatic since eddy currents were not expected to be sufficient to impact on the large magnetic fields developed, and to ensure the correct B/H relationship is enforced⁴¹.

⁴⁰ FEMM library data from 1.7–2.3 T.

⁴¹ FEMM time-harmonic analysis uses an approximate linearisation of the B/H relationship for the field solutions and assumes sinusoidal H .

The SF of the DAX8 core was determined in section 9.1.2 to be >0.96 , indicating a mean interlamination insulation/air gap of notionally 0.017 mm. This was widened to 0.05 mm to allow sufficient meshing in the gap, with the relative permeability of this region increased to 2.9 to maintain the same reluctance. The air in the joint region was maintained at a relative permeability of 1.

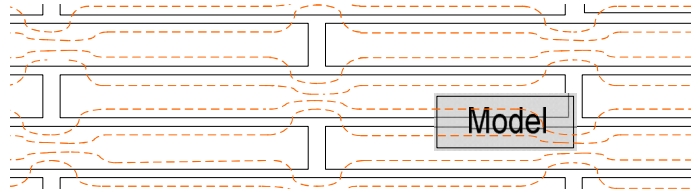


Figure 10.6 Lamination joints with flux streamlines (red) and model region (not to scale)

The required total flux and prevention of flux leakage in the Z direction was enforced by uniform Dirichlet boundaries along BC & AD and Neumann boundaries on AB & DC in Figure 10.7. The B/H curve for the CDW Toroidal model steel (measured and extrapolated peak values) determined in section 10.3 was used. There was no permeability adjustment for stacking factor, since here the interlamination air gap was explicitly modelled. The FE magnetostatic model⁴² flux density (by colour) and flux streamlines plot at a mean flux density of 1.2 T, is shown in Figure 10.7. This shows the flanking lamination at the joint saturated at a flux density of 2.2 T with now a significant flux density of 0.2 T in the joint’s air path. The FE model B/H values were plotted against the material’s Toroidal model characteristics and the experimental stator core test result in Figure 10.8, showing a close alignment with experimental values.

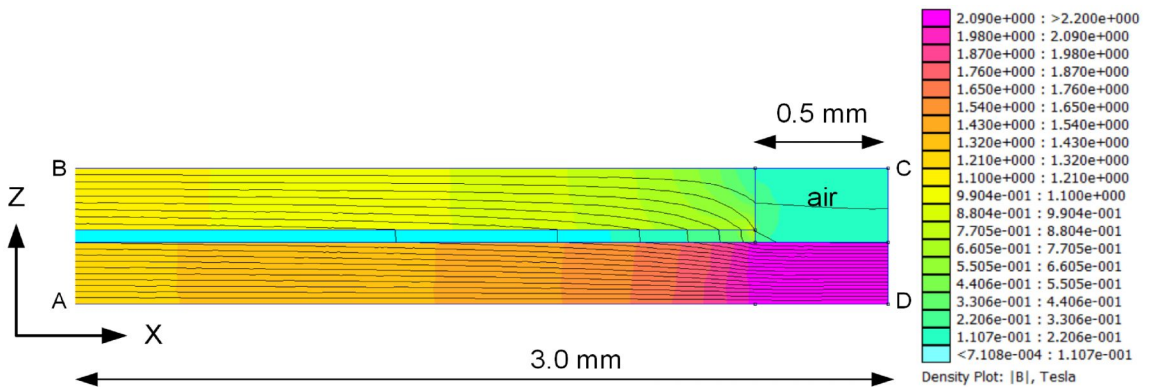


Figure 10.7 Lamination joint flux density FE model at 1.2 T stator flux density

The modelled effect on stator test excitation is shown in Figure 10.9, where the total excitation mmf increase of the FE modelled lamination 1.0 mm joints reaches a peak at 1.2 T, increasing by 199% over the core modelled without joints. This is compared with test results where the measured DAX8 stator excitation mmf is compared to that predicted

⁴² The full model was 221 mm long with 40,172 nodes. Only the last 3 mm is shown where the principal flux diversion occurs.

from the CDW Toroidal Model steel data without joints and reached a peak of 193% at 1.2 T. Both were normalised for equal average excitation mmf at <0.5 T, such that the increase would solely reflect the influence of the joints. The test results were limited to 1.4 T by the available power.

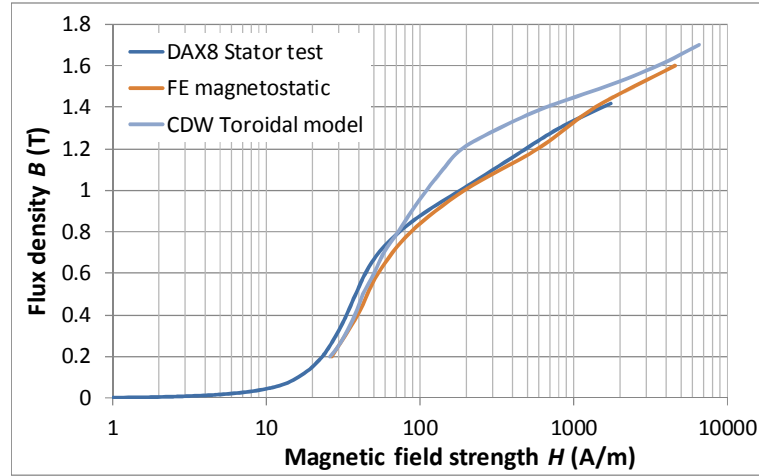


Figure 10.8 FE magnetostatic model B/H curve and test results

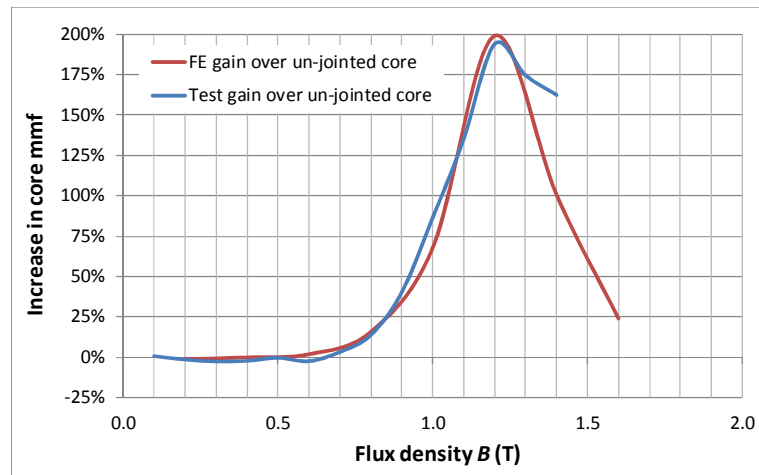


Figure 10.9 DAX8 core excitation increase due to lamination joints.

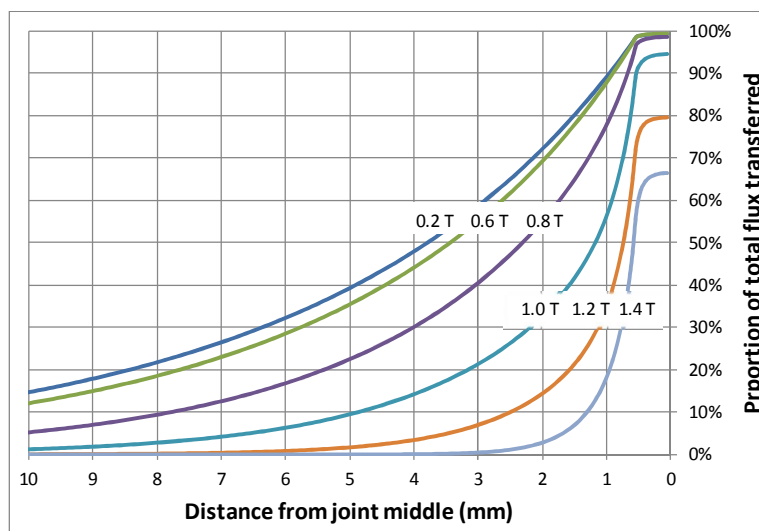


Figure 10.10 Proportion of total lamination flux transferred to flanking lamination with increasing flux density.

The flux transfer between laminations was also examined in the region of the joint, and the cumulative proportion transferred with distance from joint plotted in Figure 10.10. It can be seen that the increasing reluctance of the flanking lamination as it saturates, causes the flux transfer to be concentrated ever closer to the joint, such that by 1.4 T, ~90% of the flux that actually transfers does so in the final 1 mm before the joint. This concentration effect was also noted by Stoll [263].

10.5. Lamination joint time-harmonic FE model and experimental study

The purpose of this investigation is to verify that the lamination joints are the sole contributor to the increased core reluctance, by confirming that the elevated mpd only occurs every 4 stator slots. (The 12 joint regions occur mid-slot.) Test results were recorded of the ac mpd across each slot at a low 0.56 T and higher 1.06 T flux density level with a Chattock potentiometer. The 1.06 T flux density waveform was distorted, being somewhat ‘flat-topped’, with computed fundamental component of 1.13 T. The measurements were compared with the FE model using a time-harmonic 50 Hz analysis at the same 1.13 T flux density. The mpd was computed for all slots by integration of H along the mean flux core yoke path for the length of one tooth pitch (127 mm).

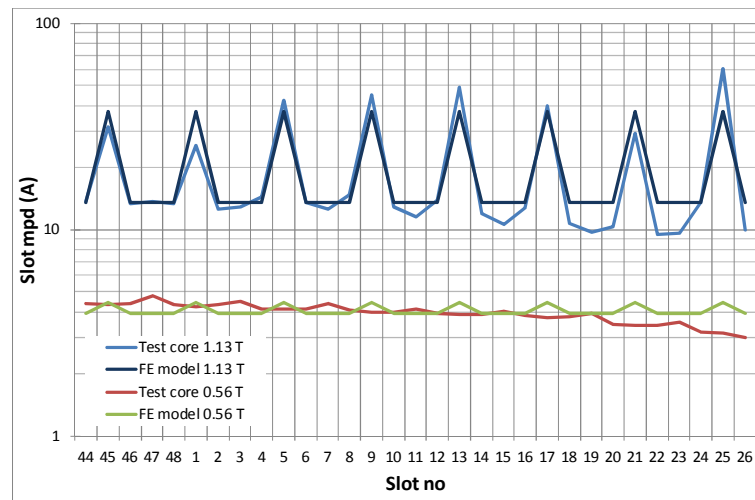


Figure 10.11 Slot mpd of test and FE models

The FE model had to use a linearised permeability for the harmonic model, which did not perfectly match its performance in the test core. This was accommodated by scaling the results such that the total FE excitation mmf matched the measured value. It can be seen in Figure 10.11 that the model provides a fair prediction of the high slot mpd expected at the joint slots when joint core saturation is occurring, with no unexpected rise elsewhere. The drift in measurements at slots >22 was believed to be due to excitation winding proximity, which was in the region of slots 28–40.

10.6. Discussion and review of test and manufacturing impacts

The test standards and related advice give typical HFT induction data that is very similar at 1.4 T flux density. Given that this is also matched by the DAX8 results, this is assumed to be from the practical experience of the authors, and is a surprisingly close agreement given the wide variety of stator core designs and materials. However their poor match at lower flux density levels, and universal recommendations to use unadjusted steel specification data, reduces confidence in their authority. Further, in the above analysis, it was observed that all five test authorities mistakenly interpret the H field from steel B/H data curves as the excitation ‘current’ per metre i.e. rms value rather than peak.

Although lamination joint reluctance has appeared relevant to researchers considering shaft voltages and detail lamination flux distributions, this knowledge appears unrecognised by the design and test communities. The phenomenon is probably of low importance for electrical machine design where the pole air gap dominates the magnetic circuit reluctance. However when inducing high flux density levels for stator testing, the magnetic path is solely toroidal and considerably affected. Without allowance for lamination joint saturation, permeability anisotropy, and magnetic field strength crest factors, the estimated stator core excitation current may be substantially in error.

The HFT use of slightly under full flux density is shown as common in section 2.2. Thus when estimating the required excitation from electrical steel B/H data (and correctly interpreting H as peak magnetic field strength), the rms excitation at worst case of ~ 1.2 T may be $\sim 200\%$ greater than expected due to joint reluctance, but over estimated by typically 25% due to anisotropy and by 1.4 due to a current crest factor of 2 vs 1.4. The toroidal reduction of 25% from steel anisotropy only benefits the unsaturated core, not the saturated joints. Thus the total rms excitation percentage increase compared to assuming basic B/H values may be typically computed from the net impact of the two ratios affecting the core’s reluctance times the crest factor impact

$$((100\% - 25\%) + 200\%) \times 1.4 / 2.0 = 193\% \quad (10.10)$$

This value will vary with anisotropy and especially the geometry and number of lamination joints. However if this 93% increase is not recognised, inadequate excitation power supply may be provided for the test, leading to under-testing if thermal scaling for reduced flux density is not applied.

Another issue is that the prescription of peak flux density levels in standards may encourage measurement of core peak flux density levels, however the concern is induced voltage heating in a resistive fault. Thus to compensate for any flux waveform distortion,

the flux sense coil signal should be measured with an rms-measuring instrument (as is common), and which will permit more reliable scaling of the thermal signal.

It can also be seen that the 0.56 T flux density test shows a small but consistent mpd decrease at the joints rather than the small increase which would be expected, and which the FE model also shows. This effect has also been seen at lower flux density levels and in other cores, but is so far unexplained.

The core reluctance is traditionally considered unaffected by the lamination butt joint spacing, on the assumption that all the flux will have switched to the flanking laminations before the joint, thus there is no flux crossing the air gap. However at service flux density levels the flanking laminations are in saturation for just over the width of the joint, thus the joint width does affect the reluctance. This has potential implications for manufacturing, in maintaining the gaps both small and uniform in the stacking, and also uniform circumferentially to minimise shaft voltage development⁴³.

10.7. Summary

At the service flux density levels in stator cores, magnetic saturation occurs at the half-overlap lamination joints. This causes the overall toroidal reluctance to rise substantially, approaching 200% above that expected from the steel B/H data. It has also been conversely shown that the natural anisotropy of even non-oriented electrical steel can modestly reduce the unsaturated toroidal permeability by 19–31% over that expected, while rising crest factors due to magnetic saturation reduce the net rms excitation mmf.

The DAX8 overall B/H curve was predicted using Epstein Frame measured material data, a new model of the saturation performance and FE modelled joints. This was shown to match the measured DAX8 stator very closely. It also closely matched the 199% test increase in total mmf over measured material parameters at 1.2 T, validating the extrapolated prediction from Stoll [244] of 180% increase for an 1.0 mm joint at 1.3 T. An experimental study of the DAX8 stator core magnetic fields confirmed the modelled prediction that the saturation in the joint regions is the source of the reluctance rise.

While the effect of lamination joints is long predicted by researchers, the impact on magnetic circuit design and especially high flux testing remains apparently unrecognized in the industry. The impact on a high flux test is to require typically 93% more excitation current than expected, with the potential risk that if it is not available, the core will be under-tested since thermal scaling for reduced flux density is not prescribed.

⁴³ Due to the development of non-symmetrical, non-rotating magnetic fields. This was studied extensively by Alger and Samson [241]

Chapter 11. Experimental Verification of Buried Fault FE Models

While reasonable confidence has been developed by researchers of the EL CID detection sensitivity of faults on the bore surface, this has not extended to faults buried in the stator teeth or core yoke (buried faults). Ho developed 3D FE models of both surface and buried core faults, however he only progressed to verification of the surface faults. Construction of the DAX8 stator core provided the means to also verify the buried faults, by developing methods to artificially apply calibrated buried faults.

The study shows that the original 3D FE model's omission of packet air gaps, imperfect modelling of fault current, circumferential interfering images, as well as the intrusion of the test fault, all affected the modelled fault magnetic potentials. To quantify and compensate for these effects, further FE models were constructed to finally validate the 3D FE model results.

11.1. The problem of buried faults

While the majority of accidental core faults occur on the core surface, the aging deteriorations discussed in section 1.2 can cause many faults to occur within the core teeth or yoke ('buried'). In consequence the fault's surrounding steel causes the surface mpd detected by the Chattock sensor to be considerably reduced. Whilst some 2D FE modelling has been completed on buried faults (e.g. [97, 158, 162, 164]), this is expected [72] to be substantially inaccurate for short faults. No reliable experimental work is reported on buried faults, the sole study from EPRI [57] failed to make consistent (or any) contact on the buried faults and had no means of calibrating them. In consequence there is no dependable EMT means of quantifying the threat from a detected buried core fault.

Ho [72] developed 3D FE models of a range of stator core faults both on the core surfaces and buried. However he only progressed to verification of the surface faults on an experimental core, the 'TCS' core, based on a Brush DAX7 [232] stator that is no longer available. In consequence a new similar DAX8 core was constructed, described in Chapter 9, and the scaling factor between these two cores established. Calibrated buried faults could then be applied and their detected signals compared to those predicted by the 3D FE model, to verify the modelled detection sensitivity. Since the models omitted the conventional packet air gaps included in the DAX8 stator, further research was needed to

investigate the effect of the air gaps, as well as the effect of the experimental buried fault intrusions, to validate the conclusions.

11.2. Fault position and application

The DAX8 test core had the parameters given in Table 9.3. Unfortunately Ho did not document the precise positions of the 3D FE modelled buried faults (Fault_4, Fault_5, Fault_6 & Fault_7), either in the thesis or the retained files. In consequence the positions had to be estimated from the image shown in Figure 11.1. The three surface faults are also identified for reference. Fault_7 was demonstrated by Ho to be too close to the core rear to generate any detectable signal, so was omitted from the study.

Since the DAX8 core yoke is ~11% deeper than the TCS core, the results could not be directly compared without compensation. It was concluded that since the radial depth is considered the dominant factor for fault signal attenuation, the same yoke depth as the TCS fault was used for the two core yoke faults (Fault_4 & Fault_6). The results were then compensated for the higher flux coupled into the fault, the electromagnetic effect of the fault's hole, and geometric scaling of tooth root pitch to subtended fault magnetic field for direct comparison to Ho's results.

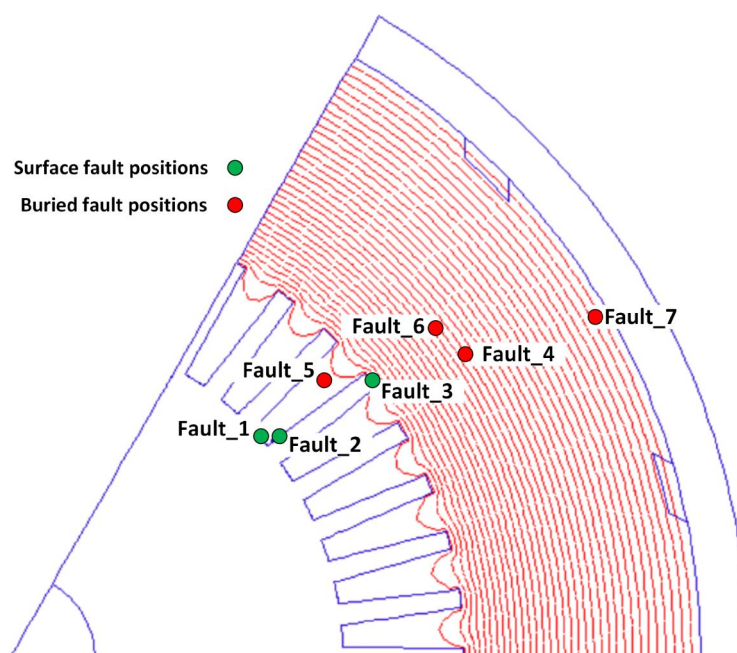


Figure 11.1 FE model of surface and buried faults (from [72] Fig. 6.2)

The tooth fault (Fault_5) was set the same radial proportion down the tooth from the tooth tip as modelled, since this should maintain the same proportion of magnetic field strength from the fault as that modelled. The resultant depths and proportions of depth are given in Table 11.1.

Label	Position	Depth in 3D FE model (TCS)	Depth in DAX8
Fault_4	Under tooth	116 mm from slot base (38%)	116 mm from slot base (34%)
Fault_5	Mid tooth	103 mm from tooth tip (67%)	125 mm from tooth tip (67%)
Fault_6	Under slot	107 mm from slot base (35%)	107 mm from slot base (31%)

Table 11.1 Buried fault positions in Ho's FE model and DAX8

Ho modelled 10, 20 and 40 mm long faults on the TCS core at buried fault positions Fault_5, Fault_6, & Fault_7. The original test results were accessed and the Imaginary (*Quad*) current that had been used for Ho's figures 7.25–7.27 retrieved. The output files that contained the data, listed in Table 11.2, recorded the Real and Imaginary mpd across several tooth pairs⁴⁴. Due to the close proximity of the modelled faults (with Fault_5 in tooth 19, Fault_6 under the slot of toothpair 19/20 and Fault_4 under tooth 20), it was concluded that toothpair 19/20 was an appropriate result source for all three of them.

Fault \ Length	10 mm	20 mm	40 mm
Fault_4 (under-tooth)	Job 13 Toothpair 19/20	Job 14 Toothpair 19/20	Job 15 Toothpair 19/20
Fault_5 (mid-tooth)	Job 17 Toothpair 19/20	Job 18 Toothpair 19/20	Job 19 Toothpair 19/20
Fault_6 (under-slot)	Job 21 Toothpair 19/20	Job 22 Toothpair 19/20	Job 23 Toothpair 19/20

Table 11.2 FE records for buried faults

11.3. Design and FE modelling of buried fault test sites

The only practical means of temporarily applying a fault within the body of an assembled stator core is to bore a hole, then apply the fault within the hole by pressing a conductor against the bare lamination edges. However a hole interferes with the electromagnetic field and fault current paths in the region, depending both on its size and if on the radially internal (front) or external (rear) side of the fault. There is thus a trade-off between ease and reliability of application of the fault (larger diameter hole) and minimising disturbance (smaller hole). To study the effect of these issues, a FEMM [204] FE model was developed of the DAX8 core, and varying sized holes placed either to the front or rear of the fault positions to determine the impact on the measured mpd. This model is of course 2D, whereas the problem and the results being verified are 3D. However the hole is inevitably the full core axial length, hence in effect 2D. Thus it was considered this model would provide a sufficient indication of the scale of any effect.

⁴⁴ On the TCS core, the teeth were identified, whereas on the DAX8 core the more normal convention of numbering the slots was followed.

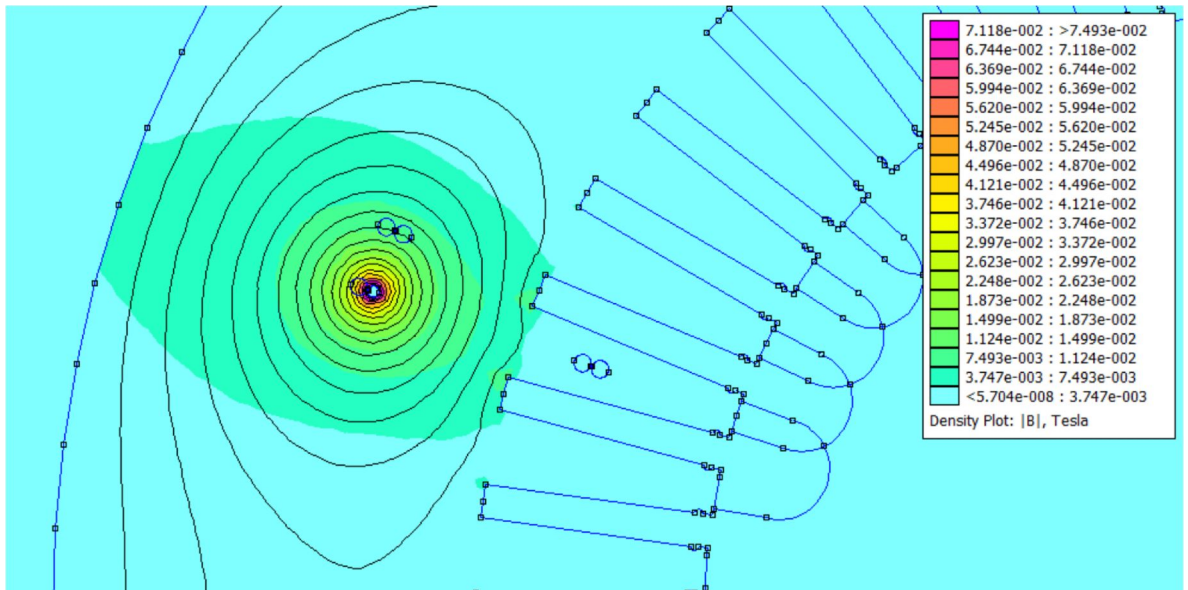


Figure 11.2 FE Model of three buried faults, with Fault_4 active

The FE model applied a current of 1 A in the fault, then measured the developed mpd across the teeth for the several slots near the fault from a notional Chattock placed across the teeth. This is shown in Figure 11.2 with Fault_4 active. The results indicated that there was <1% difference in measured mpd for a hole in front of the fault compared to at the rear. There was also a reduction from 6.1% to 4.3% of increased detected mpd for a reduction in hole size from 14 to 9 mm for a hole in front of the fault. It was thus decided that a 9 mm hole would be preferable if possible, and be towards the bore (front), since this would mean the current flow from the fault to the keybars would be unaffected by the hole (a problem not possible to model in the 2D FE model). The fault sites are Fault_4 (under-tooth), Fault_5 (mid-tooth) and Fault_6 (under-slot) and shown in their positions on the DAX8 core in Figure 11.3. Slot 45 was scanned to assess the EMT signals detected for Fault_4 & Fault_6, and slot 43 for Fault_5.

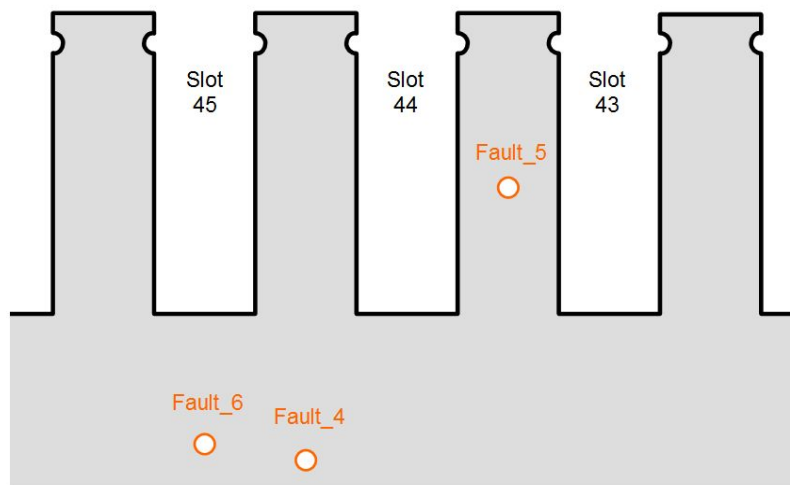


Figure 11.3 Buried fault actual DAX8 locations

Test fault sites were prepared inside 9 mm holes bored through the core in the three positions, and electro-etched fault-free⁴⁵ in the same manner as the surface faults in Chapter 9.5. The NiCr resistance wire to simulate the fault (with contact test wires for current measurement discussed in section 11.6), was supported on an adhesive rubber pad on the side of a bifurcated 8 mm Delrin rod shown in Figure 11.4. This was expanded in the 9 mm hole with a 2 mm stainless steel blade to pressurise the contact between wire and internal laminations. The faults were all applied centrally in the 50 mm packet.

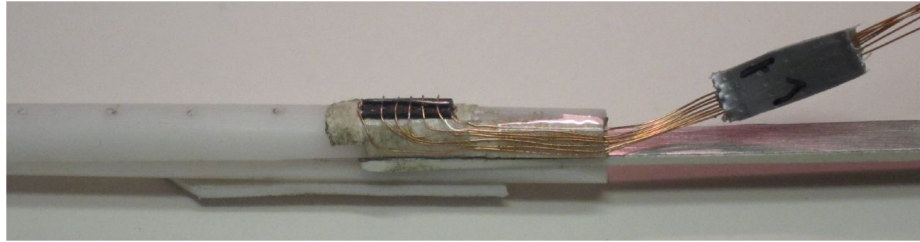


Figure 11.4 Buried fault test jig

11.4. Scaling between 3D FE model and DAX8 core

The depth in the core yoke of Fault_4 and Fault_6 means that not all the excitation flux couples with the fault circuit, nor is this proportion radially linear due to the core reluctance increasing radially and thus the flux density reducing as the flux path lengthens. A 2D FE axial model of the DAX8 core with toroidal flux induced by a 1 A/slot central excitation current is shown in Figure 11.5(a). The flux density variation with radius in Figure 11.5(b) shows there will be lower excitation flux coupled in the fault than expected from linear scaling assuming uniform flux density. The mean flux radius was found to be 31 mm less than the geometric mean.

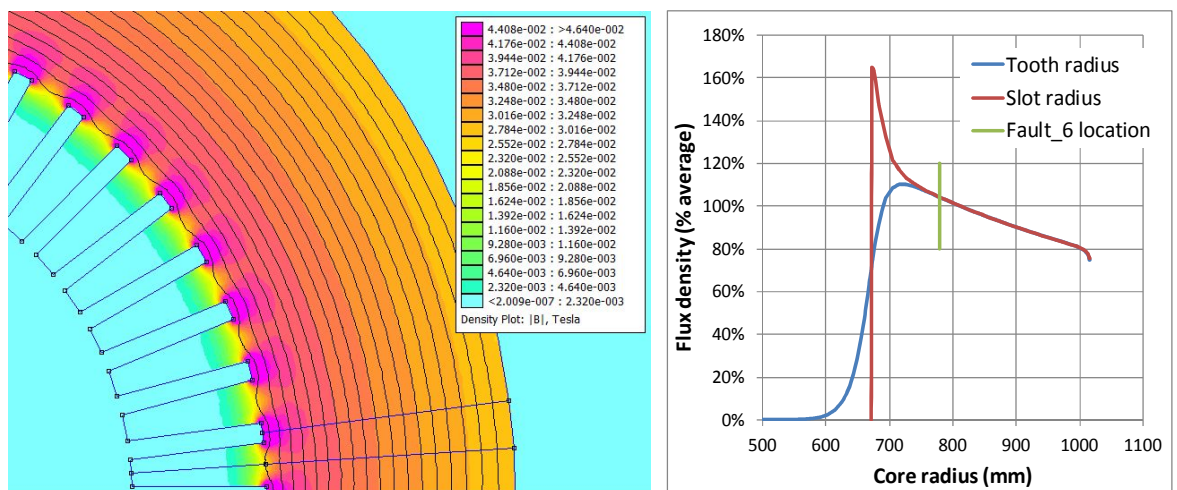


Figure 11.5 (a) Flux density distribution in DAX8 yoke, (b) flux density variation with radius

⁴⁵ Fault sites were initially electromagnetically tested until all electromagnetic change from the etching ceased (<5 mA). However due to the high attenuation from buried fault to core bore surface, this is not a reliable measure of fault absence, so the final success of the etching was tested by scans down the holes with thermocouples during a 1.04 T high flux test. A final maximum 1.2 °C local temperature rise was recorded.

This distribution was assumed to have similarly occurred in the 3D FE model (given the reducing number of flux streamline contours with radius in Figure 11.1), and was used to scale the DAX8 results to equal the coupled fault flux in the 3D FE (TCS) model.

The readings from Fault_4 and Fault_6 were also compensated for the change in tooth pitch geometry, due to greater proportion of the magnetic field strength presented to the two teeth on the DAX8 core, across which the Chattock measures. This was computed in proportion to the tooth root pitch change in subtended angle λ shown in Figure 11.6. No tooth pitch correction was made for Fault_5.

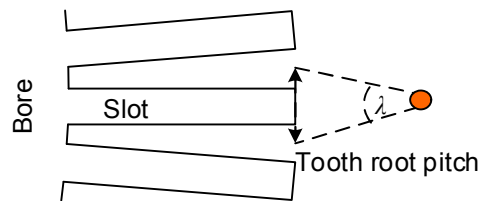


Figure 11.6 Detected signal dependence on slot root pitch

The 3D FE modelled faults assumed the resistivity of 0.45 mm dia. NiCr wire which were maintained for the DAX8 tests. Table 11.3 gives the total proportional coupled flux, and resultant scales for the detected *Quad* signals to equate to the 3D FE core geometry and flux density, allowing comparison to Ho's results.

	3D FE (TCS)	DAX8
Mean test flux density	0.0565 T	0.0563 T
Test axial voltage field	3.829 V/m	4.301 V/m
Resistivity of 0.45 mm dia. NiCr wire	1.09 $\mu\Omega\text{m}$	1.08 $\mu\Omega\text{m}$
Fault_4 coupled flux proportion of total	55.5%	59.9%
Fault_5 coupled flux proportion of total	100%	100%
Fault_6 coupled flux proportion of total	58.4%	62.6%
Fault_4 & 6 tooth pitch angle	36.6°	41.5°
Net <i>Quad</i> scaling of Fault_4, DAX8 to 3D FE		71.9%
Net <i>Quad</i> scaling of Fault_5, DAX8 to 3D FE		88.2%
<i>Quad</i> scaling of Fault_6, DAX8 scaled to 3D FE		72.7%
3D FE images correction scaling	111.9%	

Table 11.3 DAX8 to 3D FE compensations for equal core flux density

Further compensation was needed due to images inevitable in the 3D FE study. The FE core model was of 8 slot segments out of 48 slots, which resulted in another 5 fault images repeating around the missing core. This effect is studied in Chapter 6. Each image effectively generates circulating fault flux around the core which causes an increased opposing mpd at the fault, reducing its detected mpd. Only a single image occurs on the full 48 slot DAX8 core. Thus assuming uniform *Quad* recovery, image correction was achieved by scaling the 3D FE model *Quad* signal results by $8/7 \times 47/48 = 111.9\%$.

11.5. Measurement results of buried faults at equal flux

The most direct comparison is to compare the test results such that the coupled total flux in each fault is equal to the 3D FE flux, scaled as given in Table 11.3. The scaled rms *Quad* signals were converted to peak and compared to the 3D FE model peak results corrected for images. These are plotted in Figure 11.7 below for 10, 20 and 40 mm long faults, with the reference position of the 50 mm DAX8 core packet shown symbolically. The flux scaled results show quite a close comparison, on average the 3D FE model was only 4.5% over the measured values (averaged over all fault lengths). The common amplifying factor seen on all the longer 40 mm fault test results is likely to be the packet air gaps, which is investigated later.

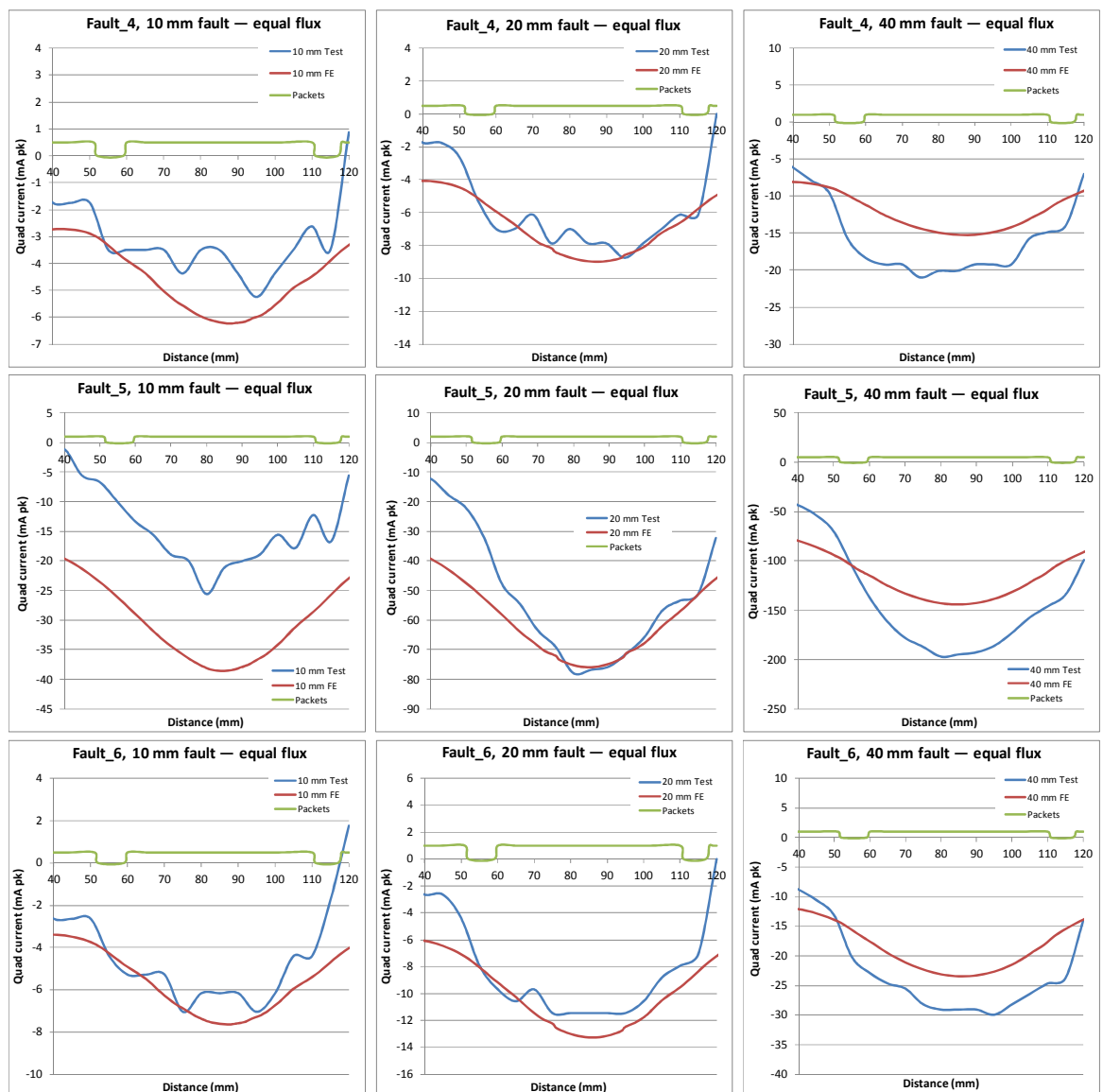


Figure 11.7 Measured and 3D FE buried fault *Quad* signals scaled to 3D FE flux

11.6. Fault current measurements

The 3D FE model fault currents shown below in Figure 11.9 were found to be too ideal, being totally constant over the fault length and 95–104% of theoretical value predicted from solely fault resistivity. By contrast Ho's analytic model ([72] section 4.2.2) had demonstrated significant non-uniformity of short fault currents, with the current reducing at the ends at these levels of fault current, as also found in practice. It was also found below that the peak currents developed in the test faults were substantially lower than the 3D FE model predicted.

The faults were fitted with sense wires contacting the fault wire as shown in Figure 11.4, to enable the voltage and hence current distribution along the fault to be measured⁴⁶. The sense wires were 35 SWG enamelled wires having uninsulated contact tips under the NiCr fault wire, with the voltage difference between selected pairs amplified by a differential amplifier. Four sense wires were spaced at 2 mm intervals from each end (1 mm intervals for 10 mm fault) with one in the middle (nine in total). This was not a very precise local current measure as a 10% change can arise from just a 0.2 mm positioning error, but enabled an estimation of the current distribution shape. The mean current measured over the whole length was more accurate.

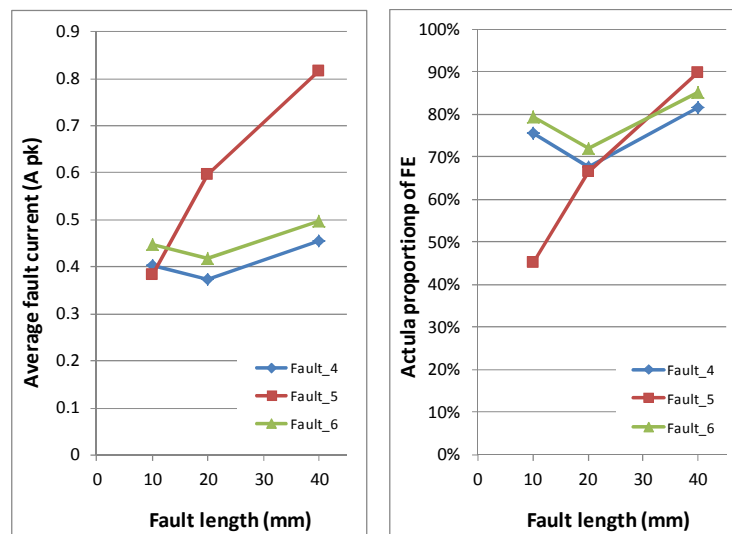


Figure 11.8 (a) 3D FE flux scaled, mean fault currents from test, (b) scaled test current as proportion of 3D FE model

The mean fault current was calculated from the measured end-end differential voltage and wire resistance, assuming effective contact lengths of 90% of the fault wire

⁴⁶ While inductive emf on the sense wire could affect this measure, the sense wires return alongside the resistance wire, and all are within the same hole in the steel core. The steel surround minimises any difference in coupled voltage, thus any induced voltage in the fault wire will be offset by the same voltage in the sense wire when sensed differentially.

lengths. The DAX8 fault currents were scaled to equal the 3D FE model flux using the same proportions as in section 11.5 (hence equal axial voltage field).

The results are shown in Figure 11.8(a), and compared to the fault region currents derived from the modelled integrated current density (Jds) values in Figure 11.8(b). From this, it is clear that the scaled faults are not achieving the maximum currents predicted from simple resistivity computation in Table 11.3, nor the expected currents in the FE model. Fault_5 is especially dependent on fault length to approach the modelled value.

The sense wires on the fault conductor allow the measurement of the fault current distribution along the faults (only nearer the ends for the 40 mm faults). The sense voltages were converted to segment currents and averaged laterally to reduce the uncertainty from sense wire position error. The results are shown in Figure 11.10, scaled to equal the 3D FE flux, to compare with the model currents shown in Figure 11.9.

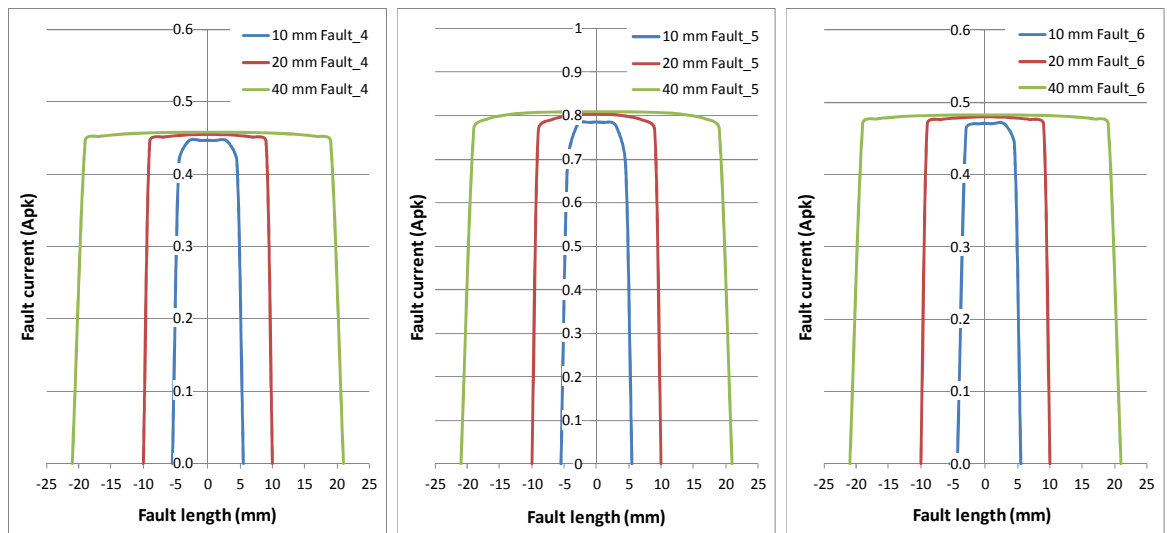


Figure 11.9 3D FE model fault current distributions (a) Fault_4, (b) Fault_5 and (c) Fault_6

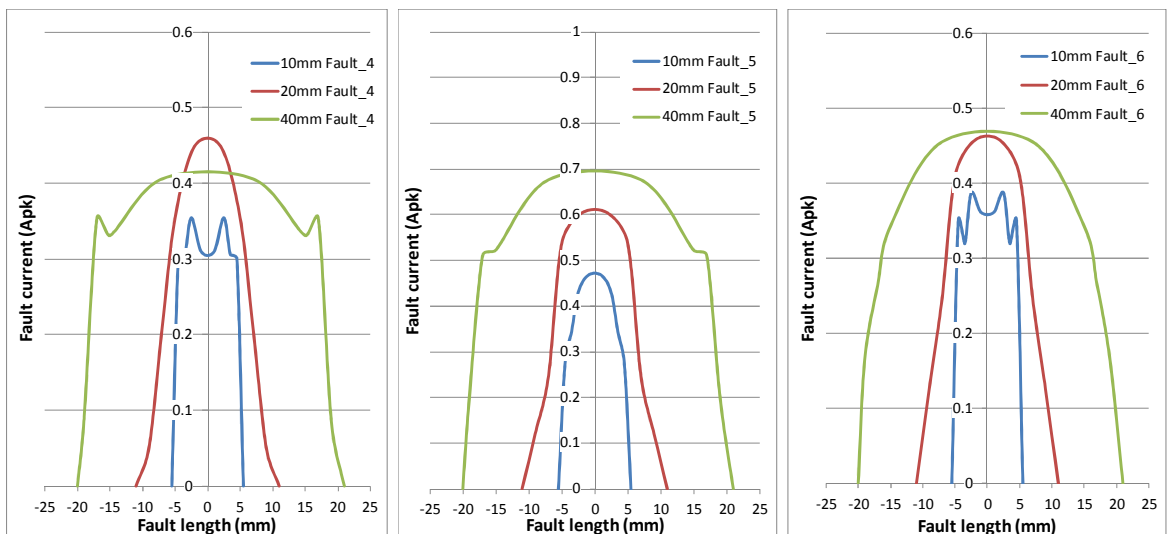


Figure 11.10 Test fault current distributions, 3D FE flux scaled (a) Fault_4, (b) Fault_5 and (c) Fault_6

11.7. Measurement results of buried faults at equal fault current

While the comparison at equal coupled flux should be the best overall comparison, this includes both the accuracy of the 3D FE modelling of the fault currents and their electromagnetic detection. However it appeared that the fault currents were unrealistically modelled. In order to separately compare the 3D FE modelling of the electromagnetic detection with test results, the measured *Quad* signals were linearly scaled such that the mean fault current over each fault matched the 3D FE values. They were also corrected for the differing slot root pitch described in section 11.4. The results are plotted in Figure 11.11.

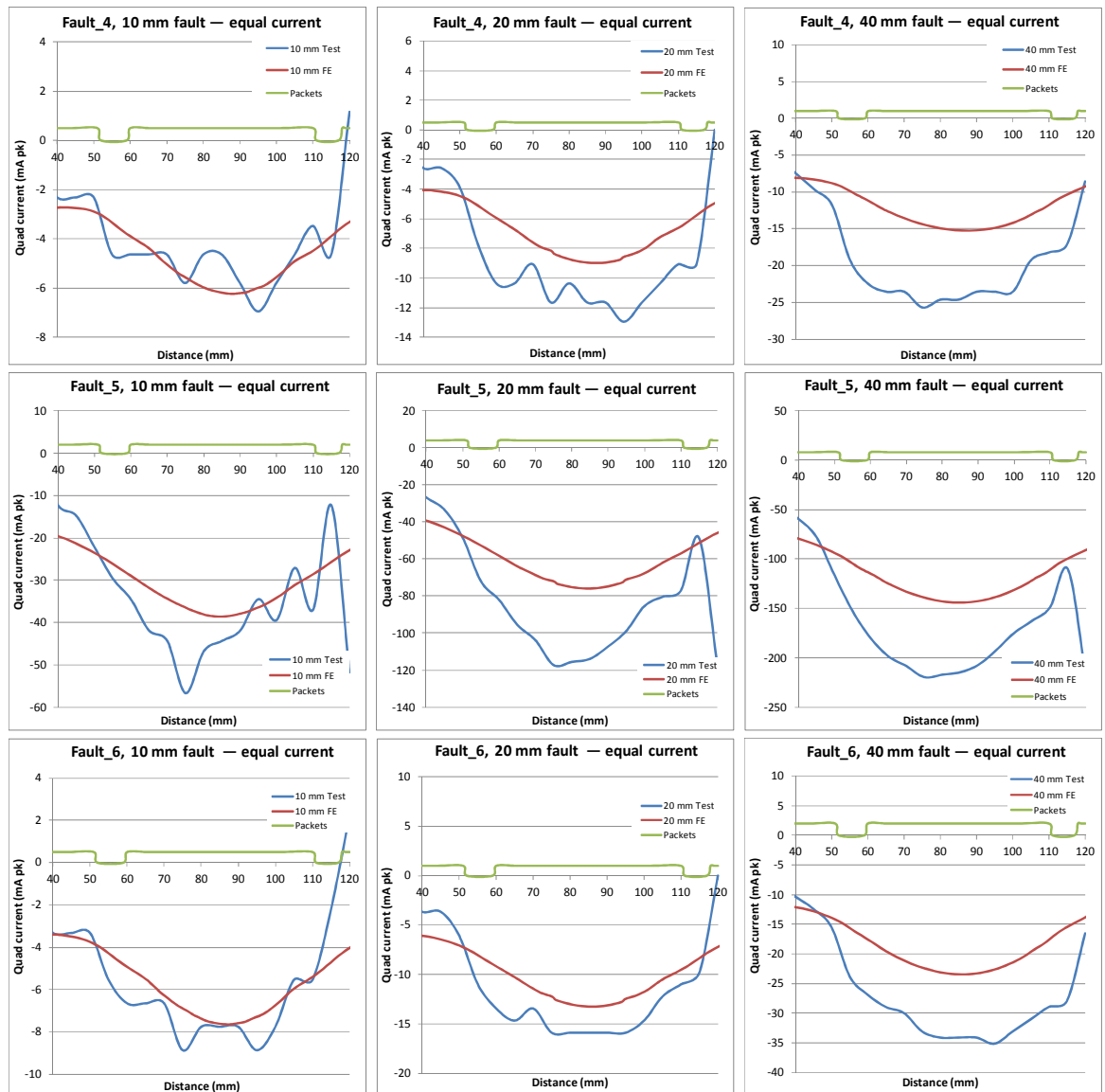


Figure 11.11 Measured and 3D FE buried fault Quad signals at equal fault current

The poor modelling effectiveness demonstrated in Figure 11.11 for faults >10 mm is most likely caused by the 3D FE model having a long (620 mm), axially continuous, core devoid of any packet gaps. By contrast the DAX8 core has 7.8 mm wide packet air gaps

either side of the 50 mm long packet carrying the fault, a very conventional construction. The flux from the experimental faults is thus constrained by the packet air gap barriers and hence the flux density and resultant magnetic field strength are amplified over the unconstrained case. This is supported by the fact that the best matched 10 mm DAX8 faults have a further 200% of their length of unfaulted packet laminations either end, whereas the worst matched 40 mm faults have only 13% either end before the air gap. This showed there was a need to determine and compensate for the effect the air gaps would cause.

11.8. Modelling the impact of packet air gaps on buried faults

A model to better quantify the theory that the packet air gaps are amplifying the detection would ideally be done in 3D. However the software used by Ho suffered serious convergence problems because of the large changes in permeability across the air / steel axial interfaces at the packet air gaps. These could not be readily resolved, hence the model omitted the air gaps. Thus the cost and complexity of proving alternate 3D FE software that would reliably achieve this, reconstructing the model and validating on the experimental core would be great. In consequence a less intensive method was developed that would provide a two-dimensional approximation of the three-dimensional problem, following the approach of Reece and Preston [205] (§12.3, where the bulk parameters are adjusted to approximate any 3D asymmetry). The 2D models section the laminated structures comparable to the 2D FE model in Chapter 6, allowing the differing planar and effective axial permeability in the core to be modelled and adjusted.

Fault currents flowing in the laminations to and from the core rear keybars develop a flux that circulates both around the fault and around the core body, shown in Figure 11.12. Any increase in that which circulates around the core body will reduce the flux density and hence magnetic field strength developed across the slot (under the tooth roots) by the fault. The flux that circulates around the core will diverge axially in the core away from the fault plane around the core body, despite the low axial permeability (reflecting the stacking factor). This causes the core body reluctance to the fault flux to fall, and thus the amount of fault flux that circulates around the core body to rise above that simply predicted by a 2D axial model. Further the flux that flows around the short fault, which will be shown to be primarily induced by the fault current returning in the laminations, may also diverge axially in the core in the region of the tooth roots, thus reducing the magnetic field strength developed there.

Finally the Chattock detects the magnetic potentials at the teeth tips, not the tooth roots. Since there is no significant flux flow between the opposing tooth tips, the axial attenuation of magnetic potential up to the tooth tip from the root will be controlled by the difference between radial reluctance of the tooth and the reluctance of the air in the slot between the teeth. The latter is increased by the presence of packet air gaps which limit the axial extent of the tooth slot that can contribute.

It can be seen that all these three effects are affected by the presence or absence of packet air gaps, since these substantially change the regional axial permeability of the core. This study uses a series of 2D FE models to estimate the differential change in these identified effects the presence of packet air gaps will cause. While any flux flow axially between laminations will also be resisted by lamination eddy currents, these can only realistically be modelled in a 3D FE modeller that can also model the constraint of laminar structures. (Eddy currents are similarly ignored by Reece and Preston.) The laminated model developed in Chapter 6 was considered impractical here due to the higher lamination count and very variable depths, and also the modelled constraining effect of the eddy currents appeared more severe than sometimes occurs in the field. The very high reluctance of the magnetic circuit between the teeth via the tooth tips, analysed in section 11.8.4, will further inhibit eddy current development.

An approximate system of 2D FE models in FEMM [204] was thus developed of a buried fault with the ability to vary the permeability of the packet air gaps, thus modelling with and without air gaps so as to obtain a metric for their differential effect. The model utilised axial and transverse sections of the core around the fault to investigate the axial spread of flux and its impact on developed mpd. (The transverse models are transverse to the plane of the laminations.) Initially a conventional axial stator 2D FE model was constructed, consisting of the whole core to avoid the complexity of image artefacts. Fault_6 was chosen for its convenient symmetry under a slot.

The resultant magnetostatic axial 2D FE model (28,678 nodes) of the DAX8 core is shown in Figure 11.12 with Fault_6 injected at 1 A current⁴⁷. The inside and outside is air, with the steel having a uniform relative permeability of 3000 (as used by Ho in the 3D FE models). This naturally ignores the packet air gaps, but since the faults do not extend beyond the centre packet, there is no need to adjust the aggregate permeability.

⁴⁷ An injected fault current was used in preference to the more realistic approach of an induced current from an central excitation current and resultant flux, to enable the fault fluxes to be more readily separated and analysed. This is also the only practical approach possible in the following transverse FE models.

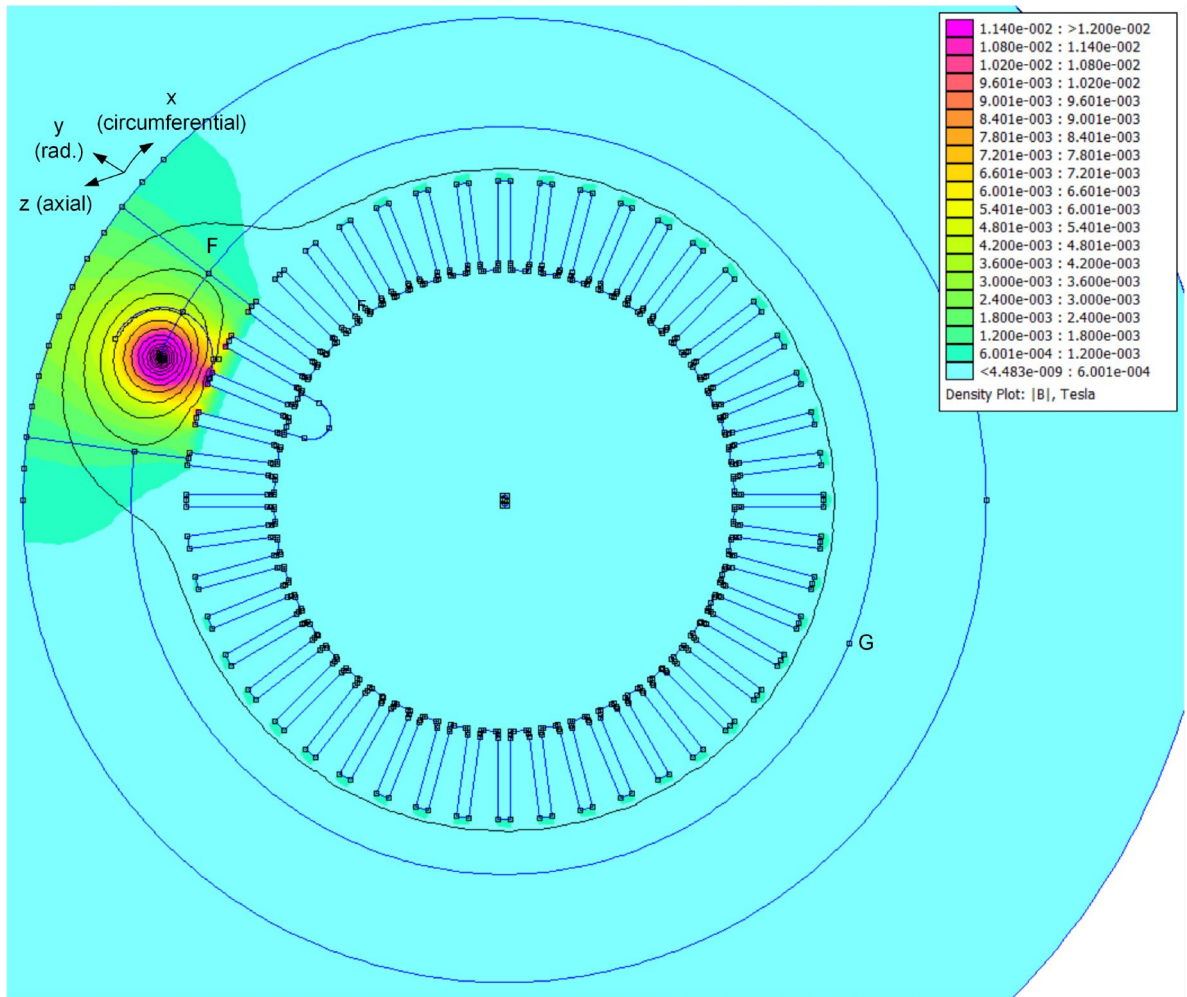


Figure 11.12 DAX8 axial 2D FE model with Fault_6 active (detail in Figure 11.13)

The fault region is shown in detail in Figure 11.13 with axes defined as $x =$ circumferential, $y =$ radial and $z =$ axial along the core axis. Two regions of the whole core are defined for analysis; the four slots nearest the fault where the fault flux circulates is termed the ‘fault region’, the rest of the core yoke containing the remaining 44 slots is the ‘core body’. The Chattock locus detecting the fault signal mpd is illustrated across the tooth tips.

For the infinite length fault in the axial 2D FE model, the modelled mpd at the Chattock is 0.196 A, i.e. a fault current detection sensitivity of 19.6%. The mpd across the tooth tips will normally be equal to that at the tooth root centres, due to lack of any flux flowing within the tooth. To demonstrate this is the case, the mpd along the 41 mm locus for half a tooth pitch from D to E in Figure 11.13 is 0.093 A, where DE is a constant radius from the fault current and D subtends from the fault to centre of the tooth root. Thus the 2D axial mpd error from using the potential at the tooth root rather than tooth tip is only 5%. A further important, though unsurprising, observation is that the great majority of the

induced fault flux flows around the fault, with in this case only 13% circulating instead around the core yoke.

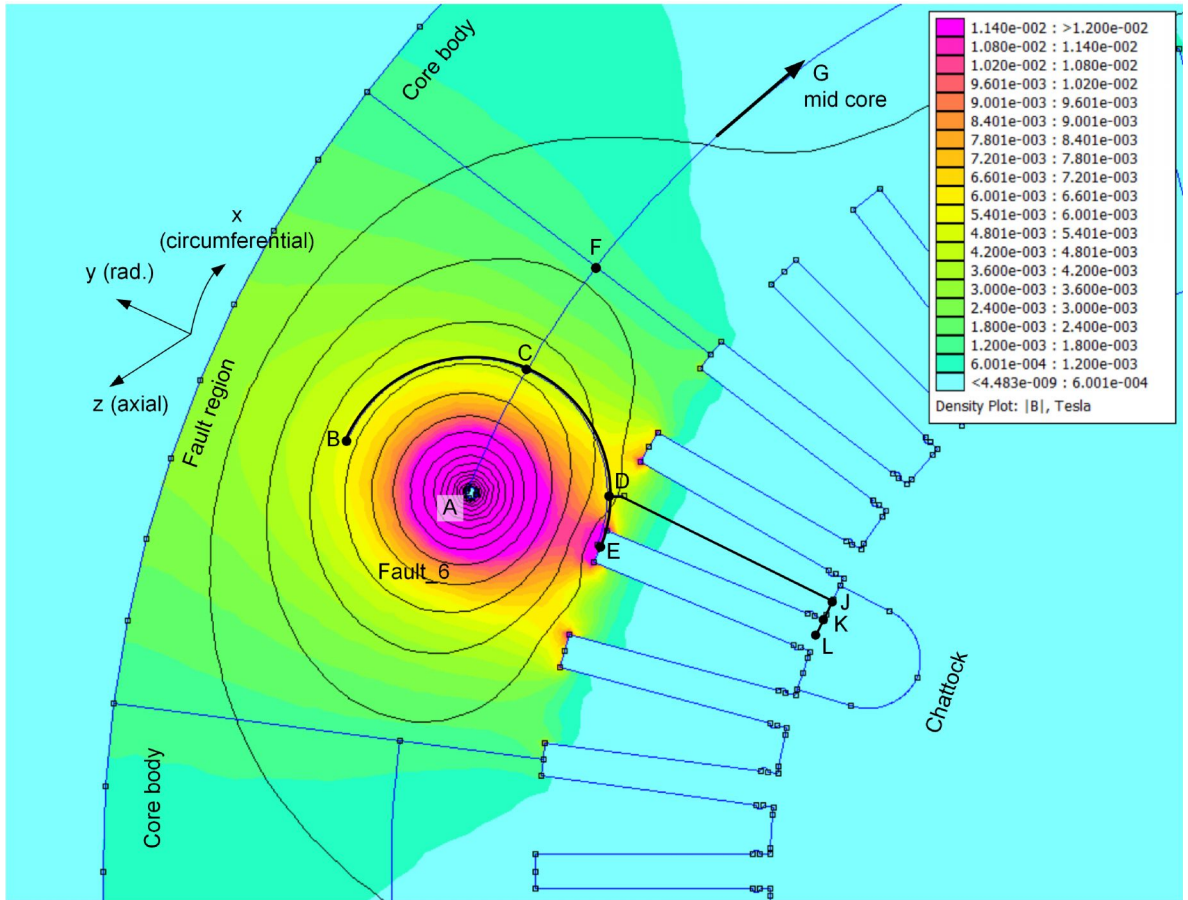


Figure 11.13 DAX8 axial 2D FE Fault_6 model detail

The extra 3D attenuations over the 2D model occurring in practice are thus substantial, with the measured Fault_6 detection sensitivity varying from 2–8% for the 10–40 mm lengths (as shown in Figure 11.25) compared to 19.6% in the 2D model above. This extra attenuation comes from many sources, in particular since the Chattock mpd developed in the 2D model is solely derived from the infinite axial fault current. The actual short axial fault current develops a much smaller magnetic field strength, and the impact of this is analysed below.

11.8.1. Magnetic potential developed by axial fault current

The magnetic field strength directly caused by a short constant axial fault current can be derived from *Biot-Savart*. This analysis ignores the effect of the radial lamination currents which are assumed to approximately offset each other, and the return axial currents in the core rear keybars being much more distant. In the model shown in Figure 11.14, a short fault current I in the z -axis direction extends from $-z_1$ to z_1 , with midpoint at $z = 0$. The current induces a field H negative to the x -axis (thus into the page) at

measurement point M distance y_1 from the current axis, in the x-y plane. The current segment is distance $|r|$ from M along unit vector \hat{r} , such that the vector distance is $|r|\hat{r}$ and has an elemental current segment $I.dz$.

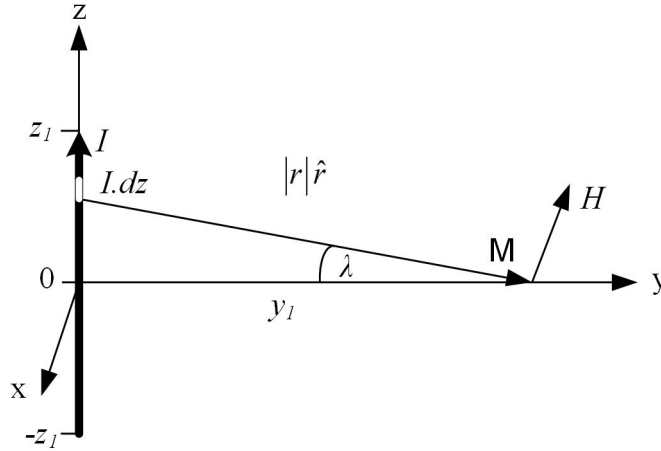


Figure 11.14 Biot-Savart model of short fault

The magnetic field strength dH from current element $I.dz$ is given by *Biot-Savart* in equation (11.1)

$$dH = \frac{I \times \hat{r}}{4\pi |r|^2} dz, \quad (11.1)$$

hence
$$H = \frac{1}{4\pi} \int_{-z_1}^{z_1} \frac{I \cos \lambda}{|r|^2} dz. \quad (11.2)$$

Since
$$\cos \lambda = \frac{y_1}{|r|} \quad \text{and} \quad |r| = \sqrt{z^2 + y_1^2}, \quad (11.3)$$

and I and y are constant with z , equations (11.3) and (11.2) give

$$H = \frac{I}{4\pi} \int_{-z_1}^{z_1} \frac{y_1}{(z^2 + y_1^2)^{3/2}} dz. \quad (11.4)$$

Integrating equation (11.4) gives the magnetic field strength H for a fault length of $2z_1$

$$H = \frac{I}{4\pi y_1} \left[\frac{z}{(z^2 + y_1^2)^{0.5}} \right]_{-z_1}^{z_1}. \quad (11.5)$$

The peak mpd developed across the 88 mm pitch of the adjacent tooth roots for Fault_6 where $y_1 = 0.107$ m was computed from equation (11.5), and compared to measured results in Table 11.4. These are all scaled to a common 1 A peak fault current. Since the mpd detectable from the axial fault current is much less than the measured signals, it indicates that the large majority of the mpd measured from these buried faults does not come from the axial current. It must thus be developed by the flux created by the

fault's radial currents in the laminations to the rear keybars, circulating around the fault. Hence these radial currents are the main determinants of induced flux in any FE models.

Fault_6 length (1 A fault current)	10 mm	20 mm	40 mm
2D modelled mpd across tooth-tips	196 mA	196 mA	196 mA
Measured mpd across tooth-tips	22.7 mA	39.5 mA	85.5 mA
<i>Biot-Savart</i> axial current slot pitch mpd	6.1 mA	12.2 mA	24.0 mA
<i>Biot-Savart</i> axial current mpd proportion	27%	31%	28%

Table 11.4 Biot-Savart prediction of detected Fault_6 mpd

11.8.2. Core body transverse 2D FE model of axial flux divergence

The flux induced by the radial fault currents (those shown in red in Figure 1.1) is the dominant source of the flux that flows in the x-y plane around the axial fault current in the fault region and core body region. While these fluxes will not be the same magnitude as shown in the 2D axial model Figure 11.12, it does model the proportions depending on their relative reluctances. This enables modelling of the change in the proportion of flux that flows around the axial fault current, due to changes in the reluctance of the core body caused by the presence of packet air gaps, and its impact on the fault mpd on locus DE in Figure 11.13.

Since the core body region has a much longer mean path of 5303 mm, it will have the higher reluctance. However axial flux divergence, potentially limited by packet air gaps, will cause this flux path to have a lower reluctance than predicted in the axial 2D FE model. The consequence will be higher core body flux, hence reduction of the flux circulating around the fault behind the slots, and lower local magnetic field strength generated there. The analytic modelling by Ho ([72] Chapter 4) and results from this exercise have shown that in the current profile for <1 A faults the majority of the current returns near the ends of the fault. In consequence it is a reasonable approximation to model the fault current in just the end laminations.

To determine the magnitude of the flux divergence, a transverse magnetostatic FEMM model for the three lengths of fault was developed around half the core circumference along the core fault radius, following the same approach as Chapter 6. This followed central packet locus ACFG in Figure 11.13 and Figure 11.12, assuming axial and circumferential mirror symmetry. To better understand the magnetic model section, the visualisation in Figure 11.15 shows the fault current in red (currents flow radially in end laminations) and the modelled cross-section in yellow, extending off-image around the

core body to mid-point G. The visualisation has the 2D axial flux lines image superimposed for reference.

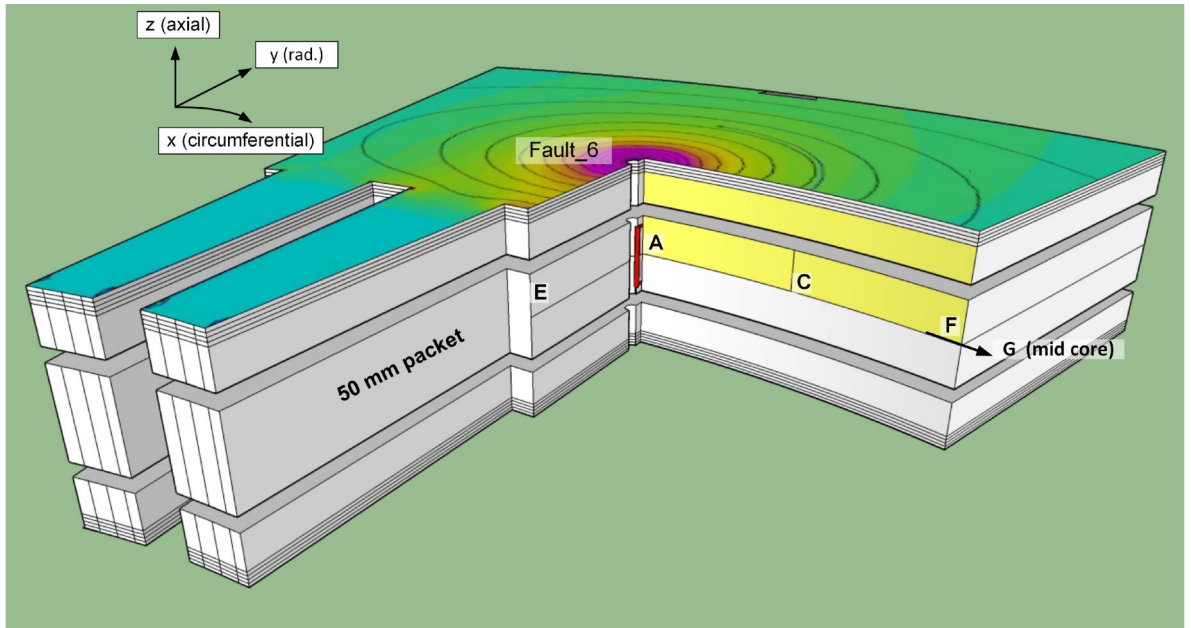


Figure 11.15 Core body transverse model section, locus visualisation

In a 2D FE magnetic model there is no flux density in the un-modelled 3rd dimension, in this case the radial y-axis. While this is not true for the fault region, it is essentially true for the great majority of the core body, as seen in Figure 11.12. In consequence, the model is a valid means of estimating the difference in x-axis core body reluctance due to flux divergence with/without packet air gaps.

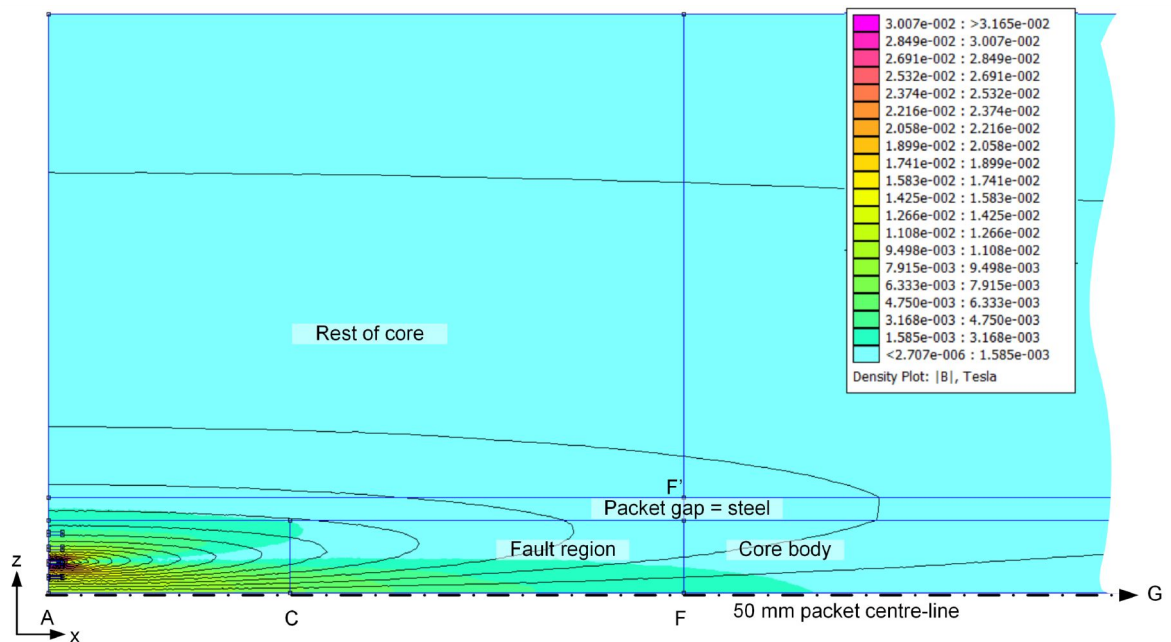


Figure 11.16 Core body transverse 2D FE model for 20 mm Fault_6 without packet air gap

The core body transverse 2D FE model was formed of half the 50 mm lamination packet being 25 mm high, an 8 mm packet air gap above which can be steel or air, and

above that a 200 mm high rest-of-core steel packet to absorb any stray flux. It assumed mirror symmetry about the 50 mm packet centre-line. The presence or absence of packet air gaps was achieved by switching the permeability of the packet air gap region. A 0.5 A fault current was imposed in a 1x5 mm lamination element, simulating a 10 mm wide 1 A total current path in the laminations, in the same manner as in Chapter 6.3. The 2D FE model is shown for the first ~500 mm in Figure 11.16, with a 20 mm fault and no air gap (i.e. packet air gap region set to same material as steel laminations). The steel was set to normal relative permeability of 3000 in the x/y-axis and 25 in the z-axis, to reflect the stacking factor of 0.96 measured in the DAX8 core⁴⁸. A Dirichlet boundary enforces the mirror symmetry on boundary ACFG, with a Neumann condition on all other boundaries.

It can be seen that with no packet air gap the flux density reduces rapidly and thus the effective reluctance of the circumferential core body is a lot less than that in the axial 2D model. However even with a packet air gap, the core body flux density reduces circumferentially quite significantly, thus it was necessary to determine the impact on the axial 2D model of both presence and absence of the packet air gap. To determine the differential effect, the core body transverse model was calibrated initially with all the steel having effectively zero (0.01) z-axis relative permeability, emulating the flux in the axial model. The net reluctance of the path AG was then computed as 1850 and compared to 1720 A-t/Wb computed from the axial model, i.e. only 7.5% error. This was considered acceptable given the difference in the models. The change in reluctance of the core body 25 mm packet (total mpd along locus FG divided by the magnetic flux entering the core body packet across locus FF') was then determined due to packet air gaps, for the three fault lengths.

To determine the effect of changes in core body reluctance, the permeability of the core body region can be varied in the 2D FE axial model (Figure 11.13). This varies the proportion of fault flux that passes around the core without affecting the fault's local magnetic circuit, from which the changes of the mpd generated across the tooth roots can be determined on symmetric locus DE. The core body relative permeability was adjusted in the 2D axial model from 1,000 to 100,000 (c.f. normal relative permeability of 3,000) and the resultant reduction of generated Chattock fault mpd with reducing core body reluctance is plotted in Figure 11.17. To simplify use of this curve, a curve fit predictive formula (11.6) shown overlaid in Figure 11.17 was derived with M_{DE} the predicted mpd change across DE for core body reluctance R change from normal R_0 .

⁴⁸ Ho's 3D models used an infeasible stacking factor of 0.98.

$$M_{DE} = 0.5 \left(2 - 0.8e^{-5R/R_0} - 1.2e^{-50R/R_0} \right). \quad (11.6)$$

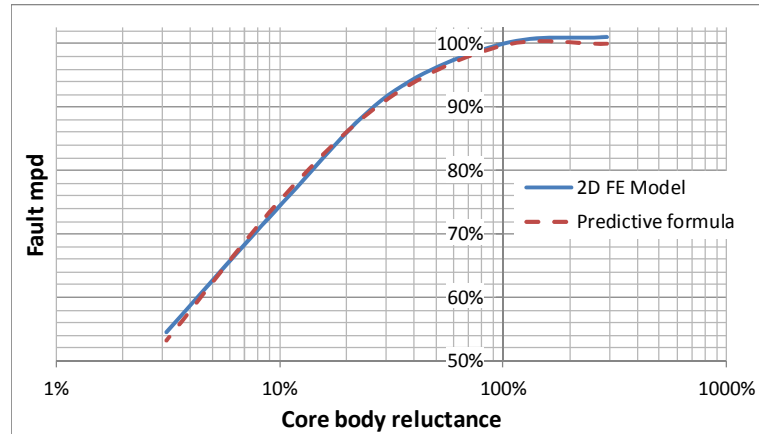


Figure 11.17 Fault mpd variation with core body reluctance.

Finally the reluctance change determined from the core body transverse FE model was used in the predictive formula (11.6) to establish the fault mpd attenuation for each fault length (with and without packet air gap), due to increase in whole body flux over the axial model in Figure 11.18. This predicted a net 8–11% increase in detected fault mpd over the 3D FE model from the presence of packet air gaps around the core body.

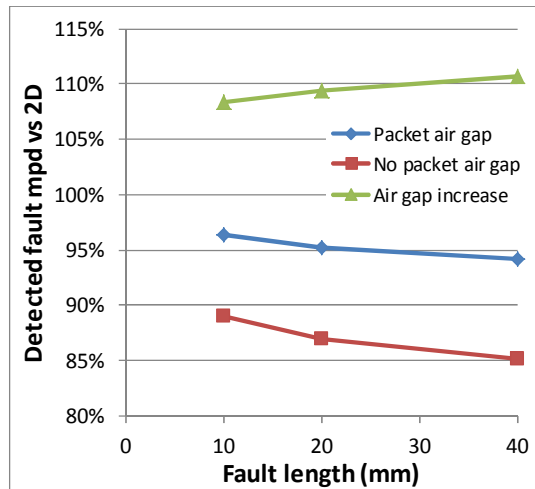


Figure 11.18 Detected fault mpd increase with fault length and packet air gap

11.8.3. Fault region transverse 2D FE model of fault mpd

To determine the impact of axial divergence of fault flux due to packet air gaps on the development of the fault mpd across the tooth roots, the fault region was modelled in two further transverse cross-sections, in the same manner as section 11.8.2.

The fault region transverse 2D FE model is an axial semi-circular section (336 mm periphery) centred on the fault current, cutting the 50 mm core packet along the locus BCDE in Figure 11.13 and with its end E on the slot base midline. In an alternate visualisation it is coloured yellow in a sectioned view in Figure 11.19 (with inset rotated view for clarity). The locus DE on the model is the 40 mm span from the slot centre to the

tooth root centre, and is the region across which the half the magnetic potential is developed to present up the teeth to the Chattock sensor. As discussed in section 11.8.2, the locus BCDE also essentially follows the flux flow lines, maintaining the 2D FE model assumption of zero flux normal to the model plane.

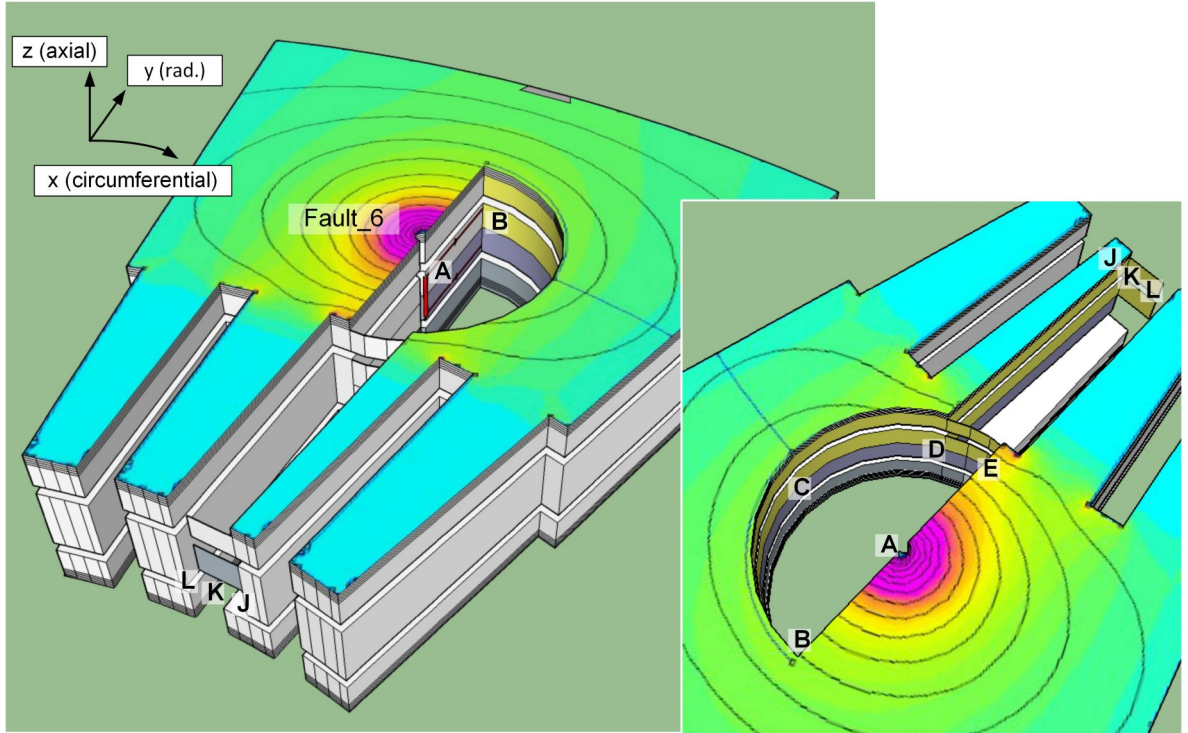


Figure 11.19 Fault and tooth region transverse model loci visualisations

As in the core body transverse 2D FE model in section 11.8.2, mirror symmetry was used to model only the top half of the fault, with the boundaries and fault current models also the same as the core body transverse model in Figure 11.16. The result is shown in Figure 11.20 for a 20 mm fault with no air gap (i.e. steel laminations in the packet air gap).

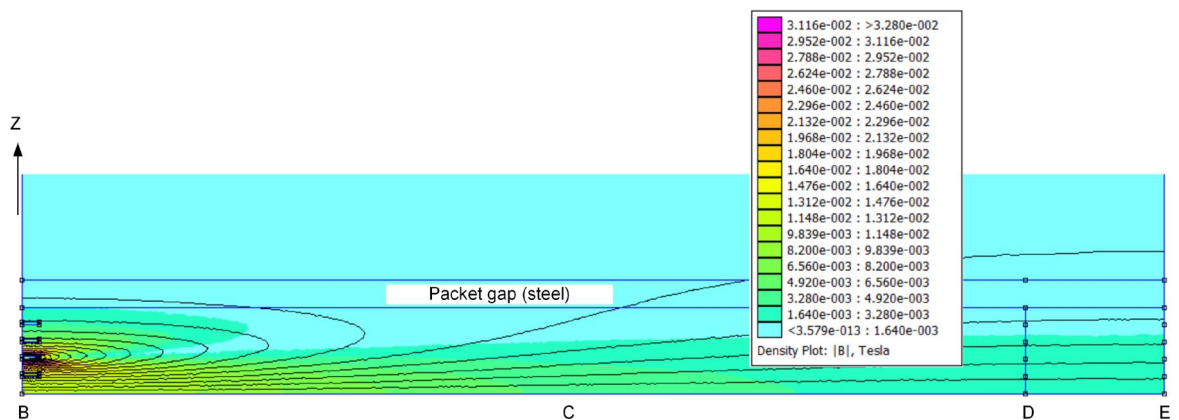


Figure 11.20 20 mm Fault_6 fault transverse 2D FE section model

It can be seen that the flux diverges and the flux density falls towards the tooth root region DE. In consequence given the uniform permeability, the local H field reduces. Also, despite the low axial (z -axis) permeability, a considerable amount of the induced flux

circulates locally around the radial fault current path, increasing the local magnetic field strength and thus reducing the proportion of the field developed in the remainder of the path for shorter faults.

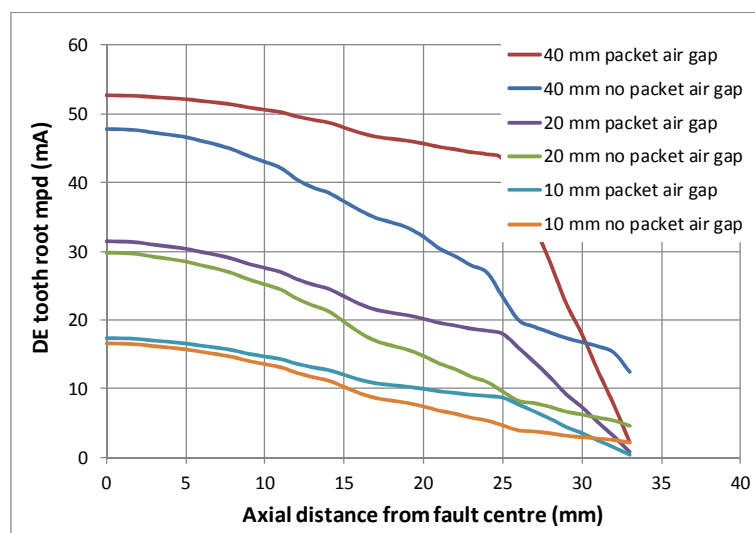


Figure 11.21 MPD developed across section DE along z-axis with and without packet air gaps for 1 A fault current

The section locus DE at the end reflects the mpd developed across the tooth centre-line to slot centre. The resultant mpd across DE for a 1 A fault current was computed from the magnetic field strength recorded on the x-axis at point D (assumed constant in the DE region since the flux is almost uniformly planar here), and the mpd variation along the z-axis for 10, 20 and 40 mm faults, with and without packet air gaps, plotted in Figure 11.21. It can be seen that the air gap has a modest effect on the shorter 10 and 20 mm faults, but a more substantial effect on the 40 mm fault.

11.8.4. Transverse tooth 2D model of axial flux divergence

The magnetic potentials at the tooth root from the transverse fault models for locus DE are not directly detected by the Chattock, since this senses the mpd across the tooth tips. In order to determine this, the mpd generated by the fault region transverse model across DE is presented to a third model of the tooth structure up to the tooth tip. This model is similarly affected by the presence or absence of the packet air gap. The necessary transverse tooth model is developed along the locus DJKL in Figure 11.13, being a symmetric half, from tooth root to tooth tip slot centre, of the complete magnetic path. This is also illustrated in the tooth in the 3D cross-section visualisation in Figure 11.19. The reluctance of the model is very high due to the reluctance of the slot's air in locus KL, consequently this model will not 'load' the magnetic field from source DE significantly. The model follows the same approach as the core body and fault region in sections 11.8.2

and 11.8.3, modelling half the axial and circumferential extents with an assumption of mirror symmetry along loci DJKL and RL in Figure 11.22.

A modelling problem is the slot which provides the air path for flux to flow across it to the (un-modelled) other tooth along the whole tooth length. However due to the constraint of a transverse 2D model, this air path can only be placed at the end. Since the slot reluctance will always be much greater than the steel, gradual slight flux loss up the slot will only have a small effect on the magnetic field strength developed in the steel, so the effective reluctance of the slot can be aggregated at the 13 mm width end section KL, representing the half-slot reluctance. The mean tooth half-width on the x-axis is ~ 24 mm, and is thus the nominal 2D depth for the steel section of the tooth along locus DJK in Figure 11.22. However the 2D depth for the slot reluctance region KL is the slot length (y-axis) and is 186 mm. A 2D FE model assumes constant 2D depth (into the page), thus to approximate the difference the x-axis relative permeability of the slot reluctance region was set at $186 / 24 \approx 8$.

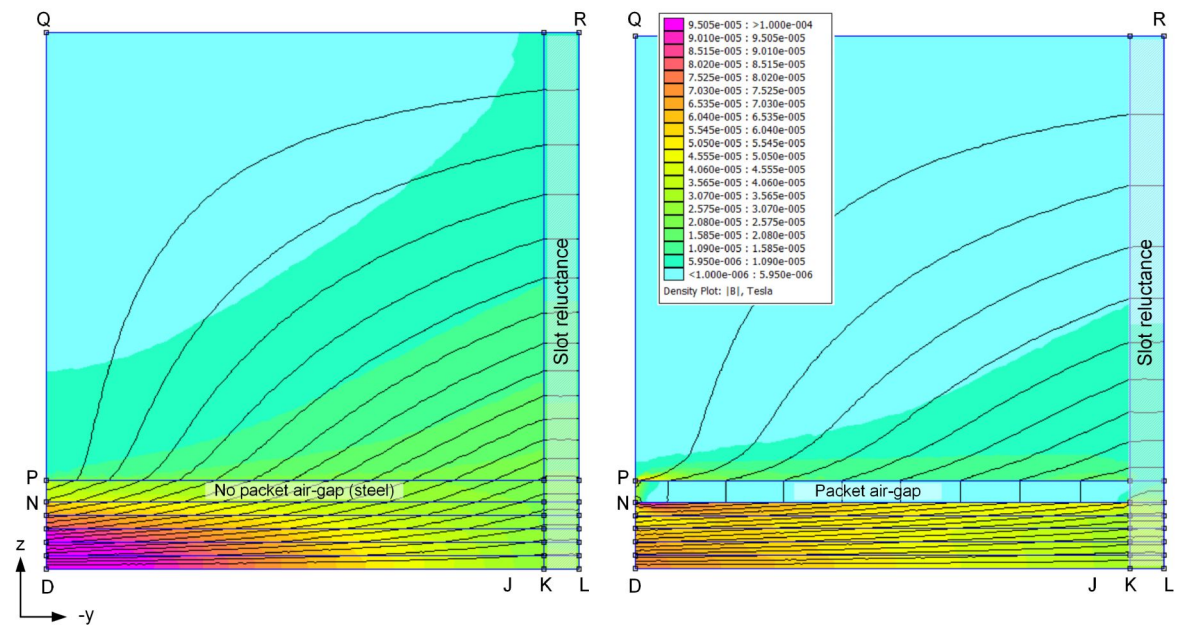


Figure 11.22 (a) 20 mm Fault_6 tooth transverse 2D FE model without packet air gaps, (b) with packet air gaps

A problem arose, in that FEMM is an A-V electromagnetic modeller where the H field is derived from the computed magnetic flux density and cannot be imposed. It is only possible to establish a flux density field through Dirichlet boundary conditions, or to impose a current. This was resolved by using a calibration variant of the tooth transverse 2D FE model to calculate the input reluctance profile.

The calibration 2D FE model was the same as Figure 11.22, but by asserting a linearly increasing Dirichlet boundary condition, it had a constant flux density imposed on

the DP boundary along the y-axis for 0–15 mm in the z-direction for 10 & 20 mm faults and 0–25 mm (the whole half-packet) for 40 mm faults. The mpd developed along the full y-axis was then recorded at 5 mm steps up the z-axis from 0–33 mm (D to P), with and without packet air gaps. This enabled an input reluctance profile to be computed at the y-axis boundary DP in six sections from point D to the top of the packet air gap P. No flux was imposed above this point, since the fault region transverse model showed that the developed fault magnetic field strength above this point was diminishing rapidly. Dirichlet boundary conditions of no flux were maintained along locus PQR to ensure the model represented the zero flux developed by the rest of the core, and along locus DJKL to preserve mirror symmetry.

From the required mpd and calibration input reluctance, the input flux density and required Dirichlet (**A** vector) boundary profiles for the transverse 2D FE tooth models were computed in linearised 5 mm steps on the z-axis to achieve the input H field. Differences between the required and actual developed mpd values (since the resultant flux density field did not have the same profile as the calibration field) were normalised by matching the mean of the model locus DL mpd for the five modelled steps from points D to N to the same mean input from the fault region transverse model (only -3% to +4% variances).

The flux lines in Figure 11.22(a) show that in the absence of a constraining packet air gap, the flux and hence magnetic field strength developed by the fault at the tooth root spreads axially very substantially down the tooth. However when the packet air gap is present in Figure 11.22(b), this more substantially constrains the flux within the packet, reducing the adjacent packet's fault signal while increasing the magnetic field strength developed in the central packet. As expected, this effect is most evident on the 40 mm fault model.

11.8.5. Application of transverse 2D models to 3D FE models

The final Fault_6 2D model results were derived by extracting the y-axis flux density profile along the slot edge K in Figure 11.22, and averaged 4 mm axially (z-axis) to simulate the spatial averaging of an EL CID Chattock. This allowed the final slot mpd across the full width 26 mm slot to be computed, with and without the packet air gap, since the flux becomes essentially uniform and x-planar in the low relative permeability of the slot. The fault mpd decreases with and without the packet air gap from the core body region model, were also applied. This gave the final increase in the 3D FE fault signal due to the packet air gap, as predicted by the 2D transverse models, shown in Table 11.5.

11. Experimental Verification of Buried Fault FE Models

Fault length (mm)	3D FE signal increases due to 2D FE packet air gap		
	Core body	Fault region and teeth	Total
10	8.3%	16.6%	26.3%
20	9.5%	18.8%	30.0%
40	10.7%	26.6%	40.1%

Table 11.5 Packet air gap correction factors from 2D FE transverse models

These correction factors were applied to the Fault_6 3D FE model values and compared again to the measured DAX8 results scaled to the 3D FE geometry and equal fault current in Figure 11.23.

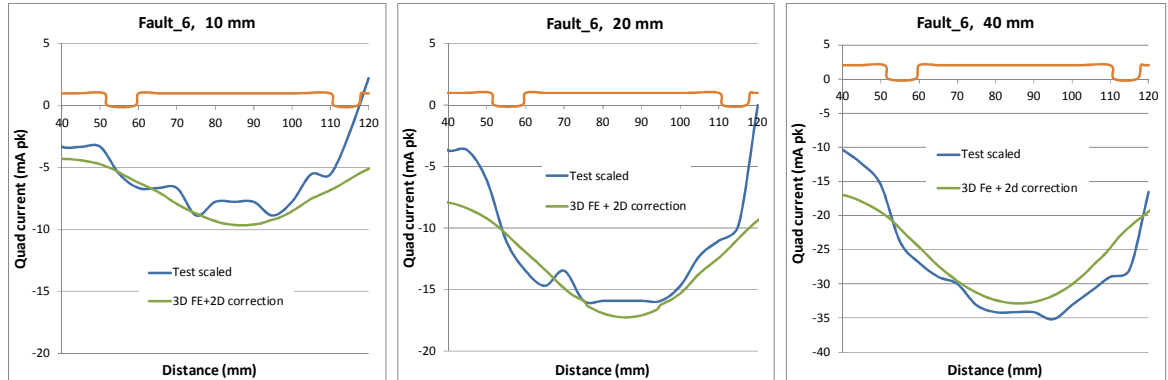


Figure 11.23 Air gap corrected 3D FE model results compared to tests at equal current

In these graphs it is clear by the comparison with Figure 11.11 (third row) that the revised modelled Fault_6 signal detection sensitivity to reflect the effect of packet air gaps has resulted in a close match between 3D FE model and experiment.

11.9. Analysis of errors

While the 2D FE transverse models only explicitly considered Fault_6, the other faults are expected to be affected similarly. Fault_4 has similar depth, and is thus assumed to be similarly affected by packet air gaps. Fault_5 is however 2/3 of tooth length down from the tooth tip thus will not fully be affected by the tooth's transverse flux divergence. However the magnetic field developed in the regions not presented to the Chattock will also be affected by the air gaps, and thus affect the proportion presented in a manner not known. In consequence, lacking further study, the same correction as Fault_6 is applied to Fault_5.

Using the above extrapolations, three statistical studies were performed of the outcomes, computing each 3D FE model's error in predicting the measured *Quad* signal against the experimental results. The experimental results were firstly compensated to equal coupled fault flux and geometry, then secondly scaled to equal fault model currents and geometry. Finally the 3D FE model was air gap corrected using the 2D FE transverse models as given in section 11.8.5, and compared against the experimental results

compensated for equal fault current and geometry. The prediction errors were averaged over each fault’s length. The results are given in Table 11.6.

	Length (mm)	3D FE error at equal flux	3D FE error at equal current	3D FE + air gap correction error at equal current
Fault_4	10	20%	-10%	14%
	20	13%	-32%	-11%
	40	-28%	-41%	-17%
Fault_5	10	66%	-25%	-5%
	20	-2%	-34%	-14%
	40	-26%	-34%	-7%
Fault_6	10	6%	-16%	6%
	20	13%	-18%	6%
	40	-22%	-33%	-7%
Mean error		4.5%	-26.9%	-3.8%
SD		27.6%	9.7%	9.8%

Table 11.6 Analysis of error of 3D FE prediction of buried fault test results.

The mean error provides an indication of the overall success of the 3D FE model in predicting a variety of buried fault test results. The standard deviation shows the variance of those predictions. The results are plotted in Figure 11.24(a) to show the error distribution scatter and Figure 11.24(b) to show the aggregate impact with fault length.

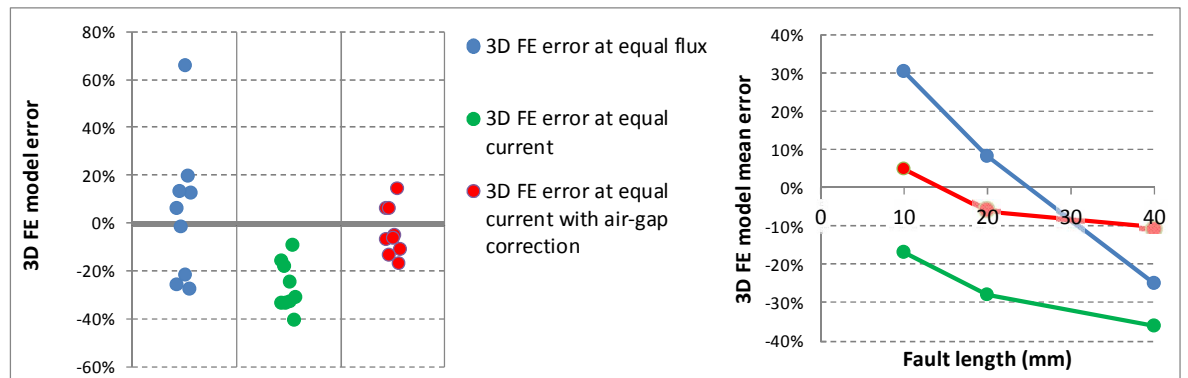


Figure 11.24 (a) 3D FE model error distributions, (b) model average error by fault length

11.10. Detection sensitivity of fault currents.

The knowledge of the mean fault currents also allows measurement of the EL CID detection sensitivity of faults on the stator core, expressed as the proportion of the fault current detected as the *Quad* signal. The maximum detected *Quad* signal is conventionally interpreted as the fault intensity/current metric [26]. For buried faults Fault_4–6, the DAX8 measured maxima were corrected for the effect of their application hole, for tooth pitch to correlate back to the 3D FE core geometry, and to equal modelled and measured fault current determined as the mean of the current over 90% of the fault length. The resultant

Quad fault signal sensitivities to fault current predicted by the 3D FE model (as corrected for packet air gaps) and measured sensitivity results are given in Table 11.7.

Ho [165] published his 3D FE modelled and experimental measured studies on the three surface faults, Fault_1–3 on the TCS core, but there was no measurement of the actual fault current. However Ho’s models of these currents appeared more realistic in being substantially ‘rounded’ at the axial ends, with the shortest fault currents being ~15% less than the longest. Thus the mean of the modelled current over 90% of the fault length (as used for the buried faults analysis above) was used to provide the most comparable measure. These are also given in Table 11.7.

Length/ Fault	10 mm		20 mm		40 mm		60 mm	
	Model	Measure	Model	Measure	Model	Measure	Model	Measure
Fault_1	0.350	0.288	0.505	0.472	0.617	0.646	0.690	0.747
Fault_2	0.265	0.250	0.418	0.449	0.607	0.650	0.704	0.767
Fault_3	0.167	0.157	0.283	0.320	0.469	0.537	0.600	0.767
Fault_4	0.017	0.015	0.024	0.027	0.046	0.055		
Fault_5	0.063	0.067	0.122	0.142	0.244	0.263		
Fault_6	0.020	0.019	0.036	0.033	0.068	0.072		

Table 11.7 Quad fault current detection sensitivities, 3D FE modelled and measured

The use of mean fault current gives an overall 6.2% increase in detection sensitivity for Fault_1 to Fault_3 by comparison to Ho who used maximum fault current. The 3D FE modelled *Quad* fault current detection sensitivity is plotted for all six faults on the TCS core in Figure 11.25, overlaid with the experimental measured results.

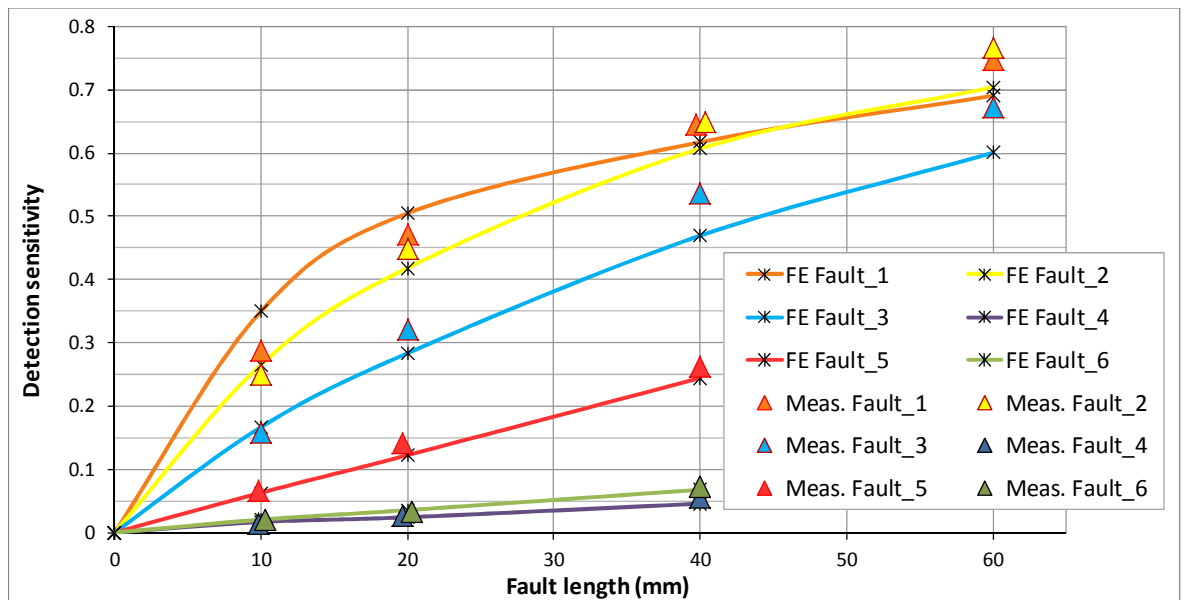


Figure 11.25 3D FE modelled and experimental Quad fault current detection sensitivities

11.11. Discussion

The relatively close mean match of the equal fault flux results is surprising since it is a test both of the modelling of the fault current and its electromagnetic detection. It was found to come from the accidental offsetting effect of the lower actual fault currents (than the idealised FE models) with the higher than modelled fault current detection sensitivity (due to absence of packet air gaps). However since these operated differently on differing length faults, it exacerbated the variance in the results, spreading from +66% to -28%. While the comparison had a mean error under 5%, it was >20% in error for the majority of the faults. In consequence the model's predictions were not fully validated by the simple comparison, though they were shown to be of the right order.

Once the effect of the fault current errors were removed ('equal current') the variance reduced substantially, however the problem of the 3D FE model omitting packet air gaps led to a strong under-prediction of measured buried fault signals. As expected this was seen to be worst for the longest faults due to the close proximity of the constraining air gaps. Applying the 2D FE air gap correction to the 3D FE model finally achieved a close mean prediction with only -3.8% error and similar variance. This is a good match considering the FE modelling complexity.

In section 9.6 it was shown that the scaled DAX8 core measurements may have a -5.4% mean error to the equivalent 3D FE/TCS value. This was not statistically proven, but indicates that the mean combined FE model error may be nearer to -9%, depending on the degree of covariance. (There is some indication of correlation with fault length between the two data sets, but the sample sizes are too small to draw reliable conclusions.) This still demonstrated that the combined FE models can predict the signals from substantially buried faults with less than the 10% mean error considered acceptable for stator core condition monitoring [177].

A number of limitations in the study arose and are considered. The problem that the boring of a hole in the core to apply a buried fault will disturb the electromagnetic signals detected from the fault was studied, and the expected effect determined. It is possible that the predicted and compensated 2D effect (~5%) of short faults was not fully accurate in 3D, but is unlikely to have a significantly different effect since the hole was continuous in the z-axis, like the 2D model.

Linear scaling was used to accommodate for increased DAX8 core size over the 3D FE core model, which alters the tooth pitch and thus the proportion of the buried fault magnetic field detected. This proportion was simply geometrically determined however

there is the possibility that this scaling is non-linear for short faults. It also assumed that the 20% deeper DAX8 slots would have negligible effect on signal detection, given the high slot reluctance.

The non-uniform core back flux density was modelled and used to compute the expected scaling of flux coupled into the faults between the 3D FE and DAX8 cores. This assumed a linear permeability model, whereas the steel's permeability is known to be increasing quite substantially at the test flux density levels, and thus likely to have a slight further impact on the coupled flux proportion, not accommodated in this study. The steel's anisotropic permeability (studied in Chapter 10) may also have a second order effect on the 2D transverse FE model predictions. However the use of uniform and isotropic permeability followed the practice in the 3D FE models.

The test fault currents achieved fell short of the currents predicted in the 3D FE models, ranging from 45–90%, on average 74% of prediction. Further the predicted currents were remarkably idealised, spanning from 95–104% of the theoretical maximum and showing no sign of the expected axial 'rounding' of the current distribution as measured and also predicted by Ho. This very close approach to theoretical maximum is considered to be caused by the 3D FE model using a large fault area (12.5 mm^2) with adjusted conductivity rather the actual NiCr wire area (0.16 mm^2) due to FE meshing limitations. This will greatly reduce the effect of local lamination resistivity affecting the fault current. In addition, the experimental use of applied fine fault wires will also add contact resistance to the lamination circuits, further tending to 'round' the current distribution due to current sharing between laminations. While revised experimental methods may reduce contact resistances, real faults involve the presence of multiple parasitic interlamination contacts, which differ substantially to a large uniform conductor⁴⁹. Thus experimentally perfecting an unrepresentative uniform fault experimental model is not worthwhile once the model differences are accounted for.

While it was not expected that the 2D FE transverse models would be particularly accurate in absolute terms (rather than as an estimate of differential change), they predicted results with packet air gaps ranging from +43% at 10 mm fault length to only +23% error at 40 mm, quite close considering the major 2D approximations made. This is considered to come from the fact that the majority of the magnetic field strength developed behind the core teeth from buried faults results from the magnetic flux induced by radial fault current

⁴⁹ Unpublished research shows that Holm contact areas on electrical steel needed to achieve the fault currents modelled are very small, $<0.1 \text{ mm}^2$.

flow, not axial, and this flux is constrained by packet air gaps. This supports the use of the 2D FE transverse model differential corrections as reasonable estimates for the presence of packet air gaps.

A limitation with the 2D FE models was that any flux flowing axially between laminations will in practice also be resisted by eddy currents developed in the laminations. However these are only realistically modelled in a 3D FE software package that can support eddy currents within the constraint of laminar structures, not possible here for reasons given earlier. In consequence this effect had to be ignored.

There were a few practical problems. While the application of the buried faults was the most effective way that could be devised to apply the necessary high forces in a very small enclosed area, a fault could not be re-applied to within <10% of the previous attempt's current. However since the overall current was measured, this error was compensated for in the analysis, though secondary effects of non-uniformity were not. It is possible that a hydraulic or pneumatic system may prove more effective in applying faults with uniform repeatable pressure than mechanical wedging. Regardless the method was comparable to the successful validation of the surface faults by Ho et al. [165], and much more representative and repeatable than the welded faults used by EPRI [57] and recently by other researchers such as Müller et al. [171].

The method of measuring current distribution was limited in precision, since it relied on the manual positioning of trace wires on adhesive tapes to sub-millimetre accuracy, and for this assembly to remain stable under pressure down the fault hole. The mean current was less affected since it used the total length of the fault. A possible improvement might be a custom printed conductor assembly whose geometry is more accurate and stable.

While the prime concern of this study was the validation of the 3D FE models of buried core faults, this also usefully quantified their detection sensitivity to the EMT measure of *Quad* signal. This showed that the buried tooth fault, had a relative sensitivity of ~30% of comparable tooth/slot surface faults, while faults buried ~30% of the yoke depth had a relative sensitivity of ~10%. While this detection sensitivity is very low, it still shows that Gandshu et al.'s [97] claim that 'the fault is practically undetectable when locates deeper than ¼ of yoke height' is overly pessimistic.

Low detection sensitivity to buried faults would appear to lead to potentially damaging local temperatures, since the nominal 100 mA/10°C correlation described in Chapter 4 is for surface faults of ~15 mm length of sensitivity 0.31. This implies that, at the 100 mA warning threshold, the buried tooth Fault_5 would achieve ~30 °C and the

buried core yoke faults ~ 100 °C for the same length fault. (These would of course be less for longer faults.) However these regions are surrounded by the substantial thermal resistance of the steel, and it is thus quite possible that this would sufficiently attenuate the higher source temperature before reaching the thermally critical winding insulation. Conversely it does indicate that quite modest *Quad* signals from clearly buried faults need to be considered seriously, since >300 mA may indicate buried temperatures in the yoke reaching the pyrolysis threshold of the interlamination insulation, and thus able to initiate a runaway core fault [18].

11.12. Summary

Ho had developed but not verified a 3D FE model of stator core faults buried in the teeth and yoke of the core. A new experimental methodology was developed to apply the faults non-destructively and measure their currents on the DAX8 test stator core. Further FE models were used to determine and compensate for the effect the intrusive holes would have on the results. After compensation for the differences between the modelled and experimental stator cores, the nine 3D FE results showed a close mean prediction but unsatisfactorily high variance of the fault signals at equal fault flux. The high variance was found to be due to imperfect fault current modelling.

Correction of the results to eliminate the difference in fault currents gave a much reduced variance, but now under-prediction of results. This was considered to be due to the presence of packet air gaps, absent in the 3D model, increased the signal mpd due to flux concentration, particularly on longer faults approaching the packet length. A system of transverse 2D FE models was constructed of the principal fault flux paths in the core to determine the reduction in axial flux divergence due to constraint by the packet air gaps. This approach also demonstrated that the majority of the mpd developed between the core teeth for short faults results from the flux induced by radial fault current flow, not axial.

This effect was shown to occur both within the core yoke and particularly in the development of the mpd between the tooth tips across a stator slot. Correction of the 3D FE model results using the new 2D FE models produced a mean prediction error of -3.7% with $<10\%$ standard deviation. The EL CID detection sensitivity to the buried faults was shown (as expected) to be substantially reduced, from 30–10% of comparable surface fault sensitivities, completing the set of comparative detection sensitivity measures for varying fault lengths.

Chapter 12. Conclusions

12.1. Review of presented work

Modern societies' dependence on electricity naturally requires a high service reliability of generation plant. This is addressed through condition monitoring regimes seeking signs of degradation in advance of failure, such that preventative action can be taken. In ac generators, and related high power motors, the stator core interlamination insulation is very reliable, representing just 4% of major generator stator core failures. However interlamination insulation failure can have catastrophic consequences, while even modest faults cause local heating which can shorten the life of high voltage winding insulation. Consequently improving the reliability of the offline stator core test and interpretation metrics will directly improve the competence of condition monitoring programmes. This thesis investigates aspects of the electromagnetic stator core test, particularly the dominant EL CID, where its capability or interpretation remains uncertain.

12.1.1. Literature review and comparison of stator core tests

A thorough literature review was conducted of all approaches to testing for stator core interlamination insulation damage, considering both those in use and abandoned, and research into understanding and modelling the test processes.

The high flux stator core test (HFT, introduced in the 1950s) is time-consuming and hazardous. An alternate low flux electromagnetic test system (EMT) was developed in 1979 known as EL CID, which senses the magnetic field (*Quad* current) from induced fault currents. This is now the dominant system in use. The most common alternative EMT system, DIRIS, uses an alternate metric of equivalent fault power. Analysis of the detection sensitivities shows that the test warning thresholds (EL CID at 100 mA and DIRIS at 15 W) are in fact closely aligned for short faults <30 mm. It was further shown that the actual fault temperature can vary 10:1 with length for both unvarying fault metrics. Other EMT systems in significant local use are Siemens' SMCAS operating in the same manner as EL CID, and Russian EMK systems. The EMK fault metrics of both fault power and '*Ka*' are analysed and shown to also reasonably correlate to EL CID *Quad* current signals. All other known approaches were reviewed.

All above systems require offline machine access. The Generator Condition Monitor is the only online stator core test system with some limited success, however it is not considered a reliable monitor of incipient stator core faults. Shaft voltage monitoring was

found to be of very limited competence, while research attempts to detect developing core faults by external electromagnetic fields or electrical parameter change show little promise.

Research into the development of stator core faults is sparse, with no proven process of fault initiation known, though studies have modelled the development of runaway faults once sufficient fault connectivity has occurred. Research into electromagnetic stator core fault detection is also limited, with the first authoritative study in 1995 and models in 2D FE from 1999. The use of 3D FE models only commenced from 2006 when the only study of buried faults occurred, but these were not validated. Modelling the full 3D interaction of a fault with a laminated conductive core currently remains incomputable, thus all studies have relied on some approximation.

12.1.2. Analysis of EL CID electromagnetic test

Despite commercialisation since 1982, gaps remain in the understanding of the EL CID test. The development of the power in a core fault, and the detection of the current as the *Quad* metric, is analysed including the interaction with core loss. It was shown that the 100 mA fault metric is modestly affected by core loss for faults dominated by resistance, however as the fault becomes more severe, the *Quad* signal can be substantially attenuated or inverted when fault reactance exceeds resistance. This can have important consequences for fault interpretation if the fault severity is not visible.

The measurement of the *Quad* signal is achieved by phase sensitive detection that works on the principle of synchronous detection. Analysis of the common ‘square wave’ EMT demodulation process showed that odd harmonics may also be demodulated as a *Quad* signal. EMT instruments using DSP demodulation with sine wave references are not susceptible to harmonic demodulation.

12.1.3. Correlation of EMT and HFT in the field

EMT stator core tests are undertaken assuming the commonplace 5–10 °C/100mA correlation with the HFT thermal measure, however the evidence for it is uncertain. This study investigated 106 records to determine the correlation actually occurring in the field between fault heating and EL CID *Quad* signal, and the test variables that can affect it. Test parameters can substantially affect results and five normalisation corrections were applied where possible. An experimental EPRI study reported very poor correlation, but after adjustment for normalisation corrections and errors was also shown to closely fit the assumed correlation.

The overall result is encouraging evidence that the HFT and EL CID tests are in practice quite strongly correlated, and that the industry expectation of 5–10 °C/100mA is supported with central quartiles of 6–12 °C/100mA. Furthermore 95% of tests will correlate under 18 °C/100mA, consequently the probability of an EL CID test failing to detect a serious core fault, which a HFT would have detected, is very low.

12.1.4. Interaction of multiple faults

If there is axial alignment of multiple severe faults, their EL CID *Quad* signals can interact. An opposite fault signal occurs proportioned around the local circumference, causing misleading reduction of other fault signals. This newly discovered phenomenon, called ‘Quad recovery’, is the result of the sensing and reference methods.

It was investigated using a transverse 2D FE magnetostatic model with the lamination segmentation, stacking and packet air gap structure explicitly modelled. This showed the recovery of the imposed fault current potentials remained very biased towards the fault region, unlike that seen in the field. However use of a time-harmonic model to also allow eddy current formation in the individual laminations, showed these currents to be quite effective in linearising the recovery around the stator. An algorithm to assist in the field compensation of the effect of Quad recovery was developed, with field examples.

12.1.5. Impact of varying core loss and permeability on electromagnetic tests

The standard model for the EMT assumes that the core is composed of lamination steel with uniform magnetic properties. However circumferential variances in core loss and permeability caused by non-uniform steel (e.g. differing suppliers) have been shown to give rise to substantial fault signal artefacts, not due to actual interlamination insulation defects.

An analytic study showed that at low flux densities, up to +/-50% variation in core loss or permeability is quite feasible, and that significant fault signals above the 100 mA warning threshold can be developed in stator cores with <50% magnetic non-uniformity and no fault present. While the artefact signals are not electrically separable from actual fault signals, their shape and distribution are predicted to differ from actual faults to allow their elimination, and the detection of genuine faults is shown not to be obscured by the artefacts. The phenomena was experienced and validated in the field.

12.1.6. Impact of varying and non-linear permeability on electromagnetic tests

The permeability and hysteresis of electrical steel varies substantially with flux density at the low flux density excitation levels used in an EMT. The use of sinusoidal

magnetic flux density thus results in harmonics being generated in the toroidal excitation magnetic field strength, which if non-uniform around the core, may be demodulated as fault signal artefacts. The non-linearity is due to Rayleigh hysteresis, a parameter not specified in commercial steels. Thus a method to estimate the Rayleigh hysteresis from commercial steel data with improved reliability was developed.

Sinusoidal flux density is shown to prevent an analytic solution of the resultant magnetic field strength, thus numeric integration was used to compute the harmonic and potential *Quad* signals for a range of steels. Due to fortuitous harmonic phase angles and filtering, the impact of these is shown to be minor.

12.1.7. Impact of lamination joint reluctance on stator core tests

The toroidal induction of a segmented stator core where saturation flux density levels are reached at half-overlap lamination joints, develops large magnetic fields at these joints. This causes the overall toroidal reluctance to rise substantially, such that by flux density levels of 1.2 T the excitation for a typical core increases by ~190% over that expected. It was conversely shown that the magnetic anisotropy that still exists in non-oriented electrical steel can modestly reduce the prediction of the toroidal reluctance. A new method to analytically extrapolate electrical steel saturated performance was developed to allow an assembled stator B/H curve to be predicted using measured and extrapolated material data and FE modelled joints. It was shown to closely match the measured stator.

While this effect was long predicted by researchers, the impact on magnetic circuit design and especially high flux testing remains apparently unrecognized in practice. The issue is normally of low importance for electrical machine magnetic design, however without allowance for lamination joint saturation, permeability anisotropy, and excitation current crest factors, the required stator core excitation can be 93% more than estimated, leading to under-testing.

12.1.8. Experimental verification of buried fault FE models

A previous researcher (Ho) developed 3D FE models of a range of stator core faults both on the bore surfaces and within the core body ('buried'). However Ho only progressed to verification of the surface faults on a matching experimental core, now unavailable. A new experimental stator core (DAX8) was constructed, and Ho's experiments repeated to prove the geometric scaling between the modelled and 14% larger DAX8 cores was correct.

The impact on the detected electromagnetic field strength due to the intrusion of buried fault test sites was modelled to allow compensation. A further correction was needed to compensate for the circumferential images developed in the 3D FE model, due to the attenuation from the Quad recovery effect. The fault results showed a close mean correlation but unsatisfactorily high variance of the fault signals at equal coupled flux in the fault, due to imperfect fault current modelling. Correction of the results to equalise modelled and measured fault currents allowed measurement of just the detection sensitivity. This gave a much reduced variance, but 27% mean under-prediction of results.

This difference was considered to be due to the presence of packet air gaps, absent in the 3D model due to modelling limitation. A transverse 2D FE model system was developed of the principal fault flux paths in the core and teeth, to determine the increase in signal mpd due to flux concentration by packet air gaps. The resultant correction of the original 3D FE model results produced a mean error of -3.8% with 9.8% standard deviation, a prediction within the experimental error margins.

This research provided evidence of the detection sensitivity for two new classes of short fault, those buried in the tooth and core yoke. They are shown to be substantially reduced at the depths modelled, being 30–10% of comparable surface fault sensitivities.

12.2. Significant contributions of thesis

- i. Completed first review of all published stator core tests, off and online, comparing their competences.
- ii. Correlated the differing fault current and fault power EMT parameterisations.
- iii. Demonstrated that the commonplace but unproven correlation between EL CID and HFT is statistically validated in the field.
- iv. Revealed and analysed the interaction of multiple circumferentially aligned faults and developed an analytic compensation procedure, corroborated on field projects.
- v. Researched how fault signal artefacts can occur due to lamination material variation and their impact on test results, also validated in a field project.
- vi. Researched the impact of Rayleigh hysteresis on harmonic generation and showed, with experimental verification, that for common electrical steels it has only a minor effect on test results.
- vii. Identified the poor industry appreciation of the problem of stator core lamination joint reluctance. A new analytic saturation model for electrical steel to use in an FE

model enabled its effect to be predicted which matched experimental evidence. Its impact on high flux stator core testing was also quantified.

- viii. Developed an experimental means of validating modelled results of buried faults. Demonstrated that the original 3D FE buried fault models suffered from circumferential image problems and errors from absence of radial ventilation gaps. New FE compensation methods were developed for these, which showed a close experimental correlation to models. A set of short fault detection sensitivity curves for buried fault detection was validated.

12.3. Limitations of the research

The research has inevitably had to accept limitations on the extent and detail of the study that could be completed. These are identified and their likely impact described in the discussion related to each contribution.

The work has concentrated on the EL CID system due to its dominance. In general the results will also apply to the SMCAS system since it also uses a quadrature signal resolution system. However other systems using phase angle change (DIRIS and EMK) will need further study to determine the applicability and scale of the results.

It will be evident that the research has focussed particularly on turbo-generators, and experimentally in the ~100 MW region. While wherever possible the general case has been considered, this leaves open the variation that may occur with greatly differently sized or geometrically different machines such as hydro-generators.

12.4. Published work from this research

The following papers have been published. Those peer reviewed are marked ©.

- [203] D. R. Bertenshaw and B. Chapman, 'EL CID results interpretation in the presence of substantial core faults,' in *EPRI European Turbine Generator User Group Workshop* Madrid, Spain: EPRI, 2009, p. 6.
- [210] © D. R. Bertenshaw, J. F. Lau, and D. J. Conley, 'Evaluation of EL CID indications not associated with stator core interlaminar insulation faults,' in *Electrical Insulation Conference*, Annapolis, USA: IEEE, 2011, pp. 254-260.
- [189] D. R. Bertenshaw, 'Analysis of EL CID - High Flux test field correlation ' in *EPRI Turbine Generator Users Group Meeting*, J. Stein, Ed. Barcelona: EPRI, 2011, p. 8.
- [190] © D. R. Bertenshaw and A. C. Smith, 'Field correlation between electromagnetic and high flux stator core tests,' in *PEMD 2012, The 6th IET International Conference on Power Electronics, Machines and Drives*, Bristol, UK: IET, 2012, pp. 0025/1-6.

- [23] D. R. Bertenshaw, 'A history of stator core testing,' in *EPRI 2013 Winter Turbine Generator User Group Workshop*, Savannah, USA: EPRI, 2013, p. 40.
- [214] © D. R. Bertenshaw and A. C. Smith, 'The impact of non-linear permeability on electromagnetic stator core tests,' in *PEMD 2014, The 7th IET International Conference on Power Electronics, Machines and Drives* Manchester, UK: IET, 2014, pp. 0052/1-6.
- [239] © D. R. Bertenshaw and A. C. Smith, 'Lamination joint reluctance in stator cores — a forgotten problem?,' in *PEMD 2014, The 7th IET International Conference on Power Electronics, Machines and Drives*, Manchester, UK: IET, 2014, pp. 0053/1-6.

12.5. Relevance to Industry

As noted in the introduction, electromagnetic stator core testing, especially with the dominant EL CID system, is in use around the world to assess the condition of major generation plant. Important and expensive maintenance decisions are made on the basis of the test results, and thus improvements in the reliability of the test and its interpretation have direct economic benefit to society. This can come from either better identification of real faults that might otherwise develop unnoticed, or avoidance of wasted costs and time investigating phantom defects. Improvement in confidence of the correlation between the EMT and HFT will also assist by reducing the need for expensive double testing. The new verified detection sensitivity data for detection of buried faults allows more reliable fault interpretation to be made in the very challenging region of the core yoke.

The research results have already directly assisted several industrial projects. The issued reports are listed below (anonymised) with their thesis subject Chapter.

TR004	Report on EL CID and Flux Tests on ABB Core at **, 2009	Chapter 6
TR024	Report on EL CID tests on Stator from ** NPP, 2010	Chapter 7
TR027	EL CID detection of faults on ** NPP, 2010	Chapter 7
TR034	Notes on Banded Core for **, 2011	Chapter 7
TR051	** Unit 3 Review of Stator Core Condition Reports, 2012	Chapter 6
TR057	** Unit 2, Review of Stator Core EL CID Tests, 2013	Chapter 11

12.6. Future work

The studies in this thesis have established a number of new fault interpretation metrics for the EMT, and identified areas where non-fault variances can cause misleading results. At the onset of the work it was clear that the research could only tackle a limited number of such issues within the given time and resources. This left many remaining, while the work has inevitably identified further issues warranting study.

-
- i An unexplained phenomenon is that at low flux density levels a small but consistent decrease in magnetic field strength is measured at the joints, rather than the increase which would be expected, and which the FE models in both Chapter 6 and Chapter 10 show. This possibly has non-linear permeability as its source and should be investigated. It may have relevance to fault interpretation.
 - ii It is important to demagnetise a stator core before an EMT, as any remanence not only increases excitation current but affects the fault-indicating *Quad* signal, which becomes increasingly variable. The reason for this is unknown, and is important in the field since demagnetising a full stator is normally impractical.
 - iii The standard model of a stator core fault assumes the fault inductance is solely that from the toroidal flux path. This simplification is shown to be flawed, both in the tendency for the toroidal fault flux path to have lower reluctance than expected, as well as the development of significant local flux circulation around the radial fault currents. A 3D model reflecting the lamination currents is needed to quantify this, and thus better determine when severe faults become inductively limited.
 - iv The study of the Quad recovery phenomenon showed that an important fault flux constraining phenomena is the development of a complex array of nearly opposing eddy currents in the lamination segments, however the field results showed that this level of constraint was not always borne out in practice. While currently the solution of a half-core stator 3D FE model at segmented lamination level is computationally impractical, studies should continue on means of more realistically modelling fault current and simulating constraining eddy currents.
 - v While the impact of electrical steel loss and permeability variances on EMT results has been shown, core pressure is also known to affect test results and is variable in service. This would similarly benefit from study and quantification.
 - vi The unexpected constancy of the correlation between HFT and EMT for the greatly reduced axial voltage field levels in hydro-generators indicates that possibly the tooth geometry is an important aspect of the HFT sensitivity. This warrants further investigation to determine the root cause for this effect, so that the EMT can be applied with greater confidence on hydro-generators.
 - vii The HFT and EMT both established their thresholds from the perceived thermal threat to the winding insulation. The actual correlation of this threat from both the

thermal and electromagnetic fault signals for wound stators (where the winding obscures IR thermography) remains unresearched. and information on this would improve assessment of the true threat of a detected fault.

REFERENCES

- [1] F. Nebeker, 'The Electric Century', *IEEE Spectrum*, vol. 37, issue: 6, 2000, pp. 68-74.
- [2] 'The history of CIGRE'. Paris: CIGRE, 2011.
- [3] S. Matthewman and H. Byrd, 'Blackouts: a sociology of electrical power failure', *Social Space Scientific Journal*, vol. socialspacejournal.eu, issue: 2/2013, 2013, pp. 31-56.
- [4] J. Horner, 'Talking Point - What will Europe's power sector look like in 2020', Pennwell, Power Engineering International, May ed., 2014.
- [5] E. Davey, 'Electricity market reform: consultation on proposals for implementation', London: Energy and Climate Change, HMG, 2013, p. 288.
- [6] P. Tavner, L. Ran, J. Penman, and H. Sedding, 'Condition monitoring of rotating electrical machines', 2 ed.: Institution of Engineering Technology, 2008.
- [7] P. J. Tavner, 'Review of condition monitoring of rotating electrical machines', *Electric Power Applications, IET*, vol. 2, issue: 4, 2008, pp. 215-247.
- [8] G. Klempner and I. Kerszenbaum, 'Handbook of large turbo-generator operation and maintenance', 2 ed.: IEEE Press / Wiley, 2008.
- [9] 'Generator maintenance, inspection and test programmes', CIGRE, Paris, TB 386, August 2009.
- [10] 'Main generator on-line monitoring and diagnostics', EPRI, Palo Alto, USA, TR-107137, 1996.
- [11] A. Lemberg and K. Tornroos, 'GE generator fleet experience and available refurbishment options', GE Energy, GER-4223, January, 2004.
- [12] 'Survey of hydrogenerator failures', CIGRE, Paris, TB 392, October 2009.
- [13] T. Kunz and A. Schwery, 'Generator refurbishment', in IEEE PES Swiss chapter - Workshop June 2008, Grimsel 2008, p. 45.
- [14] B. G. Cunningham, 'Testimony of Barry G. Cunningham', PacifiCorp, Utah, Public Service Commission of Utah, read: 12-1-2006, 2001.
- [15] 'Repair and testing guide for generator laminated cores grounded at the core outside diameter', EPRI, Palo Alto, USA, Report 1007441, 2002.
- [16] C. Maughan, 'Maintenance of turbine-driven generators', 3 ed http://66.165.147.87/index_files/Page352.htm: Private book publication, 2014, p. 248.
- [17] G. C. Stone, I. Culbert, E. A. Boulter, and H. Dhirani, 'Electrical insulation for rotating machines: design, evaluation, aging, testing and repair', 2 ed.: Wiley, 2014.
- [18] P. J. Tavner and A. F. Anderson, 'Core faults in large generators', *IEE Proceedings, Electrical Power Applications*, vol. 152, issue: 6, November 2005, pp. 1427-1439.
- [19] J. S. Edmonds, A. Daneshpooy, S. J. Murray, and R. A. Sire, 'Turbogenerator stator core study', in SDEMPED 2007, IEEE International Symposium on Diagnostics for Electric Machines, Power Electronics and Drives, Cracow, Poland, September 2007, pp. 441-446.
- [20] H. R. Tomlinson, 'Interlaminar insulation test for synchronous machine stators', *Power Apparatus and Systems, Part III. Transactions of the American Institute of Electrical Engineers*, vol. 71, issue: 1, January 1952, pp. 676-677.
- [21] J. Sutton, 'EL CID: an easier way to test stator cores', UK, Electrical Review, 207, 4 July 1980.
- [22] R. M. Tallam, S. B. Lee, G. C. Stone, G. B. Kliman, J. Yoo, T. G. Habetler, and R. G. Harley, 'A survey of methods for detection of stator-related faults in induction

- machines', *IEEE Transactions on Industry Applications*, vol. 43, issue: 4, July/August 2007, pp. 920-933.
- [23] D. R. Bertenshaw, 'A history of stator core testing', in EPRI 2013 Winter Turbine Generator User Group Workshop, Savannah, USA, January 2013, p. 40.
- [24] A. P. Chattock, 'On a magnetic potentiometer', *Proc. Phys. Soc. London*, vol. 9, 1887, pp. 23-26.
- [25] 'EL CID (Electromagnetic - Core Imperfection Detector) testing of large steam-turbine-driven generators', CIGRE, Paris, TB 257, 2004.
- [26] 'EL CID user manual', V5.5 ed. Toronto, Canada: Iris Power, 2011.
- [27] C. Ginet, R. Joho, and M. Verrier, 'The turbogenerator – a continuous engineering challenge', in *Power Tech*, 2007, Lausanne, July 2007, pp. 1055-1060.
- [28] R. H. Parsons, 'The early days of the power station industry': Cambridge University Press, 1940.
- [29] V. J. Vickers, 'Recent trends in turbogenerators', *Proceedings of IEE*, vol. 121, issue: 11R, November 1974, pp. 1273-1306.
- [30] S. P. Thompson, 'Polyphase electric currents and alternate current motors'. London: Spon, 1895.
- [31] F. R. Harris, 'The Parsons Centenary - a hundred years of steam turbines', *Proceedings of the Institution of Mechanical Engineers, Part A*, vol. 198A, issue: 9, May 1984, pp. 183-224.
- [32] G. Neidhofer, 'The evolution of the synchronous machine', *IEE Engineering Science and Education Journal*, vol. 1, issue: 5, 1992, pp. 239-248.
- [33] P. Beckley, 'Electrical steels for rotating machines', vol. Power and Energy series: IEE, 2002.
- [34] L. W. James, 'Large turbine generators, the British story', *IEE Electronics and Power*, vol. 9, August 1973, pp. 304-306.
- [35] P. Richardson, 'Developments in large turbo-type generators', *IEEE Transactions on Power Apparatus and Systems*, vol. 82, 1963, pp. 639 - 646.
- [36] R. F. Gray, L. Montgomery, R. Nelson, J. Pipkin, S. Joki-Korpel, and F. Caguiat, 'Designing the cooling systems for the world's most powerful turbogenerator - Olkiluoto unit 3', in IEEE Power Engineering Society General Meeting, 2006, Montreal, Canada, October 2006, p. 5.
- [37] 'Nuclear power plants for Poland NPPP, ' Siemens, Warsaw
http://apw.ee.pw.edu.pl/tresc/-eng/15-n3p06_SIEMENS.pps, 2006.
- [38] K. Abegg, 'The growth of turbogenerators', *Philosophical Transactions of the Royal Society of London. Series A, Mathematical and Physical Sciences*, vol. 275, issue: 1248, 1973, pp. 51-67.
- [39] J. P. Harbord, 'Some tests on modern high-speed turbo alternators', *IEE Students' Quarterly Journal*, vol. 24, issue: 93, September 1953, pp. 3-9.
- [40] C. Maughan, 'Testing of turbine-generator stator core lamination insulation', in EPRI 2004 Winter Workshop and Turbine & Generator Users Group (TGUG) Meeting, Albuquerque, USA, January 2004, p. 6.
- [41] P. G. Ross, 'Factory testing of large synchronous machines', *Electrical Times*, March - April 1955.
- [42] G. K. Ridley, 'High flux core test', to D. R. Bertenshaw, Private communication, UK, 07 January, 2011.
- [43] J. H. Walker, 'Large synchronous machines - design, manufacture and operation', 2 ed. Oxford: Clarendon Press, 1981.
- [44] J. W. Shelton and B. M. Reichman, 'A comparative analysis of turbogenerator core inspection techniques', in Proceedings of the American Power Conference, Chicago, USA, 22-24 April 1985, pp. 643-650.

- [45] I. Lodge, 'Flux testing of generator stator cores', CEGB, SSD/NE/R293, 1975.
- [46] IEEE Std 56-1977, 'Guide for insulation maintenance of large alternating-current rotating machinery (10 000 kVA and Larger)', IEEE, USA, 1977 (reaffirmed 1991).
- [47] IEEE Std 432-1992, 'Guide for insulation maintenance for rotating electric machinery (5 hp to less than 10 000 hp)', IEEE, USA, 1992.
- [48] IEEE Std 62.2-2004, 'Guide for diagnostic field testing of electric power apparatus', IEEE, USA, 2005.
- [49] J. Lau, 'IEEE Std62-2 high flux 10C background', to D. R. Bertenshaw, Private communication, Charlotte, USA, 2 October, 2010.
- [50] RD 34.45-51.300-97, 'Volumes and norms for testing electrical equipment', RAO UES of Russia, 1997.
- [51] P. Ungureanu and C. Veres, 'Dyagnosys for the magnetic core of power generators, using infrared thermovision', in IFAC Workshop ICPS'07, Cluj-Napoca, Romania, 9-11 July 2007, pp. 246-250.
- [52] 'Guidelines - guidance on assessing the technical condition of turbine generators, exhaust stipulated normative life', RAO UES of Russia, 2008.
- [53] L. Cickaric, M. Sencanic, and N. Simic, 'Stator core imperfection detection on large turbogenerators using the rated induction method', in The 6th International Power Systems Conference, Timisoara, Romania, 3-4 November 2005, pp. 147-154.
- [54] J. Stein, 'EL CID and full flux core testing survey (22 responses)', EPRI, Palo Alto, USA, 2008.
- [55] C.-G. Richter, 'Testing stator cores of turbo generators using the ring flux method', in POWER-GEN Europe 2013, Vienna, June 2013, p. 19.
- [56] D. R. Bertenshaw, T. Chan, A. C. Smith, and C. W. Ho, 'Computational modelling of stator core faults in large hydrogenerators and turbogenerators', in Hydro 2004, Porto, Portugal. , October 2004, pp. 17.4, 1-8.
- [57] 'Generator core overheating risk assessment - core model studies', EPRI, USA., Report 1009855, 2004.
- [58] D. C. Renew, 'Core faults on 500MW generators. Part 1 historical review', CEGB, RD/L/N152/76, 1976.
- [59] 'CEGB Breakdowns investigated', Electrical Review, 29 January 1970.
- [60] D. J. Wallis and S. Kilmartin, 'Can you believe your GCM', in Eighth EPRI Steam Turbine - Generator Workshop, Nashville USA, 25-27 August 2003, p. 14.
- [61] J. Sutton, 'History of EL CID and fundamentals', in EPRI Motor & Generator Predictive Maintenance & Refurbishment Conference, Orlando, USA, November 1995, p. 10.
- [62] J. Sutton, M. Sasic, and D. R. Bertenshaw, '30 years experience with EL CID stator core testing', in Iris Rotating Machine Conference, Long Beach, USA, 17 June 2008, pp. 1-14.
- [63] 'Digital EL CID', ADWEL International, 2005.
- [64] 'Iris Power EL CID Evolution', http://www.irispower.com/hydro_offline_elcid.aspx, Toronto, Iris Power 2013.
- [65] J. Sutton, 'EL-CID - an easy way to test stator cores', *CEGB Research*, issue: June 1982, June 1982, p. 7.
- [66] D. R. Bertenshaw, 'Analysis of stator core faults - a fresh look at the EL CID vector diagram', in Hydro 2006, Porto Carras, Greece, September 2006, pp. 15.02, 1-10.
- [67] G. K. Ridley and D. R. Bertenshaw, 'A deeper insight into EL CID', *International Journal on Hydropower and Dams*, vol. 12, issue: 4, 2005, pp. 87-91.
- [68] J. Sutton, 'Procedures for the use of electromagnetic core imperfection detector (EL CID)', CEGB, RD/L/R 2023, 1981.

- [69] M. Hobelsberger, I. Kirchhoff, E. Nodwell, and Z. Posedel, 'Method and device for inspecting laminated iron cores of electrical machines for interlamination shorts', US Patent Office, US 6,815,957, 2004.
- [70] Z. Posedel, 'Method and apparatus for inspecting laminated iron core stacks for interlamination shorts ', US Patent Office, US 4,996,486, 1991.
- [71] Z. Posedel, 'Inspection of stator cores in large machines with a low yoke induction method—measurement and analysis of interlamination short-circuits', *IEEE Transactions on Energy Conversion*, vol. 16, issue: 1, March 2001,
- [72] C. W. Ho, 'Detection of stator core faults in electrical generators'. vol. PhD Thesis: University of Manchester, 2006, p. 262.
- [73] T. J. Roberts, 'Determination of the thermal constants of the heat flow equations of electrical machines', *Proceedings of the Institution of Mechanical Engineers, Conference Proceedings*, vol. 184, issue: 9, September 1969, pp. 84-92.
- [74] D. Zlatanaovici and R. Zlatanaovici, 'Diagnosis of the electric generator stator core by means of the low induction iron test, PROFIM', *Journal of sustainable energy - Faculty of Power Engineering, Oradea, Romania*, vol. 2, issue: 2, 2011, pp. 24-29.
- [75] D. Zlatanovici and R. Zlatanovici, 'Metode off-line si on-line de diagnoza a generatoarelor electrice de mare putere utilizand instrumentatia virtuala', in Conferinta Nationala de Invatamant Virtual – CNIV 2004, Bucharest, Romania, September 2004, pp. 59-64.
- [76] R. Zlatanaovici and D. Zlatanaovici, 'Stator core faults detection with low flux density method', *University Politehnica of Bucharest - Scientific Bulletin Series D*, vol. 75, issue: 2, 2013, pp. 207-217.
- [77] S. B. Lee, M. R. Shah, G. B. Kliman, T. W. Mall, N. K. Nair, and R. M. Lusted, 'An advanced technique for detecting inter-laminar stator core faults in large electric machines', in Industry Applications Conference, Conference Record of the 38th IAS Annual Meeting. , 12-16 October 2003, pp. 1374-1381.
- [78] S. B. Lee, G. B. Kliman, M. R. Shah, T. W. Mall, N. K. Nair, and R. M. Lusted, 'An advanced technique for detecting inter-laminar stator core faults in large electric machines', *IEEE Transactions on Industry Applications*, vol. 41, issue: 5, September/October 2005, pp. 1185- 1193.
- [79] S. B. Lee, G. B. Kliman, M. R. Shah, N. K. Nair, and R. M. Lusted, 'An iron core probe based inter-laminar core fault detection technique for generator stator cores', *IEEE Transaction on Energy Conversion*, vol. 20, issue: 2, June 2005,
- [80] S. B. Lee, G. B. Kliman, M. R. Shah, D. Kim, T. W. Mall, N. K. Nair, and R. M. Lusted, 'Experimental study of inter-laminar core fault detection techniques based on low flux core excitation', *IEEE Transactions on Energy Conversion*, vol. 21, issue: 1, March 2006, pp. 85-94.
- [81] S. B. Lee, G. B. Kliman, and T. W. Mall, 'Test probe for electrical devices having low or no wedge depression ', US Patent Office, US 6,927,598, 2005.
- [82] S. B. Lee, G. B. Kliman, M. R. Shah, and T. G. Richter, 'Test probe', US Patent Office, US 6,847,224, 2005.
- [83] S. B. Lee, D. Kim, and T. W. Mall, 'Manual probe carriage system and method of using the same ', US Patent Office, US 7,208,971, 2007.
- [84] G. B. Kliman, R. J. Carl, M. R. Shah, and S. B. Lee, 'Universal sensor probe with adjustable members configured to fit between a plurality of slot openings of varying widths ', US Patent Office, US 7,466,126, 2008.
- [85] 'Generator test and inspection fact sheet', GE Energy, GEA13004B, 2011.
- [86] C. Markman and R. J. Zawoysky, 'Generator in-situ inspections', http://site.ge-energy.com/prod_serv/products/tech_docs/en/downloads/GER3954C.pdf, GER3954C, 2012.

- [87] 'Recommended maintenance practices for electrical distribution system equipment', Hartford Steam Boiler (Munich re), USA, No. 420, 2010.
- [88] 'Generator In-Situ Inspection—Fast, Accurate Generator Inspection Without Field Removal', GE Power Generation Services, https://powergen.gepower.com/content/dam/gepower-powergen/global/en_US/documents/service/generator%20services/GEA16025C_Generator_In-Situ_Insp_R1.pdf, GEA16025C, April 2014.
- [89] 'FASTGen generator inspections', Turbocare, USA, http://www.turbocare.com/fastgen_generator_inspections.html, 2009
- [90] M. W. Fischer, J. W. Shelton, and M. J. Metala, 'Electromagnetic stator insulation flaw detector', US Patent Office, US 6,791,351, 2004.
- [91] M. W. Fischer, M. J. Metala, and J. W. Shelton, 'Siemens electromagnetic Core Analysis System (SMCAS) for generator inspections', in EPRI Turbine Generator User Group Meeting, Phoenix, USA, July 2007, p. 7.
- [92] M. Fischer, M. Metala, W. Abbasi, and J. Shelton, 'Siemens Multi-Frequency Core Analysis System (SMCAS) - progress update ', in EPRI Turbine Generator Users Group Meeting St Louis, USA, 18-20 August 2010, p. 8.
- [93] M. Fischer, 'EL CID workshop at Siemens, Pittsburgh', to D. R. Bertenshaw, Private communication, 8 November, 2010.
- [94] V. B. Berezhansky, L. I. Chubraeva, and G. V. Rostik, 'Experience with modified iron fault control technique for the stator cores of electrical machines', in Proc. IEEE Stockholm Power Tech Conference. Int. Symp. Electr. Power Eng., Stockholm, Sweden, 18-22 June 1995, pp. 108-112.
- [95] F. A. Polyakov, 'The steady temperature field in the region of a local short circuit of the iron laminations of the stator core of a turbogenerator', *Electrical Technology Russia*, vol. 4, 2000, pp. 49-57.
- [96] V. V. Gorodov, A. G. Vdovikov, Y. U. N. Samorodov, and V. N. V. Grechenkov, 'Facility testing fault of sheets of active steel in cores of stators of ac electric machines', Russian Patent Office, RU2195681-C1, 2003.
- [97] V. M. Gandshu, V. V. Gorodov, S. Dubitsky, and V. Podnos, 'Theoretical analysis of the ELCID method using QuickField FEA package', in ICEM2006 XVIIth International Conference on Electrical Machines, Chania, Crete, 2-5 September 2006, pp. OTA3-5.
- [98] 'Introskan-IS200 system for automated control circuits active sheet steel cores of electric machines', *Elektrotekhnicheskie Sistemy 1 (ES1)*, http://ets1.spb.ru/?page_id=95, read: 1-4-2010, 2010.
- [99] V. V. Gorodov, A. P. Lashitsky, and J. N. Samorodov, 'New tools for diagnosis of insulation condition of stator powerful electric machines', *Power 2003.*, vol. 9, 2003, pp. 1-7.
- [100] V. V. Gorodov, A. G. Vdovikov, V. M. Gandshu, and A. P. Lashitsky, 'The criterion of the defectiveness when using an electromagnetic method of detecting short-circuits between laminations of electrical machines (in Russian)', *ЭЛЕКТРОТЕХНИКА (Elektrotekhnik)*, issue: 4, 2003, pp. 35-41.
- [101] 'Pruebas de baja induccion en estatores de grandes generadores y motores core imperfection detection – ELCID test', Inducor Ingenieria S.A., Buenos Aires, Argentina, www.inducor.com.ar/articulos tecnicos/pruebas_de_baja_induccion_en_estatores_de_grandes%20generadores.pdf, 2013.
- [102] M. Sasic, 'Another EL CID! ', to D. R. Bertenshaw, Private communication, Toronto, 25 September, 2014.

- [103] M. Gavric, M. Senjamin, and M. Kotlica, 'Comparative analysis of stator iron core damage using nominal and reduced flux', in *Electrical Insulation Conference and Electrical Manufacturing & Coil Winding Conference*, Cincinnati, USA, October 26-28 1999, pp. 619 - 621.
- [104] J.-M. Bourgeois and F. Lalonde, 'Apparatus and method for evaluation a condition of a magnetic circuit of an electric machine', US Patent Office, US 5,990,688, 1999.
- [105] G. B. Kliman, S. B. Lee, M. R. Shah, R. M. Lusted, and N. K. Nair, 'A new method for synchronous generator core quality evaluation', *Proceedings of IEEE Power Engineering Society General Meeting*, vol. 3, issue: 3, July 2003, pp. 1888-1893.
- [106] G. B. Kliman, J. A. Mallick, and M. R. Shah, 'Method and system for detecting core faults', US Patent Office, US 6,469,504, 2002.
- [107] G. B. Kliman, M. R. Shah, and S. B. Lee, 'Differential sensor apparatus and method for laminated core fault detection', US Patent Office, US 6,873,152, 2005.
- [108] ELIN-UNION, 'Arrangement for measuring magnetic characteristics', Austrian Patent Office, AT390522B, 1984.
- [109] J. Ramirez-Nino and A. Pascacio S, 'Novel method for detecting interlamination short-circuits in a stator core based on measurement of eddy-current losses in power generators', *Institute of Physics Publishing Measurement Science and Technology*, vol. 14, 2003, pp. 2104-2110.
- [110] M. Ruiz, 'Alstom Hydro HF stator core tests', to D. R. Bertenshaw, Private communication, Bilbao, Spain, 6 April, 2010.
- [111] M. Baca, P. Haschke, C.-G. Richter, and H.-B. Twellmann, 'Laminated core testing device', European Patent Office, EP 1601985B1, 2007.
- [112] J. Sutton, 'A method and apparatus for testing laminated cores of electrical machines', UK Patent Office, GB 2382878B, 2005.
- [113] M. Sasic and D. R. Bertenshaw, 'EL CID testing of turbo-generators at higher frequency', in *EPRI Turbine Generator Users Group Meeting St Louis, USA*, 18-20 August 2010, p. 12.
- [114] M. Hobelsberger, 'Method for detection of interlaminar sheet short circuits in the stator sheet core of electromachines', US Patent Office, Application US2011/0012637, 2011.
- [115] J. Stein, 'On-line monitoring of shorted laminations in generator stator core ', EPRI, (Call for proposals), 30 June, 2004.
- [116] L. P. Grobel and C. C. Carson, 'Overheating detector for gas cooled electric machines', US Patent Office, US 3,427,880, 1969.
- [117] I. Lodge, 'Prevention of catastrophic failure of large generators by early detection of overheating', in *Proc. Int. Conf. of Electrical Machines-Design and Applications*, IEE, London 1982, pp. 123-130.
- [118] IEEE Std 1129-2014, 'IEEE Guide for online monitoring of large synchronous generators (10 MVA and above)', IEEE, USA, 2014.
- [119] 'On-Line condition monitoring tools for large turbine generators', CIGRE SC A1, Paris, ID45VER31, <http://a1.cigre.org/content/download/10580/329505/version/1/file/TG+Online+Monitoring1ID45VER39.doc>, October 2004.
- [120] R. Miller and M. Twerdochlib, 'Core monitor that uses rotor shaft voltages', US Patent Office, US 5032826, 1991.
- [121] S. C. Barton, C. C. Carson, R. S. Gill, W. V. Ligon, and J. L. Webb, 'Implementation of pyrolysate analysis of materials employing tagging compounds to locate an overheated area in a generator', *IEEE Transactions on Power Apparatus and Systems*, vol. PAS-100, issue: 12, 1981, pp. 4983-4989.

- [122] 'Gen-Tags', Environment One, New York, USA, http://s3.amazonaws.com/EONE_PUBLIC_WEB/public_files/EONE-Gen-Tags-brochure.pdf, 2013.
- [123] A. Gonzalez, S. Baldwin, M., J. Stein, and N. E. Nilsson, 'Monitoring and diagnosis of turbine-driven generators'. EPRI: Prentice Hall, 1995.
- [124] 'Guide for online monitoring of turbogenerators', CIGRE, Paris, TB 437, December 2010.
- [125] C. Maughan, 'Generator condition monitor evolution and capability', in Tenth EPRI Steam Turbine-Generator Workshop Phoenix, USA, 13-15 August 2007.
- [126] D. Reinhardt, 'Shaft voltages in electrical machines', *Energie und technik*, vol. 17, issue: 5, 1965, pp. 183-189.
- [127] J. L. T. Exon, 'Alternator core faults', CEGB, RD/L/N 152/70, 1970 (revised 1974).
- [128] R. J. Jackson, D. C. Renew, and M. L. Brown, 'The use of shaft voltage measurements to monitor turbogenerator stator cores', CERL, RD/L/N 32/80, 1980.
- [129] S. P. Verma, 'Damages due to shaft-potentials in modern generators', in Athens Power Tech, 1993. APT 93. Proceedings. Joint International Power Conference, 1993, pp. 842-846.
- [130] P. Nippes and E. S. Galano, 'Understanding shaft voltage and grounding currents of turbine generators', Magnetic Products and Services Inc., <http://gaussbusters.com/images/uploads/articles/Understanding%20Shaft%20Voltage%20and%20Grounding%20Currents%20of%20Turbine%20Generators.pdf>, 2014.
- [131] 'Generator stator core condition monitoring by tracking shaft voltage and grounding current', EPRI, USA., Report 1020275 (Abstract), http://my.epri.com/portal/server.pt?Abstract_id=00000000001020275, 2010.
- [132] K. Lee, J. Hong, K. Lee, S. B. Lee, and E. J. Wiedenbrug, 'A stator-core quality-assessment technique for inverter-fed induction machines', *IEEE Transactions on Industry Applications*, vol. 46, issue: 1, January/February 2010, pp. 213-221.
- [133] X. Wang and H. Liu, 'A model-based detection method for stator core fault in induction motors', *Advanced Materials Research* vol. 588 - 589, 2012, pp. 1068-1071.
- [134] R. Romary, R. Corton, D. Thailly, and J. F. Brudny, 'Induction machine fault diagnosis using an external radial flux sensor', *The European Physical Journal - Applied Physics*, vol. 32, issue: 02, 2005, pp. 125-132.
- [135] R. Romary, S. Jelassi, and J. F. Brudny, 'Stator interlaminar fault detection using an external flux density sensor', *IEEE Transactions on Industrial Electronics*, vol. 57, issue: 1, January 2010, pp. 237-243.
- [136] R. Romary, S. Jelassi, J. F. Brudny, and M. Mimouni, 'Detection of short circuits between stator laminations of electrical machine by analysis of external magnetic field', in ICEM 2008 - 18th International Conference on Electrical Machines, 2008, pp. 1-5.
- [137] R. Romary, C. Demian, P. Schlupp, and J. Roger, 'Off-line and on-line methods for stator core fault detection in large generators', *IEEE Transactions on Industrial Electronics*, vol. 60, issue: 9, 2013, pp. 4084-92.
- [138] A. Bytnar and R. Krok, 'Thermal diagnostics of stator core teeth of large turbogenerator', *Maszyny Elektryczne*, vol. 83, 2009,
- [139] M. H. J. Bollen, 'Literature search for reliability data of components in electric distribution networks', Eindhoven University of Technology, Faculty of Electrical Engineering., Eindhoven, EUT Report 93-E-276, 1993.

- [140] J.-L. Drommi, 'Stator core case studies of large turbo generators at Electricite de France', in EPRI International Workshop on Maintaining Integrity of Generator Cores, San Antonio, USA, 28 November 2001.
- [141] 'Report on large turbine generator maintenance practices', CIGRE, Paris, France, TB 002, August 1987.
- [142] 'Robotic Inspection Vehicle (RIV)', Toronto, <http://www.irispower.com/Upload/Brochures/RIV%20Flyer%20v3%20-%2011-13.pdf>, 2013.
- [143] D. D. Schoeler and P. O. Miranda, 'Improved unit reliability & availability through optimised predictive maintenance ', Siemens AG, Germany, ID269, 2003.
- [144] 'DIRIS® air gap robot diagnostic inspection', Alstom, Baden, 2010.
- [145] 'State of the art and capacity for robotic inspection of turbogenerators', CIGRE, Paris, France, TB 503, 2012.
- [146] 'Experience with limited access generator inspections. A study of inspections done with robotic equipment and their effectiveness as compared with conventional inspections where the generator rotor is removed', EPRI, Palo Alto, USA, Report 1000100, 2000.
- [147] D. R. Bertenshaw, C. Maughan, B. Milano, R. Ferguson, B. Wolf, M. Sasic, and J. Kapler, 'Round Table June 2010 - stator core testing '. vol. http://www.generatortechnicalforum.org/portal/articles.php?article_id=6: International Generator Technical Community Forum, 2010, p. 2.
- [148] K. Ridley, 'EL CID - application and analysis', 3 ed. Watford, UK: Adwel International Ltd, 2007.
- [149] D. R. Bertenshaw, A. C. Smith, C. W. Ho, T. Chan, and M. Sasic, 'Detection of stator core faults in large electrical machines', *IET Electric Power Applications*, vol. 6, issue: 6, July 2012, pp. 295-301.
- [150] R. J. Jackson, 'An electromagnetic mechanism for core fault initiation - preliminary note', CEGB Memorandum, LM/ELEC/040, 1976.
- [151] R. J. Jackson, 'Interlamination voltages in large turbogenerators', *Proceedings IEE*, vol. 125, issue: 11, November 1978, pp. 1232-1238.
- [152] R. J. Jackson, 'Discussion on interlamination voltages in large turbo-generators', *IEE Proceedings*, vol. 127, Pt C, issue: 2, March 1980, pp. 114-120.
- [153] R. L. Ny, A. E. Guile, and A. F. Anderson, 'Mechanism of "meandering" breakdown of insulation in an electrical machine', in First International Conference on Conduction and Breakdown in Solid Dielectrics, Universite Paul Sabatier, Toulouse, July 1983, pp. 395-399.
- [154] A. F. Anderson and A. E. Guile, 'An unusual type of interlaminar breakdown found in an electrical machine', in 6th Int. Conf. Gas Discharges and their Applications,, Heriot-Watt University, Edinburgh, September 1980, p. 4.
- [155] R. Platt, L. C. Kerr, and A. F. Anderson, 'Measuring flux and interlaminar voltage in turbine generator end regions', in International Conference on Electrical Machines – Design & Applications, July 1982, pp. 201-205.
- [156] A. F. Anderson, 'A note on generator core failures', A. F. Anderson, <http://www.antony-anderson.com/failure1.htm> read: 1-8-2009, 2007.
- [157] J. Sutton, 'Method of and apparatus for testing laminated magnetic cores', UK Patent Office, GB 2044936A, 1979.
- [158] J. Sutton, 'Theory of electromagnetic testing of laminated stator cores', *Insight – Journal of the British Institute of Non-Destructive Testing*, vol. 36, issue: 4, April 1994, pp. 246-251.

- [159] D. R. Bertenshaw and J. Sutton, 'Application of the EL CID Test with circulating currents in stator windings', in *Inductica 2004*, Berlin, Germany, 15-17 June 2004, pp. 128-134.
- [160] T. Otaka, T. Tokumasu, S. Nagano, H. Hasegawa, H. Shimada, S. Uemoto, and T. Kakiuchi, 'Evaluation of excitation circuit effects on EL CID test by analysis and testing', in *EPRI TGUG Winter 2004 Technical Workshop, Generator Core Inspection (EL CID) User Group Meeting*, Albuquerque, USA, 20th January 2004 2004, p. 7.
- [161] K. Ridley, 'Further development of the EL CID vector diagram', *International Journal on Hydropower and Dams*, issue: Issue Four, 2007, pp. 96-101.
- [162] R. Rettler and J. Brauer, 'Computer simulation of inter-laminar insulation failure and EL CID testing', in *Joint CIGRE and EPRI Rotating Machine Colloquium*, Florida USA 1999, p. 21.
- [163] D. Makuc, M. Berlec, and K. Lenasi, 'Investigation of ELCID testing using FEM analysis and test core measurements', in *Studies in Applied Electromagnetics and Mechanics, Electromagnetic Fields in Mechatronics, Electrical and Electronic Engineering - Proceedings of ISEF'05*, August 2006, pp. 199-204.
- [164] A. C. Smith, D. R. Bertenshaw, C. W. Ho, T. Chan, and M. Sasic, 'Detection of stator core faults in large turbo-generators', in *IEMDC2009*, Miami, USA, 3-6 May 2009, pp. 911-918.
- [165] C. W. Ho, D. R. Bertenshaw, A. C. Smith, T. Chan, and M. Sasic, 'Three-dimensional finite element analysis of large electrical machine stator core faults', *Electric Power Applications, IET*, vol. 8, issue: 2, 2014, pp. 60-67.
- [166] J. L. Müller, A. Benabou, T. Henneron, F. Piriou, J. P. A. Bastos, and J.-Y. Roger, 'Study of different FEM models to analyze homogenized iron lamination with electrical fault', in *COMPUMAG 2009*, Florianopolis, Brazil, November 2009, pp. 739-40.
- [167] J.-Y. Roger, E. Vrignaud, T. Henneron, A. Benabou, and J.-P. Ducreux, 'Electromagnetic modelling of short circuited coreplates', *COMPEL: The International Journal for Computation and Mathematics in Electrical and Electronic Engineering*, vol. 28, issue: 3, 2009, pp. 762 - 771.
- [168] T. Henneron, F. Piriou, and J.-Y. Roger, 'An approach to determine the circulation of magnetic field in FEM computation code with vector potential formulation', *IEEE Transactions on Magnetics*, vol. 47, issue: 5, May 2011, pp. 1354-1357.
- [169] J. L. Müller, A. Benabou, T. Henneron, F. Piriou, J. P. A. Bastos, and J.-Y. Roger, '3D FE modelling of interlamination short-circuits taking into account the building bars', in *COMPUMAG 2011*, Sydney, July 2011, pp. 1084-5.
- [170] G. Neidhoefer and A. Schwengeler, 'The application and significance of magnetic materials in large generator construction. ', *Journal of Magnetism and Magnetic Materials*, vol. 9 July 1978, pp. 112-122.
- [171] J. L. Müller, R. Romary, A. Benabou, T. Henneron, F. Piriou, J. P. A. Bastos, and J.-Y. Roger, 'Interlaminar short circuit detection: modeling and measurement', *COMPEL*, vol. 31, issue: 5, September 2012, pp. 1448 - 1457.
- [172] R. Romary, C. Demian, P. Schlupp, J. Y. Roger, and T. Szkudlapski, 'Real scale experimental devices for stator core fault analysis', in *2011 IEEE International Symposium on Diagnostics for Electric Machines, Power Electronics & Drives (SDEMPED)*, 5-8 September 2011, pp. 71-76.
- [173] G. Klempner, 'Ontario Hydro experience with failures in large generators due to loose stator core iron', in *EPRI - Utility Generator Predictive Maintenance and Refurbishment Conference*, Phoenix, USA, 1-3 December 1998, p. 6.

- [174] Y. B. Danilevich, I. I. Elin, E. V. Kazaryan, V. B. Kaplunov, and I. Y. Cheremisov, 'Electromagnetic and thermal processes in a turbogenerator stator core with shorting of active-steel laminations', *Soviet Electrical Engineering*, vol. 51, issue: 4, 1980, pp. 104-110.
- [175] K. Ridley, 'Evaluating interlamination circulating current at core joints in large machine stators', *International Journal on Hydropower and Dams*, vol. 15, issue: 6, 2008, pp. 106-114.
- [176] K. Ridley, 'Increased accuracy in determining interlamination fault current at stator core joints', *The International Journal on Hydropower and Dams*, vol. 16, issue: 6, 2009, pp. 104-107.
- [177] K. Ridley, 'Evaluation of interlamination circulating current at core joints in large machine stators', in *Hydro 2010*, Lisbon, 27-29 September 2010, pp. 1-9.
- [178] W. Rogowski and W. Steinhaus, 'Die Messung der magnetischen Spannung', *Archiv für Elektrotechnik*, vol. 1, issue: 4, 1912, pp. 141-150.
- [179] D. A. Ward and L. T. Exon, 'Using Rogowski coils for transient current measurements', *IEE Engineering and Science Journal*, June pp. 105-113.
- [180] D. R. Bertenshaw, 'Has the traditional EL CID vector diagram always been wrong?', to J. Sutton and D. Paley, Private communication, 17 August, 2005.
- [181] 'Power Core M310-50A electrical steel', ThyssenKrupp Steel Europe, 2009.
- [182] 'Material data sheet - electrical steel sheet M310-50A', C.D. Wälzholz, 2011.
- [183] 'Cogent non oriented electrical steel. Typical data', Surahammars Bruks AB, 2013.
- [184] J. Sutton and B. Chapman, 'Electromagnetic detection of damaged regions in laminated cores', in *IEE International Conference on Electrical Machines - Design and Application*, July 1982, pp. 119-122.
- [185] K. Ridley, 'Hydrogenerator EL CID results referred to High Flux Ring Test results', in *CIGRE Session*, Paris, France, August 2002, pp. 1-9.
- [186] 'Hydropower asset management using condition assessments and risk-based economic analyses + Appendix E', in *hydroAMP (Hydropower Asset Management Partnership) Guidebook USA: US Army Corps of Engineers*, 2006, p. 89.
- [187] G. Klempner, 'Experience and benefit of using EL CID for turbine-generators', in *Motor and Generator Predictive Maintenance and Refurbishment Conference*, Orlando, USA, 28 November 1995, pp. 1-16.
- [188] D. Barnett, 'Case study of a 400 MW generator core problem, results of EL CID, loop testing and continued operation', in *EPRI International Workshop on Maintaining Integrity of Generator Cores*, San Antonio, USA, 28 November 2001.
- [189] D. R. Bertenshaw, 'Analysis of EL CID - High Flux test field correlation', in *Turbine Generator Users Group Meeting Barcelona*, April 2011, p. 8.
- [190] D. R. Bertenshaw and A. C. Smith, 'Field correlation between electromagnetic and high flux stator core tests', in *PEMD 2012, The 6th IET International Conference on Power Electronics, Machines and Drives*, Bristol, UK, March 2012, pp. 0025/1-6.
- [191] 'Cogent non-oriented electrical steel', Surahammars Bruks AB, 2013.
- [192] S. J. Murray, J. S. Edmonds, J. R. Foulds, R. A. Sire, and W.-M. Chi, 'Modeling fault propagation in an electric generator stator core', in *Eighth EPRI Steam Turbine-Generator Workshop*, Nashville USA, 25-27 August 2003.
- [193] R. S. Gill and J. M. Kostoss, 'Comparison of electromagnetic core imperfection detector (El-Cid) and conventional core ring test results on X833', GE, Schenectady, USA, TGE 84-14, 1984.
- [194] C. Rickson, 'Electrical machine core imperfection detector', *IEE Proceedings*, vol. 133, issue: Pt B, No 3, May 1986, pp. 190-195.

- [195] E. J. Faria and E. L. Mazolla, 'Evaluation of the stator core quality and determination of imperfections in the insulation between sheets', in HydroVision 2006, USA 2006, pp. 1-6.
- [196] B. McNamara, 'Electromagnetic Core Imperfection Detection (ELCID), a collection of case studies', in Latin America Power 2000, Caracas, Venezuela, , May 2000, pp. 1-20.
- [197] D. B. Paley, B. McNamara, G. Mottershead, and S. C. Onken, 'Verification of the effectiveness of EL CID on a hydrogenerator stator core', in Hydrovision '98, USA, June 1998, pp. 1-14.
- [198] J. Sutton and B. Chapman, 'Stator core testing and partial restack of a hydrogenerator', in Doble 2004 Spring Conference, USA, April 2004, pp. 1-9.
- [199] A. S. Godoy, 'Experiencias en tecnicas de inspección a nucleos magneticos, parte I: turbogeneradores', in NOVENO Congreso Nacional de Máquinas Eléctricas Rotatorias, Cd. de Veracruz, October 1999, p. 6.
- [200] 'Generator core overheating risk assessment: J. T. Deely core investigation', EPRI, Palo Alto, USA, Report 1008378, 2003.
- [201] B. Clark, 'Stator lamination stacks: condition monitoring and repair of lamination short-circuits', Sensoplan, http://www.sensoplan.com/literature_42864/Loop_Test_and_Core_Repair.pdf, read: 7-11-2008, 2008.
- [202] Y. Abe, 'Generator back-of-core burning', in EPRI European Turbine Generator User Group 2009 Workshop, Madrid, Spain, June 2009 2009.
- [203] D. R. Bertenshaw and B. Chapman, 'EL CID results interpretation in the presence of substantial core faults', in EPRI European Turbine Generator User Group Workshop, Madrid, Spain, June 2009, p. 6.
- [204] D. C. Meeker, 'FEMM: Finite Element Method Magnetics', 4.2 ed: <http://www.femm.info>, 2013.
- [205] A. B. J. Reece and T. W. Preston, 'Finite element methods in electrical power engineering': Oxford University Press, 2000.
- [206] K. F. Riley, M. P. Hobson, and S. J. Bence, 'Mathematical methods for physics and engineering', 3 ed.: Cambridge University Press, 2006.
- [207] K. J. Binns, P. J. Lawrenson, and C. W. Trowbridge, 'The analytical and numerical solution of electric and magnetic fields': John Wiley & Sons, 1992.
- [208] P. Allaire, 'Basics of the finite element method'. Iowa, USA: Wm. C. Brown, 1985.
- [209] B. C. Mecrow and A. G. Jack, 'The modelling of segmented laminations in three dimensional eddy current calculations', *IEEE Transactions on Magnetics*, vol. 28, issue: 2, March 1992, p. 4.
- [210] D. R. Bertenshaw, J. F. Lau, and D. J. Conley, 'Evaluation of EL CID indications not associated with stator core interlaminar insulation faults', in Electrical Insulation Conference, Annapolis, USA, June 2011, pp. 254-260.
- [211] BS EN10106:2007, 'Cold rolled non-oriented electrical steel sheet and strip delivered in the fully processed state', CEN, 2007.
- [212] Z. Popovic and B. Popovic, 'Introductory electromagnetics', 1 ed.: Prentice Hall, 1999.
- [213] E. McDonald, 'Siemens stator donut core replacement update', in 6th EPRI Turbine Generator Technology Transfer Workshop and Turbine Generator Users Group meeting, St Louis, USA, 16-17 August 2010.
- [214] D. R. Bertenshaw and A. C. Smith, 'The impact of non-linear permeability on electromagnetic stator core tests', in PEMD 2014, The 7th IET International Conference on Power Electronics, Machines and Drives, Manchester, UK, 8-10 April 2014, pp. 0052/1-6.

- [215] C. P. Steinmetz, 'On the law of hysteresis', *Transactions of the American Institute of Electrical Engineers.*, vol. 9, issue: 1, 1892, pp. 1-64.
- [216] D. Jiles, 'Introduction to magnetism and magnetic materials', 2 ed.: Taylor & Francis Ltd, 1998.
- [217] R. M. Bozorth, 'Ferromagnetism': D. Van Nostrand Company, 1951.
- [218] L. Rayleigh, 'On the behaviour of iron and steel under the operation of feeble magnetic forces', *Philosophical Magazine Series 5*, vol. 23, issue: 142, 1887, pp. 225-245.
- [219] B. D. Cullity and C. D. Graham, 'Introduction to magnetic materials': IEEE Press - John Wiley & Sons, 2009.
- [220] G. Bertotti, 'Hysteresis in magnetism'. London: Academic Press, 1998.
- [221] W. B. Ellwood, 'Magnetic hysteresis at low flux densities', *Physics*, vol. 6, issue: 7, 1935, pp. 215-226.
- [222] G. Dietzmann and M. Schaefer, 'Rayleigh hysteresis with sinusoidal wave form of magnetic induction', *Journal of Magnetism and Magnetic Materials*, vol. 110, issue: 1-2, 1992, pp. 151-160.
- [223] G. Stevenson, 'Mathematical methods for science students', 1 ed. London: Longmans, Green and Co Ltd, 1966.
- [224] J. A. Baldwin, J. Revol, and F. Milstein, 'Failure of the Rayleigh hysteresis law in low magnetic fields', *Physical Review B*, vol. 15, issue: 1, 1977, pp. 426-428.
- [225] J. A. Baldwin, 'Magnetic hysteresis in simple materials. I. Theory', *Journal of Applied Physics*, vol. 42, issue: 3, March 1971, pp. 1063-1068.
- [226] Y. Saito, Y. Kishino, K. Fukushima, S. Hayano, and N. Tsuya, 'Modeling of magnetization characteristics and faster magnetodynamic field computation (invited)', *Journal of Applied Physics*, vol. 63, issue: 8, 1988, pp. 3174-3178.
- [227] E. Both, 'The permeability of silicon-iron at very low flux densities', *Transactions of the American Institute of Electrical Engineers, Part I*, November 1953,
- [228] E. P. Wohlfarth, 'Handbook of magnetic materials: V.2: A handbook on the properties of magnetically ordered substances', 1 ed. vol. 2. Netherlands: North-Holland, 1980.
- [229] S. Zurek, F. Al-Naemi, A. J. Moses, and P. Marketos, 'Anomalous B-H behaviour of electrical steels at very low flux density', *Journal of Magnetism and Magnetic Materials*, vol. 320, issue: 20, October 2008, pp. 2521-2525.
- [230] S. Zurek, 're paper: "Anomalous B-H behaviour of electrical steels at very low flux density', *Journal of Magnetism and Magnetic Materials*,", to D. R. Bertenshaw, Private communication, 2014.
- [231] C. Heck, 'Magnetic materials and their application', 2 ed. London: Butterworths, 1974.
- [232] 'DAX 2-Pole turbogenerators', BRUSH Electrical Machines, SM0000247M-31.01.2011, 2011.
- [233] BS 5268-2, 'Structural use of timber - Part 2: Code of practice for permissible stress design, materials and workmanship', BSI, UK, 2002.
- [234] BS EN60404-13:2007, 'Magnetic materials —Part 13: Methods of measurement of density, resistivity and stacking factor of electrical steel sheet and strip', BSI/CENELEC, 2006.
- [235] M. M. Znidarich, 'Hydro generator stator cores part 1 – constructional features and core losses', in 2008 Australasian Universities Power Engineering Conference (AUPEC'08), Sydney, Australia, December 2008, pp. P-051 p1-8.
- [236] J. H. Walker, G. J. Rogers, and R. L. Jackson, 'Pressing and clamping laminated cores ', *Proceedings of the Institution of Electrical Engineers*, vol. 111, issue: 3, March 1964, pp. 565-577.

- [237] B. Milano, 'Hydrogenerator core considerations and core loop test', International Generator Technical Community, <http://resources.generatortechnicalforum.org/download/attachments/558124/PDFGenerator+Core+Document+April+2008.pdf?version=1&modificationDate=1320092580000>, read: 1-11-2011, 2008.
- [238] BS EN60404-2:1998+A2:2008, 'Magnetic materials —Part 2: Methods of measurement of magnetic properties of electrical steel strip and sheet by means of an Epstein frame', BSI/CENELEC, 2006.
- [239] D. R. Bertenshaw and A. C. Smith, 'Lamination joint reluctance in stator cores - a forgotten problem?', in PEMD 2014, The 7th IET International Conference on Power Electronics, Machines and Drives, Manchester, UK, 8-10 April 2014, pp. 0053/1-6.
- [240] H. Bohle, 'Magnetic reluctance of joints in transformer iron', *IEE Journal*, vol. 41, issue: 191, 1908, pp. 527 - 532.
- [241] P. L. Alger and H. W. Samson, 'Shaft currents in electric machines', *Transactions of the American Institute of Electrical Engineers*, vol. XLIII, 1924, pp. 235 - 245.
- [242] H. W. Phear and R. R. M. Mallock, 'The effect of the joints in the plates of a laminated iron core on the d.c. ampere-turns required for its magnetization', *IEE Journal*, vol. 79, issue: 479, 1936, pp. 560 - 564.
- [243] O. I. Butler, 'Determination of the d.c. magnetization characteristics of laminated cores using overlapping joints', *IEE Journal - Part II: Power Engineering*, vol. 94 issue: 37, 1947, pp. 27 - 32.
- [244] R. L. Stoll, 'The effects of butt joints in large a.c. machine cores', in International Conference on Electrical Machines - ICEM 1976, Vienna, 13-15 September 1976, pp. G9 1-7.
- [245] D. Howe, A. G. Jack, and J. Bennett, 'Discussion on --- Examination of flux distribution in segmented stator cores', *Proceedings of IEE*, vol. 127, issue: C, 1980, pp. 114-120.
- [246] A. G. Jack and B. C. Mecrow, 'Computation and validation against measurements of stator end-region fields in synchronous generators', *IEE Proceedings C - Generation, Transmission and Distribution*, vol. 133, issue: 1, 1986, pp. 26 - 32
- [247] T. Nakata and Y. Kawase, 'Analysis of the magnetic characteristics in the straight overlap joint of laminated cores', *Electrical Engineering in Japan*, vol. 102, issue: 1, February 1982, pp. 78 - 87.
- [248] J. R. Barr and R. D. Archibald, 'The design of alternating current machinery', 1 ed. London: Whittaker & Co, 1913.
- [249] E. B. Moullin, 'The principles of electromagnetism', 3 ed.: Oxford, Clarendon Press, 1955.
- [250] K. Shima, K. Ide, M. Takahashi, and K. Oka, 'Steady-state magnetic circuit analysis of salient-pole synchronous machines considering cross-magnetization', *IEEE Transactions on Energy Conversion*, vol. 18, issue: 2, 2003, pp. 213 - 218
- [251] M. G. Say, 'The performance and design of alternating current machines', 3 ed. London: Isaac Pitman & Sons, 1958.
- [252] J. D. Edwards, 'Electrical machines and drives', 3 ed.: Palgrave Macmillan, 1991.
- [253] I. Boldea, 'The electric generators handbook - synchronous generators', 1 ed. Boca Raton: Taylor and Francis Group, 2006.
- [254] J. Pyrhonen, T. Jokinen, and V. Hrabovcova, 'Design of rotating electrical machines', 1 ed.: John Wiley & Sons, 2008.
- [255] P. G. S. Kumar, 'Low cost detection of magnetic core imperfection in turbo generators and novel approach of global vacuum pressure impregnation for

- rectification', *International Journal of Conception on Electrical & Electronics Engineering*, vol. 1, issue: 2, December 2013, pp. 11-15.
- [256] K. Stols, 'Power flux test on a stator core', EE Publishers (Pty) Ltd, Energize, August 2006.
- [257] A677 - 12 (03.04), 'Standard specification for nonoriented electrical steel fully processed types', ASTM American Society for Testing Materials, 2012.
- [258] 'Typical data for SURA M310-50A', Cogent Surahammars Bruks AB, 2008 2008.
- [259] M. Shiozaki and Y. Kurosaki, 'Anisotropy of magnetic properties in non-oriented electrical steel sheets', *Textures and Microstructures*, vol. 11, issue: 2-4, 1989, pp. 159-170.
- [260] A. E. Umenei, Y. Melikhov, and D. C. Jiles, 'Models for Extrapolation of Magnetization Data on Magnetic Cores to High Fields', *IEEE Transactions on Magnetics*, vol. 47, issue: 12, 2011, pp. 4707-4711.
- [261] Q. Tang, Z. D. Wang, and P. Jarman, 'Electrical steels and power transformer cores in deep saturation', in 2012 International Conference on Condition Monitoring and Diagnosis, 2012, pp. 1035-1038.
- [262] 'Kaye & Laby - Tables of physical and chemical constants', 16 ed <http://www.kayelaby.npl.co.uk/>: NPL, 2011.
- [263] R. L. Stoll, 'Eddy-current losses at the joints of laminated cores', in International Conference on Electrical Machines - ICEM 1978, Brussels 1978, pp. G23.1-12.
- [264] Z. Posedel, M. Sasic, J. Sutton, and D. Paley, 'Discussion and closure on "Inspection of stator cores in large machines with a low yoke induction method—measurement and analysis of interlamination short-circuits"', *IEEE Transactions on Energy Conversion*, vol. 16, issue: 4, December 2001,
- [265] B. Mark, 'DIRIS low flux test on stator core', Alstom, Switzerland, November 2001.
- [266] 'Alstom Test Services', in Power-Gen 2003, Düsseldorf, Germany, 6-8 May 2003.
- [267] 'Analogue EL CID operators manual', V2.0C ed.: Adwel International Ltd, 1998.
- [268] G. B. Kliman, S. B. Lee, M. R. Shah, R. M. Lusted, and N. K. Nair, 'A new method for synchronous generator core quality evaluation', *IEEE Transactions on Energy Conversion*, vol. 19, issue: 3, September 2004, pp. 576-582.
- [269] V. Polyakov, 'Turbo-generator, used normative service life', *News of Electrical (Russia)*, vol. 6, issue: 54, 2008,
- [270] D. V. Kuznetsov, V. V. Maslov, V. A. Pikulskii, V. I. Polyakov, F. A. Polyakov, A. N. Khudyakov, and M. I. Shandybin, 'Defects in turbogenerators and methods for their early diagnostics', *Power Technology and Engineering (Springer Science)*, vol. 38, issue: 4, July 2004, pp. 230-235.
- [271] ORDER 28.03.2007 № 200, 'Thermal electrical stations. Procedures of the estimation of the state of basic equipment', RAO UES of Russia, 2007.
- [272] V. B. Berezhanskij, A. V. Moiseev, and G. V. Rostik, 'Method for testing short-circuiting of active sheets of cores of electric machines and device which implements said method', Russian Patent Office, RU 2082274, 1997.
- [273] V. V. Gorodov, A. G. Vdoviko, and J. N. Samorodov, 'Insulation check sensor for electrical machine laminated core stampings', Russian Patent Office, RU 2206951, 2003.
- [274] P. Torchio, 'Classification of large turbo generator failures', *Transactions of the American Institute of Electrical Engineers*, , vol. XXXIX, issue: 1, January 1920, pp. 903-913.
- [275] J. Stein, 'Invitation to EPRI International Workshop on maintaining integrity of generator cores', in EPRI International Workshop on Maintaining Integrity of Generator Cores, San Antonio, USA, 28 November 2001.

-
- [276] J. Stein, 'Survey about life expectancy of generator cores', to D. R. Bertenshaw, Private communication, Palo Alto, USA, February, 2002.
- [277] E. Verloop and X. Shuzhen, 'Stator core damage - a case study', in 13th EPRI Steam Turbine Generator Workshop, Charlotte, USA, August 2013.
- [278] IEEE Std 43-2007, 'IEEE recommended practice for the design of reliable industrial and commercial power systems', IEEE, USA, 2007.
- [279] G. Traxler-Samek, A. Schwery, and J. L. Amundsen, 'Investigations on the water-cooled Svartisen hydrogenerator after consecutive short-circuits', in Hydro 2007, Granada, Spain, 15-17 October 2007, p. 19.05.
- [280] M. M. Znidarich, 'Hydro generator stator cores part 2 – core losses, degradation mechanisms, testing and specification', in 2008 Australasian Universities Power Engineering Conference (AUPEC'08), Sydney, Australia, December 2008, pp. P-052 p1-9.
- [281] B. Gibson, 'Life extension overview', in ASME Power, Orlando, USA, 22-24 July 2008, p. 6.
- [282] 'GB Electricity Ten Year Statement (ETYS)', National Grid, <http://www2.nationalgrid.com/UK/Industry-information/Future-of-Energy/Electricity-ten-year-statement/Current-statement/>, November, 2013.
- [283] 'Electricity: chapter 5, Digest of United Kingdom energy statistics (DUKES)', Department of Energy & Climate Change, HMG, London, UK.
- [284] 'neta - The New Electricity Trading Arrangements', in *NETA* UK: http://www.bmreports.com/bsp/bsp_home.htm, 2014.

Appendix A. Analysis of Alternate Electromagnetic Test Systems

A.1 The DIRIS System

A.1.1. Overview

The only significant, low flux density, interlamination insulation measuring system alternative to EL CID used internationally is the Alstom DIRIS (Diagnostic Investigation with Rotor in Situ) [144] system. Originally developed by ABB, it is not sold commercially, but used in-house by some ABB and Alstom offices for service work. The system can not only measure interlamination insulation but also wedge tightness, and carry a variety of inspection cameras. It can operate on an autonomous tractor as shown in Figure A.1(b) or a wire-guided system through the air gap of a generator with rotor in place.

The system was first described in ABB's patent [70] dated 1991, as an improvement on an old ELIN design from 1984. It uses two radially spaced (to the core), air-cored coils spanning a core slot, whose voltage and phase shift is measured when the core is toroidally excited with a low flux density level. The lower coil's signal amplitude and phase shift is analysed to determine any increase in local mpd over normal, which is ascribed to fault current. The radial distribution of any fault current's magnetic field can be determined in terms of the phase difference and change in amplitude of the voltage induced between the two coils (the patent's inventive step). Since faults are generally smaller than the coils, the measured fault currents are much less than the actual current, thus are calibrated against a test loop simulating a known fault current and length. The result is then ascribed an equivalent full flux total fault power (not fault current). This is elaborated further in Alstom's later 2004 patent [69] which explains that the signal from the coil is analysed into real and imaginary directions, with the real direction representing the fault signal.

A.1.2. Detection process

The system becomes somewhat clearer from the explanations given in inventor Posedel's paper and discussion [71, 264], taken together with other sources [265, 266], where the core is toroidally excited to a low flux density of 0.03–0.1T. The basic system uses a single flat air-cored pickup coil which spans one slot and two teeth shown in use in Figure A.1(a). The coil width is undisclosed, but scaling from the pictures in EPRI's

DIRIS tests [57] where the packets are known to be 62 mm long, the coil housing is ~30mm wide, thus the internal coil can be assumed to be ~25mm wide.

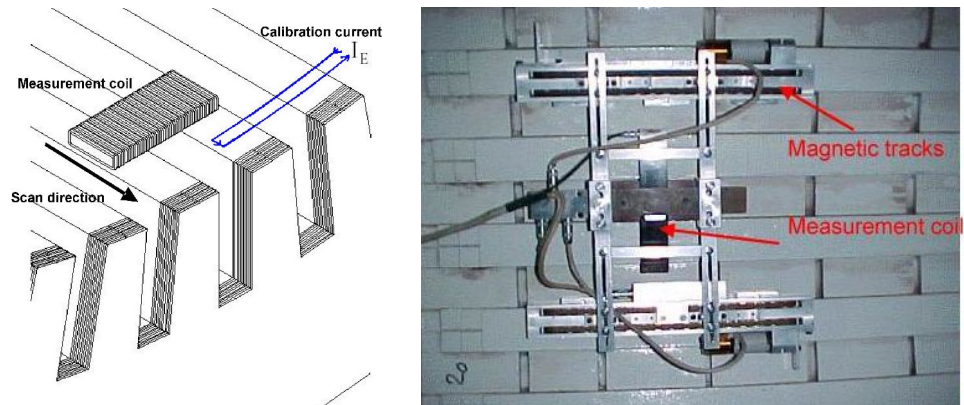


Figure A.1 (a) DIRIS measurement coil with calibration loop [71], (b) DIRIS sensors in use (© Alstom [266])

For a coil which is comparable or larger than the fault, Ho [72] showed that the mpd detected from short faults scaled quite linearly up from zero for faults <2x the coil diameter. Thus for a DIRIS coil of ~25 mm width, the current from all small-medium faults will scale linearly with length, and of course current⁵⁰. Recognising this, Posedel calibrates the system with a known current x length, with examples of 10 mm x 1 A for EPRI [57] and a 5 mm x 2 A in the Alstom DIRIS presentation [265]. Thus it seems standardised at 10 Amm. The calibration signal is a small current loop laid on the core surface under the coil centre shown in Figure A.1(a).

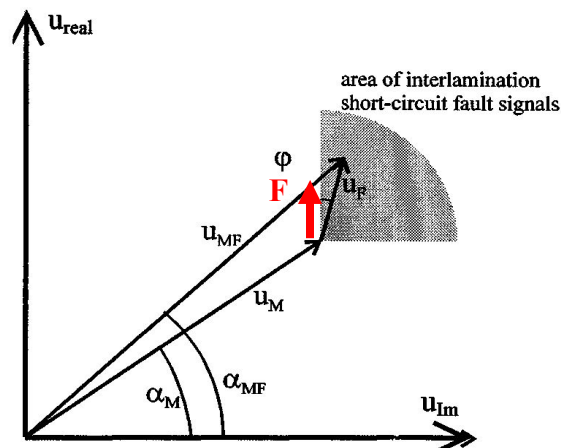


Figure A.2 DIRIS phasor diagram (© IEEE [71])

The signal from the coil is measured with respect to the excitation voltage, so that the phasor diagram shown in Figure A.2 occurs [71]. The Y-axis (U_{real}) is assumed to be the

⁵⁰ Posedel criticises the Chattock in EL CID assuming it is similarly large compared to the fault, and thus detection is also dependent on fault size. This is not true for longer faults, but later it is shown that the Chattock's reducing sensitivity on short faults in fact causes it to almost match DIRIS.

excitation voltage, and is thus taken as the induced fault voltage (neglecting excitation winding resistances). The U_M phasor is the magnetising field across unfaulted core, lagging the induction voltage with core loss α_m . The U_F phasor is the fault current induced, giving a resultant U_{MF} detected signal. The parameter of interest is the change in detected signal phase angle over the core's normal value $\alpha_{mf} - \alpha_m$. By using the phase angle change, this effectively detects only the proportion in quadrature to the excitation phasor. Thus being in phase with the fault voltage means it truly reflects the heat generating component. In this sense it is effectively the same as EL CID⁵¹ except the total fault power is determined, not the fault current.

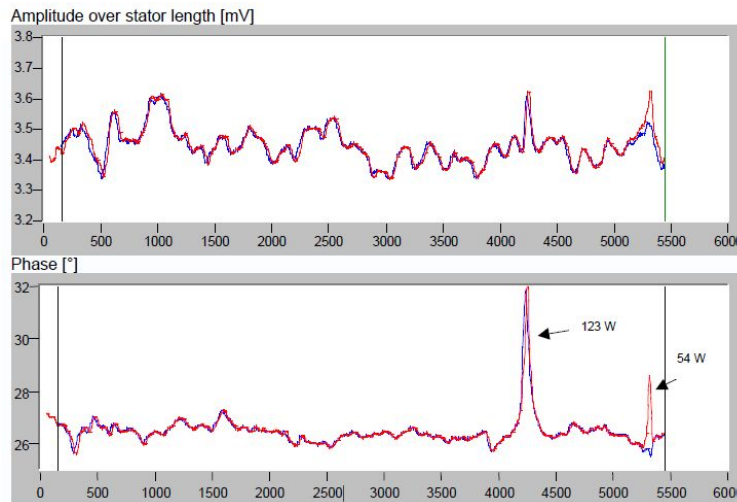


Figure A.3 DIRIS slot plots (© Alstom [265])

The measurements of signal amplitude and phase are recorded at 3 mm intervals down the core, giving a series of plots for each [265] shown in Figure A.3. The critical phase angle swings are noted and their peaks recorded. Having made a measurement of both the calibration signal⁵² and real fault, the fault signal product $I_f L_f$ is then evaluated [71]. For fault current I_f , calibration current I_c , fault length L_f , calibration loop length L_c , normal phase angle α_m , fault phase angle α_{mf} and calibration phase angle α_c , the product of fault current and length becomes

$$I_f L_f = I_c L_c \frac{\alpha_{mf} - \alpha_m}{\alpha_c - \alpha_m}. \quad (1)$$

⁵¹ In EL CID the quadrature signal is not detected strictly in quadrature to the flux, since this would include a proportion of the excitation vector, but in quadrature to the excitation. The error is around $\cos(12 \text{ to } 20^\circ)$, so only about 6% and avoids the intrusion of varying excitation current in the Quad signal.

⁵² It is unspecified what the phase angle of the calibration current is. It can be assumed that the current comes simply from the excitation mains supply, which if resistively limited would make it in phase with induced fault voltages. This is supported in the DIRIS polar calibration plot shown in the Deely core [57].

DIRIS resolves the measured result as a total fault power, not current, as given in Alstom's patent [69]. The action of equation (1) is to compute for smaller angles where $\sin x \approx x$ (up to 40° angle is only an 8% error), the proportion of any fault current in the real direction marked F in red in Figure A.2. This is in phase with the fault voltage and the power may thus be determined from $I_f L_f$ multiplied by the induction voltage expressed as shown in equation (2)

$$\begin{aligned} \text{Fault current voltage} &= V_f, \text{ Core excitation} = V_c \text{ (V/m)} \\ \text{Power in fault} &= \frac{I_f L_f}{L_f} V_c L_f = I_f L_f V_c. \end{aligned} \quad (2)$$

This power is then square-law scaled to the full service axial voltage. To confirm this, from the EPRI study [57] the calibration power computed as above is 31.8 W, which closely aligns with the reported 33 W. Similar comparability within 5% was achieved on the other EPRI study computed fault power levels.

DIRIS uses the patented 2-coil process to measure field gradient to better determine if the fault is on the tooth surface or down slot, but again Posedel does not suggest just how strong this effect is. Some simple FE analysis could probably show it in better detail, but is not really justified, as an examination of Figs. 11 & 12 in his paper [71] indicates that it is really only tooth-tip faults that have strong gradients. Once the fault is down the slot, the mpd across the teeth will remain fairly constant with depth. From this, for a coil that spans both teeth, it is also clear that DIRIS discriminates between tooth-tip and down-slot faults by the same inclusivity method that EL CID uses.

A.1.3. Fault power considerations

In considering fault powers, Posedel assumes the current will only be limited by the typical lamination resistance of 5–10 mΩ, concluding that total fault power will rise to the square of the fault voltage and hence length. He suggests as rule of thumb that a fault will potentially become critical once it exceeds 4–10 mm for turbo-generators and 10–20 mm for hydro-generators (due to their lower V_c). However this ignores fault circuit inductance which will proportion to length, as shown in section 3.5. It also fails to appreciate that when the fault exceeds 3 laminations, the end laminations will share the current, greatly reducing the lamination element of the circuit resistance so the fault resistance through the fault path starts to dominate, which also proportions to length.⁵³ There is further no

⁵³ He suggests that for very severe faults with 'full contact' there will be zero fault resistance, so no fault power, thus high flux tests will fail to detect any heating. This is irrational, even a 'perfect' short achieved by

consideration of the increased cooling that longer faults may enjoy, which is vital since the whole purpose of the measurement is to determine if the heating effect from the fault poses a threat to the machine's integrity.

The declared DIRIS total fault power threshold for risk of core damage for all machines is 15 W, with the fault lengths considered critical being 4–10 mm for turbo-generators and 10–20 mm for hydro-generators⁵⁴. Posedel advises in his paper [264] from 'trials and experience' that this is 'the lowest level at which an iron fire can arise.'

This is not obviously comparable to EL CID's 100 mA. It appears to be both a very different measure⁵⁵ and a substantially higher threshold than EL CID's 100 mA *Quad* current. For a larger turbo-generator which typically has a 5 V/m axial voltage field at 4% flux density, a 100 mA EL CID fault would apparently need to be 48 mm long to dissipate 15 W at full power, so a 10 mm fault, it would need ~500 mA. While this appears to mean that DIRIS uses a considerably higher warning level than EL CID, however it is not the case if allowance is made for Chattock attenuation.

A.1.4. Correlation with EL CID

EL CID has substantial and increasing attenuation for shorter faults and Ho [72] has shown this becomes severe at very small lengths. The 3D and experimental results were plotted in Figure A.4 and a power curve of Chattock relative sensitivity S_R fitted to the points, according to equation (3) where F is fault length:

$$S_R = 0.5(2 - e^{-F/70} - e^{-F/26}). \quad (3)$$

The recorded power is that in the total fault, while the cooling in the core will differ with length, thus the fault temperature will vary. This study scaled the signals from the EL CID reading back to true fault currents, and achieved an estimate of the expected temperature rise for various length faults. It is assumed for simplicity that the cooling is predominantly planar in the laminations. The specific thermal conductivity is axially k_a and radially k_r , and the axial dimension is $X\%$ of the radial (typically 10%). The fault is assumed to be cylindrical of diameter d (typically 10mm) and length F . It is also assumed

melting/welding will have the quite high silicon steel resistivity. It is also seen in practice that core melt faults suffer a massive resistive heating effect even once melted into a homogenous melt zone, which remains molten while the fault propagates longitudinally.

⁵⁴ The rather wide DIRIS sensor in practice prevents reliable estimation of fault lengths < 20 mm.

⁵⁵ It may not be as differently derived as it appears. In the 1990s the Analogue EL CID user manual [267] contained an appendix computing the likely service fault power in a 10 mm long, 100 mA fault and allowing for estimated Chattock attenuation found it to be 14 W. Maybe Posedel simply followed an already established threshold?

that the classic 100 mA = 10°C correlation is for a 15 mm fault, thus the expected steady state temperature rise can be computed for other length faults.

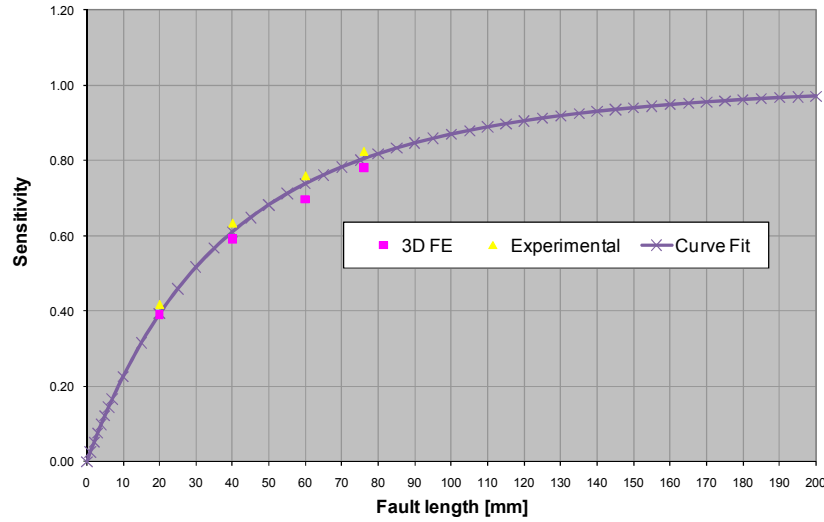


Figure A.4 Chattock relative sensitivity curve fitted to 3D FEA and experimental (© C. W. Ho [72])

At steady state, the power W is all dissipated in the total axial and radial conduction paths and the temperature rise ($^{\circ}\text{C}$) is ΔT . The basic heat conduction formula for combined radial and axial conduction is thus

$$\Delta T = W / \left(Xk_r\pi(d/2)^2 + (k_rF\pi d) \right), \tag{4}$$

where k_r is a constant set so that $W = W_b$ normalised at length $F = 15$ mm (with 100 mA EL CID *Quad* @10 $^{\circ}\text{C}$), and can be computed for values at length F_{15} and ΔT_b .

$$k_r = W_b / \left(\Delta T_b (X\pi(d/2)^2 + F_{15}\pi d) \right). \tag{5}$$

From this the final temperature rise for actual length F is computed in equation (5). This gives us the temperatures shown in the fifth column of Table A-1 where temperatures of over 50 $^{\circ}\text{C}$ can be seen as possible in 2 mm faults. The results are graphed in Figure 2.7.

It can be seen that the fault power for short 100 mA *Quad* EL CID surface faults in the third column is quite constant with fault length, and is also very close to DIRIS’s 15 W. This leads to the surprising conclusion that the DIRIS and EL CID thresholds for fault warning are very comparable for fault lengths up to 30 mm, despite seemingly being very different measures. It is stated that the DIRIS threshold was set empirically, thus may have been on model faults that gave the classic 10 $^{\circ}\text{C}$ high flux test result to which EL CID is known to correlate at ~100 mA.

Fault powers – DIRIS 15W vs. EL CID 100 mA *Quad*.
 Power from 100 mA *Quad* fault at 4% flux density scaled to full flux density.
 Typical *STV* at 4% test flux density = 5 V/m.
 Fault dia. 10 mm with axial thermal conductivity 10% of radial.
 Thermal conductivity **normalised** for EL CID to record 100 mA @ 10 °C for 15 mm fault.

Fault Length (mm)	Chattock relative sensitivity	EL CID <i>Quad</i> 100 mA fault power (W)	<i>Quad</i> for 10 °C temp rise (mA)	Fault temp. at <i>Quad</i> 100mA (°C)	Fault temp. at DIRIS 15 W (°C)
2	0.051	12.2	18	55.8	68.5
5	0.122	12.8	40	25.1	29.3
10	0.226	13.8	72	13.8	15.0
15	0.316	14.9	100	10	10.1
20	0.393	15.9	124	8.1	7.6
30	0.517	18.1	162	6.2	5.1
40	0.610	20.5	191	5.2	3.8
50	0.649	24.1	203	4.9	3.1

Table A-1 Total fault powers and temperatures for 100 mA EL CID detected faults

In the fifth column the expected EL CID *Quad* signal that would thus be expected for a 10°C temperature rise is scaled. It particularly demonstrates why for very short faults of say 2 mm (being <4 laminations joined together) that a 10 °C hot-spot would record as hardly 20 mA. This would normally go unnoticed in natural *Quad* signal variations but probably show as a pinprick of heat in an IR scan, hence the common user complaint that EL CID appears to miss very small/short faults.

Equally significant is the computation performed in the last column. Here it is recognised that the DIRIS coil, being much wider than the majority of the fault lengths considered here, will have an almost linear attenuation of its sensitivity with fault length until the fault is greater than the coil width. In consequence for a constant indicated 15W fault power, the predicted fault temperature rise is slightly more than EL CID. Thus it will similarly suffer the problem of short fault visibility noted above.

A.2 The GE Iron-cored Probes

A.2.1. The GE ‘Racer’

GE Energy developed the Racer stator core test system which reached field trials in 2007, but by 2012 only the EL CID was offered for stator core testing [86]. It is described between 2003–8 in a series of papers [77-80] and patents [81-84]⁵⁶. The claimed goals were to improve reliability in fault detection, ease step-iron testing and reduce re-test time due to false positives from EL CID noise. Lee et al. [78] reports how surface iron-cored probes [94, 268] have major difficulties with varying probe-surface spacing in real life, causing greatly varying readings. This inhibits reliable condition monitoring.

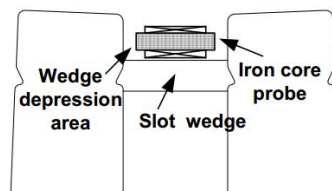


Figure A.5 GE iron core probe in slot (© IEEE [77])

Lee proposed the idea of the in-slot probe as shown in Figure A.5 such that the air gap sum at both ends will be essentially constant so is not a source of signal disturbance.

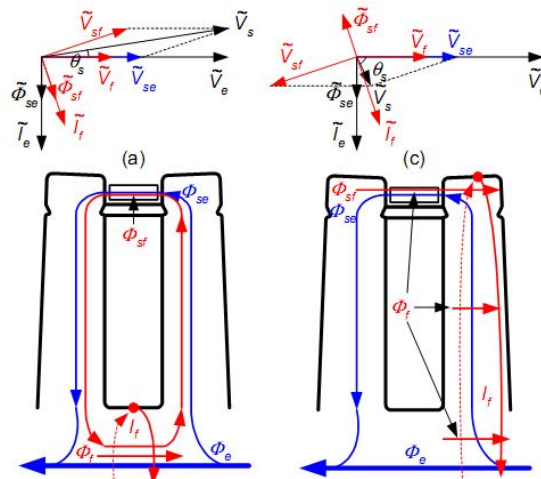


Figure A.6 GE iron core probe phasor diagrams for different faults, left slot base, right tooth tip (© IEEE [79])

From the papers and patents, the probe has 300 turns, with an aggregate total air gap of 3–5mm⁵⁷. The basic phasor diagram in Figure A.6 totally ignores core loss. While this does make it easier to understand, it is a surprising simplification. It is also the reason why, after test, they have to compute a mean V_{s0} value to determine the fault-free phasor

⁵⁶ The main inventor was Sang Bin Lee when at GE, now a Professor in Korea.

⁵⁷ This means you need many different probes for differently sized machines, however patent [84] proposes flexible/telescopic probes to reduce the range needed.

direction, since this is not simply in quadrature to the current. This nulls out the standing core loss.

A.2.2. GE probe analysis

The probe basically operates (though not disclosed in the references) by sensing how much leakage flux can be detected across 1 slot from the full core toroidal fault flux induced, in the two fault situations shown in Figure A.6. The Φ_{sf} fault flux shown must flow around the whole core. The result is that when detecting sub-wedge faults, since the probe has a small air gap it will shunt out much of the aggregate fault flux and get better ‘sensitivity’. However for tooth surface faults no such benefit exists and will thus be detected with much lower sensitivity. This is not discussed. Also faults on the probe axis will be invisible, and though not a very large region, again are not mentioned.

The theory is then expanded assuming essentially a 2D fault, ie infinite fault currents like basic EL CID theory. Lee et al. [80] develops an algorithm for the detected (sub-wedge) slot fault, which is then processed to compute a fault current, based on an aggregate (assumed fault-free) V_{se0} value for the slot and computed θ_s . The formula in equation (6) looks just like the *Quad* signal computation for EL CID, by using the excitation per-slot mmf as the comparator signal that gives V_{s0} .

$$I_{fault} = I_{excitation-per-slot} \cdot \frac{V_s}{V_{se}} \cdot \sin \theta. \quad (6)$$

The succession of papers clearly show the development of the signal processing, as rudimentary signal measurement changed to development of a current measuring, fault algorithm. This process does not work as well in the step-iron region since the probe reluctance (hence sensitivity) varies compared to the main slots, so the proportionality to excitation current varies. The aggregate step-iron region is instead used to compute a special profile for this region.

There is a problem at radial ventilation ducts, as the excitation flux signal drops for no fault, but the phase angle does not, so the user must monitor the phase angle to ensure correct defect detection. The dips are claimed as an advantage, as they allow distance counting/verification down the core.

To assess how poorly the tooth-tip fault is detected, an FEMM 2D [204] axial FE model ($\mu_r = 2000$, $o/d = 1.8$ m, 48 slots) with a 5 mm dia. iron-cored sensing probe having a 2 mm side air gap was constructed. A simple 2D fault of 1A applied, first on the slot base and then tooth tip. No excitation flux was induced, as there was no desire to determine how

this is detected. The plots showing the flux density around the fault and the flux charted in a traverse across the probe are given in Figure A.7 and Figure A.8. The probe side air gap was also increased to 5 mm to determine if this made any significant difference.

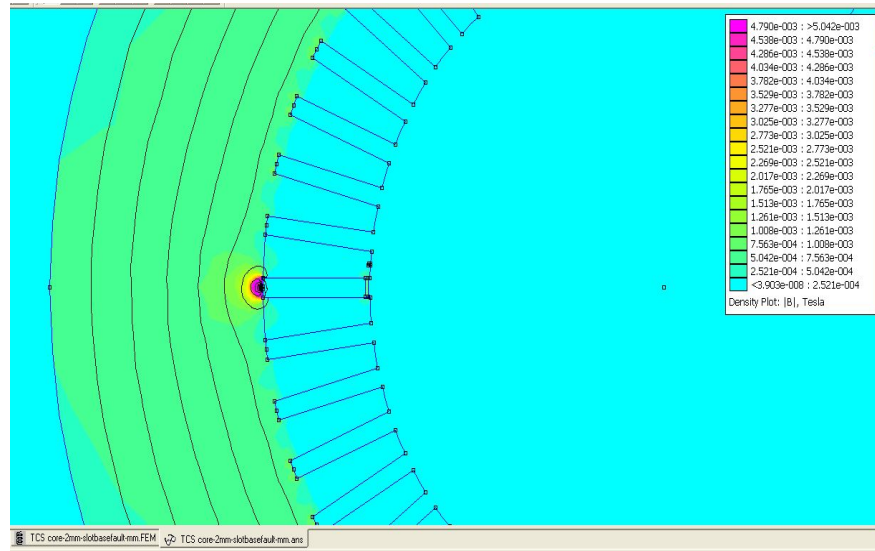


Figure A.7 GE iron core probe FE model with slot base fault

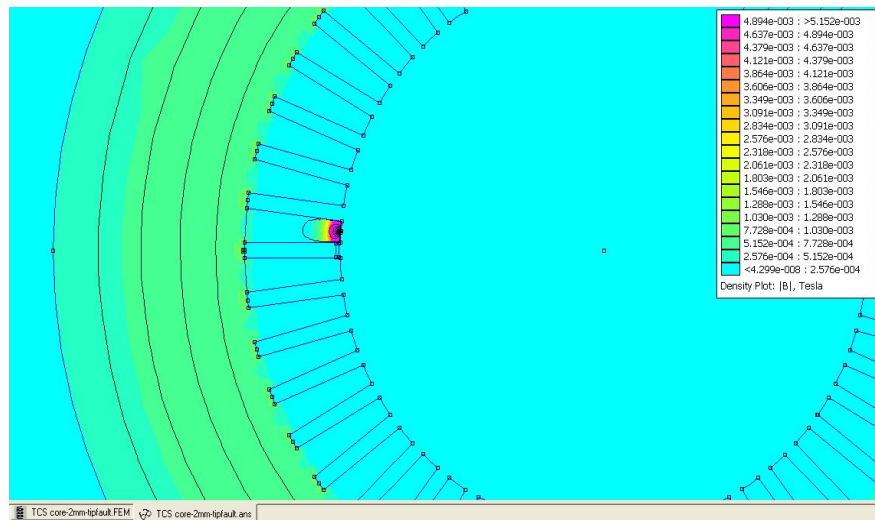


Figure A.8 GE iron core probe FE model with tooth tip fault

Fault position	Probe air gap	Sensor probe flux density (B)	Tooth tip sensitivity as % of slot base
Slot base	2 mm	9.0×10^{-4} T	
Tooth tip	2 mm	2.0×10^{-5} T	2.2%
Slot base	5 mm	4.0×10^{-4} T	
Tooth tip	5 mm	1.5×10^{-5} T	3.8%

Table A-2 Iron-cored probe FE model results

The results are listed in Table A-2. This shows the design is very poor at detecting faults on the tooth tip, with a massive 97.8% attenuation compared to the slot base. It also shows that the sensitivity to faults is as expected quite sensitive to probe air gap, with a 56% attenuation for a change from 2 to 5 mm gap. Whilst little change will occur within a

machine, between machines there will be similar or greater variation, making clear the need for a machine-specific calibration process.

Later papers [78, 79] show some test results, where it seems 10+ laminations welded together are needed to obtain reliable detection on tooth tip or slot base. Curiously paper [78] seems to show poorer detection of down-slot welded faults, where 10 welded laminations were hardly detected, with better detection of surface faults. To reliably detect only a severe welded fault is not impressive. Since all tests were done on welded faults, no attempt was made actually measure the fault current and calibrate against it.

For machines with little or no wedge recess, the technique also has a problem. There is claimed to be little effect on the computed fault current detection if the probe is raised above the core, as the ratio of fault to detected excitation current remains constant. However the radial spacing must be kept constant (unspoken) since otherwise the normalisation of V_{se0} will fail. Patent [81] describes a special design of probe that has magnetic ‘wings’ that tuck back to the slot teeth lips to maintain a constant air gap spacing.

A.3 Russian Stator Testing and the Russian EMKs

In Russia, there is considerable concern over the age and reliability of the RAO UES generation fleet. Polyakov [269] reports that 60% of the fleet are life-expired (30+ years). Kuznetsov et al. [270] consider that 70% of generators over 50MW are now on borrowed time, with many stators faulty due to core end or tooth defects. There is thus substantial interest in assessing the true technical state of these machines to allow successful life extension.

A.3.1. Russian stator testing

The basic Russian tests for stators is contained in the Norma for Electrical machines, with the current 6th edition [50] dated 1997. It contains only a high flux test specification, but does note that a low flux test exists that can be used, without any detail. To encourage the better assessment of generator condition, new technical standards⁵⁸ were issued in 2007 [271], followed in 2008 by Guidelines on assessing life-expired turbo-generators [52] (Life-expired Guidelines). The importance of controlling the interlamination insulation is stressed, describing the risk of an ‘iron fire’ developing regardless of packet spacers and insulating barriers.

The Life-expired Guidelines specified either the use of high flux test, repeating the Norma method, or the low flux electromagnetic method. The high flux test uses a specified flux for a specified period, 1.4T, for 45 minutes⁵⁹ or 1.0 T for 90 minutes, with the final temperatures reflecting acceptable hot-spot differences. In case the flux is not exactly 1.4 T (or 1.0 T), the test time t_{isp} is re-computed for flux B_{isp} in equation (7) below:

$$t_{isp} = 45 \left(\frac{1.4}{B_{isp}} \right)^2 \quad \text{or} \quad t_{isp} = 90 \left(\frac{1.0}{B_{isp}} \right)^2. \quad (7)$$

The general temperature rise of the teeth must not exceed 25 °C and hot spots not exceed 15 °C differential rise. As can be seen, all tests have the same total energy input, thus they are equivalent for the control over the whole stator heating⁶⁰. However for clearly measurable hot spots that stabilise within 45 minutes, then there is no compensation for the changing power input. This is only present for buried faults, where the slow propagation of

⁵⁸ In many cases, aligning with EN60034.

⁵⁹ 1.4 T for 45 minutes is mandatory for water-cooled stators and all machines made after 1977

⁶⁰ At the low temperatures used, core cooling is minimal, with the temperature rate of rise dominated by thermal capacity.

thermal signals to the teeth surface is enhanced by the elongated time, which will provide some compensation for reduced power depending on the precise circumstances.

A.3.2. Russian EMK

The Life-expired Guidelines also specify an alternate electromagnetic control system, the EMK developed in the VNIIE, using a flux density level from 0.02–0.05 T (assumed peak values). There was sufficient confidence in this method to make it the recommended stator core periodic test in the Life-expired Guidelines, and state that a core found fault-free by this method need not be high flux tested. It is noted as equivalent to the EL CID method in foreign countries. Kuznetsov et al. [270] also consider the EMK method preferable, and report an incident where the EMK method detected a major core fault that was not detected by the high flux test. Berezhansky et al. [94] also claimed the EMK method detected two core melt-downs that had evaded a high flux test.

The EMK method detailed in the Life-expired Guidelines specifies an air-cored Rogowski sensor with the detected phase change converted to a total fault power at operating flux. The acceptance levels are described in Table A-3.

Fault Power	Interpretation
<20W	No fault
20–40W	Fault may exceed the high flux test acceptance level (15 °C)
40–70W	Fault may exceed the generator operational capability
70–120W	Fault may damage the winding insulation
>120W	Risk of stator core ‘iron fire’.

Table A-3 Interpretation of EMK fault levels

Berezhansky et al. from the VNIIE first described the EMK method in 1995 [94] and a 1997 patent [272]. In this a iron-cored sense coil spans a pair of teeth, with a second identical sensor placed in a fault-free region. The phase shift between the sensors is used as a measure of the fault. They conclude that the phase angle is a prime variable, but that the amplitude also carries important information. No thresholds are given.

By 2000, Polyakov [95] described the VNIIE system as now having a 10 mm dia. Rogowski sensor, which after testing 150 turbo-generators hadn’t missed any faults also detected by high flux test. His models of the thermal loadings showed fault powers in the 80–120 W range gave a winding bar insulation temp of 105 °C, presumed to be a critical limit. It seems likely this led to the Life-expired Guidelines limits.

A.3.3. Introskan-IS200

Gorodov et al. in 2002 [96] alternately to the VNIIE claimed to use a classic horseshoe iron-cored sensor, though by 2006 [97] it was shown as a 20x2 mm flat sensor, together with a flux sense coil around the stator for reference. Here the increase in signal phase angle β from the fault-free value is used as the measure of damage. In 2003 Gorodov et al. [273], realised that the sensor pole bridging the whole tooth would be only 50% sensitive to a mid-tooth fault (as demonstrated in the paper), and proposed an improvement where an auxiliary coil was added to the sensor end. This does not seem to have been put into practice.

By 2003 the product was commercialised as the Introskan-IS200 core tester [98] from company Electrotechnicheskie Systemy 1, shown in Figure A.9. It is presumed to still use an iron-cored probe. Gorodov et al. [99] described it to be like EL CID, then used this (incorrect) label in the rest of their paper. The test flux density is set between 0.02–0.05 T (assumed peak), thus is a little lower flux density than EL CID, and in a pictured scan has 0.8 A sensed slot mpd. The sensor coil is not described, but the signal is processed to measure the change in phase angle between sensor and a flux sensing coil.

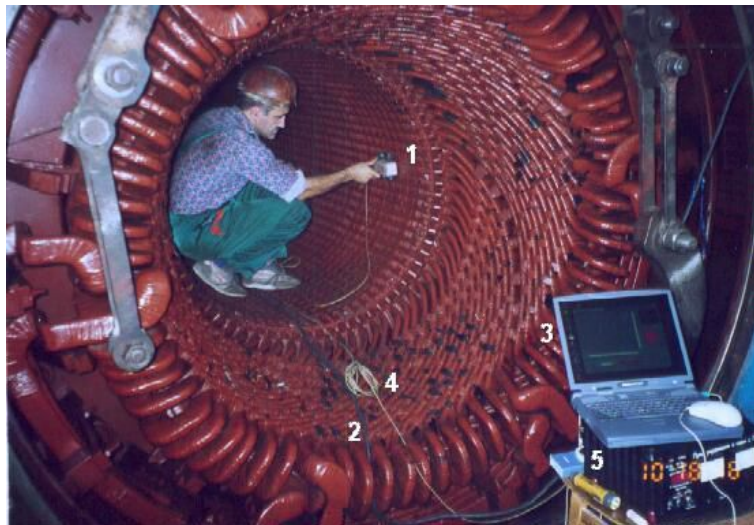


Figure A.9 Introskan-IS200 in use (© ESI [99])

Gorodov et al. [100] then go on to argue that the EL CID 100 mA threshold is dependent on the instrument and parameters, does not relate to the power developed in the fault, and is thus a poor measure. Similarly they argue that uniform fault power thresholds (quoting <20 W as acceptable and >70 W as dangerous) should not be applied to all classes of machine regardless of the geometry.⁶¹ Instead they considers the fault power should be

⁶¹ These values remain in the 2008 Life-expired Guidelines, so it seems they did not win the argument.

assessed in proportion to that section of the core’s normal power loss, as this would indicate the degree to which it can tolerate extra burden.

From this premise, assuming negligible fault inductance and a generic full flux steel loss of 2 W/kg, Gorodov et al. compute the proposed metric of relative loss K_a from the above angle β . The formula reduces to $K_a = 1 + 0.08\beta$ for small β . Based on experience they propose $\beta = 3\text{--}4^\circ$ gives $K_a = 1.24\text{--}1.32$ which is acceptable, whereas if $\beta > 10^\circ$ this gives $K_a > 1.8$ which may exceed the high flux test recommended temperature values (260 mA is equivalent to 40 W fault power in 50 mm packet fault).

In EL CID the *Quad* signal has been shown to be proportional to excitation for low flux density levels [26], since the fault phase angle change with flux density remains low. The phase angle β can thus be correlated to ‘normal’ 4% flux density EL CID test levels on larger turbo-generators, of typically 1.5 A/slot and 5 V/m. The recommendations [99, 100] are found to be comparable to EL CID practice and the Life-expired Guidelines for a one-packet fault (~50 mm long) as discussed by Gandshu and Gorodov et al. in their paper [97]. This is laid out in Table A-4.

Gorodov	EL CID / HFT	Life-expired Guidelines
$K_a < 1.3$ ($< 3\text{--}4^\circ$) normal background Power < 15 W	< 100 mA Normal background HFT $< 5\text{--}10$ °C	Power < 20 W No fault
$K_a = 1.3\text{--}1.8$ ($4\text{--}10^\circ$) warning region for monitoring/inspection Power 20–40 W	100–260 mA Warning region, HFT $\sim 10\text{--}25$ °C	20–40 W Fault may exceed the high flux test acceptance level (15 °C)
$K_a > 1.8$ ($> 10^\circ$) core heating beyond admissible limits Power > 40 W	> 260 mA Danger region HFT > 20 °C	Power 40–70 W Fault may exceed the generator capability
		Power 70–120 W May damage winding insulation
		> 120 W Risk of stator ‘iron fire’

Table A-4 Correlation between Gorodov’s K_a , EL CID *Quad* and fault power

All detected faults and their currents or phase angle representations are assumed to be 100% detected, whereas it is known that Chattock detection sensitivity reduces with shorter faults [72], being 70% at 50 mm length. This is for a 4 mm dia. round Chattock, thus the 20 x 2mm Introskan sensor [97] (20 mm being in the axial direction, hence like the DIRIS sensor) will probably suffer considerably greater attenuation. However this is not taken into consideration in this comparative assessment.

The parameter K_a has similarity to EL CID's Quad parameter, however as it uses just the loss angle, the fault power falls in proportion to per slot test mmf as well as flux density. Both metrics thus result in lower fault power warning thresholds for smaller cores, whereas the Life-expired Guidelines have a single fault power for all machines. Since the majority of faults occur in the teeth, the reducing tooth cross-section in smaller machines will limit fault thermal dissipation, so a reducing threshold has merit.

Further the HFT for core faults has solely a local temperature rise criteria, not scaled with core power loss.⁶² Thus as the fault lengthens, the fault dissipation and thus temperature rise will become proportional to power density (per unit length), not total fault power. To study the relative merits of the alternate metrics, a series of typical electrical machines is defined in Table A-5. A 50 mm fault was studied as this gives equal starting weight to the K_a and fault power metric for the default large turbo.

Machine type	4% Test excitation	Core mean dia.	No. slots
large turbo	5 V/m	2.5 m	54
medium turbo	4 V/m	2.0 m	66
smaller turbo	3 V/m	1.6 m	78
Larger hydro	2.5 V/m	4.0 m	216
large motor/hydro	1.5 V/m	1.3 m	90
medium motor	0.8 V/m	1.0 m	102

Table A-5 Typical electrical machines excitation voltage field

Based on these, the fault power and power/metre of tooth width were computed for the five voltage excitation levels for a constant $K_a = 1.3$ ($\beta = 4^\circ$), a constant EL CID 100 mA *Quad* and a constant 20 W fault power. No attempt was made to compensate for Chattock attenuation, as this would have affected all three sensors to some degree.

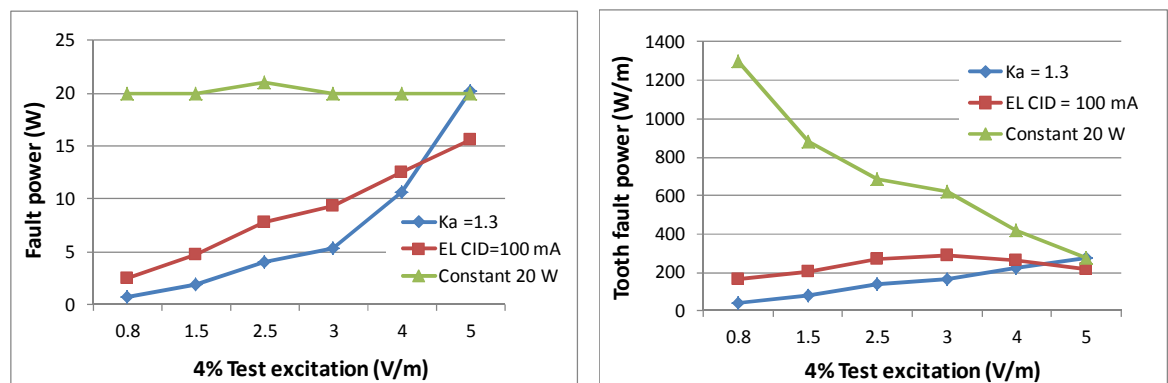


Figure A.10 (a) Total 50 mm fault tooth power, (b) specific fault power per unit tooth width

From the results in Figure A.10(a) it can be seen that the K_a metric rapidly reduces the total fault power threshold on smaller machines, more so than EL CID. In Figure A.10(a) and (b) it also shows a falling measure of specific fault power (per unit tooth

⁶² However the specific core power loss is also a controlled parameter in the Norma [50].

width) in smaller machines, whereas EL CID is fairly constant. Of course the constant 20 W fault power metric escalates rapidly, and could not realistically be applied to other than medium to large turbo-generators.

A.3.4. Introskan-IS200 FE model

An extensive 2D FE analysis has been done of the Introskan-IS200 by Gandshu et al. [97] using the FE software 'Quickfield'. The fault considered was a quite severe one packet length of 50 mm. The sensor was an iron-cored coil, 20 mm wide (axially) x 2 mm thick (radially), spanning two teeth to get the best signal. Varying the coil core material choice (inc. air) did not affect the signal phase, just amplitude. The flux induced in the modelled core frame did not exceed 1% of main core, thus was ignored⁶³.

Modelling of faults down slot walls to slot base showed no change in detection. Modelled faults inside a tooth, albeit 50% attenuated in the middle, are essentially unaffected with tooth depth. However for faults under slot base or tooth root, sensitivity falls off rapidly, and they conclude that faults deeper than 25% of yoke back depth are essentially invisible.⁶⁴

Gandshu investigated fault inductances, and noted that surface faults had reactance $X = 0.01 \Omega$ for 0.5Ω faults (equivalent to ~ 350 mA *Quad* signal at 5 V/m), so the phase shift from these is very small, and not disturbing. Even in the core back, the X/R ratio only rose to 0.12. This him led to discuss if the inductive phase shift might be a problem. However it is clear Gandshu is resolving the detected signal phase angle to the flux density phasor (in later graphs) and thus its quadrature component to the current. This will eliminate any inductive phase error, as it will just present the resistive heating component.

Gandshu then went on to model higher frequency testing, up to 5 KHz. Here he noted that for buried faults, the inductance rapidly dominates. Since the background core losses also rise with HF, resolving to excitation current fails, instead he computes a coefficient of additional losses, K_{real} applying the same thresholds as for K_a ($<1.3 = \text{OK}$, $>1.8 = \text{fault}$). This showed that for even very severe surface faults, there was little inductive limiting to 2000 Hz, and still modest to 5000 Hz.⁶⁵ However once a fault is 10% buried, above 500 Hz

⁶³ This quite a useful result. The EL CID test has been applied always assuming that the machine frames would not significantly affect the results, but without much evidence.

⁶⁴ This assumes a single slot scan, whereas it is known with EL CID to assess 2-3 slots to improve Quad detection, since the signal is now spread out across several slots.

⁶⁵ This is much more benign than Adwel's experience, shown by [113].

faults saturate at $K_{real} = 2.0$. This of course limits the ability to differentiate between modest and severe faults. They suggest a compromise frequency of 500–1000 Hz.

Appendix B. Stator Reliability Studies

Apart from the CEGB crises in the 1970s, serious⁶⁶ stator core faults remain fortunately a rare event, however specific reliability statistics are scant. As early as 1920 Torchio [274] describes out of a total of 55 US turbo-generator failures, two from ‘heating of iron’, representing a core failure rate of 4% of total failures. GE report [11] that in the ‘recent months’ up to 2004, the core represented 14 in 340 total stator and rotor turbo-generator failure events, still around 4%. EPRI [275, 276] in 2001–2 report an informal survey which indicated that of about 160 cores in operation for more than 200,000 hours, one generator core failed (assumed catastrophically) and six will require a core repair. However core looseness contributed another 20 failures and loose cores are known precursors of lamination insulation failure [15]. Further this study considered only machines that had survived 200,000 hrs without major work, thus is skewed toward the machines that proved most reliable. From this if the base turbo-generator MTBF is 50,000 hrs, then the core fault rate is 1%, rising to 2.5% if half the loose cores are also included, and up to 5% if the MTBF of the EPRI study population is assumed twice that of the base level. From this a stator core failure proportion of 4% remains credible.

There is somewhat more information on overall turbo-generator failure rate. Verloop [277] considers the generator (all aspects) causes 13% of all power plant losses. Tavner’s 2008 survey [7] gave an MTBF of 273,750 hrs, whereas IEEE Std493-2007 [278] gives just 51,834 hrs (continuous operation). The very extensive 1993 survey by Bollen [139] showed the massive variability in MTBF data (8 days to 140 years). However when the effects of prime mover unreliability are minimised by focussing on just steam turbine driven plant, then the data spread becomes 1.7–2.2–5.9–8.3–140 years. From the above data, a median MTBF of ~50,000 hrs (5.7 years) becomes credible.

Large motors are seen as more reliable, with Tavner indicating around 150,000 hrs MTBF, a figure supported by Bollen, with IEEE Std493-2007 proposing an average of 112,000 hrs. While stator failures are around 30% [278], these are dominated by winding failures, and it has not been possible to ascribe a failure rate to the stator core itself.

For hydro-generators, a 1984 CIGRE survey [13] showed that core faults (excluding winding) consume 15% of all outage time, though this includes wedging and frame faults etc. Later in 2009 CIGRE [12] surveyed 1,199 machines, over a 10+ year period, and

⁶⁶ One that puts the machine at risk, including a core melt.

reported 69 significant failures that exceeded 10 days outage. This data gives a MTBF of 544,000 hrs assuming 25% duty cycle. There was one ascribed to a core hot spot which triggered fire damage and caused a 90 day outage, which crudely indicates that stator core faults represent around 1.4% of all hydro-generator faults.

Traxler-Samek et al. [279] describe how successive power line shorts on a 410 MVA hydro-generator also caused serious core damage, requiring a 95 day repair. This helps to dispel the idea that because hydro-generators are less electrically stressed, they are much less likely to suffer core faults due to the power in a fault being in proportion to the axial voltage squared. Znidarich [280] also considers a molten core fault in them quite possible, while Walker [43] (§4.4) believes poor lamination insulation quickly led to a 10 cm dia. hydro-generator core melt. Consequently serious hydro-generator stator core interlamination faults are rare, however when they occur they still require a disproportionately long time to repair.

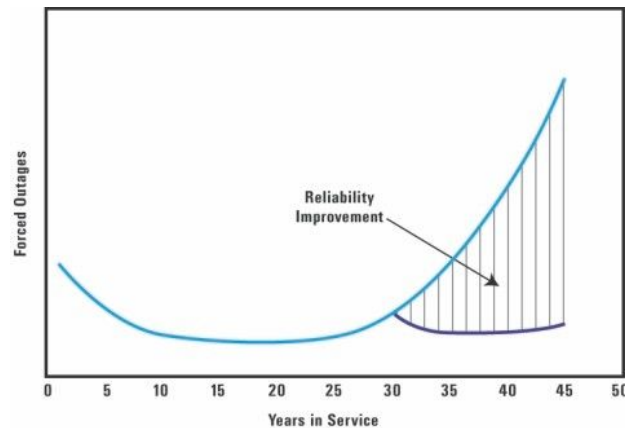


Figure B.1 Generator reliability and improvement possibility (© GE Energy [11])

Another issue is the aging of the world's (especially western) generation fleet. It has been shown in section 2.1 how the 1 GW generator capability level had been reached in the 1970s, thus once these larger machines were installed the operational and efficiency imperative to replace them fell away. A 2008 survey by Sciencetech Corporation [281] found that 97% of all North American fossil power plants are over 30 years old, with nearly 40% over 40 years old. Thus a majority of these generators are at or beyond their expected life of typically 30 years. GE [11] consider that original machine unreliability starts to rise significantly after 30 years, as shown by their marketing illustration in Figure F.2. In the UK, the 'dash for gas' in the 1980s–90s drew in large amounts of new CCGT plant, though even by 2013 the mostly over 30 year old coal, nuclear and hydro plant still accounted for 46% of generating capacity [282] and 58% of output [283].

In Russia, Polyakov [269] reports in 2008 that 60% of total generators are now life-expired in the RAO UES system, and there is urgent need to assess their condition. He observes that since many of the 50 MW machines are now 60 years old, there is no reason for the base load 300–800 MW machines to not achieve this age providing action is taken. However the failure rate of many of these larger machine stator cores is increasing in the last decade due to fleet age, with 11 machines reported that recently had core burnouts or ‘grave short-circuit damage’ [270].

From this it can be seen that a serious stator core interlamination failure, while a very low probability of occurrence, has a massive effect on generator availability and thus profitability. Not managing this might remain a tolerable risk on younger machines, but as the fleets age the risk can rise to unacceptable levels, and is considered below.

Considering the reliability impact, an example 300 MW mid-range generator, running at 50% duty, would achieve 21,900 service hours between the typical 5 year major services [9]. At the aggregate MTBF rate of 50,000 hrs, with 4% of failures stator core related, there would be a 1.8% chance of serious core failure during that period, i.e. 0.4% p.a. Such a failure would incur a repair cost of at least £500K (costs have exceeded £10M [125]) and take 60–90 days to correct. Lost generation revenue is often the largest loss. Using UK 2014 NETA [284] generation prices of around £4/MWh, and assuming a 50% duty, and 50% fuel and other cost savings leads to a lost margin of >£500K, giving a total cost of £1M. Thus if it can be assumed that testing at a major service outage, and correcting any incipient core faults will prevent failure until the next outage, the aggregate value saved is potentially $1.8\% \times £1M = £18K$.

Compared to the cost of an EMT of between £5–10K, at first sight this seems to indicate that testing is worthwhile. However testing and correcting any incipient faults core faults may not assure a fault-free 5 year service interval. Several reports describe cores which failed soon after return to service where testing showed no defect. Drommi [140] reports a new core failed after one year, while the catastrophic Hunter failure [14] occurred 17 months after an overhaul where ‘all tests showed this machine to be in good operating condition’. Thus the testing regime has to be at least 40% effective to make the economic case, a number that is by no means certain.

The large motor MTBF is 10x that of generators, and failure costs are much lower, since repair or substitution can usually be achieved much quicker. In consequence EMT testing of such machines is not routinely justified and normally restricted to factory quality assurance or critical machines.

It is of course impossible to know what the failure rate of generator stator cores would be if the now routine testing regime was halted, while the above observations indicate that testing only every 5–7 years offers no surety of core reliability in the interim period. Regardless, the main incentive to test is aversion to the massive cost of failure. Few utilities (and especially their insurers) willingly accept the risk of £M+ failures which they could at least partially mitigate with a short, cheap test.

The 1987 CIGRE survey of utilities [141] before EL CID became internationally common showed the HFT used in only 29% of major services, with the remainder not testing. However by 2010 [9] the high flux test had fallen to 20% but the rate for EL CID test had risen to 64% of major services. Thus a technique such as the EL CID test has won popularity, since it can be completed in a day, often while other work proceeds. By comparison the high flux test is only performed on higher risk machines due to its cost, length of time and monopolisation of the machine [40]. However it is frequently still applied with EL CID before a major stator core repair [8] (§11.2.1) to obtain maximum information and confidence about the defect.

Appendix C. Field Experience with Quad Recovery

C.1 Three field studies

Firstly a 250 MVA stator core had a melt-down fault on a side-wall of slot 13 at ~ 0.2 m from the core end, shown in Figure C.1(a) from within the stator bore. The stator also had a significant secondary fault similarly ~ 0.2 m from the core end at slot 1, thus circumferentially aligned and masked by the Quad recovery effect. This was studied by Bertenshaw and Chapman [203]. It can be seen that the molten damage extended several packets, which generated a Quad recovery potential of ~ 100 mA/slot. When applied as a correction to slot 1, Figure C.1(b) shows that a seeming tolerable 95 mA peak becomes an unacceptable 180 mA fault signal. This was in fact discovered by a high flux test shown in Figure 2.3(a) which with an 18°C temperature rise, reflected the usual $10^\circ\text{C}/100$ mA correlation.

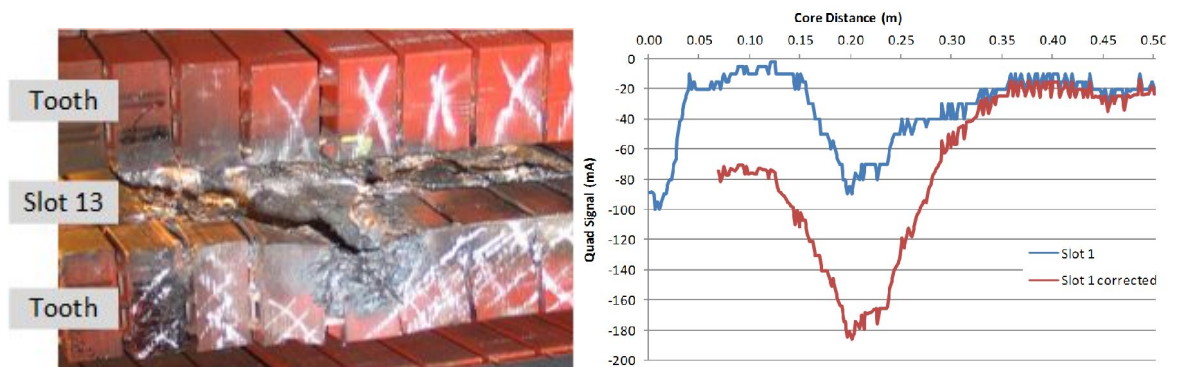


Figure C.1 (a) Melted core fault in slot 13, (b) Quad signal before and after Quad recovery correction on slot 1

Secondly the EPRI Model Core study [57] was a situation where multiple severe faults were applied to the stator core resulting in EL CID readings that were misleading. In this case it caused the researchers to cast severe doubt on the commonplace $5\text{--}10^\circ\text{C}/100\text{mA}$ correlation between high flux and EL CID tests. Only after correcting for several errors and especially the Quad recovery effect, was the correlation shown to be still holding with some confidence. This is analysed in section 4.4.2,

Thirdly a 109 MVA stator core that had been bead blasted to remove old insulation resin during a rewind, had suffered extensive surface interlamination insulation damage from the blasting. This is thermally illustrated in Figure 2.3(b). It became impossible to analyse the EL CID results since there were virtually continuous fault and fault recovery

signals everywhere, thus the technique described in section C.2 was developed to discriminate the actual fault levels.

C.2 Quad recovery correction algorithm

To resolve the problem of the above third stator requires determining the total fault current and also what *Quad* signal on the core represents ‘fault-free’. From section 6.1, the *Quad* values around the core surface must sum to zero, and the *Phase* values sum to the excitation current (as usually expected). In reality since the Chattock is normally set to span the opposite sides of the teeth across a slot, there is double-counting of the potentials across each tooth surface. For the Quad recovery potential deriving from the circulating flux this is a small potential referred to the tooth surface and may be ignored (or a notional -10% allowed). However any fault on a tooth tip is counted twice, and must be fully allowed for in the summation.

For the *Quad* values to sum to zero requires that all fault *Quad* currents must be balanced by an opposing Quad recovery mpd to give a net zero sum around the bore. It is assumed that the Quad recovery is evenly distributed around the bore at every slot (including the fault slots) as analysed in Chapter 6. If Q_{in} and Q_n are the indicated *Quad* signal and actual fault *Quad* value for slot n at each core axial position/packet, and ε a global error value from any error in the EL CID phase reference, each slot signal at an axial position/packet on a core of N slots will thus be

$$Q_{in} = Q_n - \frac{\sum_N^1 Q_n}{N} + \varepsilon. \quad (1)$$

Summing round the bore gives

$$\sum_N^1 Q_{in} = \sum_N^1 Q_n - \sum_N^1 Q_n + \varepsilon N \quad \text{thus} \quad \varepsilon = \frac{\sum_N^1 Q_{in}}{N}. \quad (2)$$

Hence around each packet the *Quad* values should only accumulate the standing error values. However in order to determine the actual fault values, it must be assumed or known that at least one or more slots are unfaulted, thus their positive value (assuming negative *Quad* signals are indicative of a fault, as is conventional) represents only the recovery potential. Further, in a normal stator core, natural core loss variations lead to natural *Quad* fluctuations around the bore, not representative of fault or measurement error. A further variance value C_q of 10–50 mA may be added to ε to reflect the age and dilapidation of the machine to avoid overstating any fault.

Unfaulted slots will carry a positive *Quad* signal averaged⁶⁷ as Q_{+max} which may vary with packet/region. In this case, assuming uniform Quad recovery around the core, from equation (3)

$$Q_{+max} = -\frac{\sum_N^1 Q_n}{N} + \varepsilon + C_q. \quad (3)$$

Thus for each slot in the packet, the true *Quad* signal can be estimated from equation (4)

$$Q_n = Q_{in} + \frac{\sum_N^1 Q_n}{N} - \varepsilon - C_q = Q_{in} - Q_{+max}. \quad (4)$$

This is amenable to a spreadsheet analysis. A set of the maximum *Quad* +ve values for each packet or studied region are ranked to check that there are no odd-looking values which might derive from human input error, and that the maximum +ve values seem to be trending to a stable value. This indicates that the hypothesis that at least one or two slots in each packet are unfaulted is true. The mean of these maximum +ve values is then computed and true fault values determined from equation (4). The value of C_q can only be a subjective judgement.

The resultant false colour map of the final *Quad* signals for the third stator example in section C.1 was plotted in Figure F.2, using a generous 100 mA allowance for the variance C_q . This showed 12% of *Quad* values >1000 mA, peaking at -2595mA, and was comparable to the high flux thermal image in Figure 2.3(b).

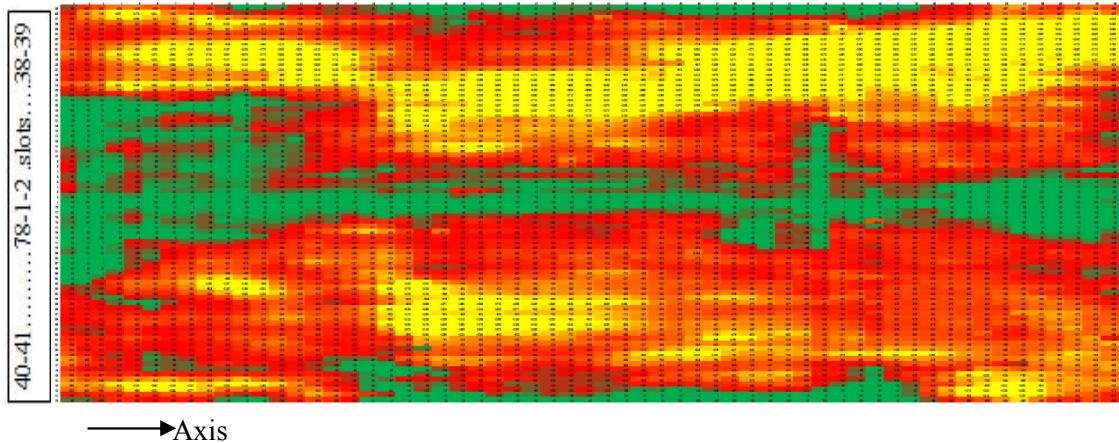


**Figure C.2 False colour map of *Quad* signals
(Green <-100mA, Red >-100mA, Yellow >-1000mA)**

If it is judged that Quad recovery is not uniform around the stator, a slot weighting factor would need to be introduced to reflect the slot count distance from the apparent fault in equation (4)

⁶⁷ In one study, each packet's 8 most positive values were ranked. The mean was then taken of the lowest 7 to reduce any bias from one-off 'spikes', less 10% to allow for double-counting of the mpd across tooth tips.

C.3 Quad recovery uniformity in the field

Knowledge of the uniformity of the Quad recovery is important to allow compensation for its effect. To consider the variation in the field, three stator core tests where major faults occurred were identified and the variation in the *Quad* signal recorded around the core in the central region of the fault. In example stator core A, this is the previously mentioned 250 MVA stator core with major fault illustrated in Figure C.1(a). This showed a fair uniformity, with strong consistency around ~70% of the core, dropping to ~50% at the most distant part of the circumference.

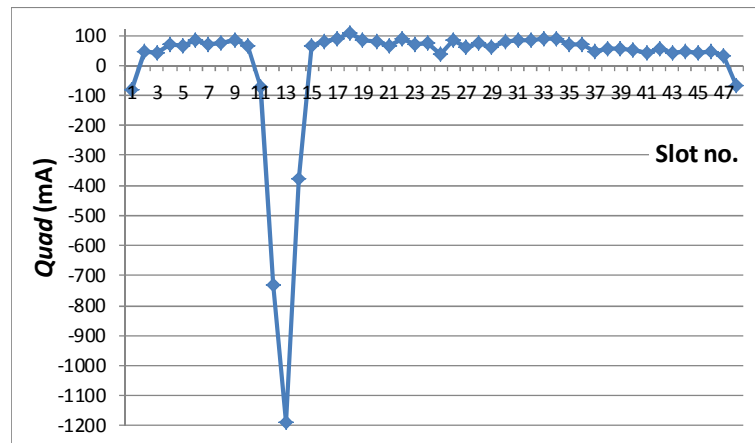


Figure C.3 *Quad* signal recovery around faulted region of stator core A

In the second example stator core B, a 100 MVA turbo-generator stator with a similar severe fault, the *Quad* signal around the core is plotted in Figure C.4. Again it can be seen that the recovery potential is relatively constant, falling by ~30% at the most distant region.

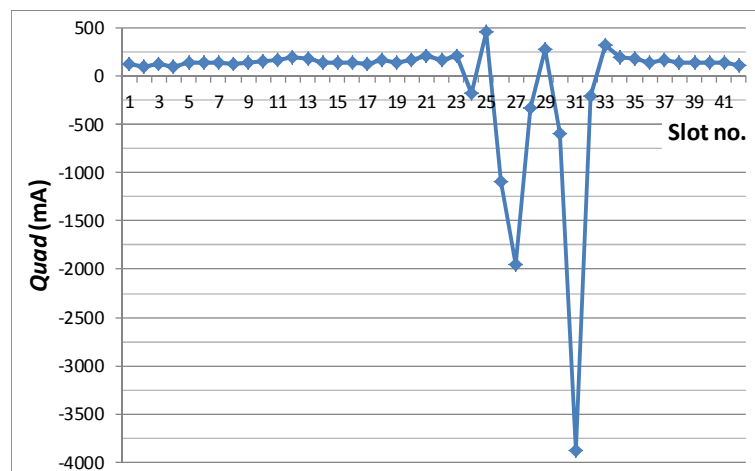


Figure C.4 *Quad* signal recovery around faulted region of stator core B,

However in the third example of stator core C where a severe winding fault occurred also burning the stator iron, the Quad recovery potential suffered severe attenuation away from the fault as shown in Figure C.5. No reason can be ascribed for the difference in this stator. Whilst smaller, the stator's construction was conventional, excepting by the time the EL CID test was conducted, some of the damaged teeth had been machined away.

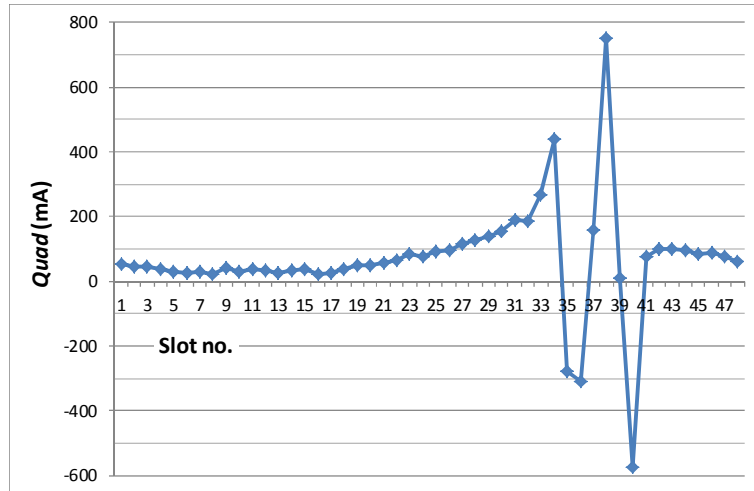


Figure C.5 Quad signal recovery around faulted region of stator core C

Appendix D. Power in Stator Magnetic Fields

The change in spatial energy density ΔW_M in a spatially uniform magnetic field strength \mathbf{H} for a change in induced flux density \mathbf{B} from B_1 to B_2 is defined [212] as

$$\Delta W_M = \int_{B_1}^{B_2} \bar{H} d\bar{B}. \quad (1)$$

Since the vectors \mathbf{B} and \mathbf{H} are co-axial in a stator core, this is equivalent to integrating the region as shown in the scalar B/H curve for the stator core steel in Figure D.1(a), which results in the total stored energy being equal to the area above the curve in Figure D.1(b).

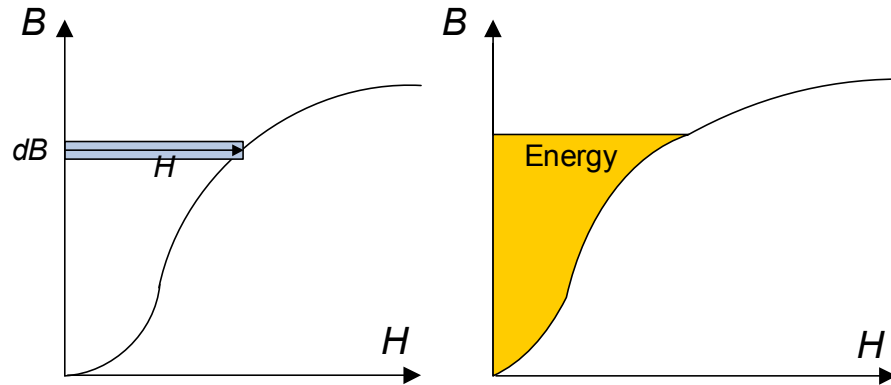


Figure D.1 Energy in B/H curves (a) elemental and (b) integrated

In order to determine the power consumed, the total energy absorbed and released over a complete ac cycle must be computed. If \mathbf{B} and \mathbf{H} are considered as rotating phasors, where the \mathbf{H} phasor leads \mathbf{B} , the instantaneous power density change is given in equation (2). This is cognisant of the hysteresis loop, since it is the area within the loop that reflects the net energy dissipated by the iron.

$$\text{Instantaneous power density change} = \frac{dW_M}{dt} = H \frac{dB}{dt}. \quad (2)$$

Non-constant permeability with flux density gives rise to non-sinusoidal magnetic field waveforms in stator cores. The flux field is normally induced by a low impedance voltage source, so is controlled through the back-emf of the excitation winding to closely approximate to the supply sinusoidal waveform. The excitation current developing the \mathbf{H} field must then follow the requirements of any varying permeability and also the cyclic history imposed by the hysteresis.

Any non-sinusoidal repetitive waveform can be expanded into a Fourier series of harmonics of the fundamental frequency. Flux density \mathbf{B} can be defined as a sinusoid with

instantaneous value b , peak value B and angular frequency ω . Similarly the non-sinusoidal magnetic field strength \mathbf{H} with instantaneous value h can be defined as a *Fourier series* of sinusoid harmonics of order n , fundamental peak value H and proportional harmonic values k_n (thus $k_1 = 1$), each leading the flux density by angle θ_n . From this we obtain

$$b = B \sin(\omega t)$$

hence $\frac{db}{dt} = \omega B \cos(\omega t)$ (3)

and

$$h = H [k_1 \sin(\omega t + \theta_1) + k_2 \sin(2\omega t + \theta_2) + \dots]$$

hence $h = H \sum_{n=1}^{\infty} [k_n \sin(n\omega t + \theta_n)]$. (4)

Mean core loss spatial power density P_L is integrated over one supply cycle of period $2\pi / \omega$, hence

$$P_L = \frac{\omega}{2\pi} \int_0^{2\pi/\omega} H \sum_{n=1}^{\infty} [k_n \sin(n\omega t + \theta_n)] \omega B \cos(\omega t) dt. \quad (5)$$

This needs to be considered for each harmonic. For the fundamental harmonic, $n = 1$, applying normal trigonometric identities gives power density P_{L1}

$$P_{L1} = \frac{\omega^2}{4\pi} HB \int_0^{2\pi/\omega} [\sin(2\omega t + \theta_1) + \sin(\theta_1)] dt. \quad (6)$$

Equation (6) integrates to

$$P_{L1} = \frac{\omega^2}{4\pi} HB \left[-\frac{1}{2\omega} \cos(2\omega t + \theta_1) + t \sin(\theta_1) \right]_0^{2\pi/\omega} \quad (7)$$

which reduces to equation (8) (or just $\omega HB \sin \theta_1$ if rms values are used for H and B).

$$P_{L1} = \frac{\omega HB \sin \theta_1}{2}. \quad (8)$$

For the first harmonic $n = 2$, we get

$$P_{L2} = \frac{\omega^2}{4\pi} HB \int_0^{2\pi/\omega} [k_2 \sin(3\omega t + \theta_2) + \sin(\omega t + \theta_2)] dt. \quad (9)$$

By inspection of equation (9), it can be seen that this and all higher order harmonics will integrate to zero over a complete mains cycle, thus there is no net power carried in the \mathbf{H} phasor harmonics. Hence it is shown from the power input given in equation (8) that the core loss density P_L is the rms phasor cross product of \mathbf{B} , fundamental of \mathbf{H} and ω .

The phasors may be resolved as illustrated in the phasor diagram of Figure D.2 for a stator core whose induced flux density is lagging the excitation current by angle θ due to

core loss. The \mathbf{H} field developed in the stator has components $H_{inductive}$ in phase with the flux density, and H_{real} in quadrature with the flux density. From equation (9) it can be seen H_{real} is the sole power-carrying component. This enables the effects of variance of core loss and permeability on the phase resolved mpd to be separately assessed.

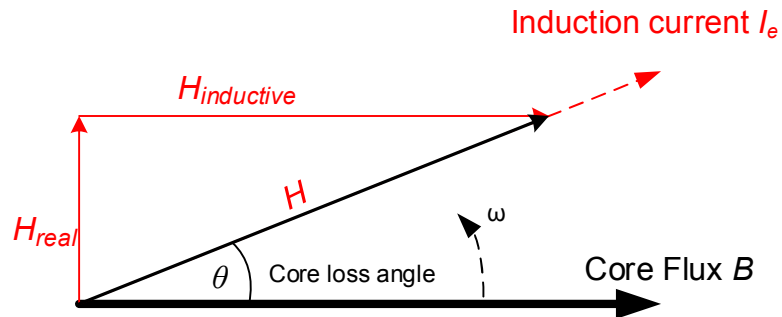


Figure D.2 \mathbf{H} field components

Appendix E. Test Equipment

The following items in Table E.1 of ENELEC Ltd test equipment were used, having either formal calibration (*), cross calibration against known measures, or functional check.

No.	Description	Model	Serial No
1	Micrometer (0–1")	Mitutoyo 103-131	n/a
2	Vernier Caliper (0–150 mm)	Mitutoyo Digimatic 500-196-20	09066567
3	DVM	Metrix MX54	54601831
4 *	DVM	Chauvin Arnoux MTX3282	10027937
5 *	Bench DVM (7½ digit)	Datron 1071	7094
6	Arbitrary Signal Generator	TTi TG5011	344719
7	Avometer	Model 8, Mk III	102309.869
8	DC Power Supply	Caltek PM2/5A	070107907
9	EL CID Calibrator	ENELEC Custom (error <0.5%)	n/a
10	Chattock Calibrator	ENELEC Custom (error <0.5%)	n/a
11	Power Amplifier	Behringer EP4000A	S1105217A37
12	Lock-in Amplifier	EG&G 5210	IR34371
13	AC Current clamp	Chauvin Arnoux MN73	P01120421
14	9" (225 mm) Chattock	20070 (calibration 108%)	9391
15	PC oscilloscope (12 bit)	Picoscope 4224	YSR98/025
16	IR Camera (hired)	FLIR 60	49000540
17	Digital thermometer (K thermocouples)	RS 615-8212	06900648
18	Differential Amplifier	Tektronix AM 502	8056947
19	Power Analyser	Voltech PM100	AX117/2535

Table E.1 Test equipment

Appendix F. DAX8 Excitation Drive and Linearisation

F.1 Excitation drive problem

At low flux density levels, the relative measured permeability of the DAX8 core rises from 1000 to 3800, shown in Figure F.2 using a sinusoidal flux density. The increase in permeability in the test region will cause a non-linear I/V characteristic in the excitation.

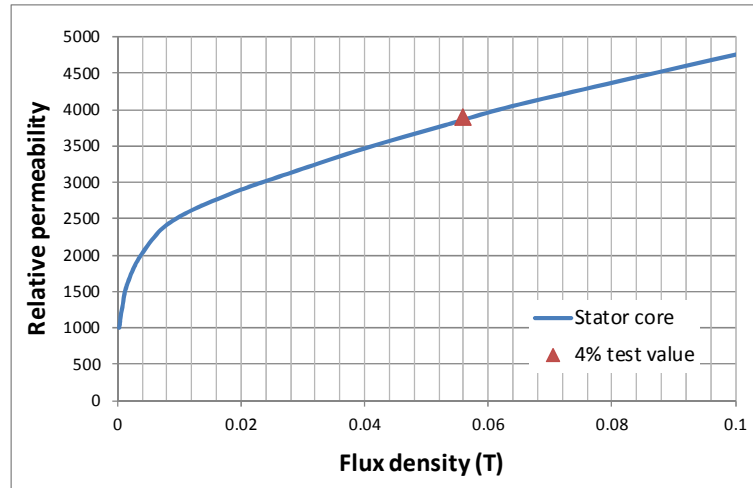


Figure F.1 Relative permeability at test flux density levels

For EMTs in the field, the full core length is excited, and consequently the excitation flux density closely follows the sinusoidal excitation voltage due to the dominance of the inductive back emf. However in the short DAX8 core, the relatively large winding resistance causes a larger resistive voltage drop (0.48 V) than the back emf (0.4V) per turn.

In consequence the excitation current waveform, rather than the flux waveform, will be closer to the drive voltage sine wave. This will develop harmonics in the induced flux and thus fault currents. Since harmonics are not normally present in field tests, they could affect the detection of experimental faults from their measured mpds. To reduce the resistance voltage drop to the same equivalent level as found in the field would require much heavier conductors (120 m of $>16 \text{ mm}^2$), whose weight and cost would be problematic. It was thus decided to use feedback stabilisation to linearise the flux drive, which would also have the benefit of stabilising against mains voltage variations.

F.2 Excitation drive error determination

To determine the normal balance between resistive and inductive excitation voltage drop, a number of real-life scenarios were researched in Table F.1, covering large to small turbo and hydro-generators. These models assumed excitation with 2.5 mm^2 cable axially

with conventional arrangement and 18° core loss angle. The resistive error K_E is the % the core induction back emf ($V_{core-emf}$) is reduced over the total drive voltage V_s by the excitation winding resistance, defined in equation (1) for the model shown in Figure F.2 when open-loop.

$$K_E = 1 - \left| \frac{V_{core-emf}}{V_s} \right|. \quad (1)$$

	Test core	Large turbo	Modest turbo	Small turbo	Large hydro	Med hydro	Small hydro
Station	DAX8	Drax U2	Aghada	Lucciana	Cruachan	Finlarig	Glenlee
Power (MW)	100	660	115	27	100	35	15
Core length (m)	0.094	8.24	3.5	2.1	1.7	1	1
Excitation (V/m)	4.26	5.11	3.77	1.50	3.28	2.38	1.57
Resistive error K_E	44.5%	1.9%	3.4%	1.9%	7.4%	8.9%	15.9%

Table F.1 Typical excitation drive resistive errors

From these examples it can be seen that K_E for typical turbo-generators is in the 2–4% region, while hydro-generators range from 7–15%. Since the EMT is predominantly used on turbo's, a K_E value around 3–4% is an appropriate target.

F.3 Feedback stabilisation design and test

The design used a 2 KW power amplifier (up to 100V @ 24A non-continuous) with negative feedback from a single turn, core flux sensing winding via a pre-amp, driven from a sinusoidal signal source V_s . This is shown schematically in Figure F.2.

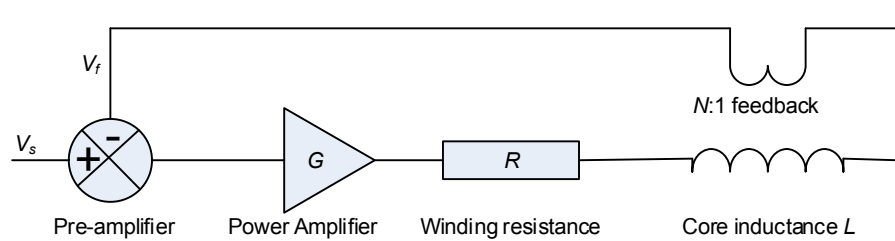


Figure F.2 Feedback flux stabilisation

The active gain G is the sum of the pre-amplifier and power amplifier, offset by the feedback winding ratio $N = 12$. The net loop gain without winding resistance is thus G/N . To determine the required gain, the feedback system was analysed. Where θ is core loss angle, ω angular frequency and $K = R/\omega L$, this gave the transfer function V_f/V_s as

$$\frac{V_f}{V_s} = \frac{G(\sin \theta + j \cos \theta)}{NK + (N + G)\sin \theta + j(N + G)\cos \theta}. \quad (2)$$

The excitation resistive error K_E can thus be computed from equation (1) and plotted in Figure F.3 which shows that for the target 3–4% error, a gain of 380–500 is required.

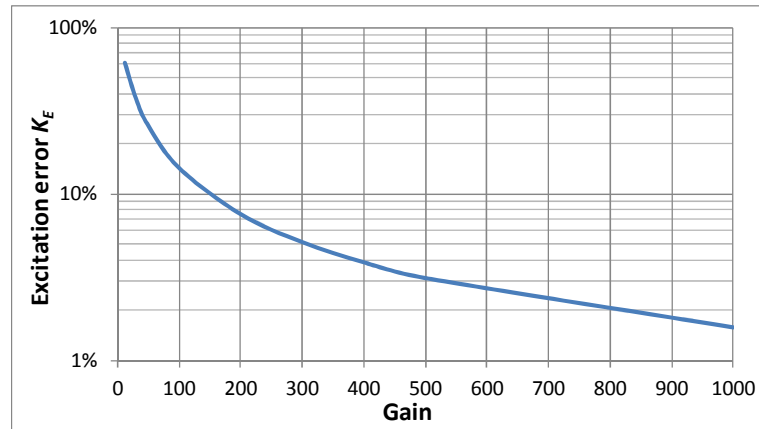


Figure F.3 Excitation error K_E with Gain

A battery-powered pre-amplifier was designed and constructed as shown in Figure F.4, having x10/x30 switchable gain. The inclusion of a large iron-cored transformer in the feedback loop causes substantial unknown phase shifts at low and high frequencies outside the normal 50/60Hz operation, thus feedback stability was determined experimentally. HF stability was maintained with a small HF roll-off, however a 1 Hz instability occurred at amplifier gains >1,000, resolved with a 0.8 Hz, 20° phase-lead, compensation network. This raised the critical gain to 1500, with the system nearly critically damped at a gain of 500 (overall loop gain = 41.7).

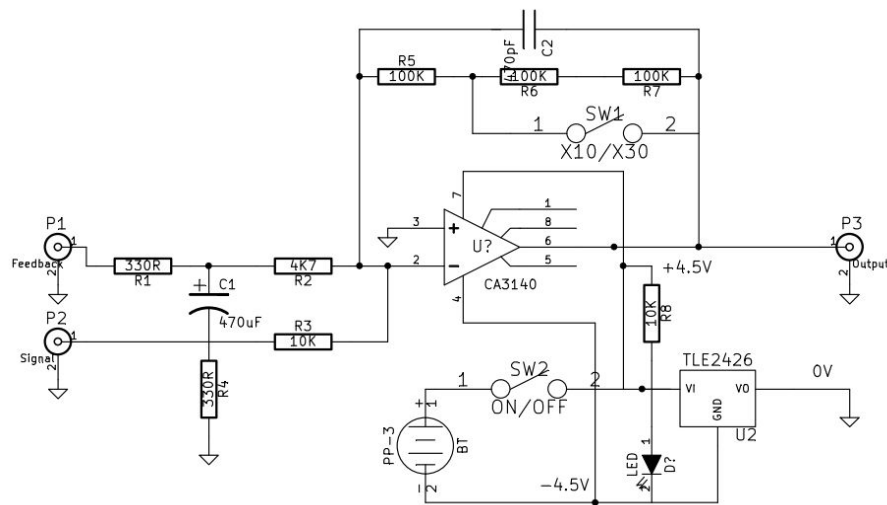


Figure F.4 Pre-amplifier schematic

F.4 Waveform synthesis

The use of mains electricity supply as excitation signal source has the problem that mains supply waveforms are notoriously ‘flat-topped’ due to non-linear loads, and the voltage is quite unstable over time, varying in practice by 1–2% quite quickly, with up to 6% changes possible. Frequency is statutorily regulated to +/-1%, though much less variation actually occurs and changes very slowly. Since a random measurement

uncertainty of >2% is undesirable, a synthetic sine wave drive was used for amplitude stability and low harmonic content, synchronised to mains to avoid beating effects with stray mains fields.

The sine wave signal generator TG5011 can operate in single-cycle burst mode, however when set to 51 Hz, so as to reliably trigger at worst-case mains of 50.5 Hz, this reduced the 3rd harmonic from -60 db to -37 db. In consequence a special arbitrary waveform shown in Figure F.5 was constructed from a 50 Hz sine wave cropped and stretched 2% such that, when run single-cycle burst at 51 Hz, the area under the two half-cycles becomes balanced to minimise distortion at 50 Hz.

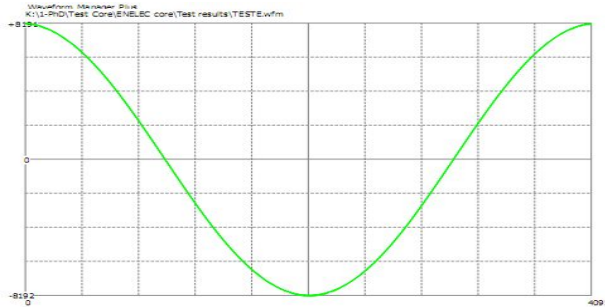


Figure F.5 50 Hz arbitrary waveform 'TESTE'

F.5 Feedback stabilisation tests

The overall system was then tested to determine its performance. The synthesised signal TESTE and excitation feedback drive was compared with a synthesised 50 Hz sinusoid directly driving the excitation winding. The voltage harmonics and THD were measured on a sense winding, and the excitation current was measured with a 0.1 Ω shunt. The values were normalised to 0 dB fundamental. All higher harmonics remained lower than the 5th. These show the flux harmonics reduced to <0.1% in Table F-2.

Test	Direct drive	Feedback stabilisation
Test level $3STV$	1.20 V	1.20 V
Test current (12 turns)	3.77 A	3.77 A
Feedback gain G	n/a	500
Excitation error K_E	45.2%	3.3%
Voltage Harmonics: Fundamental	0 dB	0 dB
3 rd	-29 dB	-60 dB
5 th	-45 dB	-75 dB
Voltage THD	3.5%	0.12%
Current Harmonics: Fundamental	0 dB	0 dB
3 rd	-31 dB	-28 dB
5 th	-48 dB	-46 dB
Current THD	2.8%	4.0%

Table F-2 Test results for excitation error and harmonic distortion

Appendix G. Lamination Toroidal Permeability

Since non-grain oriented electrical steel still exhibits significant magnetic anisotropy, this affects the net magnetic field strength needed to induce constant flux density in the curved flux path of a lamination section. A model is constructed to determine the net permeability of the lamination segment. The segment has its RD normal to the lamination midline, thus was modelled as the DAX8 example single $\pi/6$ half-section as shown in Figure G.1. The normal Epstein (50:50) measured relative permeability is μ_r and the anisotropy factor of the relative permeabilities of RD to TD, following the model for loss [211], is

$$K_A = \frac{(\mu_{RD} - \mu_{TD})}{(\mu_{RD} + \mu_{TD})}. \quad (1)$$

Rearranging terms gives

$$\mu_{TD} = \mu_{RD} / (1 + K_A) \quad \text{and} \quad \mu_{RD} = \mu_{TD} / (1 - K_A). \quad (2)$$

Thus by integrating the magnetic field strength for constant flux density along the mean flux density line the net toroidal relative permeability μ_{net} can be determined.

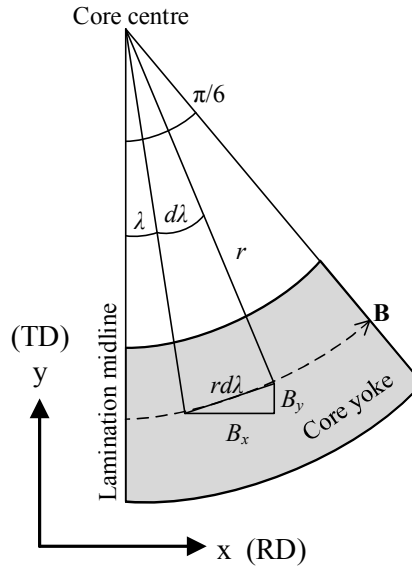


Figure G.1 Toroidal flux density path in lamination

In Figure G.1 the flux density B is assumed to be constant along the central core yoke path. Across an element $rd\lambda$ subtending $d\lambda$ at angle λ at the core centre away from the lamination mid-line, flux density vector \mathbf{B} develops components B_x and B_y parallel to the RD and TD. The magnetic field strength developed in these components, H_{RD} and H_{TD} is

$$H_{RD} = \frac{B \cos \lambda}{\mu_{RD}} \quad \text{and} \quad H_{TD} = \frac{B \sin \lambda}{\mu_{TD}}. \quad (3)$$

The mpd developed from the RD (MPD_{RD}) and TD (MPD_{TD}) magnetic field strength components in equation (3) is computed along their elemental lengths $r \cos \lambda$ and $r \sin \lambda$,

$$MPD_{RD} = \frac{rB \cos^2 \lambda d\lambda}{\mu_{RD}} \quad \text{and} \quad MPD_{TD} = \frac{rB \sin^2 \lambda d\lambda}{\mu_{TD}}. \quad (4)$$

Since the mpd between two points is independent of the integration path by *Ampère's law*, and assuming the two components are in phase, the total mpd (MPD) across the element $r d\lambda$ is simply $MPD_{RD} + MPD_{TD} = MPD$, hence

$$MPD = rB \left(\frac{\cos^2 \lambda}{\mu_{RD}} + \frac{\sin^2 \lambda}{\mu_{TD}} \right) d\lambda. \quad (5)$$

For n number of segments/circle, from equation (5) the average H field of the half lamination of angle π/n along the mean flux density line of length $r\pi/n$ is given by

$$H = \frac{n}{\pi} B \int_0^{\pi/n} \left(\frac{\cos^2 \lambda}{\mu_{RD}} + \frac{\sin^2 \lambda}{\mu_{TD}} \right) d\lambda. \quad (6)$$

In the Epstein test [238], the measure of relative permeability μ_r for the 50:50 mix of RD and TD lamination samples uses equal lengths of each sample, with identical flux density B induced in each. Summing the two sample magnetic field strengths and equation (7) gives

$$\frac{B}{\mu_r} = \frac{0.5B}{\mu_{RD}} + \frac{0.5B}{\mu_{TD}} \quad \text{hence} \quad \mu_{RD} = \frac{\mu_r}{(1 - K_A)} \quad \text{and} \quad \mu_{TD} = \frac{\mu_r}{(1 + K_A)}. \quad (7)$$

From equations (6) and (7), μ_{net} is given by

$$\frac{1}{\mu_{net}} = \frac{n}{\mu_r \pi} \int_0^{\pi/n} (1 - K_A \cos 2\lambda) d\lambda. \quad (8)$$

Equation (8) integrates to

$$\frac{1}{\mu_{net}} = \frac{1}{\mu_r} \left[1 - \frac{nK_A \sin(2\pi/n)}{2\pi} \right]. \quad (9)$$

The increase of μ_{net} over measured μ_r is evaluated from equation (9) for a range of lamination segmentation and K_A factors for CDW and Cogent M310-50A in Table G-1.

Segments/circle	μ_{net} as % μ_r	
	CDW $K_A = 22\%$	Cogent $K_A = 37\%$
6	123%	144%
8	125%	150%
12	127%	155%
18	128%	157%

Table G-1 Net toroidal permeability with lamination segmentation and magnetic anisotropy